Mechanistic Interrogation of Amoeboid T Cell Migration Reveals a Novel Role for the VPS34-PIKfyve Pathway in the Regulation of Cell Speed

Inauguraldissertation

zur

Erlangung der Würde eines Doktors der Philosophie

vorgelegt der

Philosophisch-Naturwissenschaftlichen Fakultät

der Universität Basel

von Philippe Georg Dehio

2024

Genehmigt von der Philosophisch-Naturwissenschaftlichen Fakultät

auf Antrag von

Erstbetreuer/in: Prof. Dr. Dr. Christoph Hess

Zweitbetreuer/in: Prof. Dr. Dirk Bumann

Externe/r Experte/in: Prof. Dr. Michael Sixt

Basel, den 17.10.2023

Prof. Dr. Marcel Mayor

Dekan

Table of Contents

1. Acknowledgments

Throughout and even before the course of my doctoral research, I have been fortunate to be surrounded by an amazing group of mentors, colleagues, collaborators, friends, and family. I am deeply thankful and humbled, for without their support, this journey would not have been possible.

Prof. Christoph Hess has been my supervisor and mentor since 2015, granting me the opportunity to join his laboratory as a master's student. His enthusiasm for science has been guiding me throughout this process. Without doubt, he has been integral to this thesis, my development and success. I am profoundly grateful for his unwavering support and the countless efforts he has invested to facilitate my progress.

Dr. Matthias Mehling began mentoring me when I was still a master's student and has continually guided me since that time. He has nurtured my curiosity and helped me to explore science through a different lens: Matthias, you awakened my love for microscopy and cell migration, a passion that will stay with me. I am deeply appreciative of all your support and mentorship.

Over the years, I have had the privilege of working alongside many incredibly bright individuals in the immunobiology laboratory. I wish to extend my heartfelt thanks to all past and current members of the laboratory for fostering a fantastic atmosphere and nurturing a collaborative environment. I am grateful to: Prof. Maria Balmer, Dr. Glenn Bantug, Dr. Bojana Durovic-Müller, Raja Epple, Dr. Marco Geiges, Dr. Jasmin Grählert, Dr. Patrick Gubser, Jessica Jäger, Dahye Lee, Leyla Develioglu, Dr. Jordan Löliger, Sarah Roffeis, Dr. Rebekah Steiner, Dr. Rebeccah Mistry, Sabine Tschirren, Dr. Gunhild Unterstab, Dr. Anett Jandke, Dr. Lucien Fabre, Dr. Anne Valérie Burgener, Sophie Saboz, Celia Makowiec, Elia Scanga, Ertha Xhafa, Nadia Schlauri, Dr. Fredrik Trulsson, Dr. Francesc Baixauli, Cécile Demarez, Emran Ajeti; and my esteemed colleagues in Cambridge: Dr. Adrià-Arnau Marti Lindez, Dr. Joy Edwards Hicks, Katharina Patommel, Leila Khani, and Dr. Ommar Omarjee.

Jonas shared his high hopes when they were most needed. Thank you, Jordan, for all these great ideas exchanged over tea. Adrià, may the force be with you, my friend. Jasmin, I appreciate your friendship and singing. Guni, I always look forward to our rock-paper-scissor matches after lunch. Sarah – for you, I will always have some kimchi in my fridge. Cécile, I will never forget that frozen Kinder Bueno. Elia, you have been the vino to my water. Anett, thank you for keeping us afloat. I would like to credit Maria for her mentoring and thank her for involving me in the various projects we worked on together.

Prof. Dirk Bumann kindly agreed to be a member of my PhD advisory committee, and I would like to thank him for his valuable input and time dedicated throughout this journey. Prof. Michael Sixt generously agreed to serve as the external expert on my Ph.D. advisory committee, which I deeply appreciate. His expertise has greatly helped to shape my research, and I have thoroughly enjoyed exchanging ideas with him.

Further, I would like to extend my gratitude to the many collaborators for their effort, time, and work they put into our projects: Dr. Thorsten Schäfer and Prof. Matthias Wymann gave me the tools to investigate VPS34 and PIKfyve, therefore significantly contributing to the inception of this project. Prof. Klaus Okkenhaug, Dr. Juan Carlos Yam-Puc, and Dr. Adrià-Arnau Marti Lindez provided valuable help and assistance with the in vivo mouse experiments. Dr. Lucien Fabre performed the electron microscopy. Prof. Thierry Soldati and Dr. Céline Michard's work on Dicty cells was instrumental in putting our observations in perspective. Prof. Daniel Legler kindly provided labelled chemokines. Dr. Michael Abanto, Dr. Loic Sauteur, and Dr. Ewelina Bartoszek-Kandeler from the imaging core facility always supported my microscopy endeavors. In close collaboration and with the expertise of Dr. Kim Arnold and Prof. Pablo Sinues, we were able to develop the volatile metabolomics platform, to which Dr. Kapil Dev Singh and Prof. Diego Garcia-Gomez significantly contributed. Dr. Corina Frick, Dr. Philip Dettinger, and Divya Chaudhary greatly assisted me in the beginning stages of my Ph.D., helping to set up the microfluidic device and cell migration assays. Dr. James West conducted the metabolomics analysis, and Dr. Julien Roux assisted with the transcriptome analysis.

My doctoral research was generously funded by a MD-PhD scholarship of the Swiss Academy of Medical Sciences and the Swiss National Science Foundation and a contribution of the Freiwillige Adakemische Gesellschaft Basel.

A group of close friends - Kian Hunziker, Manuel Sutter, Riccardo Hartmann, Kai Wegmann, and Matthias Meichtry - have walked with me shoulder to shoulder. Thank you for lifting me up, all the way up the rooftop terrace.

Clara Lessing – together we laugh. And when I stumble, you pick me up, and we laugh again. Thank you for being there and loving me as I am.

Finally, I want to express my deepest gratitude to my wonderful family, particularly my parents, Dr. Michaela and Prof. Christoph Dehio. You laid the foundation for everything I have achieved. Your unwavering love and embrace have carried me throughout. I remain your forever grateful son.

2. Abbreviations

ACLY: ATP-Citrate Lyase
ACSS: Acetyl-CoA Synthetase
Ca^{2+}: Calcium
CFU: Colony Forming Unit
CoA: Coenzyme A
DAG: Diacylglycerol
DC: Dendritic Cell
Dicty: *Dictyostelium Discoideum*
ECAR: Extracellular Acidification Rate
ECM: Extracellular Matrix
EE: Early Endosomes
ELC: Non-muscle Myosin IIA Essential Light Chain
ER: Endoplasmic Reticulum
ETC: Electron Transport Chain
FYVE Domain: FYVE Zinc Finger Domain
GEF-H1: Guanine Exchange Factor H1
HEV: High Endothelial Venules
IFN-γ: Interferon-γ
IP: Intraperitoneal
IP$_3$: Inositol Trisphosphate
IP$_3$R: Inositol Trisphosphate Receptor
ko: knock-out
LE: Late Endosome
LmOva: Ovalbumin expressing *Listeria monocytogenes*
LPS: Lipopolysaccharide
MCS: Membrane Contact Sites
ME2: Malic Enzyme 2
Mg^{2+}: Magnesium
MLCK: Myosin Light Chain Kinase
MLCP: Myosin Light Chain Phosphatase
MLIV: Mucolipidosis Type IV
MS: Mass Spectrometry
MTMRs: Myotubularins
MTOC: Microtubule-Organizing Center
Myosin IIA: Non-muscle Myosin IIA
NAADP: Nicotinic Acid Adenine Dinucleotide Phosphate
OCR: Oxygen Consumption Rate
OGDH: Oxoglutarate Dehydrogenase
PDMS: Polydimethylsiloxane
PI: Phosphatidylinositol
PI3KC1 / -2 / -3: Phosphatidylinositol-3-kinase Class 1, 2 or 3
PKM: Pyruvate Kinase
RLC: Non-muscle Myosin IIA Regulatory Light Chain
ROCK: Rho-associated Coiled-coil-containing Kinases
SESI-HRMS: Secondary Electrospray Ionization-High Resolution Mass Spectrometry
SHMT2: Serine Hydroxymethyltransferase 2
SLO: Secondary Lymphoid Organs
TCA Cycle: Tricarboxylic Acid Cycle
TGN: Trans-Golgi Network
TPC: Two-pore Channel
VOCs: Volatile Organic Compounds

3. General Summary

This thesis explores the intricate regulatory mechanisms governing amoeboid cell migration. It follows a cumulative format, beginning with an introduction, followed by a section delineating the aims of this thesis. The results chapter is divided into four sections (Sections I-IV), comprising a preprint, a set of unpublished data, and two published research articles. The final chapter, "Conclusion & Future Perspectives" relates the presented findings to a broader context and outlines possible directions for future studies.

In the results *Section I*, titled "*Engagement of the VPS34–PIKfyve Axis at the Uropod Promotes Fast Amoeboid Migration*", we reveal a novel role of the VPS34–PIKfyve lipid kinase pathway on endo-lysosomes at the uropod of migrating T cells. The findings, detailed in a preprint accompanied by extended data, underscore the necessity of VPS34 and PIKfyve activity for rapid migration of T cells. VPS34 and PIKfyve promote myosin IIA and retrograde actin flow, which are critical for T cell propulsion. Notably, this effector function of the VPS34–PIKfyve axis on amoeboid migration speed is conserved across myeloid cells, and the social amoeba *Dictyostelium discoideum*. This section encapsulates the main outcomes of my doctoral research.

Section II of the results, titled "*Interrogation of Chemokine-Induced Metabolism in Naïve CD8$^+$ T cells*", unveils findings from an investigation into the chemokine-induced metabolic alterations in T cells in a set of unpublished data. These results elucidate alterations in glycolytic metabolism and mitochondrial respiration initiated by chemokines and provide first insights into the scope of chemokine-induced metabolic rewiring.

The results in *Section III*, titled "*Acetate Modulates Memory CD8$^+$ T Cell Effector Function, Survival, and Migration During Bacterial Infections*", contain a published manuscript that explores the modulatory effects of acetate on memory CD8$^+$ T cell function during bacterial infections. In this context, an investigation unraveled an inhibitory effect of acetate on the migration of memory $CD8^+$ T cells *in vitro*, aligning with alterations in cell numbers at sites of acetate treatment *in vivo*.

Lastly, *Section IV,* titled "*Development of a Volatile Metabolomics Platform for Dendritic Cells to Investigate Cellular Metabolism in Real-Time*", comprises a published manuscript describing the development of a platform capable of real-time monitoring of dendritic cell metabolism in the volatile phase. We demonstrate the ability of this novel experimental platform to discern varying metabolic states of dendritic cells and trace the incorporation of isotopically labeled glucose.

4. Introduction

4.1. Biological Processes Underpinning Amoeboid Cell Migration

4.1.1 Cell Migration in Organismal Homeostasis and Pathology

Cell motility is an integral process for the homeostasis of unicellular and metazoan organisms across the eukaryotic domain. The ability to migrate enables unicellular organisms to forage, sexually reproduce, and adapt to the environment. A prominent example is the social amoeba *Dictyostelium discoideum* (*Dicty*) that relies on motility to predate bacteria and to aggregate for sexual reproduction.[1,2] Further, the choanoflagellate *Salpingoeca rosetta* switches from flagella-propelled swimming to amoeboid motility in spatially confined environments. This switch of motility modes enables this organism to escape confinement.[3]

Metazoans organisms rely on cell migration for development, wound healing, and effective immunity.[4,5] The pivotal role of cell migration is notably illustrated during brain development. Neurons migrate in intricate ways to organize the various cell layers of the cerebral cortex.[6,7] Further, cell migration is required to heal wounds. Surrounding fibroblasts of damaged tissue invade and remodel the extracellular matrix of the wound bed, thereby mending the defect.[8] Moreover, cellular motility takes center stage in the defense against pathogens. Various steps of T cell-mediated immunity are facilitated by cell migration. First, naïve T cells constantly search for their cognate, pathogen-related antigen presented on dendritic cells (DCs). For this naïve T cells must actively move through lymphoid organs.[9] Upon encountering their antigen, they activate, proliferate and become effector cells. Now poised to fight the pathogen, effector T cells subsequently migrate out of lymphoid tissues and re-locate to the pathogen-affected tissue. For instance, during a *Toxoplasma gondii* infection, cytotoxic CD8$^+$ T cells infiltrate and patrol the brain in pursuit of eliminating infected cells.[10]

Consequently, alterations in immune cell migration can be catastrophic and contribute to the development of human diseases. T cells from patients harboring an autosomal-recessive loss-of-function mutation in the DOCK8 gene struggle to coordinate their cytoskeleton. This causes a migration-dependent shattering and demise of protective T cells in dense microenvironments such as the skin. As result, these patients are broadly immunocompromised and particularly susceptible to viral infections of the skin.[11,12] On the other hand, dysregulated cell migration contributes to the pathogenesis of autoimmune disease such as multiple sclerosis. In patients suffering from multiple sclerosis, autoreactive B- and T-cells infiltrate the central nervous system and demyelinate neurons.[13] This situation, however, presents a therapeutic opportunity that has been successfully exploited. Effective treatment strategies for patients with multiple sclerosis include both blocking T cell egress from lymph nodes and preventing adhesion to the brain endothelium.[14]

Fundamentally, cell migration is a critical biological phenomenon and essential to a multitude of homeostatic processes in both unicellular and metazoan organisms. It is integral in the progression of various human diseases and insights into the underlying mechanisms governing cell migration have provided the basis for the development of therapeutic strategies.

4.1.2 Modes of Eukaryotic Single-Cell Motility

Given the central role of cell migration, substantial efforts have elucidated different modes of cellular locomotion and the underlying cellular mechanisms. Generally, metazoan cells demonstrate two predominant modes of single-cell motility: mesenchymal and amoeboid, along with less common modes such as swimming, flagellar, and osmotic engine motility.[15] These methods are distinguished through unique propulsion mechanisms, cytoskeletal structures, migration speeds, interactions with the extracellular matrix (ECM), and specific cellular organization.

Typically exemplified by fibroblasts, mesenchymal migration features slow migration speeds (~0.5 μm / min.), irregular cellular shapes with multiple protruding edges, and significant interactions with the ECM through focal adhesions and actin stress fibers.[16] In contrast, amoeboid migration is characterized by rapid migration speeds (exceeding 5 μm / min.) facilitated by dynamic cytoskeletal rearrangements, and a defined front-to-back polarity.[17] Neutrophils, DCs, and T cells, as well as unicellular eukaryotes like *Dicty* perform amoeboid migration. Amoeboid migrating cells exhibit a distinct polarization with a leading edge (cell front) and uropod (cell rear).[18] Within the amoeboid mode, migration is further subdivided into pseudopod, stable bleb, and bleb-based amoeboid migration.[19] Pseudopod migration is characterized by actin polymerization-driven cell protrusion at the leading edge. In contrast, stable bleb and bleb-based modes are defined by single, respectively multiple, actin-free cell membrane protrusions.[20] However, these sub-modes are not strictly isolated but interact synergistically to facilitate amoeboid cell movement.[21]

The interaction with the ECM varies noticeably between mesenchymal and amoeboid movement. Notably, amoeboid migration can occur without the strict necessity for adhesion proteins like integrins, facilitating cellular movement.[22] Meanwhile, mesenchymal migration depends on focal adhesions for propulsion. Mesenchymal migrating cells even transition to an amoeboid migration in environments with low adhesion and confinement.[23,24] Contrary to amoeboid migration, mesenchymal movement remodels the ECM by pericellular proteolysis.[25]

Furthermore, some cell types, such as T cells, exhibit swimming motility in suspension, characterized by a retraction of cellular protrusions and/or transmembrane molecules from the leading edge to the uropod.[26,27] Since swimming is observed in amoeboid migration cells, it may be considered a subclass of amoeboid migration. Another distinct motility type is the osmotic engine, observed in spatially confined migrating cancer cells. The osmotic engine utilizes polarized water channels (aquaporins) and ion pumps (Na^+/H^+ pumps) to propel cells forward by displacing water from the front to the rear end.[28,29] Flagellar propelled swimming is predominantly observed in unicellular organisms. In humans, sperm cells rely on flagellar motion for movement.[30]

In conclusion, metazoan organisms have developed a diverse range of cell migration modes to facilitate the movement of cells. Amoeboid migration is conserved across the eukaryotic domain and its hallmarks encompass cellular polarization with a clear front-to-back axis and fast migration speeds relying on cytoskeleton dynamics.

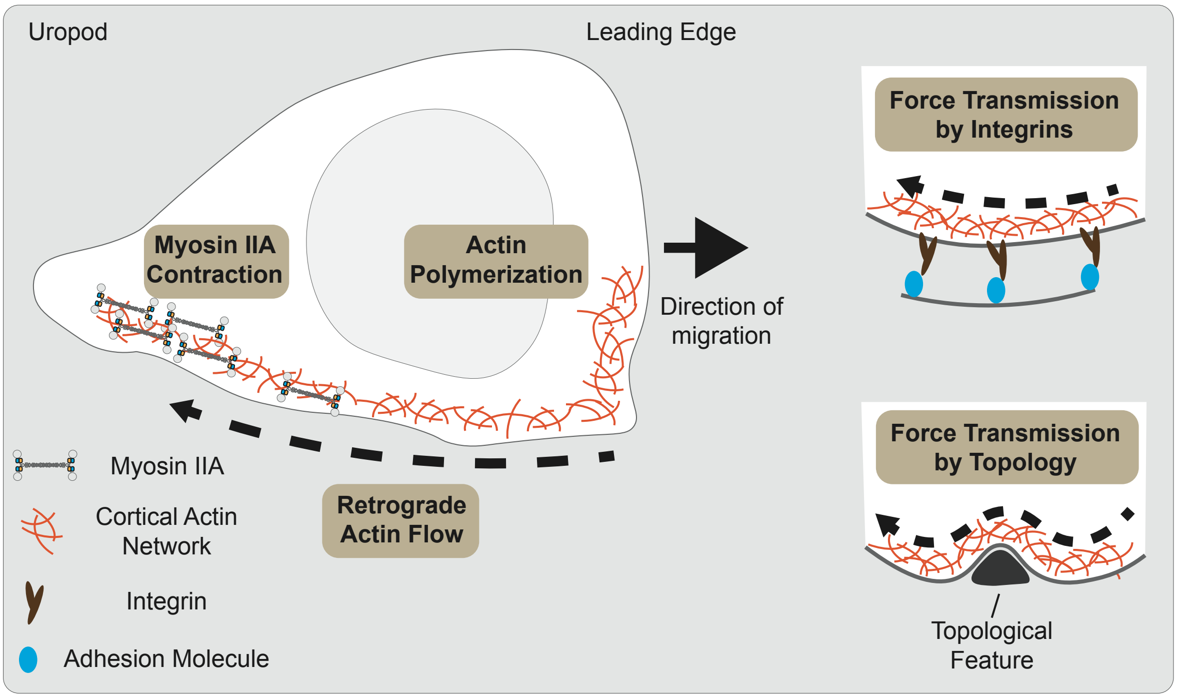

Figure 1: Amoeboid Cell Propulsion and Force Generation I The propulsion forces that facilitate amoeboid cell migration are primarily generated through retrograde actin flow. This process necessitates two concurrent actions: actin polymerization at the leading edge, and myosin IIA-mediated contraction of the actin network at the uropod. The force generated through this process is transmitted to the extracellular matrix via integrins, which establish connections between the actin flow and cellular adhesion molecules or by pushing against extracellular topological features.

4.1.3 Amoeboid Cell Propulsion

Cell propulsion requires the generation of an internal force, which is transmitted to the extracellular space. The fundamental mechanism driving amoeboid cell migration hinges on dynamics of the actin cytoskeleton, which generates the requisite force (**Fig. 1**). Actin polymerization at the leading edge and contraction of the actin network by non-muscle myosin IIA (myosin IIA) at the rear end of the cells results in a cortical actin flow toward the uropod (i.e. retrograde actin flow).[22,31–36] This actin flow entails the force transmitted to the extracellular environment. Actin polymerization also protrudes the plasma membrane forward in the direction of migration, generating a pseudopod. Alternatively in bleb-based amoeboid migration, increased intracellular pressure, also provided by myosin IIA contraction, pushes the cell membrane at the leading edge forward.[17] Cell protrusions at the front and cell retractions at the uropod are synchronized by myosin IIA activity, thereby preserving a coherent cell shape.[33]

The force generated within cells is conveyed to the extracellular environment by a process analogous to the functioning of a clutch. The type of clutch engaged depends on the specific characteristics of the microenvironment. T cells couple the retrograde actin flow via the integrin LFA-1 to extracellular adhesion molecule ICAM-1. Thereby, the force from the actin flow is transmitted and propels the cell forward.[37] DCs similarly engage in integrin-dependent migration when adhesion molecules are available. However, DCs without any integrins cannot couple the retrograde actin flow but still manage to maintain comparable migration speeds.[31] In fact, DCs without integrins migrate efficiently through 3D matrix pores but they fail to adhere and migrate on 2D surfaces.[22] In confined spaces like a 3D matrix, amoeboid cells utilize the topography of the microenvironment (e.g. collagen fibers) to transmit force, making integrins dispensable (**Fig. 1**).[38]

Thus, amoeboid cell propulsion entails a coordinated mechanism involving actin polymerization at the cell front and actin network contraction by myosin IIA at the uropod, fostering retrograde actin flow and consequently, force generation. The same mechanism also preserves a coherent cell shape during cell migration. The force generated by actin flow is transmitted to the extracellular environment by either integrins or topological features in confined environments.

4.1.4 Cellular Polarization of Amoeboid Migrating Cells

Forming and maintaining a stable cellular polarization with a leading edge and uropod is indispensable for effective amoeboid migration. This front-to-back axis defines the direction of actin flow and thereby the direction of motion. The process of cellular polarization within the context of amoeboid migration is fundamentally self-organizing. Yet, pro-migratory stimuli (e.g. chemokines) can initiate and sustain this polarization.

Spontaneous directed actin flow (i.e. symmetry-breaking) is already observed in simplistic systems, such as meiotic cytoplasm from Xenopus egg extracts in spatially confined oil droplets. In this system, inhibition of myosin IIA reduces the speed of retrograde actin flow but is not pivotal for symmetry breaking.[39] However, in cells - specifically in fish keratocytes - spontaneous polarization is prefaced by myosin IIA activity at the evolving uropod, which initiates directional actin flow and cell migration.[40] These observations resonate with findings in other cellular systems. For instance, T cell polarization is impaired by myosin IIA inhibition. The transition from mesenchymal to amoeboid migration, instigated by confinement and low adhesion, is contingent on myosin IIA activity.[23,41] Thus, the establishment of a front-to-back axis in cellular polarization is orchestrated through both actin polymerization and myosin IIA contractility.

Even though cell polarization occurs spontaneously, pro-migratory stimuli (such as chemokines) initiate and sustain cell polarization by RhoA and Rac1/-2 GTPase signaling. Chemokines are secreted proteins that activate chemokine receptors and induce G-protein- and subsequent GTPase-signaling.[42] Chemokine receptor signal transduction is further detailed in the introduction section *4.3.2*. RhoA activates myosin IIA via ROCK at the uropod, while Rac1/-2 promotes actin polymerization through Cdc42 at the leading edge.[43–45] The small GTPases, RhoA and Rac1/-2 mutually inhibit each other, thereby self-organizing spatially delineating the zones of actin polymerization and myosin IIA activity.[46,47]

Thus, cell polarization is primarily a self-organized process that necessitates a myosin IIA-mediated actin network contraction, thereby establishing a directional axis for the force-producing actin flow. Polarization occurs spontaneously but external stimuli (e.g. chemokines) induce and sustain this self-organizing process by inducing Rac1/-2 and RhoA signaling.

4.1.5 Structure, Regulation, and Pharmacological Interventions of Myosin IIA

Myosin IIA plays a pivotal role in the polarization and force generation in amoeboid migrating cells. Belonging to the myosin superfamily, this motor protein has been thoroughly studied for its ability to convert chemical energy into physical force. Its activity can be pharmacologically modulated to alter cellular migration.

The structure of myosin IIA consists of three pairs of peptide chains: non-muscle heavy chain, regulatory light chain (RLC), and essential light chain (ELC). The heavy chain itself is structured into a globular head, a neck and a tail domain that partners with another heavy chain to form the myosin IIA hexamer.[48,49] The globular head domain binds to F-actin and includes a magnesium (Mg^{2+})-ATPase motor domain. Both RLC and ELC are non-covalently attached at the neck domain (**Fig. 2A**).[50]

In the resting state, the tail domain is bent, thereby inhibiting the Mg^{2+}-ATPase motor domain. Myosin IIA activation begins with the phosphorylation of RLC at Serine 19 by the myosin light chain kinase (MLCK) and Rho-associated coiled-coil-containing protein kinase (ROCK). This process liberates the tail domain from the globular head, initiating the Mg^{2+}-ATPase activity.[51–53] Further amplification of Mg^{2+}-ATPase activity occurs through Threonine 18 phosphorylation by MLCK.[54] Conversely, RLC is deactivated by the myosin light chain phosphatase complex (MLCP; **Fig. 2A)**.[55]

MLCK and ROCK kinase activity are regulated by two distinct pathways. Increased cytosolic calcium (Ca^{2+}) binds to calmodulin, thereby activating MLCK and can be pharmacologically blocked with ML-7.[52,56,57] Alternatively, ROCK activity is triggered by RhoA and can be inhibited by the compound Y-27632.[58,59] In turn, RhoA activity is promoted by the guanine exchange factor H1 (GEF-H1). GEF-H1 is inactive when associated with microtubules.[60–62] Notably, the application of microtubule destabilizing agents like Nocodazole amplifies myosin IIA activity by releasing GEF-H1 (**Fig. 2B**).[33,63]

Active Myosin IIA forms homotypic bipolar filaments, which connect to F-actin. The binding of ATP to the Mg^{2+}-ATPase dissociates the globular head domain from F-actin. The subsequent ATP hydrolysis instigates a conformational shift by straightening the neck domain and allows re-attachment to F-actin. The subsequent phosphate release causes re-bending in the neck domains, thereby exerting force onto the bound F-actin strands (**Fig. 2C**).[50] Blebbistatin directly inhibits myosin IIA activity by binding to the Mg^{2+}-ATPase.[64]

To summarize, myosin IIA requires activation through the Ca^{2+}-Calmodulin-MLCK and / or RhoA-ROCK pathways to promote amoeboid cell migration. Bending and re-bending of the myosin IIA neck domain generates force and is fueled by ATP hydrolysis. Pharmacological inhibition of either regulatory pathway or ATP hydrolysis is commonly exploited in amoeboid cell migration studies to manipulate myosin IIA activity dynamics.

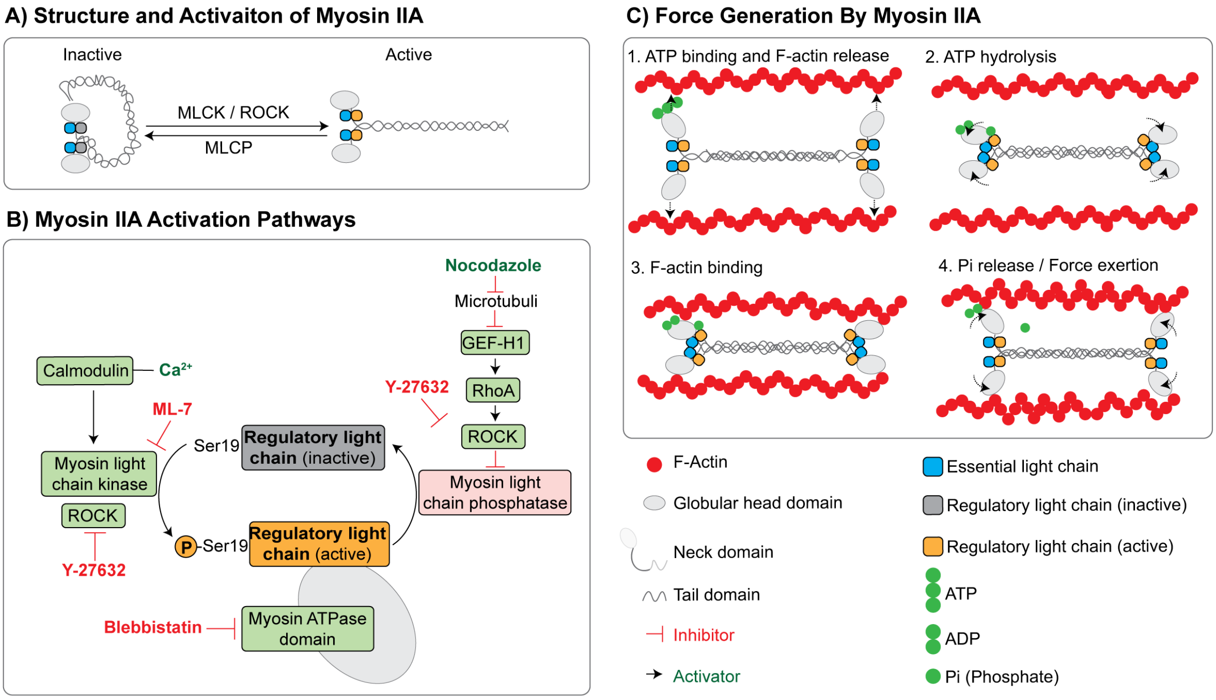

Figure 2: Myosin IIA Activation Pathway and Related Force Generation I A) The myosin IIA heavy chain is composed of pairs of globular head, tail, and neck domains. The latter binds to both the essential light chain (ELC) and the regulatory light chain (RLC). The phosphorylation of myosin IIA by MLCK and / or ROCK induces a conformational change that enables the activity of the Mg^{2+}-ATPase. This change can be reversed by MLCP. **B)** The regulatory pathways controlling myosin IIA activity include the Ca^{2+}-calmodulin-MLCK pathway and the RhoA-ROCK pathway. Various elements within these pathways, including the Mg^{2+}-ATPase, can be pharmacologically targeted to modulate myosin IIA activity. **C)** Once activated, myosin IIA forms homotypic dimers and binds to F-actin. ATP binding to the head domain triggers the release from F-actin, initiating a cycle of conformational changes. The hydrolysis of ATP induces straightening of the head domain, enabling it to bind to F-actin again. The subsequent release of phosphate causes the neck domain to bend once more, exerting force onto the attached actin filament.

4.1.6 Organelle Positioning in Amoeboid Migrating Cells

Polarization in amoeboid migrating cells reorganizes cellular ultrastructure beyond the cytoskeleton and extends to organelles as well (**Fig. 3A)**. In fact, the reorganization of cell organelles supports amoeboid migration in various capacities. Resting T cells are barely motile and round but polarize and migrate upon chemokine exposure.[65,66] Therefore, they can be employed as a cellular system to study cell polarization and organelle redistribution in the wider context of amoeboid migration.

In T cells, chemokines induce mitochondrial fission and relocate along with microtubules and the microtubule-organizing center (MTOC) to the uropod. Here, mitochondrial ATP synthesis promotes myosin IIA RLC phosphorylation (**Fig. 3B**). Blocking either microtubule-dependent translocation or fragmentation of mitochondria, decreases the fraction of polarized T cells and impairs their migration.[67,68] However, the location of the MTOC in amoeboid migrating cells is a subject of debate. An *in vivo* study reported that the MTOC of migrating neutrophils is located in front of the nucleus[69]. This contrasts various other studies where the MTOC is found in the uropod in neutrophils, DCs, *Dicty* and T cells.[63,70–72] The role of the MTOC and the arising microtubules in amoeboid migration remain incompletely understood. Manipulation of microtubules indirectly affects myosin IIA activity by the aforementioned interplay with GEF-H1. This confounds inference of the role microtubules in amoeboid migration. However, this effect was exploited to demonstrate that microtubule-mediated myosin IIA activation controls amoeboid cellular shape in complex environments.[63]

Similar to the MTOC the Golgi apparatus' location is contested. In migrating T cells, it is located in the uropod, while in DCs it has been reported to be located in front of the nucleus and also in the uropod.[73–75] However, the localization of the MTOC and Golgi apparatus behind the nucleus away from the leading edge is distinct for polarized amoeboid ultrastructure. Mesenchymal cells position their Golgi apparatus together with the MTOC in front of the nucleus towards the leading edge, for instance during wound healing in fibroblasts.[76–79]

The positioning of the endoplasmic reticulum (ER) in amoeboid cell migration is not well documented. In DCs, the inositol 1,4,5-trisphosphate receptors (IP_3R) on the ER regulates Ca^{2+} efflux to activate calmodulin–MLCK–myosin IIA and enables migration in spatially confined environments.[80] A special role has been assigned to the nucleus. The nucleus functions as a ruler to measure the pore size of the extracellular matrix and choose the path of least resistance.[81] Other organelles such as early endosomes and endo-lysosomes are also located in the uropod. They significantly contribute to amoeboid cell migration and are discussed in the subsequent sections *4.1.7* and *4.1.8*.

Together, a considerable body of evidence suggests an accumulation of most cell organelles (including mitochondria, the Golgi apparatus, endocytosis machinery, and endo-lysosomes) at the uropod (**Fig. 3A**). Nevertheless, this localization may vary depending on the cell type or specific context. Crucially, the strategic placement of these organelles at the uropod and their associated pathways directly augments amoeboid cell migration by optimizing myosin IIA activity.

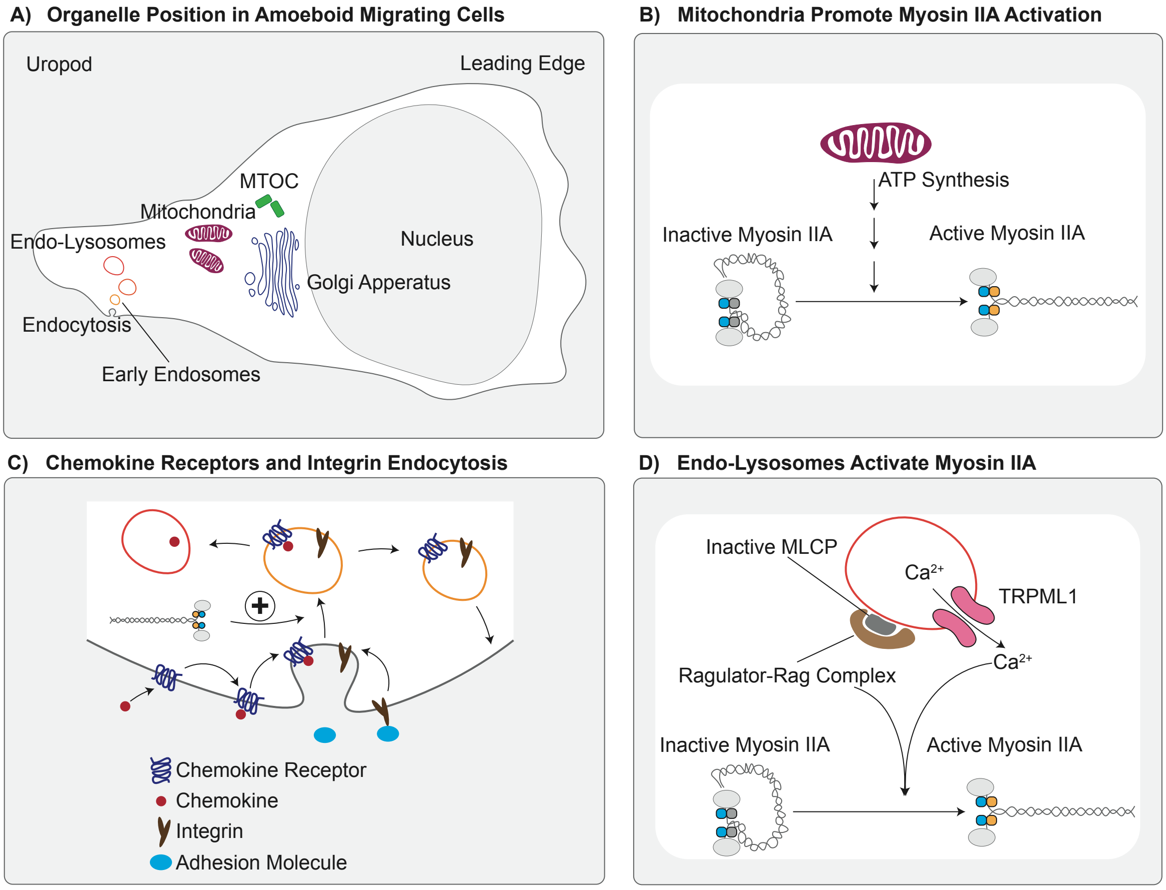
A) Organelle Position in Amoeboid Migrating Cells

B) Mitochondria Promote Myosin IIA Activation

C) Chemokine Receptors and Integrin Endocytosis

D) Endo-Lysosomes Activate Myosin IIA

Figure 3: Organelle Positioning in Amoeboid Migrating Cells I A) In polarized cells, most studies indicate the majority of cell organelles to be located at the uropod. **B)** The activity of myosin IIA is augmented by mitochondrial ATP production. **C)** Endocytosis at the uropod aids in the removal of integrins and ligated chemokine receptors from the plasma membrane, a process dependent on myosin IIA. This promotes the recycling of these membrane proteins and assists in the detachment of the uropod from the extracellular space. **D)** Endo-lysosomes play a critical role in myosin IIA activation, primarily by facilitating Ca^{2+} efflux via TRPML1 channels and through the inactivation of MLCP by the Ragulator-Rag complex.

4.1.7 The Endo-Lysosomal System in Amoeboid Cell Migration

The various functions of the endo-lysosomal system intersect with different facets of amoeboid cell migration. The endo-lysosomal system consists of a spectrum of intracellular vesicles enabling cells to take up, deliver, recycle, and degrade extracellular and cellular material. Early endosomes (EEs) are formed through endocytosis by invaginating and budding parts of the plasma membrane.[82] EEs either undergo homotypic fusion or mature to late endosomes (LE). Some cycle back to the plasma membrane as recycling endosomes, thereby enabling membrane protein recycling. EEs are characterized by the membrane effector protein Rab5 and are weakly acidic (pH ~6.2).[83] The maturation of EEs to LE is mediated by a Rab switch (Rab5 to Rab7).[84] LEs, in turn, are part of a cycle wherein LEs fuse with lysosomes, thereby delivering material for degradation. These vesicles later resolve by fission and fuse again with LEs.[85] This fusion and fission cycle of LE and lysosome represents a continuum of vesicles, making a distinction between LEs, lysosomes, or intermediate forms difficult. Thus, they arguably represent a functional unit and are here referred to as *endo-lysosomes*. Endo-lysosomes are characterized by the membrane proteins Lamp1 and / or Rab7. EEs and endo-lysosomes are bidirectionally connected with the trans-Golgi network (TGN). Vesicles transport effector proteins such as hydrolases from the TGN to EEs or endo-lysosomes.[86,87] Conversely, EEs or LEs also recycle transmembrane proteins to the TGN.[88]

Endocytosis and early endosomes are localized at the uropod of neutrophils, T and *Dicty* cells and remove integrins from the plasma membrane.[89–94] This uncouples integrins from adhesion molecules and in turn detaches the uropod from the ECM. Likewise, upon ligation the chemokine receptors are endocytosed. When the chemokine CCL19 binds to CCR7, both are endocytosed and then trafficked in two different directions. CCL19 is directed to the endo-lysosomal system for degradation and CCR7 is recycled back to the plasma membrane, ready to signal again.[95] CCR7 receptor-mediated-endocytosis depletes CCL19 from the direct vicinity of DCs. This affects local chemokine availability and subsequent directional migration of the cell collective.[96] Myosin IIA activity enables endocytosis, unraveling an additional role of myosin IIA-dependent regulation in amoeboid migration.[91,97–99] Hence, endocytosis at the uropod is integral for the uptake and recycling of integrins and chemokine receptors and is regulated by the myosin IIA (**Fig. 3C**).

In amoeboid migrating cells, it has been postulated that endocytosed components undergo exocytosis at the leading edge, a concept known as “fountain flow”. This theory encompasses a continuous cycle where membrane and membrane proteins are endocytosed at the uropod and recycled to the leading edge. In turn, the plasma membrane flows from the leading edge to the uropod. Observations of retrograde membrane flow in *Dicty* cells experiments support this hypothesis. However, in T cells, no such membrane flow has been observed.[100,37] Formal proof of fountain-flow entails detection of exocytosis at the leading edge. In mesenchymal migrating cells, exocytosis reporters have demonstrated integrin trafficking from the Golgi to the leading edge.[101,102] Although the localization of endosomes and endocytosis at the uropod is well-documented in various amoeboid migrating cell types, evidence for exocytosis at the leading edge is lacking.

In summary, endocytosis underpins amoeboid migration by promoting cell detachment and membrane protein recycling. It requires myosin IIA and is restrained to the uropod. Here, removing integrins from the plasma membrane facilitates cell detachment. Further, ligated chemokine receptors are endocytosed enabling recycling but also shaping local chemokine availability.

4.1.8 Endo-Lysosomes Control Amoeboid Migration by Activating Myosin IIA

Recent discoveries shed light on the role of endo-lysosomes in regulating myosin IIA activation in dendritic cells (DCs). Notably, the endo-lysosomal Ca^{2+} channel, TRPML1 co-localizes with the lysosomal transmembrane protein Lamp1 at the uropod of DCs. TRPML1-knock-out (ko) cells display slower migration and diminished F-actin at the uropod, indicative of reduced retrograde flow. Pharmacological activation of TRPML1 accelerates migration and induces calcium transients in DCs. These findings indicate that Ca^{2+} release from endo-lysosomes via TRPML1 activates myosin IIA at the uropod, thereby regulating actin dynamics and DC migration speed.[103] Subsequently, Rab7b was demonstrated to regulate DC speed by linking TRPML1 to myosin IIA. Like TRPML1-ko cells, Rab7b-ko cells exhibit disrupted actin dynamics and reduced levels of RLC phosphorylation. TRPML1 activation partially rescued myosin IIA activation.[104] Endo-lysosomes at the uropod also harbor the Ragulator-Rag complex. The Ragulator-Rag complex binds MPRIP, a subunit of the MLCP, thereby increasing myosin IIA activity, promoting a cohesive cell shape and migration.[105]

Collectively, these findings underscore that in dendritic cells, endo-lysosomes are situated at the uropod and foster cell migration through myosin IIA activation. This is achieved by the efflux of calcium from endo-lysosomes via TRPML1 and the deactivation of MLCP by the Ragulator-Rag complex. Whether these mechanisms extend to other types of amoeboid migrating cells remains unexplored (**Fig. 3D**).

4.1.9 Metabolic Requirements for Amoeboid Cell Migration

Amoeboid cell migration significantly relies on energy in the form of ATP. A complex network of enzymes and chemical reactions – known as intermediary metabolism – facilitates energy generation. Intermediary metabolism also synthesizes essential metabolites required for macromolecule assembly. The production of ATP primarily occurs through glycolysis—a process where glucose is oxidized to pyruvate, and via the electron transport chain (ETC) fueling the ATP-synthase in mitochondria. The tricarboxylic acid (TCA) cycle plays a pivotal role by reducing the coenzymes and electron acceptors NAD^+ and FAD^+ to NADH + H^+ and $FADH_2$, respectively. Oxidation of NADH and $FADH_2$ by the ETC fuels the creation of a proton gradient across the inner mitochondrial membrane. A proton flux through the ATP-synthase in the inner mitochondrial membrane facilitates the production of ATP. This process, called oxidative phosphorylation, necessitates oxygen as the final electron acceptor and thereby constitutes a significant portion of cellular respiration.[106]

Chemokines modulate mitochondria in various ways, including their positioning, function, and morphology. During chemokine-induced cell polarization, mitochondria are fragmented and subsequently relocated to the uropod.[68,107] At the uropod, mitochondrial ATP synthesis is integral to T cell migration, by aiding in the phosphorylation of myosin IIA RLC.[67,108,109] Further, simultaneous treatment of chemokines and integrin augments mitochondrial respiration in T cells.[109]

Glycolysis emerges as a central metabolic pathway for amoeboid cell migration. DC and T cell migration requires the assimilation of extracellular glucose and ensuing glycolytic metabolism.[110–112] Glycolysis is induced by ligation of various chemokine receptors, including CXCR4, CXCR3, CCR4, and CCR7.[109–111,113] Additionally, several other pathways, including Toll-like receptor signaling in DCs, stimulate glycolysis, thereby promoting glycolysis-dependent migration.[112] It is noteworthy that several costimulatory molecules (LFA-1, CTLA4, and CD28) engage glycolysis and thereby modulating the migration and localization of regulatory T cells to inflammatory sites *in vivo*.[111] Mechanistically, ATP production at sites of actin polymerization by glycolytic enzymes has been proposed to provide energy for F-actin formation.[111,114] Moreover, glycolysis contributes to the oligomerization of CCR7 in DCs. This leads to efficient signaling and therefore maintains polarized cell shape and migration.[112,115]

Aligned with cellular polarization, a compartmentalized energy production has been postulated in amoeboid migrating cells.[116] This paradigm proposes a synergistic role of ATP synthesis by glycolysis at the leading edge to support actin polymerization, while mitochondrial ATP fosters myosin IIA activation at the uropod. This intricate interplay hints at a reciprocal regulation of amoeboid cell polarization and cellular ATP production. Moreover, glycolysis-driven chemokine receptor oligomerization extends the role of cellular metabolism beyond energy production. Notably, the engagement of intermediary metabolism in response to chemokine signaling, beyond glycolysis, remains relatively unexplored.

4.2 The Phosphatidylinositol Lipid Kinase VPS34–PIKfyve Axis

4.2.1 Phosphatidylinositol Lipid Pathways and Membrane Localization

Phosphatidylinositol lipids (PIs) are central to cellular homeostasis in eukaryotes. They recruit and activate effector proteins by providing molecular motifs at specific subcellular locations. Despite their importance, PIs only constitute 10% of all phospholipids and less than 1% of all lipids in cell membranes.[117,118] PIs are synthesized in the ER.[119] Then distinct lipid kinases and phosphatases modify the phosphorylations at the third, fourth, and fifth carbon in the inositol ring, bestowing unique identities to the PI (**Fig. 4A**). Structurally, PIs feature two fatty acid chains, commonly in the form of diacylglycerol (DAG), coupled with inositol through a phosphate group situated at the first position. The fatty acid chains of DAG anchor PIs into membranes.[120]

Mono-phosphorylations of the inositol ring predominantly occur on endomembranes.[121] At the Golgi apparatus, PI4KA/-B phosphorylate PI, converting it to PI(4)P.[122] VPS34, encoded by *PIK3C3*, drives the conversion of PI to PI(3)P on EEs and endo-lysosomes.[123] Additionally, PI(3)P is found on autophagosome precursor membranes (i.e. the ER and omegasomes).[124,125] The kinase, PIKfyve contains a PI(3)P-binding FYVE zinc finger domain (FYVE domain), and therefore localizes to sites of PI(3)P. PIKfyve phosphorylates PI(3)P to PI(3,5)P$_2$.[126] On the other hand, myotubularins (MTMRs) dephosphorylate the third position of the inositol ring, converting PI(3,5)P$_2$ to PI(5)P and PI(3)P to PI, respectively.[127–131]

At the plasma membrane, PI4P5K converts PI(4)P to PI(4,5)P$_2$, followed by its transformation to PI(3,4,5)P$_3$ by class 1 phosphatidylinositol-3-kinases (PI3KC1).[121] PI3KC1 are widely studied PI-kinases and relay extracellular signals to activate diverse cellular processes.[132,133] The PI3KC1 variant, PI3Kγ, participates in chemokine receptor signaling.[134–138] In polarized amoeboid migration cells, PI(3,4,5)P$_3$ is localized at the leading edge, facilitating F-actin polymerization, while PI(3,4)P$_2$ and PI(4,5)P$_2$ concentrate at the uropod plasma membrane.[139–142]

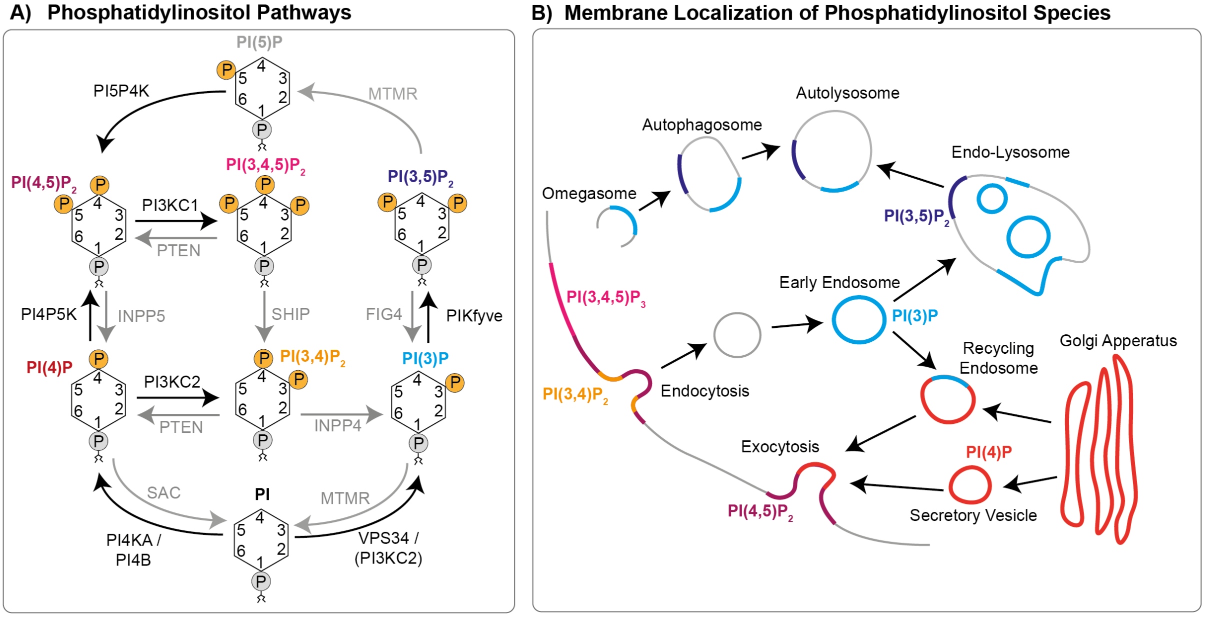

Figure 4: Phosphatidylinositol Lipid Pathways and Localization on Endomembranes I A) PI pathways with their respective kinases (in black) and phosphatases (in grey). Orange P symbols mark phosphorylation on the respective position of the inositol ring. The grey P at position 1 is the linker of the inositol group to the membrane-integrated fatty acid chains. **B)** Main membrane distribution and trafficking routes of PI species.

In contrast, class II PI3-kinases remain relatively elusive and hold distinct roles to VPS34 or PI3KC1. PI3KC2α converts PI(4)P to PI(3,4)P_2 at the plasma membrane, a critical step in endocytosis.[143] It also governs the transition of PI to PI(3)P on the primary cilium in reaction to shear stress.[144] Moreover, in liver cells, PI3KC2γ operates as a Rab5 effector on early endosomes, where it produces of PI(3,4)P_2.[145]

4.2.2 VPS34: Partners, Effectors, Function, Murine Models and Pharmacological Inhibitors

VPS34 was first described in 1990 as a protein governing vacuolar protein sorting in baker's yeast.[146] It is the only PI3K conserved across the eukaryotic domain and is the founding member of the PI3K family.[147] Human VPS34 is ubiquitously expressed and shares extensive sequence homology with its yeast counterpart.[148] The main effector mechanism of VPS34 is the local synthesis of PI(3)P on membranes thereby recruiting proteins containing PI(3)P-binding FYVE-zinc finger or PX domains.[149]

VPS34 forms two distinct complexes: Complex I with VPS15, Beclin-1, and ATG14; and Complex II with VPS15, Beclin-1, and UVRAG.[150] VPS15 is the regulatory subunit of VPS34 and anchors VPS34 complexes to membranes.[151] Beclin-1 has multiple post-translational modification sites that fine-tune VPS34 activity, and its membrane-binding capacity is essential for VPS34's function.[123,152,153]

Complex I is defined by the presence of ATG14 as a third partner and localizes to autophagosome precursor membranes.[154] Starvation-induced inhibition of MTORC1 leads to ULK1 activation, which in turn phosphorylates ATG14 in the VPS34 Complex I.[155,156] VPS34 Complex I then produces PI(3)P, thereby enabling assembly of the autophagy machinery (including ATG16L1, ATG12, ATG3, and LC3) and subsequent autophagosome formation.[157–159]

Complex II, defined by the presence of UVRAG, regulates endo-lysosomal homeostasis.[160,161] Active (GTP-bound) Rab5 binds VPS15, thereby targeting the VPS34 Complex II to early endosomes, initiating the local production of PI(3)P.[162,163] PI(3)P recruits EEA1 and Hrs, which control endosome docking, transport, recycling, and homotypic fusion.[164–167] Endosomal PI(3)P also facilitates endosome maturation by recruiting Mon-1 and Ccz1, which deactivate Rab5 and recruit Rab7.[168–171] A pool of PI(3)P resides on endo-lysosomes and facilitates lysosomal fission.[172,173] The role of the PI(3)P effector PIKfyve is discussed subsequently (*4.2.3)*.

PI(3)P can be imaged with a fusion protein of two FYVE-domains with a GFP (2xFYVE-GFP) or a PX-domain fused to GFP.[174,175] These probes bind to PI(3)P and thereby reveal the subcellular location. Studying VPS34 was long hampered by the lack of selective inhibitors and the embryonic lethality of whole-body knockouts.[176–178] However, cell-specific VPS34 deletions in mouse models revealed the importance of VPS34-dependent autophagy for normal liver and heart function and T cell survival.[179,180] Alongside, the development of highly selective inhibitors (e.g. VPS34-In1, PIK-III, and SAR405) complemented the tool box needed to study VPS34 biology.[181–185] Both genetic depletion of VPS34 and pharmacological inhibition induce an accumulation of large vesicles in cells, reflective of VPS34's central role in controlling endo-lysosomal homeostasis.[179,184,186]

Taken together, VPS34 intricately controls various aspects of endo-lysosomal homeostasis and autophagy by locally producing PI(3)P and recruiting specific effector proteins to endomembranes. Advances in biomedical research have provided valuable tools to study the complex biology of VPS34 and PI(3)P in greater detail.

4.2.3 PIKfyve Contributes to Cell Migration and Human Disease

PIKfyve is targeted to PI(3)P-containing endomembranes through its FYVE domain and thus is primarily found on early endosomes, endo-lysosomes and autophagosomes.[187–189] Like VPS34, PIKfyve functions within a complex, which is composed of scaffolding protein Vac14 pentamer and the PI(3,5)P_2 phosphatase Fig4. Steric hindrance within the complex restricts access to the membrane-bound PI species to either Fig4 or PIKfyve. The complex's lipid kinase and phosphate activities are influenced by protein phosphorylation. Autophosphorylation of PIKfyve inhibits PI(3,5)P_2 synthesis and amplifies Fig4 phosphatase activity. In a reciprocal regulation, Fig4 phosphorylation of PIKfyve promotes PI(3,5)P_2 synthesis.[126]

Precise knowledge on the role and function of PIKfyve, its product PI(3,5)P_2, and their effectors are limited. Concentration measurements are difficult due to PI(3,5)P_2's scarcity and the first reliable sensor for PI(3,5)P_2 was only recently published.[190,191] A well-characterized effector PI(3,5)P_2 is TRPML1, as detailed further in *4.2.5*.[192] The VPS34–PIKfyve axis facilitates mesenchymal cell migration by promoting integrin recycling through the SNX17-Retriever to the TGN.[188,193,194] Further, mesenchymal cancer cells migration is promoted by PI(5)P produced by VPS34–PIKfyve–MTMR3 (**Fig. 4A**). PI(5)P activates Rac1 and actin polymerization.[77,195] Likewise, PIKfyve inhibition negatively affects neutrophil migration, correlating with reduced Rac1/-2 activity.[196]

Similar to VPS34, PIKfyve deficiency leads to substantial vesicle accumulation in cells across various species (e.g. humans, mice, zebrafish, and *Dicty*).[191,194,197,198] This vesicular accumulation is characterized by increased endo-lysosomal markers Lamp1 and Rab7 and aligns with decreased endo-lysosomal fission and increased fusion.[199,200] Another parallel to VPS34 is the embryonic lethality of PIKfyve in whole-body knock outs. Hence, *in vivo* studies require cell specific deletions of PIKfyve.[201] Selective inhibitors for PIKfyve (Apilimod and YM201636) are commonly used to study PIKfyve biology. Apilimod has been and is undergoing clinical evaluation for conditions like Crohn's disease and B-cell cancers.[197,202–205]

PIKfyve contributes to several human pathologies with an apparent focus in neurodegenerative diseases. For instance, PIKfyve inhibition prevents amyotrophic later sclerosis in preclinical models.[206] The loss of PIKfyve causes neuronal spongiosis (= large vesicles) in prion diseases.[207] Additionally, mutations within the PIKfyve–Vac14–Fig4 complex have been linked to several human diseases, including Charcot-Marie-Tooth type 4J, Yunis-Varon syndrome, congenital cataract, and primary lateral sclerosis.[208] Lastly, PIKfyve inhibition halts RNA virus replication (e.g. SARS-CoV-2, Zika virus) by impairing endosomal maturation and preventing viral entry into the cell.[209,210]

In summary, PIKfyve converts PI(3)P produced by VPS34 to PI(3,5)P_2 and is required for mesenchymal and neutrophil migration. A well-established effector of PI(3,5)P_2 is TRPML1, which regulates Ca^{2+} flux from endo-lysosomes into the cytoplasm. Various studies implicate PIKfyve in the pathogenesis of human diseases.

4.2.4 TRPML1 on Endo-Lysosomes Contributes to Cytosolic Calcium Homeostasis

Calcium (Ca^{2+}), a bivalent cation and signaling molecule, plays a pivotal role in regulating diverse cellular functions, including metabolism, apoptosis, migration, and growth. Therefore, cytoplasmic Ca^{2+} concentrations are tightly controlled in a range from 100 to 1000 nM. Cells regulate these levels through multiple methods, including: (i) Exchanging Ca^{2+} with the extracellular environment via transport proteins, and (ii) buffering Ca^{2+} within organelles such as the ER, mitochondria, and endo-lysosomes.[211–213]

Endo-lysosomes are cellular Ca^{2+} stores with concentrations around 0.5 mM and actively participate in cytosolic Ca^{2+} signaling.[214,215] Both a proton / Ca^{2+} exchange and IP_3R-dependent Ca^{2+} flux from the ER (proton-independent) have been brought forward as possible hypotheses for Ca^{2+} uptake into endo-lysosomes.[216–219] On the other hand, endo-lysosomal Ca^{2+} release is regulated by two-pore channel (TPC) and TRPML1. The TPC opens upon binding of the second messenger nicotinic acid adenine dinucleotide phosphate (NAADP) and TRPML1 is activated by PI(3,5)P_2 (further detailed in *4.2.6*).[192,220,221] Ca^{2+} efflux through TRPML1 also triggers Ca^{2+} efflux from the ER into the cytosol.[222]

All Ca^{2+}-storing organelles– the ER, endo-lysosomes, and mitochondria – can be tethered to each other to form tight membrane contact sites (MCS). These MCS facilitate Ca^{2+} transport between the ER, endo-lysosomes, and mitochondria, respectively, which is mediated by IP_3R and TRPML1.[218,219,223] However, the physiological implications of MCS in Ca^{2+} handling remain elusive.

In conclusion, the ER, mitochondria, and endo-lysosomes all contribute to cellular Ca^{2+} handling. Endo-lysosomes release Ca^{2+} through TRPML1 or TPC and thereby participate in cytosolic Ca^{2+} homeostasis and signaling.

4.2.5 Regulation of TRPML1, Associated Cellular Functions and Diseases

TRPML1 (encoded by *MCOLN1*) is allosterically activated by PI(3,5)P_2, which binds to an N-terminal, positively charged domain on the cytosolic side of the endo-lysosome.[192,221] PI(3,5)P_2 induces a conformational change, opening the central pore of TRPML1 and allowing Ca^{2+} influx into the cytoplasm.[192] Conversely, PI(4,5)P_2 inhibits TRPML1-dependent Ca^{2+} flux.[224] This offers an explanation for the restriction of TRPML1 activity on endo-lysosomes. Ca^{2+} flux can also be induced pharmacologically with the TRPML1 agonists ML-SA1 and MK6-83.[225,226]

TRPML1 has various cellular functions, which rely on the activation of calcium-binding signaling proteins such as calcineurin and calmodulin. Thereby, TRPML1 controls the induction of autophagy by activating TFEB and VPS34.[227,228] Additionally, TRPML1 is required for lysosomal exocytosis.[229,230] Further, TRPML1 induces lysosomal fission and TRPML1 overexpression reverses PIKFYVE-inhibition-induced vesicle formation.[221,231] Simultaneously, it promotes lysosome fusion with phago- or autophagosomes and assists in their intracellular trafficking.[232–235] Lastly, TRPML1's role in the regulation of DC migration via activation of myosin IIA has been discussed in *4.1.8* of the introduction.

Mucolipidosis type IV (MLIV) is a rare, autosomal recessive lysosomal storage disease caused by mutations in *MCOLN1*.[236–238] Clinically, MLIV presents with ocular manifestations (e.g. retinopathy, corneal clouding and strabismus), cognitive, and psychomotor impairment.[239] MLIV patient-derived fibroblasts also exhibit increased numbers of cytosolic vesicles.[240] While most mutations introduce a premature stop codon in *MCOLN1*, a few point mutations reduce the agonistic effect of PI(3,5)P_2 on TRPML1.[226]

Thus, binding of $PI(3,5)P_2$ to TRPML1 enables Ca^{2+} flux from endo-lysosomes into the cytosol, which activates calcium-dependent proteins such as calmodulin and calcineurin. These mediators regulate various functions including vesicle fusion and fission, as well as autophagosome formation. Mutations in the TRPML1 encoding gene are causative for the rare genetic disease MLIV. Importantly, TRPML1 has been linked to amoeboid migration by activating myosin IIA in DCs.

4.3 Function and Migration of T Cells

4.3.1 T Cell Subsets and Associated Functions

T cells are instrumental for the immune system's functioning. Their vital roles have propelled extensive research efforts to decipher their functions, including aspects of amoeboid migration. Classified into several categories, each T cell subset embodies specific functions driven by their intrinsic cell biology. Broadly, these cells are separated into conventional and innate-like T cells. Conventional T cells express an $\alpha\beta$ T cell receptor (TCR) that identifies cognate peptide antigens presented on MHC-I or II molecules. This category comprises the cytotoxic $CD8^+$ and helper $CD4^+$ T cells. Whereas, innate-like T cells encompass natural killer T cells, mucosal-associated invariant T cells, and $\gamma\delta$ T cells, all of which function as innate-like immune cells. Innate-like T cells do not recognize classical peptide epitopes, unlike their conventional counterparts.[241]

Conventional naive T cells are antigen inexperienced. They navigate from the bloodstream into secondary lymphoid organs (SLOs), eventually returning to the bloodstream via the thoracic duct. Within SLOs, naive T cells scan presented antigens on antigen-presenting cells (e.g. dendritic cells). Upon TCR-binding to their cognate antigen, naïve T cells undergo activation, followed by proliferation and acquisition of effector function.[242,243] Effector T cells (or T cell blasts) then exit the SLO and relocate to their respective effector sites (e.g. sites of infection). Here, cytotoxic effector $CD8^+$ T cells target and eliminate cancerous or infected cells that display their cognate antigen on MHC-I molecules.[244] Activated helper $CD4^+$ T cells differentiate into various effector subsets (Th1, Th2, Th17, Tfh, and Treg) depending on the cytokine milieu during activation. These different $CD4^+$ T cell subsets orchestrate the immune response to different pathogen classes. For instance, Th1 cells develop in response to intracellular pathogens, while Th17 cells protect against extracellular pathogens. Regulatory CD4$^+$ T cells modulate immune reactions to mitigate potential harm to inflamed tissues.[245,246]

Following the primary immune response, a notable proportion of effector T cells undergo contraction. Few T cells persist as memory cells and serve as an immunological memory. Memory T cells mount a rapid and robust immune response to previously encountered pathogens bypassing the lengthy priming and effector maturation of naïve T cells.[247] In line, memory T cells are strategically placed in the organism to facilitate optimal responses during secondary infections. They are further stratified in central, effector and tissue-resident T cells. Central memory T cells reside in SLOs but also circulate through the blood – like effector memory T cells. Tissue-resident memory cells are restricted to non-lymphoid tissues (e.g. the skin), where they constantly scan the environment for their cognate antigen.[248]

In summary, the various subsets of conventional T cells facilitate a nuanced adaptive immune response to pathogens.

4.3.2 Chemokine Signaling Regulates T Cell Migration and Positioning

Chemokines and their respective receptors control positioning and motility of T cells. Dependent on cell type and environmental context, conventional chemokine-receptor signaling evokes various motility responses. These include chemotaxis (directed movement), chemokinesis (increased, non-directed motility), haptotaxis (directed movement along substrates with immobilized chemokines), adhesion, migratory arrest and transcellular migration (i.e., extravasation).[42,249,250] On the other hand, atypical chemokine receptors are involved in scavenging chemokines to modulate their extracellular availability. However, they are not present on T cells.[251]

Conventional chemokine receptor signaling is complex. It is primarily facilitated by pertussis-toxin-sensitive G-proteins and β-arrestin. Upon receptor ligation, a receptor-associated trimeric G-protein exchanges GDP for GTP, which detaches the βγ-subunits from the α-subunit. Subsequently, this activates PI(4,5)P_2 cleavage by phospholipase C to generate IP_3 and DAG.[252,253] IP_3 increases cytosolic Ca^{2+} level by activating IP_3R on the ER, while DAG activates protein kinase, which contributes to T cell polarity.[254,255] The G-protein signaling cascade also activates DOCK2, a guanine-exchange factor pivotal for T cell polarization and migration by fostering the activation of Rac1/-2.[256,257] DOCK2 also modulates Rap1, instrumental in uropod formation through the activation of RhoA and myosin IIA.[47,258] Further, chemokine signaling activates integrins via Rap1, facilitating T cell adhesion.[259] Together, this complex and intricate signaling network poises T cells to adhere, polarize and migrate.

Specific sets of chemokines present in the local environment and the repertoire of chemokine receptors expressed on the T cells dictate their position within the organism. Below, three prominent chemokine–chemokine–receptor systems illustrate the regulation of T cell positioning. The chemokine receptor CCR7 is key for naïve T cell homing and recruitment into T cells zones within SLOs. First, L-selectin induces T cell rolling on high endothelial venules (HEV) of lymph nodes. Then, the chemokine CCL21 on HEVs, activates the CCR7, which in turn induces LFA-1 to bind to ICAM-1 on HEVs and facilitates cell adhesion. T cells then polarize and crawl on HEVs, and subsequently transmigration into the lymph node stroma.[260] Here, fibroblastic reticular cells express CCL19 (another ligand for CCR7), and CCL21 to guide naive T cells into the T cell zone, where they encounter DCs.[261,262] Another exemplary chemokine–chemokine receptor pair is CXCL13 and CXCR5. The expression of CXCR5 on follicular helper $CD4^+$ T cells (Tfh) allows these cells to sense CXCL13 expressed in B cell follicles and therefore enter germinal centers. Here, they support B cell differentiation into memory or plasma cells and facilitate persistent antibody production.[263–265] Further, effector T cells express CXCR3. Its ligands – the chemokines CXCL9 and CXCL10 – are expressed at sites of inflammation. They recruit effector T cells from the circulation to these sites of inflammation, where they subsequently fulfill their effector role.[266]

In conclusion, chemokines and their receptor-mediated signaling dictate the T cell motility, positioning, and recruitment at various points of T cell-mediated immunity. A complex signaling network, consisting of G-proteins and small GTPases promotes cell polarization, cytoskeleton dynamics, and integrin activation. Distinct combinations of chemokine receptor expression and the localized secretion of corresponding ligands guide T cells to their designated microenvironment.

4.3.3 Cellular Metabolism Governs T Cell Functionality

The functioning of T cells is intricately connected to cellular metabolism, encompassing aspects such as activation, differentiation, proliferation, and migration. Naïve T cells are quiescent and their metabolism mainly supports cell survival.[267] However, upon antigen-induced T cell activation their metabolism must support proliferation, epigenetic remodeling, and increased bioenergetic demands, met through the reprogramming of cellular metabolism.[268,269] A central metabolic response to T cell activation is an increase in aerobic glycolysis. Glycolysis is fundamental for the acquisition of $CD8^+$ T cell effector function, including the synthesis of effector cytokines like interferon-γ (IFN-γ).[270,271] Differential metabolic repertoires that vary across T cell subsets drive their specific effector functions. This is exemplified by the glycolytic metabolism of effector memory $CD8^+$ T cells. Upon activation, an immediate increase in glycolysis enables generation of IFN-γ at a significantly quicker pace than their naïve counterparts.[272] Hence, immediate engagement of glycolysis is a prerequisite for a fast memory $CD8^+$ T cell response.

T cells are also influenced by the varying levels of metabolites present in the microenvironment. Their assimilation into the cellular metabolism alters associated T cell functions. Such a phenomenon is notably evident in tumor microenvironments, where infiltrating immune cells and tumor cells compete for nutrients.[273] Diminished glucose availability hinders T cell activation and suppresses the efficacy of tumor immunosurveillance.[274,275] Moreover, lactate in the synovial fluid of rheumatoid arthritis patients is absorbed by effector $CD4^+$ T cells and enhances the production of the proinflammatory cytokine interleukin 17. In parallel, lactate reduces glycolytic flux, thereby restricting migration and trapping T cells at the sites of inflammation, which exacerbates synovial inflammation.[110]

In summary, adequate cellular metabolism is a requirement for optimal T cell function. T cell subsets are characterized by differential metabolic capacities, supporting their specific functionalities. Moreover, extracellular metabolites are incorporated into the T cell metabolism, thereby altering their functions and, in turn, the immune response as a whole.

4.3.4 Acetate Regulates T Cell Effector Function

Acetate is a metabolite commonly detected in mammals.[276,277] In cells, acetyl-CoA synthetases (ACSS 1 and 2) convert acetate and coenzyme A (CoA) to acetyl-CoA. Acetyl-CoA participates in various reactions such as fueling the TCA cycle or providing an acetyl donor group for protein acetylation.[278,279]

In this context, acetate promotes glycolysis and enhances effector memory $CD8^+$ T cell function. During bacterial infections in mice, serum acetate levels transiently increase, and memory T cells assimilate acetate. This increases intracellular acetyl-CoA abundance, subsequently leading to the acetylation of the glycolytic enzyme GAPDH. Acetylated GAPDH exhibits increased catalytic activity. Pre-treatment of memory $CD8^+$ T cells with acetate leads to increased glycolysis following T cell activation, enhanced production of IFN-γ, and improved bacterial control.[280] Furthermore, acetate contributes to IFN-γ production by $CD8^+$ T cells in both homeostatic and glucose-restricted conditions.[281,279] Mechanistically, acetate-derived acetyl-CoA promotes histone acetylation, facilitating the expression of IFN-γ transcripts.[281]

In summary, acetate regulates T cell function under homeostatic conditions by promoting IFN-γ transcription. Additionally, increased acetate levels during systemic bacterial infections further enhance memory $CD8^+$ T cell functionality by boosting their glycolytic capacity when reencountering their cognate antigen. However, the variations of acetate levels in different microenvironments and how T cells might regulate acetate metabolism in a context-dependent manner remain unexplored.

4.4 Real-Time Monitoring of Cellular Metabolism

4.4.1 Methods to Study Cellular Metabolism in Real-Time

The metabolism of cells is central to their function, as exemplified for amoeboid cell migration and T cell function in *4.1.9* and *4.3.3*, respectively. While various direct and indirect techniques are available for assessing immune cell metabolism, only a few permit real-time monitoring. A prevalent method for evaluating real-time glycolysis and cellular respiration is the use of extracellular flux analyzers.[282,283] This approach necessitates a limited cell quantity and facilitates intra-assay injection of stimuli or inhibitors. The assessed parameters are surrogates for glycolysis (= extracellular acidification rate, ECAR) and cellular respiration (= oxygen consumption rate, OCR), offering a valuable, yet, limited view into cellular metabolic processes.

Another possibility to interrogate metabolism in real-time is the application of genetically encoded fluorescence biosensors (e.g. for glycolysis or the NAD/NADH$^+$ ratio).[284,285] However, here only a single aspect of metabolism at a time is monitored. Further, the application of these sensors entails transduction or transfection into the cell system of choice. Moreover, sensors might not be available for the metabolic pathway of choice.

Mass spectrometry (MS), coupled with liquid or gas chromatography, permits the identification of numerous metabolites found in cell lysates or medium. These techniques involve extensive sample preparation and provide end-point measurements.[286] The application of stable isotopically-labeled metabolites, such as glucose with carbon-13 (^{13}C), facilitates the tracking of metabolic pathways through MS, granting a dynamic view into cellular metabolism.[287]

An alternative for real-time cellular metabolism tracking utilizes mass spectrometry to probe the headspace of biological cultures. Typically, *in vitro* cell cultures are linked directly to secondary electrospray ionization-high resolution mass spectrometry (SESI-HRMS), which detects volatile organic compounds (VOCs) in the volatile phase. These VOCs, which evaporate at room temperature and ambient pressure, usually have a mass of up to 500 Da.[288] SESI-HRMS discerns isotopologue pairs, thus facilitating the tracing of labelled metabolites, as demonstrated in yeast cultures.[289] Previously, this non-invasive method successfully differentiated breast cancer cells from normal mammary cells *in vitro*.[290] Furthermore, SESI-HRMS are extremely sensitive as they detect VOCs emitted from 10^3 colony-forming units (CFU) of bacteria within minutes.[291] Nevertheless, this approach presents two substantial limitations: (i) only compounds produced by cells able to pass the plasma membrane into the culture medium and evaporate are detectable, and (ii) compound identification based on mass data is complex, given that these systems forgo chromatography.

In conclusion, the real-time monitoring of cellular metabolism remains challenging. Extracellular flux analysis yields insights into glycolysis and cellular respiration. Genetically encoded biosensors are not available for all metabolic pathways and solely analyze one metabolic parameter. MS analysis allows extensive metabolite identification and pathway tracking utilizing isotopically-labeled compounds but is an end-point measurement. The SESI-HRMS systems non-invasively detect metabolic processes by measuring VOCs.

5. Aims of the Thesis

Amoeboid cell migration is a complex and multifaceted process, integral to human physiology and disease. A significant layer of regulation hinges on the intricate cellular ultrastructure, which facilitates cytoskeleton dynamics to generate propulsion forces. Moreover, cellular metabolism, modulated by chemokines and the surrounding metabolic microenvironment, serves as another critical determinant of amoeboid motility. Throughout my doctoral research, I aimed to uncover new facets of the aforementioned regulators:

1. What aspects of the cellular ultrastructure are promoting amoeboid migration?

2. Which aspects of cellular metabolism are shaped by chemokines?

Given their pivotal role in host immunity, my primary focus was on T cells, offering a physiologically relevant lens to explore amoeboid migration. As a proven therapeutic target in the field of autoimmunity, enhancing knowledge on T cell migration might contribute to a broader effort in leveraging this process further. Interrogation of T cell migration also holds potential to reveal broader cell biological paradigms of amoeboid migration, as underlying mechanisms are largely conserved across the eukaryotic domain.

6. Results

6.1 Section I: Engagement of the VPS34–PIKfyve Axis at the Uropod Promotes Fast Amoeboid Migration

6.1.1 Summary

Amoeboid cell migration is a fundamental process underpinning various biological processes, including immunity and development. Our objective was to define structure-function relationships of amoeboid cell migration by studying organellar positioning and associated pathways in T cells. In the preprint titled “*An evolutionary-conserved VPS34-PIKfyve-TRPML1-Myosin II axis regulates the speed of amoeboid cell migration*”, we elucidate the role of the VPS34–PIKfyve lipid kinase pathway on endo-lysosomes in facilitating rapid amoeboid cell migration.

Imaging studies in polarized and migrating T cells demonstrate an endo-lysosomal relocation to the uropod, along with an active VPS34–PIKfyve pathway. VPS34 and PIKfyve promote myosin IIA activity and retrograde actin flow, thereby enabling efficient T cell propulsion. In the proposed molecular framework, VPS34–PIKfyve pathway produces PI(3,5)P_2, thereby inducing Ca^{2+} flux from the endo-lysosome into the cytoplasm through TRPML1 and activating myosin IIA. The ubiquitous expression of VPS34 and PIKfyve across the eukaryotic domain, directed us to test this observation beyond T cells. VPS34 and PIKfyve also regulated the migration speed in myeloid cells. Further, PIKfyve or TRPML1 orthologue knockout *Dicty* cells exhibited slower migration.

Together, our findings unveil the VPS34–PIKfyve axis as a conserved *speed control system* of amoeboid cell migration.

6.1.2 Author Contribution

This study was supervised and conceived by Christoph Hess (University of Basel and the University of Cambridge) and Matthias Mehling (University of Basel). Christoph Hess and Philippe Dehio wrote and edited the manuscript. Thorsten Schaefer (University of Basel) and Matthias Wymann (University of Basel) initially proposed inhibiting the VPS34–PIKfyve pathway, provided the necessary compounds and guided their application. Philippe Dehio performed and analyzed all live cell microscopy and migration experiments involving T cells, DCs, and neutrophils. He conducted immunofluorescence, immunoblotting, and flow cytometry experiments, and performed the sequence alignment, phylogenetic analysis, and in silico docking experiments. Lucien Fabre was responsible for the electron microscopy sample preparation and imaging. *Dictyostelium* cell migration experiments were carried out by Céline Michard (University of Geneva), with the analysis being jointly performed by Céline Michard and Philippe Dehio. Thierry Soldati (University of Geneva) supplied the *Dictyostelium* strains and contributed to the design of the *Dictyostelium* cell migration assays. The *in vivo* adoptive T cell transfer experiments were carried out by Adrià-Arnau Martí i Líndez (University of Cambridge), Juan Carlos Yam-Puc (University of Cambridge), and Philippe Dehio, with Klaus Okkenhaug (University of Cambridge) providing advice on the *in vivo* experiments and supplying the necessary mouse strains.

6.1.3 Preprint: *An evolutionary-conserved VPS34-PIKfyve-TRPML1-Myosin II axis regulates the speed of amoeboid cell migration*

The following preprint, titled "*An evolutionary-conserved VPS34-PIKfyve-TRPML1-Myosin II axis regulates the speed of amoeboid cell migration*", is currently in under peer review. It is accessible by the QR-code:

An evolutionary-conserved VPS34-PIKfyve-TRPML1-Myosin II axis regulates the speed of amoeboid cell migration

Philippe Dehio[1], Céline Michard[2], Juan Carlos Yam-Puc[3], Adrià-Arnau Martí i Líndez[4], Lucien Fabre[1], Thorsten Schaefer[5], Matthias P. Wymann[5], Klaus Okkenhaug[6], Thierry Soldati[2], Matthias Mehling[7], Christoph Hess[1,4,*]

[1] Department of Biomedicine, Immunobiology, University and University Hospital of Basel, 4031 Basel, CH
[2] Department of Biochemistry, Faculty of Science, University of Geneva, 1211 Geneva, CH
[3] MRC Toxicology Unit, University of Cambridge, Cambridge CB2 1QR, UK
[4] Department of Medicine, CITIID, University of Cambridge, Cambridge CB2 0AW, UK
[5] Department of Biomedicine, University of Basel, Cancer- and Immunobiology, Mattenstrasse 28, 4058 Basel, Switzerland
[6] Department of Pathology, University of Cambridge, Cambridge CB2 1QP, UK
[7] Department of Biomedicine, Translational Neuroimmunology, University of Basel and University Hospital Basel, 4031 Basel, CH
[*] Correspondence: Christoph Hess, email: ch818@cam.ac.uk

Graphical Abstract

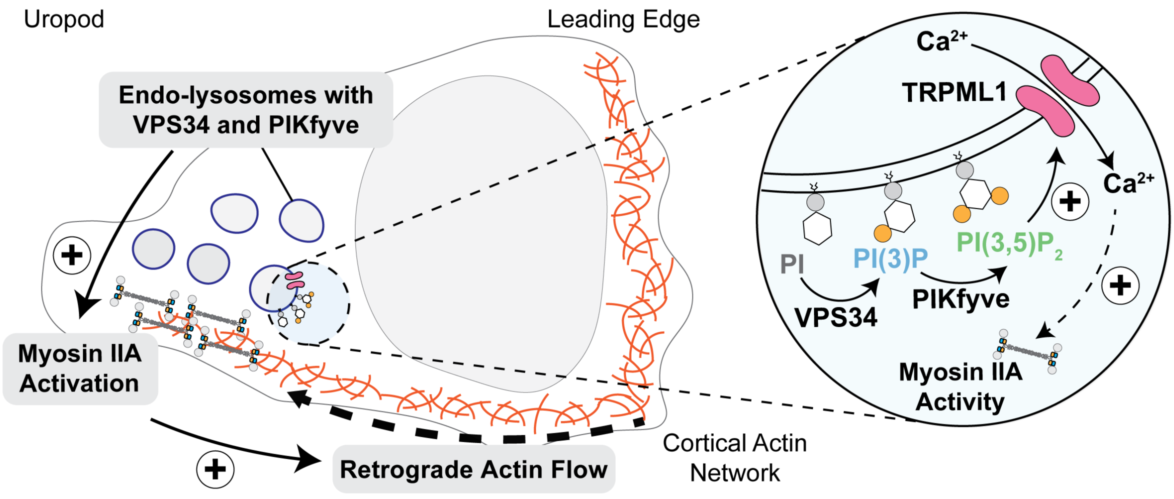

- The VPS34–PIKfyve axis is active on endo-lysosomes at the uropod of migrating T cells.
- VPS34 and PIKfyve promote myosin IIA activation and retrograde actin flow.
- Amoeboid cell migration speed is controlled by VPS34 and PIKfyve via TRPML1.
- Regulation of amoeboid migration speed is a conserved function of the VPS34–PIKfyve axis.

Abstract

Amoeboid cell migration is key to efficient T cell immunity. Spatial polarization of organelles within cells, including endo-lysosomes, is a prerequisite of migration. However, how ultrastructural polarization is linked to the signaling requirements governing T cell migration, remains unknown. Here we show that signaling molecules generated by endo-lysosome-localized kinases regulate velocity of amoeboid migration. Specifically, imaging of T cells identified accumulation of endo-lysosomes decorated with the lipid kinases VPS34–PIKfyve at the uropod of polarized cells. Activity of VPS34 and PIKfyve regulated speed, but not directedness, of migrating T cells. Mechanistically, PI(3,5)P_2 generated by the sequential action of VPS34 and PIKfyve mediated Ca^{2+} efflux from lysosomes via the mucolipin TRP cation channel 1 (TRPML1), thus controlling activity of myosin IIA and hence the generation of propulsive force through retrograde actin flow. The VPS34–PIKfyve kinases also regulated velocity of myeloid cells, as well as of the amoeba *Dictyostelium discoideum* – establishing the axis as an evolutionary conserved *speed control system* of amoeboid cell migration.

Introduction

Cell migration is critically involved not only in immunity, but also early embryonic development, tissue homeostasis and regeneration. Across the eukaryotic domain, crawling-like, or amoeboid, movement is the most prevalent mode of cellular motility, with origins predating the emergence of metazoans.[1] Amoeboid locomotion is characterized by bleb- or pseudopod-based membrane protrusion at the leading edge and retraction of the uropod – thereby establishing the direction of motion.[2–5] At the molecular level, actomyosin contractility at the uropod, and actin polymerization at the leading edge, drive a retrograde actin flow, which propels cells forward when transmitted to the extracellular space.[6–10] This directed motion of F-actin is regulated via phosphorylation of the non-muscle myosin IIA regulatory light chain (RLC).[11] RLC is phosphorylated, and hence activated, by myosin light chain kinase (MLCK) in a calmodulin and cytosolic calcium (Ca^{2+}) dependent process.[12,13] Generation of propulsive force in amoeboid migration is accompanied by, and relies on, polarization of the cellular ultrastructure. In T cells, for instance, mitochondria translocated to the uropod have been shown to locally provide the necessary energy for myosin IIA activation.[14,15] In dendritic cells (DCs), endo-lysosomes positioned at the uropod were demonstrated to support activation of myosin IIA by facilitating lysosomal Ca^{2+} release through the Ca^{2+}-channel TRPML1.[16,17] Binding of chemokines to their respective receptors triggers engagement of Rac1/2 and RhoA GTPase activity, which is affecting cell polarity and actin polymerization.[18,19] The downstream signaling events that regulate amoeboid cell migration remain unexplored.

Here we investigated the role of lysosomes as signaling hubs in controlling amoeboid migration of T cells. Broader relevance of key findings was explored in non-related cell systems, including the non-metazoan organism *Dictyostelium discoideum* (*D. discoideum*).

Results

Endo-lysosomes re-locate together with VPS34-PIKfyve to the uropod of migrating T cells

To assess the localization of organelles among resting *vs.* chemokine-activated naïve murine CD8$^+$ T cells, focused ion beam scanning electron microscopy (FIB-SEM) imaging was performed. Non-stimulated T cells were roughly circular in shape, and organelles distributed around the nucleus. Activation with the chemokine CCL19 induced cells to elongate and organelles to group towards one side of the cell (=polarization), including those with morphologic characteristics of endo-lysosomes (**Fig. 1A**). Immunofluorescence imaging of endo-lysosomes, using antibodies targeting Rab7 (late endosome and lysosome marker) and Lamp1 (lysosome marker), confirmed endo-lysosomal polarization towards one side of CCL19 activated naïve murine CD8$^+$ T cells (**Fig. 1B**, top panels and lower left panel). Stimulation with CCL19 furthermore increased colocalization of Rab7 and Lamp1, indicative of endo-lysosomal maturation (**Fig. 1B**, lower right panel). Live-cell imaging of migrating naïve murine CD8$^+$ T cells stained with a lysosomal dye also captured polarization of (endo)-lysosomes within cells, and established that endo-lysosomes accumulated at the uropod (**Fig. S1A**). Lastly, imaging naïve murine CD8$^+$ T cells migrating in fluorescently tagged CCL19 (DY-649P1-CCL19) revealed focal accumulation of labelled CCL19 in intracellular vesicular structures that maintained their position throughout an observation period of up to five minutes (**Fig. 1C**). Immunofluorescence imaging confirmed accumulation of CCL19 in Rab7$^+$ Lamp1$^+$ positive regions, i.e. endo-lysosomes, in polarized naïve murine CD8$^+$ T cells (**Fig. S1B**).

Lysosomes function as signaling hubs for various kinases, including the mechanistic target of rapamycin (mTOR). Specifically, mTOR, in conjunction with the Ragulator–Rag complex, integrates environmental signals (e.g. nutrients and cytokine signaling) on lysosomes.[20] mTOR has been suggested to be activated by chemokine signaling, and regulate T cell migration.[21–23] We thus reasoned that endo-lysosomes might control T cell migration by recruiting mTOR signaling to the uropod. Using the selective mTOR1/2 inhibitor PQR620, we blocked mTOR activity in naïve CD8$^+$ T cells migrating in a CCL19 gradient.[24] The mTOR blocking activity of PQR620 was confirmed by assessing phosphorylation of the mTOR target S6K by flow cytometry in activated CD8$^+$ T cells (**Fig. S1C**). Inhibiting mTOR did not affect velocity of naïve murine CD8$^+$ T cells in our system (**Fig. 1D**), possibly due to low mTOR activity in naïve T cells.[21–23,25]

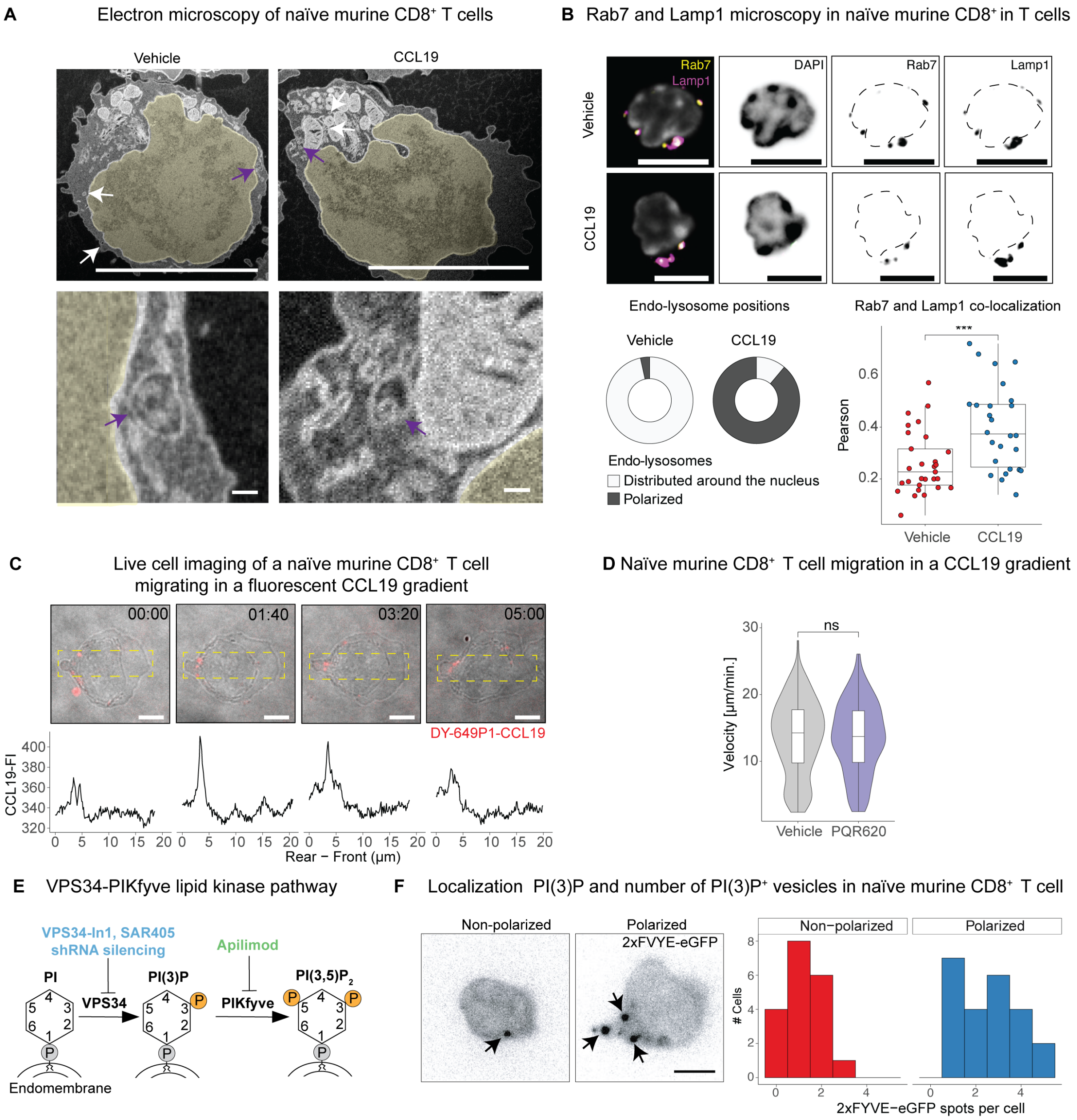

Figure 1: Endo-lysosomes decorated with VPS34–PIKfyve relocate to the uropod of polarized T cells | A) FIB-SEM microscopy images of naïve murine CD8$^+$ T cells treated with vehicle control (*left panels*) or 0.5 µg / ml CCL19 (*right panels*). Arrows indicate endo-lysosomes, further magnified examples are pointed out in purple (lower panels). The nucleus is pseudo-colored in yellow. *Scale bar: 5 µm for top panels, 100 nm for lower panels.* **B**) Immunofluorescence imaging of endo-lysosomes in naïve murine CD8$^+$ T cells treated with either vehicle control or 0.5 µg / ml CCL19. *Top panels*: Representative images of a cell stained with DAPI, Rab7, and Lamp1. The dashed line in Rab7 and Lamp1 panels indicates the outline of the nucleus. *Bottom left panel:* Fraction of cells with polarized or non-polarized endo-lysosomes assessed via Rab7 staining in presence (n = 45) or absence (n = 29) of CCL19. *Bottom right panel:* Colocalization of Rab7 and Lamp1 fluorescence signal in naïve murine CD8$^+$ T cells after treatment with vehicle control (n = 29) or CCL19 (n = 26). *Scale bar: 5 µm.* **C**) *Top panels*: Bright field images merged with DY-649P1-CCL19 signal (red) of a representative naïve murine CD8$^+$ T cell. Lower panels: Quantification of the CCL19 signal fluorescent intensity (FI) from the above image along the x-axis of the dashed box. *Scale bar: 5 µm.* **D**) Velocity of naïve murine CD8$^+$ T cells in a CCL19 gradient, following treatment with vehicle (n = 272) or the mTOR inhibitor PQR602 (n = 232). **E**) Diagram of the VPS34-PIKfyve pathway with inhibitors used (in color) and their respective targets. VPS34 and PIKfyve phosphorylate the inositol ring of phosphatidylinositol (PI) at the third and fifth position, respectively (represented by an orange circle marked with a "P"). **F**) Representative images of naïve murine CD8$^+$ T cells transfected with the PI(3)P-sensor 2xFYVE-eGFP, showing quantification of detected PI(3)P$^+$ vesicles (= 2xFYVE-eGFP spots) in polarized and non-polarized

migrating naïve CD8$^+$ T cells (n = 42). Data are pooled from three independent experiments. Arrows indicate PI(3)P$^+$ vesicles. *Scale bar: 5 µm. Panels B-D and F: Representative data from three or more independent experiments. Not significant = p-value (p) > 0.05, *** p < 0.001; Wilcoxon rank-sum test for panels B and D.*

However, endo-lysosomal membranes are also the target of the lipid-kinases VPS34 and PIKfyve, which phosphorylate phosphatidylinositol (PI) to PI(3)P and PI(3,5)P_2, respectively (**Fig. 1E**).[26] These kinases impact endo-lysosomal maturation, receptor recycling and Rac1 activity, features that have been associated with regulation of cell motility.[26–28] This prompted us to consider their role in T cell migration. A fluorescent probe consisting of two PI(3)P-binding FYVE domains fused to an eGFP (2xFYVE-eGFP) enables subcellular localization of PI(3)P, i.e. the substrate of PIKfyve by fluorescence imaging.[29] 2xFYVE-eGFP accumulated on vesicular structures at the uropod of CCL19-polarized naïve murine CD8$^+$ T cells (**Fig. 1F**), thus capturing VPS34 activity in these cells and opening the possibility for involvement of the VPS34–PIKfyve axis in regulating amoeboid cell migration. This notion was further supported by a recently published CRISPR screen that identified *PIK3C3*, the gene encoding VPS34, as a regulator of T cell migration into the central nervous system in an experimental autoimmune encephalitis model.[30]

In all, these imaging studies (i) demonstrated that chemokine exposure of naïve CD8$^+$ T cells induced endo-lysosomal maturation and polarization to the uropod, and (ii) provided evidence for engagement of lipid kinase activity on uropod-localized endo-lysosomes.

T cell velocity, but not directedness, is controlled by VPS34 and PIKfyve

Using inhibitors of VPS34 and PIKfyve, we first explored how activity of these kinases related to accumulation of endo-lysosomes in polarized T cells. Inhibition of VPS34, using the potent and selective inhibitor VPS34-In1, was verified by imaging studies (**Fig. S2A**).[31] Apilimod is a highly selective PIKfyve inhibitor in clinical development.[32,33] Importantly, both inhibitors do not affect other lipid kinases, such as class 1 PI3K (e.g. PI3Kγ), which have been implicated in T cell migration.[34] At 2 µM, i.e. the concentration used throughout, neither VPS34In-1 nor Apilimod affected the viability of murine CD8$^+$ T cell blasts after 6 hours of treatment (**Fig. S2B**). With these tools in hand, we blocked VPS34 or PIKfyve in CCL19 stimulated naïve murine CD8$^+$ T cells and examined cells using brightfield imaging. Inhibiting either kinase resulted in the appearance of large vesicles at the uropod of polarized cells (**Fig. 2A**, upper panel). The fluorescent signal from a lysosomal dye was also increased in VPS34In-1 as well as Apilimod-treated naïve murine CD8$^+$ T cells, indicative of an increase in endo-lysosomal volume (**Fig. 2A**, lower panel). These findings align with the known role of the VPS34–PIKfyve system in endo-lysosomal homeostasis.[26]

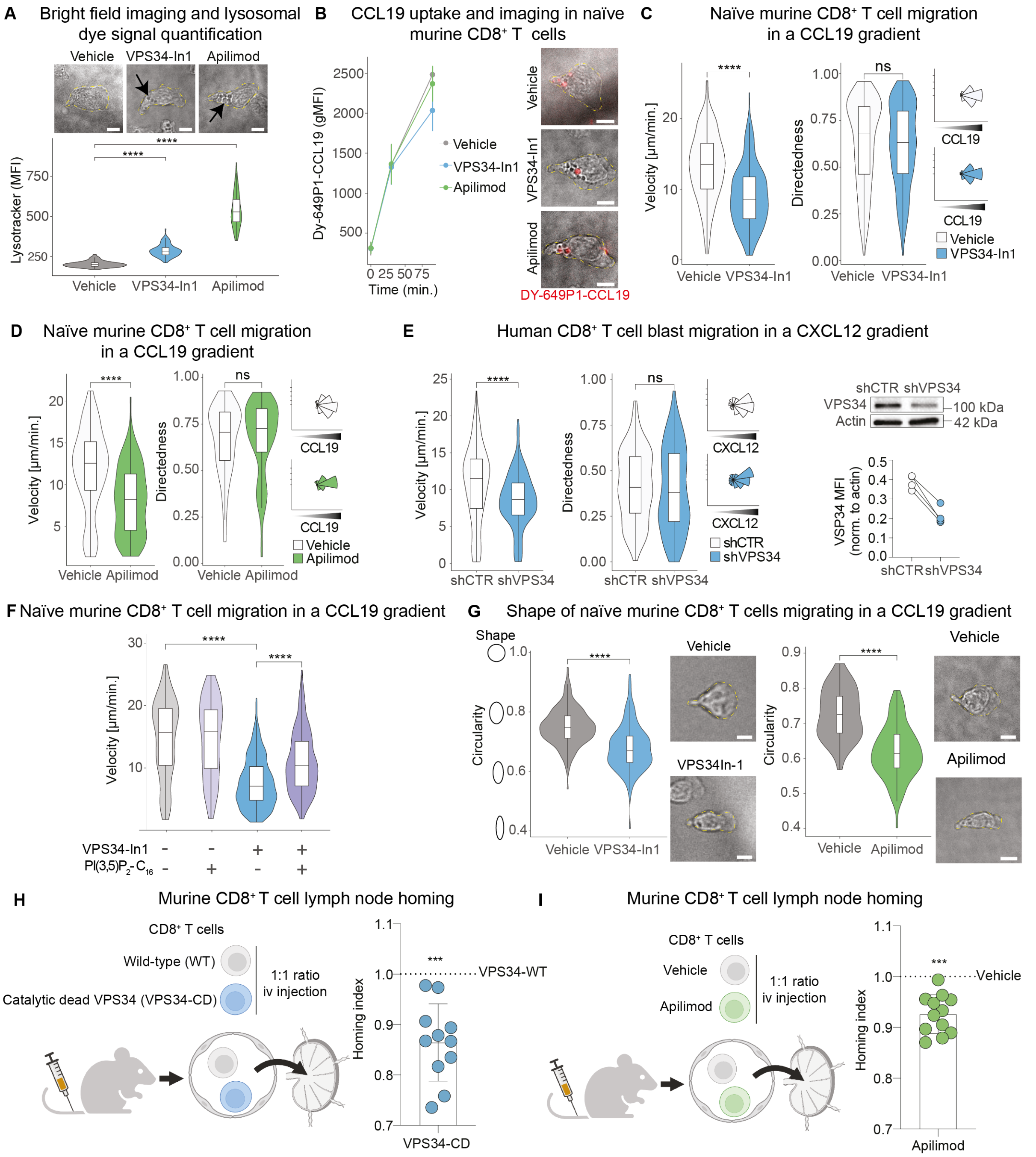

Figure 2*:* T cell velocity, but not directedness, is controlled by VPS34 and PIKfyve | A) *Upper panel:* Representative bright field images of naïve murine CD8⁺ T cells migrating in a CCL19 gradient, treated with either vehicle control, VPS34-In1, or Apilimod. Arrows point at (large) vesicles. *Lower panel:* Quantification of lysosomal dye signal (mean fluorescent intensity, MFI) per cell, treated with vehicle control (n = 60), VPS34-In1 (n = 106), or Apilimod (n = 73). **B**) *Left panel*: Time course analysis of DY-649P1-CCL19 uptake in naïve murine CD8⁺ T cells (flow cytometry, geometric mean intensity (gMFI) and standard deviation of three biological replicates). *Right panel:* Representative bright field images merged with DY-649P1-CCL19 signal (red) of naïve murine CD8⁺ T cells migrating in a CCL19 gradient, treated with vehicle control, VPS34-In1, or Apilimod. **C**) Migration metrics (velocity, directedness, and angle of migration) of naïve murine CD8⁺ T cells treated with vehicle control (n = 362) and VPS34-In1 (n = 193), or **D**) vehicle control (n = 125), and Apilimod (n = 121). **E**) *Left panels:* Migration metrics of human CD8⁺ T cell blasts transduced with scrambled control (shCTR; n = 292), or VPS34-targeting shRNA

(shVPS34, n = 255), and placed in a CXCL12 gradient. *Right panel:* VPS34 knockdown efficiency as determined by Western blotting; connections between dots link samples from the same biologic replicate. **F**) Velocity of naïve murine CD8$^+$ T cells placed in a CCL19 gradient and treated with vehicle control (n = 175), PI(3,5)P_2-C_{16} (n = 149), VPS34-In1 (n = 466), or PI(3,5)P_2-C_{16} & VPS34-In1 (n = 636). **G**) Circularity analysis and representative bright field images of naïve murine CD8$^+$ T cells migrating in a CCL19 gradient. *Left panel:* Vehicle control (n = 161) and VPS34-In1 (n = 157). *Right panel:* Vehicle control (n = 40) and Apilimod (n = 102). **H**) Schematic of experiment and result of CD8$^+$ T cell homing analysis, comparing transfer of wild-type vs. catalytically-inactive VPS34 (pooled data from two independent experiments with 5-6 recipient animals each). **I**) Comparison of vehicle vs. Apilimod-treated CD8$^+$ T cells in homing experiments (pooled data from two independent experiments with 5 recipient animals each). *Yellow dashed lines indicate cell outline, and the scale bars indicate 5 µm in panels A, B, and G. Panels A - G: Representative data from three or more independent experiments. ns = $p > 0.05$, *** $p < 0.001$, **** $p < 0.0001$; Wilcoxon rank-sum test for panels A, C-E, G-I; Aligned Rank Transform (ART) ANOVA for panel F.*

To test whether uptake and vesicular accumulation of chemokines at the uropod was affected by inhibition of VPS34 or PIKfyve, naïve murine CD8$^+$ T cells were activated using fluorescent CCL19 in presence or absence of VPS34In-1 or Apilimod, respectively. Neither inhibition with VPS34In-1 nor Apilimod affected uptake of CCL19, as measured by (i) flow cytometry after 30 or 90 minutes (**Fig. 2B**, left panel), and (ii) accumulation of fluorescence in vesicular structures at the uropod (**Fig. 2B**, right panel). This suggested that the uptake of chemokine and cell polarization were not affected by inhibition of the VPS34–PIKfyve axis. We then went on and tested how inhibiting VPS34 or PIKfyve impacted T cell motility, using an under-agarose migration assay (**Fig. S2C**). Inhibition of VPS34 and PIKfyve both reduced the migration velocity of naïve murine CD8$^+$ T cells, while not altering directedness and angle of migration towards the source of chemokine (**Fig. 2C**,**D**, **Fig. S2D**). VPS34In-1 and Apilimod also reduced the speed of murine CD8$^+$ T cell blasts in a CCL19 gradient (**Fig. S2E**). shRNA-mediated silencing of VPS34 in human CD8$^+$ T cell blasts likewise decreased their speed, while preserving directedness and angles of migration (**Fig. 2E**). Finally, the structurally non-related, selective VPS34 inhibitor SAR405 phenocopied migration deficits induced by VPS34 and PIKfyve inhibition in human CD8$^+$ T cell blasts migrating in a CXCL12 gradient (**Fig. S2F**).[35]

Assessing whether the product of the VPS34–PIKfyve axis was indeed responsible for the observed phenotype, cell culture medium was supplemented with dipalmitoyl-PI(3,5)P_2. Evidencing the importance of PI(3,5)P_2, reduced migration velocity imposed by inhibition of VPS34 in naïve murine CD8$^+$ T cells was partially rescued by addition of this synthetic PI(3,5)P_2 (**Fig. 2F**). Rapidly migrating T cells tend to be elongated and less circular.[6] Notably, inhibition of VPS34 and PIKfyve, and thus slowing their migration, also decreased the average circularity of naïve murine CD8$^+$ T cell migrating in a CCL19 gradient (**Fig. 2G**). This phenotypic constellation (decreased migration speed among less circular cells) was compatible with insufficient myosin IIA activity in VPS34–PIKfyve inhibited cells – a notion further explored below.[4,36,37] To test whether also *in vivo* migration of CD8$^+$ T cells was impacted by VPS34 and PIKfyve, adoptive transfer experiments were performed. Specifically, murine CD8$^+$ T cells expressing either wild-type or a catalytic inactive form of VPS34 were injected in a 1:1 ratio into the tail vein of recipient mice, and their homing into lymph nodes (inguinal, axillary, cervical) was quantified (**Fig. 2H**, left panel).[38] In these experiments, the number of wild-type CD8$^+$ T cells migrating into lymph nodes was consistently higher than that of cells expressing catalytic inactive VPS34 (**Fig. 2H**, right panel). Likewise, pre-treatment of murine CD8$^+$ T cells with Apilimod reduced lymph node homing relative to vehicle-treated control cells (**Fig. 2I**). Frequencies of transferred CD8$^+$ T cells in the spleen were similar to input, irrespective of VPS34 and PIKfyve sufficiency *vs.* insufficiency (**Fig. S2G**,**H**) – aligning with passive accumulation in the red pulp and marginal zone compartment.[39,40]

Together these experiments identified the lipid kinase pathway $PI \rightarrow PI(3)P \rightarrow PI(3,5)P_2$, governed by VPS34 and PIKfyve, as a modifier of endo-lysosomal turnover at the uropod of T cells, while leaving chemokine uptake unaltered. More importantly, activity of these kinases, through their end product, determined velocity of migrating CD8$^+$ T cells, without affecting chemotactic directedness.

VPS34 and PIKfyve regulate retrograde actin flow and myosin IIA activation

The flow of actin – i.e. the propulsion force underlying amoeboid cell migration – relies on synchronized actin polymerization at the leading edge, and myosin IIA-induced F-actin traction at the uropod.[6,7,9,10] The importance of myosin IIA activity in governing cell migration was specifically verified for T cells by using two distinct approaches. First, direct (blebbistatin), as well as indirect (ML-7), inhibition of myosin IIA activity reduced migration speed of human CD8$^+$ T cell blasts as well as human naïve CD8$^+$ T cells, irrespective of upstream VPS34 activity (**Fig. 3A**-**C**). Second, nocodazole, which increases myosin IIA activity, increased velocity of migration both in presence and absence of VPS34 blockade, and also restored decreased circularity induced by inhibition of VPS34 to baseline levels (**Fig. 3A**, **Fig. 3D** and **Fig. S3A**).[41–45] Given these clear data, we hypothesized that the VPS34–PIKfyve system impacted migration via regulating the activity of myosin IIA – an alternative possibility being an impact of the kinase-system on actin polymerization. The latter idea was refuted by the finding that actin polymerization in CCL19-treated naïve murine CD8$^+$ T cells was unaffected upon inhibition of either VPS34 or PIKfyve (**Fig. 3E**). By contrast, in this same system myosin IIA activity – read out by the phosphorylation status of RLC – was diminished upon blocking of either kinase (**Fig. 3F**), also aligning with elongation observed among T cells migrating in presence of VPS34 or PIKfyve inhibitors (**Fig. 2G**).

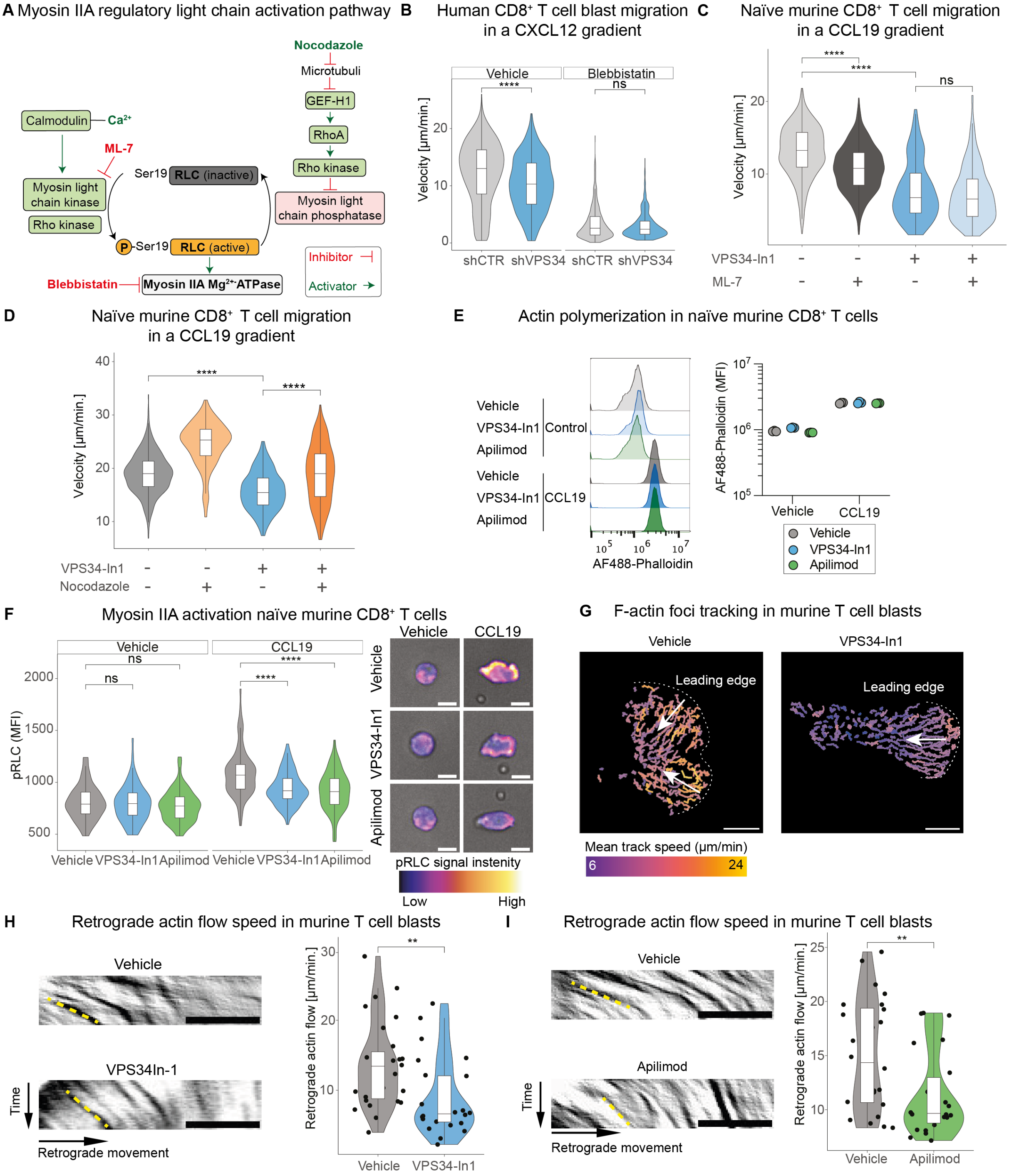

Figure 3: VPS34 and PIKfyve regulate retrograde actin flow and myosin IIA activation| **A**) Schematic of the myosin IIA regulatory light chain activation pathway. Inhibitors or inhibitory interactions are shown in red, activators or activating interactions in green. **B**) Velocity of human CD8^{+} T cell blasts transduced with control shRNA (n = 1037 for vehicle control; n = 759 for Blebbistatin) or VPS34-shRNA (n = 534 for vehicle control; n = 594 for Blebbistatin), placed in a CXCL12 gradient in presence vs. absence of Blebbistatin. **C**) Velocity of naïve murine CD8^{+} T cells in a CCL19 gradient treated with vehicle control (n = 815), ML-7 (n = 1019), VPS34-In1 (n =

199), and ML-7 & VPS34-In1 (n = 238); or **D**) Vehicle control (n = 439), Nocodazole (n = 185), VPS34-In1 (n = 243), and Nocodazole & VPS34-In1 (n = 336). **E**) *Left panel*: Representative flow cytometry histograms of F-actin staining (AF488-Phalloidin) in naïve murine $CD8^+$ T cells assessed one minute after treatment with vehicle control or CCL19. *Right panel:* Phalloidin mean fluorescence intensity (MFI, flow cytometry) of three technical replicates. **F**) *Left panel:* Per cell MFI signal (fluorescence microscopy) among naïve murine $CD8^+$ T cells stained for myosin IIA RLC phosphorylated at serine 19 (pRLC) and treated with vehicle control (no CCL19: n = 81; CCL19: n = 75), VPS34-In1 (no CCL19: n = 79; CCL19: n = 88), and Apilimod (no CCL19: n = 139; CCL19: n = 64). *Right panels:* Representative bright-field images of cells overlaid with pseudo-colored pRLC signal. **G**) Representative tracks of F-actin foci derived from actin-reporter T cell blasts with or without VPS34-In1, pseudo-colored according to speed. Dashed lines denote the leading edge, arrows indicate the direction of actin flow. **H**) Kymograph-based speed analysis of retrograde actin flow (*right panels*) in actin-reporter T cell blasts treated with vehicle control (n = 27) or VPS34-In1 (n = 24), and **I**) vehicle control (n = 25) or Apilimod (n = 26). *Left panels*: Representative kymographs of F-actin reporter signal along the cell's axis over a 30 sec period. The yellow dashed line indicates an exemplary actin trace used for speed analysis. *Scale bars in panels F-I represent 5 µm. Panels B-I represent results from three independent experiments. ns = $p > 0.05$, ** $p < 0.01$, **** $p < 0.0001$; Wilcoxon rank-sum test for panels F, H, I; ART ANOVA for panels B - D.*

To dynamically visualize dependency of actin flow on the VPS34–PIKfyve system, T cell blasts from Lifeact-GFP expressing mice were confined by serum-free agarose on a non-adhesive coating and activated by CCL19 contained in the polymer (**Fig. S3B**).[46] As expected, inhibition of either VPS34 or PIKfyve reduced the speed of cortical F-actin foci moving within cells (**Fig. 3G**-**I**).

Collectively, these findings established that VPS34 and PIKfyve regulated retrograde actin flow – the main propulsion mechanism for T cell migration – via tuning activity of myosin IIA.

VPS34 and PIKfyve regulate migration velocity of T cells via lysosomal Ca^{2+}

We next aimed to explore how activity of the VPS34–PIKfyve axis, myosin IIA activity, and T cell migration were mechanistically interlinked. Endo-lysosomes function as Ca^{2+} stores, and cytosolic Ca^{2+} promotes activation of myosin IIA (**Fig. 3A**).[16,17] We therefore imaged intracellular Ca^{2+} in naïve murine $CD8^+$ T cells migrating in a CCL19 gradient in presence or absence of inhibitors for VPS34 and PIKfyve, respectively. Inhibition of either kinase resulted in a notable increase in lysosomal Ca^{2+} (**Fig. 4A**). Substantiating specificity of this signal, chelating intracellular Ca^{2+} with BAPTA-AM caused progressive fading of the calcium indicator in lysosomes (**Fig. 4B** and **Fig. S4A**).

The flux of Ca^{2+} from lysosomes to the cytoplasm is gated by TRPML1, a process regulated by $PI(3,5)P_2$ (**Fig. 4C**).[47–49] We thus hypothesized that inhibition of VPS34 or PIKfyve, and thus depletion of $PI(3,5)P_2$, hinders lysosomal Ca^{2+} efflux – leading to accumulation of lysosomal Ca^{2+} in migrating naïve murine $CD8^+$ T cells. Functional engagement of TRPML1 should thus restore lysosomal Ca^{2+} efflux and reverse VPS34-dependent migration deficits in T cells. To test this idea we monitored migration of naïve murine $CD8^+$ T cells in presence or absence of

VPS34-In1 and/or the specific and potent TRPML1 agonist MK6-83 (**Fig. 4C**).[50] Indeed, MK6-83 reduced lysosomal Ca^{2+} sequestration and partially rescued the speed deficit imposed by inhibition of VPS34 (**Fig. 4D**,**E**). TRPML1 activation also reverted reduced myosin IIA activation imposed by inhibition of VPS34 (**Fig. 4F**).

From these experiments a molecular framework emerged, where VPS34–PIKfyve derived $PI(3,5)P_2$ was regulating TRPML1 mediated lysosomal Ca^{2+}-efflux, thereby triggering the calmodulin–MLCK pathway and hence activation of myosin IIA.

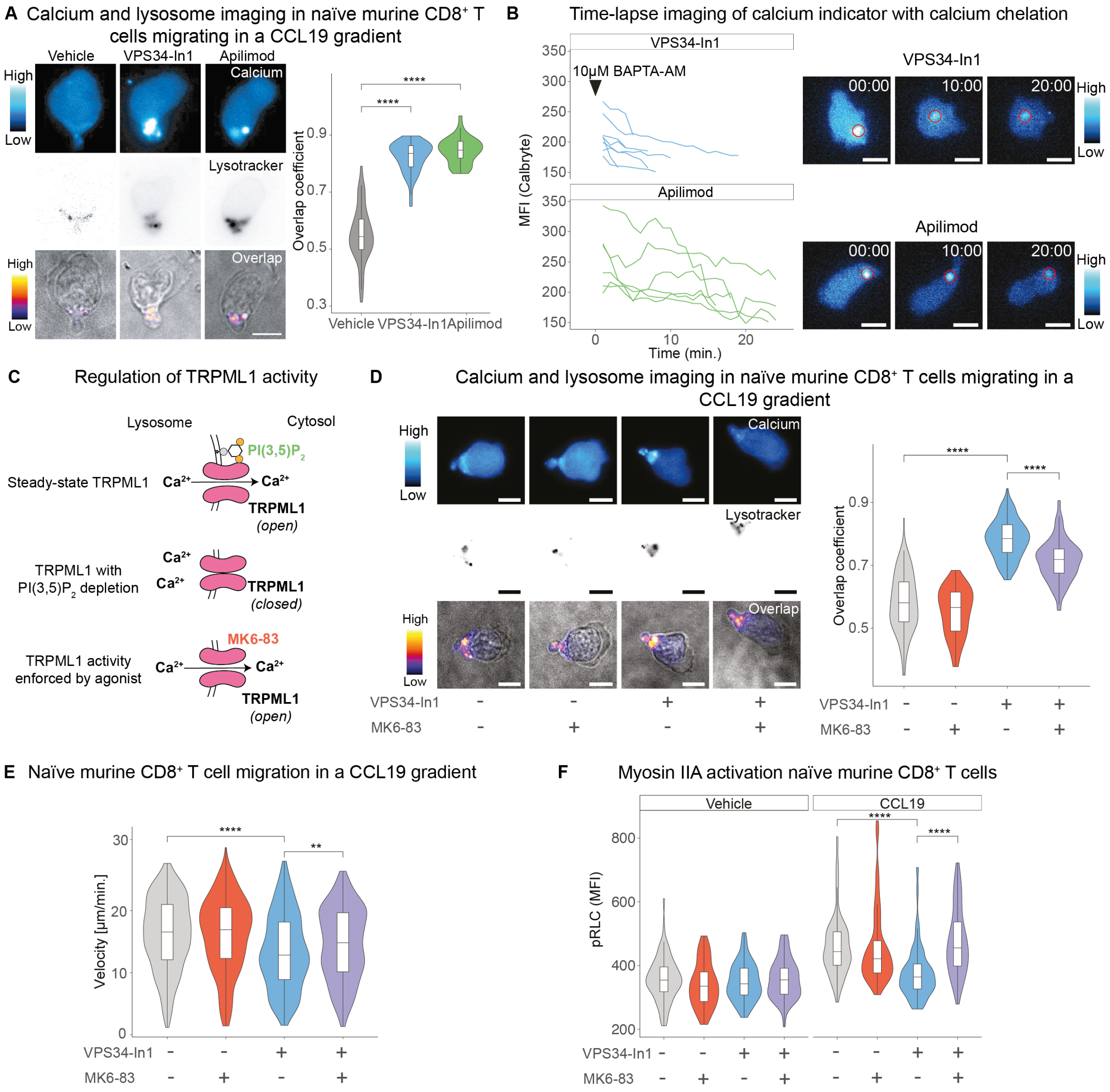

Figure 4: VPS34 and PIKfyve regulate migration velocity of T cells via lysosomal Ca^{2+} | A) *Left panels:* Fluorescence images of naïve murine $CD8^+$ T cells stained with a calcium indicator dye (Calbryte) and a lysosomal dye (LysoTracker). Bright field images were merged with a pseudo color map indicating the overlap of calcium and lysosomal signals (Pearson correlation coefficient). *Right panel:* Overlap coefficient (= colocalization) of calcium and lysosomes in cells treated with vehicle control (n = 45), VPS34-In1 (n = 44), or Apilimod (n = 37). **B**) *Left panel:* Time-course analysis of calcium indicator signal (MFI) in large vesicles induced by VPS34-In1 (n = 8) or

Apilimod (n = 6) after BAPTA-AM addition in naïve murine CD8$^+$ T cells. *Right panels:* Representative calcium indicator image of tracked vesicles, marked by a red circle. **C**) Schematic of TRPML1 activation: Green symbols denote the TRPML1 agonist PI(3,5)P$_2$ and MK6-83. **D**) *Left panels:* Fluorescence images of naïve murine CD8$^+$ T cells stained with a calcium indicator dye (Calbryte) and a lysosomal dye (LysoTracker). Bright field images were merged with a pseudo color map indicating the overlap of calcium and lysosomal signals (Pearson correlation coefficient). *Right panel:* Overlap coefficient (= colocalization) of calcium and lysosomes in cells treated with vehicle (n = 94), VPS34-In1 (n = 120), MK6-83 (n = 65) or VPS34In-1 & MK6-83 (n = 122). **E**) Velocity of naïve murine CD8$^+$ T cells migrating in a CCL19 gradient, treated with vehicle control (n = 560), VPS34-In1 (n = 408), MK6-83 (n = 418), and a combination of VPS34-In1 & MK6-83 (n = 580). **F**) Per cell MFI signal (fluorescence microscopy) among naïve murine CD8$^+$ T cells stained for pRLC and treated with vehicle control (no CCL19: n = 83; CCL19: n = 110), VPS34-In1 (no CCL19: n = 72; CCL19: n = 113), MK6-83 (no CCL19: n = 47; CCL19: n = 72), and VPS34-In1 (no CCL19: n = 71; CCL19: n = 74). *Scale bars in panels A and B indicate 5 µm. Panels A, B, D-F are representative results of 3 independent experiments. ** p < 0.01, **** p < 0.0001; Wilcoxon rank-sum test for panel A; ART ANOVA for panel D-F.*

Regulation of amoeboid migration is a conserved function of the VPS34–PIKfyve axis

To explore whether the VPS34–PIKfyve system is involved in regulating amoeboid migration also in other cell types, HL-60-derived neutrophils and murine bone marrow-derived DCs were used. Both, neutrophils in the presence of fMLP and DCs exposed to CCL19 migrated slower when blocking either VPS34 or PIKfyve (**Fig. 5A** and **Fig. 5B**, left panel). Infiltration of DCs under an agarose-matrix was likewise reduced when blocking VPS34 or PIKfyve (**Fig. 5B**, right panel and **Fig. S5A**). These findings expanded the role of the VPS34–PIKfyve system in regulating velocity of amoeboid cell migration beyond T cells. Of note, VPS34 and PIKfyve orthologues are widely expressed across all eukaryotic kingdoms (**Fig. S5B**).[51] We thus considered the idea that the VPS34–PIKfyve → TRPML1 pathway could be a conserved biological module regulating velocity of amoeboid cell migration. To test this idea, we used the social amoeba and professional phagocyte *D. discoideum*, a non-metazoan model organism that separated from the animals and fungi a billion years ago. *D. discoideum* exhibit similar vesicular alterations upon PIKfyve inhibition as metazoan cells, and its migration is myosin II-dependent.[52,53] Further, absence of the *D. discoideum* TRPML1 orthologue Mucolipin (MCLN) impairs Ca^{2+}-release from endo-lysosomes.[54] Indeed, spontaneous amoeboid migration of PIKfyve knock-out (ko) and Apilimod-treated wild-type (Ax2) *D. discoideum* cells was slower than that of respective control cells. Inhibition of PIKfyve with Apilimod did not alter the speed of migration among PIKfyve ko cells, arguing for the specificity of the inhibitor (**Fig. 5C**). Moreover, MCLN-deficient *D. discoideum* phenocopied PIKfyve deficiency (**Fig. 5D**). Supporting the notion that MCLN was the target of PI(3,5)P$_2$ also in *D. discoideum* cells, the alpha-fold model of MCLN displayed a positively charged pocket similar to the PI(3,5)P$_2$ binding pocket in the N-terminus of TRPML1 (**Fig. 5E**).[47,48] In line, 5 out of 7 amino acids in this poly-basic domain are conserved between TRPML1 and MCLN (**Fig. S5C**), and *in silico* docking analyses suggested potential binding of PI(3,5)P_2 to this pocket in MCLN (**Fig. 5E**). To explore whether regulation of amoeboid migration speed has evolved as an early feature of the VPS34–PIKfyve axis, we extracted the number proteins with zinc finger FYVE domains from the public domain.[55] PI(3)P binding to the FYVE zinc finger domain regulates function and recruitment of proteins containing this motif. Therefore, the number of distinct proteins with FYVE domains may serve as a proxy for a potential functional involvement of the VPS34–PIKfyve kinase system. While the number of proteins harboring this motif is relatively low in unicellular organisms (including *D. discoideum*), it increases in metazoans along with complexity (**Fig. S5D**). It hence is plausible that regulation of migration speed is an ancient function of the VP34–PIKfyve axis.

In all, these findings suggested an evolutionarily conserved mechanism in which PI(3,5)P_2, generated by the VPS34–PIKfyve axis, regulated TRPML1 activity, thereby controlling the release of Ca^{2+} from lysosomes at the uropod of migrating cells – and hence velocity of amoeboid cell migration.

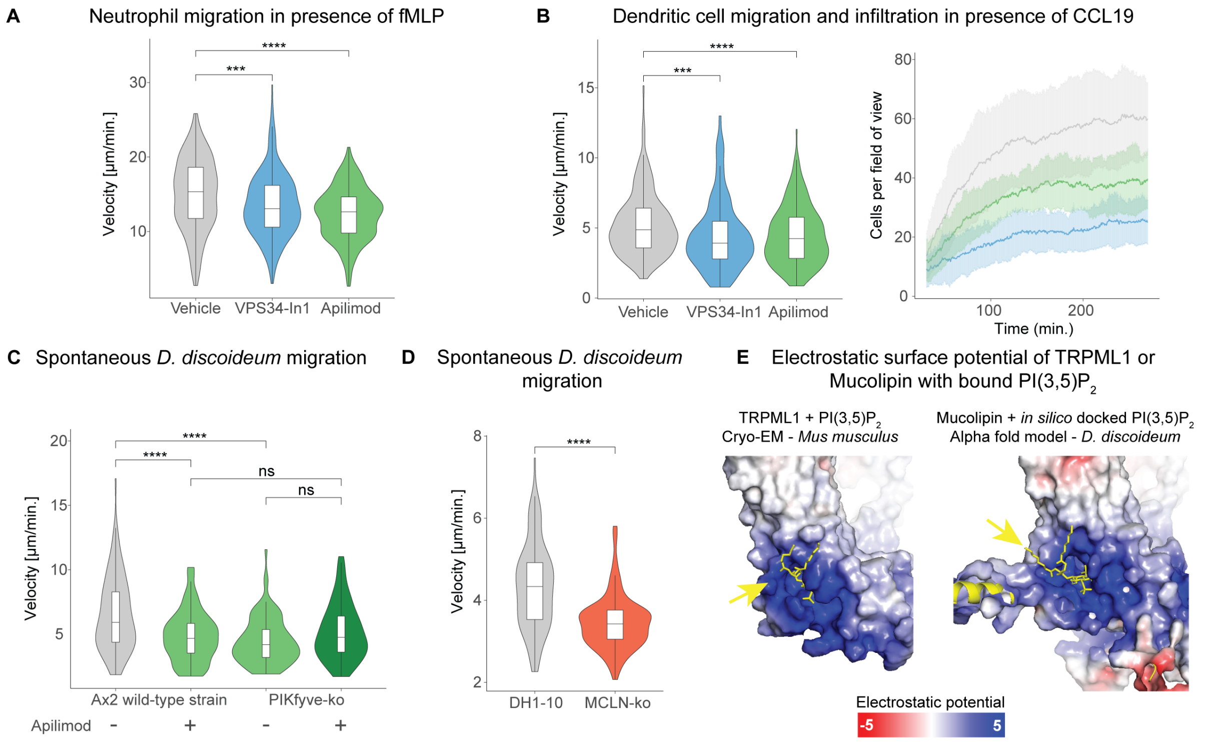

Figure 5: Regulation of amoeboid migration is a conserved function of the VPS34–PIKfyve pathway| A) Velocity of HL-60 derived neutrophils treated with vehicle control (n = 214), VPS34-In1 (n = 243), and Apilimod (n = 194), migrating in presence of the chemokine fMLP. **B**) *Left panel*: Velocity of DCs migrating in CCL19, exposed to vehicle control (n = 412), VPS34-In1 (n = 104), Apilimod (n = 205). *Right panel*: Mean and standard deviation of number of cells detected per fields of view (n = 6 per condition) infiltrating under the agarose matrix. **C**) Velocity of *D. discoideum* wild-type (Ax2) cells treated with vehicle control (n = 124) or Apilimod (n = 87), and PIKfyve-orthologue ko cells treated with vehicle control (n = 91) or Apilimod (n = 74). **D**) Velocity of DH1-10 (wild-type

strain, n = 113) and mucolipin-ko (MCLP-ko, n = 114) *D. discoideum* cells. **E**) *Left panel*: Experimentally determined structure of TRPML1 (public domain) with bound PI(3,5)P_2.[47] *Right panel*: Predicted structure of Mucolipin with PI(3,5)P_2 docked *in silico*. The structures are aligned and superimposed with electrostatic potential. *Panels A-D: Representative results from three or more independent experiments. ns $p > 0.05$, *** $p < 0.001$, and **** $p < 0.0001$; Wilcoxon rank-sum test used in panels A, B and D; ART ANOVA for panel C.*

Discussion

The key finding of this study was that the VPS34–PIKfyve axis, in association with endo-lysosomes, locates to the uropod of migrating T cells. This lipid kinase pathway is thereby ideally positioned to regulate retrograde actin flow by enabling Ca^{2+} efflux from endo-lysosomes through TRPML1, and hence myosin IIA activity. Regulation of cell migration-velocity via this molecular axis applies to various cell types, including *D. discoideum*, i.e. unicellular eukaryotic cells.

Precise positioning of lysosomes has previously been shown to be important for amoeboid migration, ensuring site-specific availability of Ca^{2+} (Refs. [16,17]). We now show that the VPS34–PIKfyve axis links local cytosolic availability of Ca^{2+} (i.e. endo-lysosomes) and Ca^{2+} appropriation from these stores to engage myosin IIA activity. An increasing understanding of how ultrastructure and function are mechanistically interlinked highlights the importance to interrogate the molecular mechanisms orchestrating context-specific spatial ultrastructural dynamics.

Microtubules, and the microtubule organizing center at the uropod of cells, are critically involved in shaping the ultrastructure of amoeboid migrating cells. In T cells, for example, mitochondria are coupled to microtubules via Miro-1, which enables their re-location to the uropod upon chemokine signaling.[15] In an analogous manner, endo-lysosomes connected to microtubules by Arl8B or RILP/Rab7, have been shown to be re-positioned within cells depending on nutrient availability.[56,57] It will be interesting to define how chemokine signaling and microtubule-dependent positioning of organelles are interlinked, and characterize the adaptor proteins that are involved in this process. Given the precise and dynamic ultrastructural adaptations happening in cells upon external input, further defining structure–function relationships of ultrastructural components, as well as their interactions, will also be relevant. At the uropod, mitochondria, endo-lysosomes, and the ER reside in close vicinity. Intriguingly, membrane contact sites physically connecting these organelles jointly regulate Ca^{2+} dynamics and provide microdomains for local signaling.[58–61] Whether such contact sites selectively form as an ultrastructural adaptation in migrating cells and, if so, their biologic roles, remains to be investigated.

In our experiments with T cells, chemokine-induced F-actin formation was unaffected by VPS34–PIKfyve. Notably, in neutrophils and cancer cells, PIKfyve has been shown to stimulate activity of the GTPases Rac1/2, which control actin polymerization.[18,27,62] It will be interesting to explore whether VPS34 and PIKfyve also control Rac1/2 in T cells and, if so, what the molecular and functional consequences of Rac1/2 activity are.

VPS34 and PIKfyve orthologues are universally expressed in eukaryotes and their appearance is known to predate the emergence of amoeboid cell migration.[51,63] Roles previously assigned to the VPS34–PIKfyve axis are regulation of endocytic trafficking and of autophagy.[64] The herein described role in governing the speed of amoeboid cell migration not only in vertebrate immune cells but also *D. discoideum*, indicates early functional assimilation of the VPS34–PIKfyve kinase system to also support this cellular process. Across taxa, F-actin polymerization and cortical actin-network contraction by myosin IIA lie at the center of amoeboid locomotion.[65,66] This study thus implicates regulation of myosin IIA activation by lysosomal Ca^{2+} via VPS34–PIKfyve–TRPML1 axis as an evolutionary conserved regulator of this core mechanism.

In all, our work identified a conserved regulatory node linking local availability of Ca^{2+} stores (endo-lysosomes) and generation of lipid-mediators with the efflux of Ca^{2+} from their storage organelles. This spatially organized biologic system governs the speed of amoeboid cell migration.

Acknowledgements

We thank the microscopy core facility of the Department of Biomedicine at the University and University Hospital of Basel for their technical support. CH was supported by the Swiss National Science Foundation (SNSF) (310030B_201277; 310030_192677; FZEB-0-180487) and the Novartis Foundation for Medical-Biological Research (NFMBR) (#23A070). PD was supported by a scholarship from the Swiss Academy for Medical Sciences (SAMW) and SNSF (183980), the NFMBR (#23A070), AlumniMedizin Basel, and the Freiwillige Akademische Gesellschaft Basel. We thank Daniel Legler for providing reagents.

Author contributions

Conceptualization, C.H. and P.D.; Investigation, P.D., C.M., J.C.Y., A.M.L., and L.F.; Methodology, C.H., M.M., T.So., K.O., and P.D.; Resources C.H., M.M., T.Sc., M.P.W., K.O., and T.So.; Writing – Original Draft C.H. and P.D.; Writing – Review & Editing T.Sc., M.P.W., M.M., C.M. and T.So.; Supervision, C.H.; Project Administration C.H.

Declaration of interests

The authors declare no competing interests.

Supplemental information

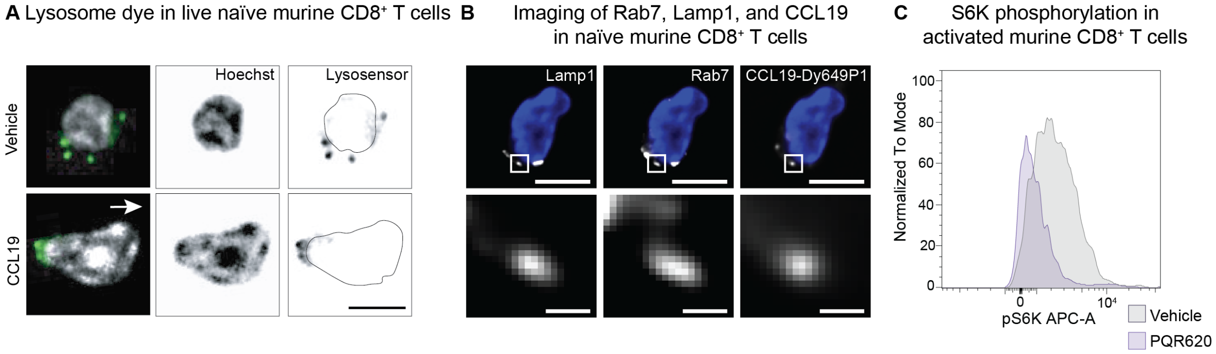

A Lysosome dye in live naïve murine CD8$^+$ T cells

B Imaging of Rab7, Lamp1, and CCL19 in naïve murine CD8$^+$ T cells

C S6K phosphorylation in activated murine CD8$^+$ T cells

Fig. S1: Endo-lysosomes decorated with VPS34–PIKfyve relocate to the uropod of polarized T cells | A) Representative live cell images of lysosomes (Lysosensor dye, *right panels*), the nucleus (Hoechst dye, *middle panels*), and a merged images (*left panels*) of naïve murine CD8$^+$ T cell treated with CCL19 or vehicle control. The arrow in the left panel indicates direction of migration and the black line in the right panels marks the nuclear outline. *Scale bar: 5 µm.* **B**) Representative fluorescence microscopy images of a naïve murine CD8$^+$ T cell treated with CCL19-Dy-649P1 (*right panels*) and stained with Lamp1 (*left panels*) & Rab7 (*middle panels*). *Top panels*: Overlay with DAPI signal (blue), the box indicating the region of interest magnified in the *bottom panel*. *Scale bar: 5 µm (top panels), 500 nm (bottom panels).* **C**) Representative histogram (flow cytometry) of pS6K expression among murine CD8$^+$ T cells activated for 24 h with CD3 and CD28 targeting antibodies and treated with the mTOR inhibitor PQR620 (purple) vs. vehicle control (grey).

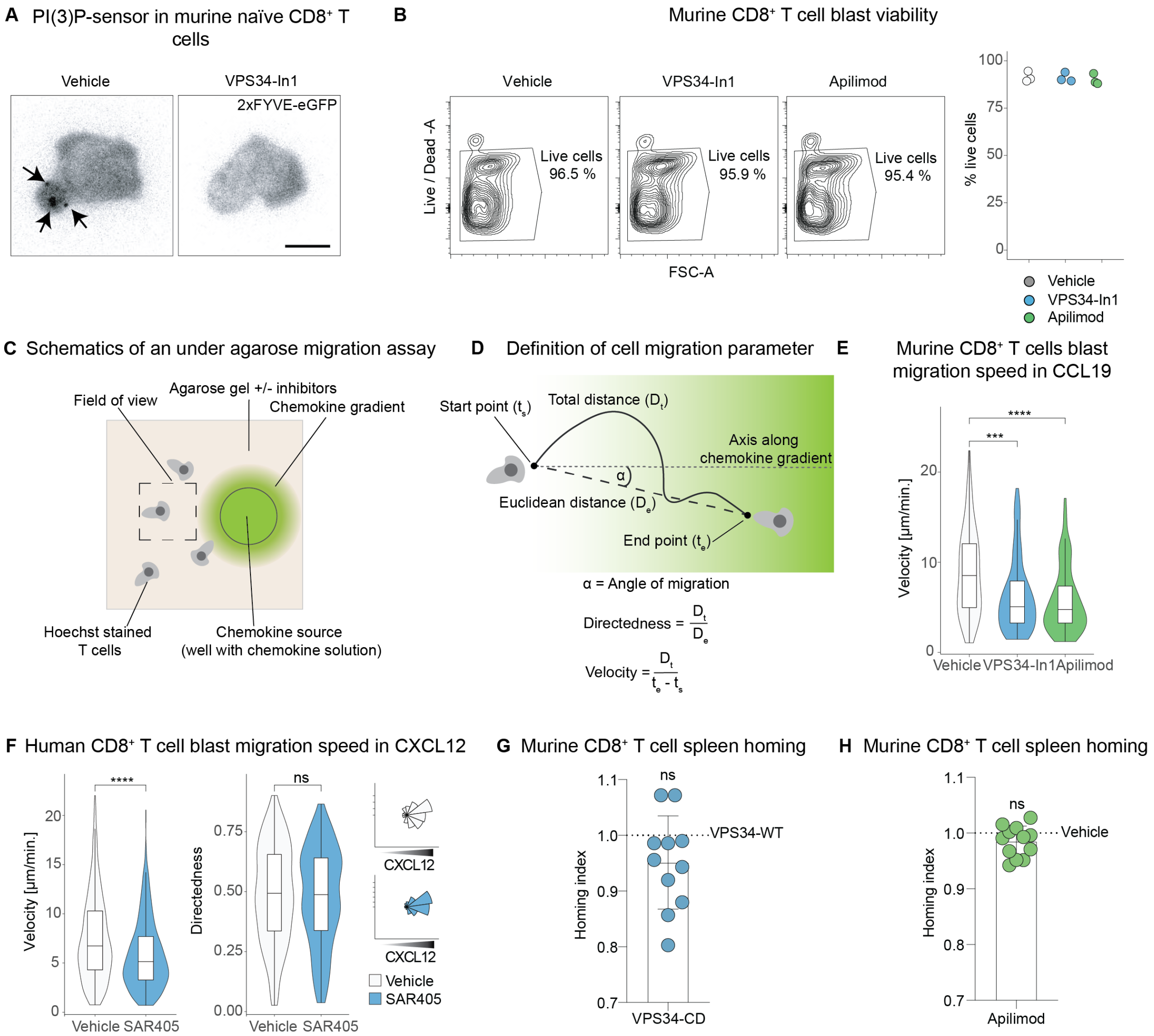

Fig. S2: T cell velocity, but not directedness, is controlled by VPS34 and PIKfyve | A) Naïve murine CD8⁺ T cells transfected with the 2xFYVE-eGFP PI(3)P sensor, placed in a CCL19 gradient and treated with vehicle control or VPS34-In1. Arrows point at PI(3)P⁺ vesicles. *Scale bar: 5 µm.* **B**) *Left panels*: Representative live/dead staining plots (flow cytometry) of murine CD8⁺ T cell blasts exposed to vehicle control, VPS34-In1, or Apilimod for 6 h. *Right panel:* Percentage of live cells of three biological replicates. **C**) Schematic (top view) of a T cell under-agarose migration assay. **D**) Definitions of cell migration metrics used in this report. **E**) Migration speed of murine CD8⁺ T cell blasts in a CCL19 gradient, treated with vehicle control (n = 66), VPS34-In1 (n = 81), or Apilimod (n = 79). **F**) Migration speed of human CD8⁺ T cell blasts migrating in a CXCL12 gradient, treated with the VPS34 inhibitor SAR405 (n = 626) or vehicle control (n = 755). **G**) Spleen homing index (normalized to each internal control) of murine CD8⁺ T cells expressing the wild-type or catalytic dead (CD) VPS34, and **H**) spleen homing index (normalized to each internal control) of vehicle or Apilimod-treated cells. *ns = p > 0.05, *** p < 0.001, **** p < 0.0001; Wilcoxon-test for panels E- H.*

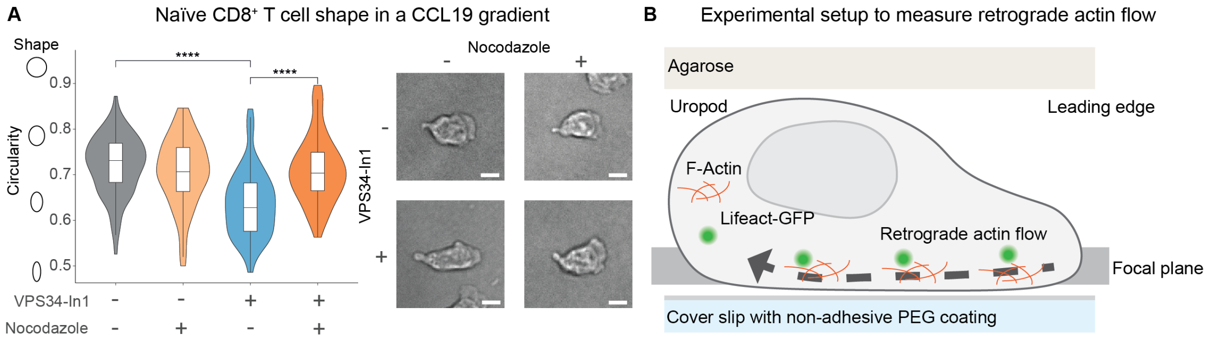

Fig. S3: **VPS34 and PIKfyve regulate retrograde actin flow and myosin IIA activation | A**) *Left panel:* Circularity of naïve CD8$^+$ T cells placed in a CCL19 gradient treated with vehicle control (n = 81), Nocodazole (n = 70), VPS34-In1 (n = 85), and VPS34-In1 & Nocodazole (n = 56). *Right panels:* representative bright field images. *Scale bar: 5 µm. **** p < 0.0001, ART ANOVA.* **B)** Experimental setup for assessing retrograde actin flow in murine T cell blasts expressing the Lifeact-GFP reporter (to visualize F-actin dynamics).

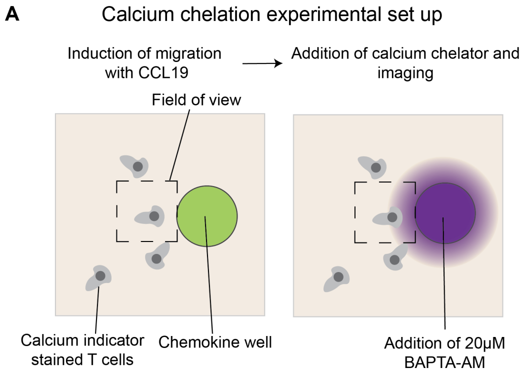

Fig. S4: **VPS34 and PIKfyve regulate migration velocity of T cells via lysosomal Ca^{2+}| A**) Experimental setup of calcium chelation experiments. Naïve murine CD8$^+$ T cells, stained with a calcium indicator (Calbryte dye), were treated with either VPS34-In1 or Apilimod and allowed to migrate in a CCL19 gradient (*left panel*). The chemokine solution in the well was then replaced with medium containing BAPTA-AM (a membrane-diffusible calcium chelator), and the calcium indicator signal in T cells was imaged over time (*right panel*).

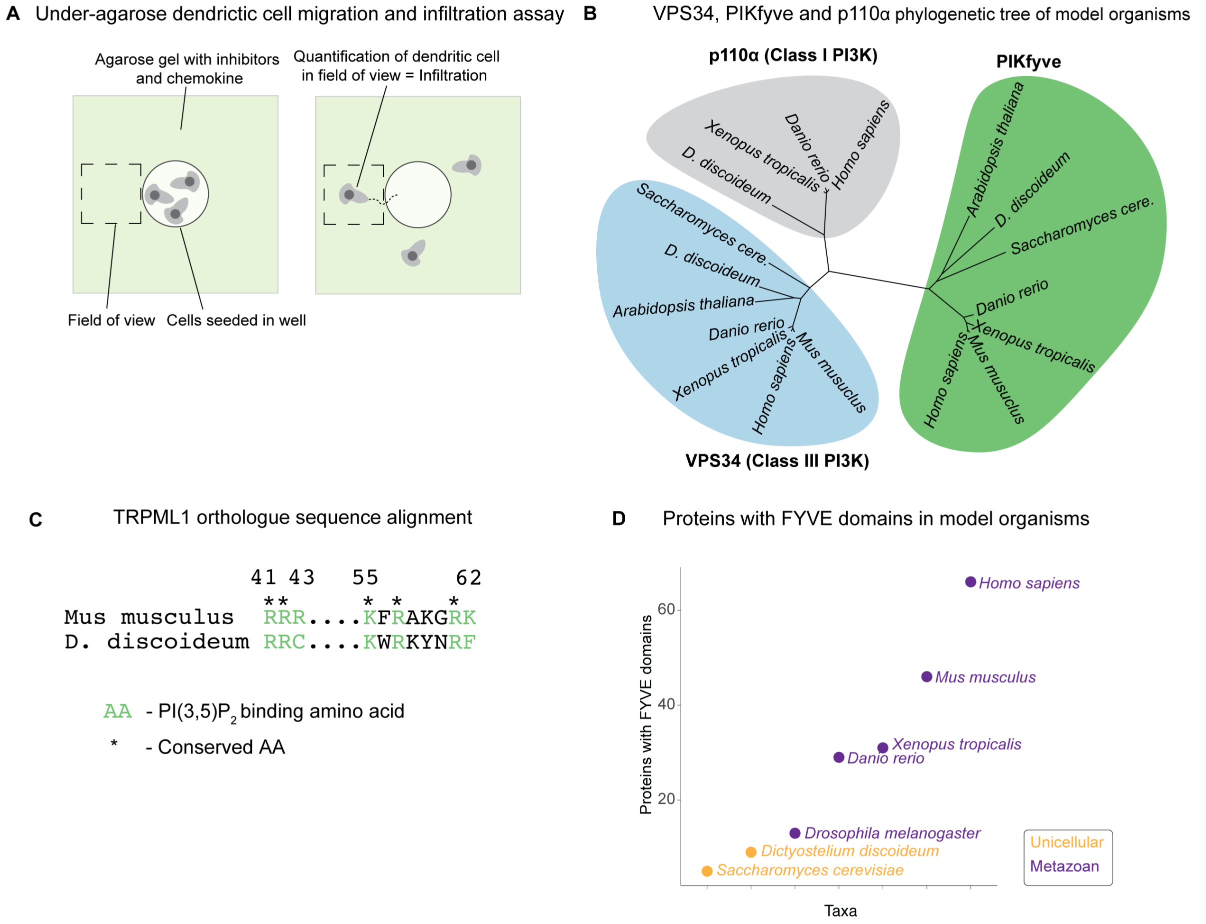

Fig. S5: **Regulation of amoeboid migration is a conserved function of the VPS34–PIKfyve pathway | A**) Schematics of the migration and infiltration assay of DCs: Cells were added to the well in the agarose (containing inhibitors and CCL19, *left panel*). DCs crawled under the gel (= infiltration) and the number of cells in the field of view was quantified (*right panel*). **B**) Phylogenetic analysis of the amino acid (AA) sequences of VPS34, PIKFYVE, and p110α (as an example for Class I PI3K). **C**) Alignment of the PI(3,5)P_2-binding protein region from *Mus musculus* TRPML1 and the *Dicty* orthologue. PI(3,5)P_2-binding AAs are highlighted in green, conserved AAs indicated by an asterisk. **D**) Number of proteins with a FYVE domain across the listed species. Orange indicates non-metazoan, purple metazoan organism.

Materials and Methods

Cell isolation and culture

Cells and cell lines were cultured in RPMI1640 (containing 25 mM HEPES and L-Glut; Gibco, Cat. # 52400-025) + 10 % heat-inactivated fetal calf serum (hiFCS; Gibco, Cat. # 10270) + GlutaMax (diluted 100x; Gibco, Cat. # 35050-038) + 50 µM β-Mercaptoethanol (Gibco, Cat. # 31350-010) + 100 U/ml penicillin and streptomycin (Gibco, Cat. # 15140-122), referred to throughout the text as *complete medium*.

Naïve murine CD8$^+$ T cells were isolated from the spleens and lymph nodes (inguinal, axillary, and cervical) from C57BL/6NCrl with a negative magnetic isolation kit, according to the manufacturer's instruction (Stemcell, Cat. # 19858; Miltenyi Biotec, Cat. # 130-104-075). Mice of the age 6-25 weeks of both genders were used for the experiments. They were bred and housed in a specific-pathogen-free facility at the University of Basel. All experiments adhered to the guidelines of the Swiss Federal Veterinary Office and were approved by local authorities. Isolated murine T cells were cultured in 10 ng / ml recombinant murine IL-7 (Peprotech, Cat # 217-17) in complete medium and used up to 5 days after isolation.

HL-60 cells (a gift from Jürg Schwaller, University of Basel) were maintained in complete medium at a density of 2 x 10^5 - 1.5 x 10^6 cells / ml and split every 2-3 days. Neutrophil differentiation was induced by adding 1.3% (v/v) DMSO into complete medium. Differentiated cells were used 5-7 days after DMSO addition.

For DC differentiation, bone marrow was harvested from femurs and tibias of C57BL/6NCrl mice, and 2 x 10^6 cells were plated in 10 cm Petri-dishes with 10 ml of complete medium containing 10 ng / ml GM-CSF (BioLegend, Cat. # 576306). At day 3 and 6 fresh medium with GM-CSF was added. On day 8, the floating fraction of cells (immature DCs) was harvested and frozen in 90 % hiFCS + 10 % DMSO and stored in liquid nitrogen. Frozen cells were thawed in a water bath at 37 ° C, added to prewarmed complete medium, and centrifuged at 200 x g for 5 min. The thawed cells were resuspended in complete medium & 10 ng / ml GM-CSF and 100 ng / ml LPS (Lucerna Chem, Cat. # abx082480) and matured for 14 h for migration experiments.

Human CD8$^+$ T cell isolation and shRNA-mediated VPS34 silencing

Peripheral Blood Mononuclear Cells (PBMCs) were isolated by density centrifugation from buffy coats of healthy and consenting donors (Blood donor center, University of Basel, male and female, 18-65 years old). CD8$^+$ T cells were isolated using anti-CD8 microbeads, following the manufacturer's instructions (Miltenyi Biotec, Cat. # 130-045-201). 2.5 x 10^6 T cells were activated for two days with CD3/CD28-complexes (25 µl / ml, Stemcell, Cat. # 10971) and 100 U / ml of IL-2 (Bio-Techne Sales Corp., Cat. # 202-IL-050). The cells were then split into two 500 µl samples and treated with 100 µl of lentivirus solution. This solution contained 30 µl of scrambled or 10 µl VPS34-targeting shRNA per target sequence to a total of 30 µl and was supplemented with 6x polybrene to reach a final concentration of 6 µg / ml (Sigma Aldrich, Cat. # TR-1003-G) in a complete medium. The cells were spinoculated for 60 min at 1000 g at 30 °C. On day 3 after activation, the medium was replaced with complete medium containing 300 U/ml of IL-2. On day six post-activation, we sorted the cells for GFP^+ expression using a FACSMelody Cell Sorter (BD). Sorted cells were expanded and maintained in complete medium containing 300 U/ml of IL-2 for up to two weeks before use in experiments. The high-titer shRNA lentivirus against human VPS34 (along with a scrambled control) was procured from VectorBuilder (shRNA 3 & 1 with EGFP; target sequences: GAGGCAAATATCCAGTTATAT, CCACGAGAGATCAGTTAAATA, GCTGGATAGATTGACATTTAG).

Under-agarose cell migration assay

The under-agarose migration assay was adapted from a previously published method.[67] Ibidi µ-Slide 8-well high Glass Bottom slides (Ibidi, Cat. # 80807) were coated with 150 µl of human plasma fibronectin (10 µg / ml; EMD Millipore, Cat. # FC010) in PBS and incubated at 37 °C for 2 h. The slides were then rinsed twice with 400 µl PBS per well. To cast the 1.2 % agarose gels, 0.48 g of ultra-pure agarose (Thermo Scientific, Cat. # 16500100) was mixed in 10 ml deionized water. Separately, 4 ml filtered hiFCS, 16 ml phenol-red free RPMI (Gibco, Cat # 11835-063), and 10 ml 2x HBSS (pH 7.2, from 10x HBSS stock; Gibco, Cat # 14065056) were combined and heated to 60 °C. The agarose was heated to a boil for three times in a microwave, interspersed with mixing. The medium, HBSS, and FCS mixture were then added to the molten agarose solution, followed by gentle mixing. Each well received 400 µl of the agarose mixture and was left to solidify with a closed lid. When inhibitors were used, 100 µl of a 5 x inhibitor solution in complete medium was added to the gel and incubated overnight at RT, sealed with parafilm. Before the migration assay, the medium solution was removed, and a well was created with a 3 mm biopsy puncher. Cells pretreated with inhibitors and stained with Hoechst 33342 (see below) were centrifuged at 200 x g for 5 min, and resuspended in complete, phenol-red free, inhibitor-containing medium at a concentration of 1 x 10^7 cells / ml. 5.5 µl of the cell suspension was injected 2-3 mm away from the punched well using a micropipette with a gel-loading tip. All fluid was aspirated from the well, which was then filled with 20 µl of complete medium containing chemokines. For human CD8$^+$ T cell blast migration assays, 2 µg / ml CXCL12 (Preprotech, Cat # 300-28A) was added, whereas for murine T cell migration assays, 2 µg / ml CCL19 (Peprotech, Cat # 250-27B) or 20 µM DY-649-P1-CCL19 (a kind gift from Daniel Legler, Biotechnology Institute Thurgau) in complete medium was added in the punched well.[68] The dish was then transferred to the microscope. For DC experiments, the agarose gel was overlaid with 5 x inhibitor / vehicle solution and 5 x CCL19 solution (final concentration: 0.25 µg / ml) and cells were added to the well. For neutrophil migration assays, gels were overlaid with 5 x inhibitor / vehicle solution and 5x fMLP (Sigma-Aldrich, Cat # F3506, final concentration at 10 nM).

Microscopy imaging modalities and analysis

Most imaging experiments (except *Dicty* cell migration assay) were conducted using Nikon inverted Ti/Ti2 microscopes (**Table 1**), equipped with a Photometrics 95B (25mm, back-illuminated sCMOS) camera. The Nikon Ti2 widefield microscope employed an LED, the Nikon Ti CSU-W1 spinning disk utilized a diode-pumped solid-state laser, and the Nikon Ti2 Cresty spinning disk used a Celesta solid-state laser as a light source. CFI Plan Apo Lambda objectives were used, with magnifications of 20x air (NA: 0.75), 40 x air (NA: 0.95), 100x air (NA: 1.45), and 60x water (NA: 1.2, Plan Apo VC). For live cell imaging, stage-top incubators maintained a constant temperature of 37 °C, 100 % humidity (20 l / h airflow), and 5 % CO$_2$.

Table 1

Experiment	**Microscope modality**	**System**	**Objective**	**Applied assay**	**Sampling rate**
Immunofluorescence of endo-lysosomes	Widefield	Nikon Ti2	100x	Fixed and mounted cells	
Immunofluorescence of RLC phosphorylation			40x		
Assessment of retrograde actin flow	Spinning disk confocal	Nikon Ti / Nikon Ti2	60x, 100x	Modified under-agarose (see below)	1 fps
Live cell migration with inhibitors	Nikon Ti2	Nikon Ti2	20x	Under-agarose	20 or 30 sec

Live cell imaging: T cell morphology	Widefield	Nikon Ti2	40x & 1.5 optical zoom, 100x	Under-agarose	
Live cell imaging: T cell with Lysosomal stains / DY-649P-CCL19 / 2x FYVE-eGFP probe / calcium indicator	Widefield	Nikon Ti2	100x	Under-agarose	10 fps or single images

Cell morphology and fluorescence intensities were measured using FIJI. Regions of interest (ROI) were manually drawn in FIJI to obtain mean fluorescence intensities and shape descriptors. Each experiment involved analyzing at least three different fields of view per condition. Cell tracking, either for nuclei or brightfield images, was conducted using either Ilastik (with Pixel Classification followed by Tracking) or TrackMate in FIJI (Log detector; Simple LAP tracker with linking max distance: 20 microns, gap-closing max distance: 20 microns, gap-closing max frame gap: 2).[69,70] Velocities and directedness were then calculated using a custom-written script in R. Colocalization analysis was performed on cropped images containing only one single cell using Huygens (Scientific Volume Imaging). For RAB7 and LAMP1 colocalization, a deconvolution step was performed in Huygens prior to the analysis.

Dictyostelium discoideum **culture and migration assay**

The *D. discoideum* strains used in this study are listed in **Table 2**. Cells were axenically grown in 10 cm Petri dishes (Falcon) at 22°C in HL5 or HL5c medium (Formedium, Cat. # HLG0101) supplemented with 100 U/ml penicillin and streptomycin (Gibco, Cat. # 15140-122). At least 24 h before the migration experiments, all the cell lines were grown in HL5 medium. 6 x 10^3 cells were seeded in each well of a 4-well µ-slide (Ibidi, Cat. # 80426) in HL5 medium and incubated 1 h at 22 °C. When necessary, 5 µM Apilimod (**Table 4**) or DMSO was added to the cells before the incubation. Time-lapse movies of 30 min with images taken at 30 sec intervals were recorded with a widefield inverted LEICA DMi8 microscope using a 40x objective. Images were processed with the Trackmate ImageJ plug-in.

Table 2

Genotype	Background strain	Source / Reference
Wild-type	Ax2	Buckley et al. 2019[52]
PIKfyve-ko		
Wild-type	DH1-10	Gift from Pierre Cosson; Lima et al. 2012[54]

Mucolipin-ko		

Assessment of retrograde actin flow

The assessment of retrograde actin flow was carried out using a modified under-agarose assay (as described above). The slides were first plasma cleaned and PEG-coated at 4 °C overnight with 200µg/ml poly(L-lysine)-PEG (SuSoS, PLL(20)-g[3.5]-PEG(2)) in PBS. The slide was washed three times with PBS and 400 µL of 1.2 % agarose solution (without any serum). The gels were then treated overnight with 100 µL of 5x solutions of either the vehicle, VPS34In-1, or Apilimod in serum- and phenol-red free RPMI1640 containing 1.25 µg / ml CCL19. Subsequently, Lifeact T cell blasts were treated with either VPS34In-1 or Apilimod for 2 h and then injected under the agarose gel (as described above).

Actin flow videos were acquired at 1 frame per second (fps) for 30 s in the GFP channel (Ex.: 488nm) using an inverted spinning disk confocal (details above). The acquired images were then analyzed with FIJI: First, cells with visible actin spots were cropped and loaded into the KymographClear plugin with the average intensity projection.[71] A line was then drawn through the cells, along the F-actin foci traces from the uropod to the leading edge, to generate a kymograph (with a line width of 5 pixels). The angle of a representative F-actin trace was analyzed, from which the speed was calculated by taking the tangent of the angle and scaling the result to µm / min. The tracking of F-actin foci was performed using Trackmate and the integrated LoG detector.

Immunofluorescence staining

8-well removable cell culture dishes (ibidi, Cat. # 80841) were coated with 100 µg / ml Poly D-Lysine (Milipore Cat. # A-003-E) in PBS for 2 hours at 37 °C and washed three times with PBS. Then, 1 x 10^5 naïve $CD8^+$ T cells were plated per well, centrifuged for 30 s at 300 x g, and treated with 0.5 µg / ml CCL19 and inhibitors according to the protocol. At the end of the treatment, prewarmed EM-grade paraformaldehyde was added directly to the medium to achieve a final concentration of 4 %. The plate was then incubated for 15 minutes at 37 °C and washed once with PBS. Cells were permeabilized with 0.2% Triton X in PBS for 15 min and blocked with 5% goat serum in PBS-T (blocking buffer) for 1 hour. Primary antibodies were incubated overnight at 4 °C and secondary antibodies for 1 h in the dark at RT, with three intermittent washes with PBS-T. The antibodies were diluted in blocking buffer (**Table 3**).

Finally, the slides were washed in PBS, mounted with a coverslip and ProLong Gold Antifade with DNA Stain DAPI (Invitrogen, Cat. # P36931) and sealed the next day with nail polish.

Immunoblotting

Human $CD8^+$ T cell blasts were harvested, washed with ice-cold PBS, and then centrifuged at 500 x g for 5 min. Cells were lysed in RIPA buffer (ThermoFisher, Cat. # 89901) supplemented with protease inhibitors (Roche, Cat. # 05892970001) and phosphatase inhibitors (Roche, Cat. # 04906845001). Cell lysates were stored at -20 °C and cleared by centrifugation at 15000 g for 10 min at 4 °C prior to use. Protein concentrations were determined with a BCA Protein Assay Kit (ThermoFisher, Cat. # 23225). For each sample, 5 µg of protein was combined with 4x Laemmli buffer (Biorad, Cat. # 1610747) and 10 % 2-mercaptoethanol, and then denatured at 95 °C for 5 min. Protein samples were loaded into 4 - 20 % precast gradient gels (Biorad, Cat. # 1704158) alongside a page ruler (ThermoFisher, Cat. # 26620), and then subjected to electrophoresis for 5 min at 80 mV, followed by 55 min at 100 mV. The separated proteins were transferred to nitrocellulose membranes (Biorad, Cat. # 1704158) using a Trans-blot turbo system (Biorad) and blocked with 5 % BSA in TBST for 1 h at room temperature (RT). Membranes were sliced at the 70 kDa mark and incubated overnight at 4 °C with either anti-VPS34 or anti-Actin antibodies (**Table 3**)**.** Following three washes with TBST, membranes were incubated for 1 h at RT with horseradish peroxidase (HRP) conjugated secondary antibodies (**Table 3**). Membranes were then washed, incubated for 5 min with chemiluminescent substrate (ThermoFisher, Cat. # 34580), and imaged on a gel doc system (Biorad).

Table 3

Antibody target	**Manufacturer**	**Cat. #**	**Dilution**	**Application**
Anti-Rab7	Abcam	ab137029	1:1000	Immunofluorescence
Anti-Lamp1		ab25245		
Anti-Phospho Myosin Light Chain 2 (Ser19)	Cell Signaling Technology	3671	1:100	
Anti-PI3 Kinase Class III		4263	1:1000	Western blot
Anti-β-Actin		3700	1:10000	
Anti-Rabbit IgG HRP		7074		

Anti-Mouse IgG HRP		7076		
Anti-Phospho-p70 S6 Kinase (Thr389)		9234	1:500	Flowcytometry
Anti-Rabbit IgG AF647	Invitrogen	A-21244	1:1000	Immunofluorescence / Flowcytometry
Anti-Rat IgG AF488		A-11006		Immunofluorescence

Treatment with Inhibitors / Agonists and Dipalmitoyl $PI(3,5)P_2$ Supplementation

All inhibitor stock solutions were prepared in DMSO, with the same DMSO concentration applied for vehicle controls. Inhibitor concentrations and manufacturers are listed in **Table 4**. The compound PQR620 was synthesized in-house at the University of Basel's Wymann Laboratory, following a published protocol.[24] Prior to experiments, cells were treated with inhibitors or vehicle control for 2 hours. Exceptions were MK6-83 and Nocodazole, which were exclusively incorporated into the agarose gel for migration assays.

$PI(3,5)P_2$-diC$_{16}$ (Echelon Biosciences, Cat. # P-3516) was conjugated to fatty-acid-free BSA (Sigma-Aldrich, Cat. # A7030) by incubating at 37 °C for 1 h. Subsequently, phenol-red free RMPI1640, preheated to 37 °C, was added to the fatty-free BSA to attain a concentration of 100 mg / ml, yielding a final stock concentration of 500 µM. Aliquots of this stock were stored at -80 °C. As needed, the stock solution was diluted in complete medium for agarose gel preparation or cell treatments, as previously described.

Table 4

Name	**Target**	**Manufacturer**	**Cat. #**	**Concentration**
PQR620	mTORC1/2	Wymann Lab (University of Basel)		2 µM
VPS34-In1	VPS34	Selleckchem	S7980	2 µM
SAR405	VPS34	EMD Millipore	533063	4 µM
Apilimod	PIKFYVE	MedChem Express	HY-14644A	2 µM
(S(-4)’-nitro-Blebbistatin	Non-muscle myosin II ATPases	Cayman Chemical	24171	25 µM
ML-7	MLCK	MedChem Express	HY-15417	10 µM
Nocodazole	Microtubules	M1404	M1404	1 µM
MK6-83	TRPML1	Sigma-Aldrich	SLM1509	5 µM
BAPTA-AM	Calcium	MedChem Express	HY-100545	20 µM

Staining of Live Cells with Fluorescent Dyes

For calcium imaging, naïve murine CD8$^+$ T cells were stained with 2.5 µM Calbryte 520 AM (AAT Bioquest, Cat. # 20650) in complete medium at 37°C for 30 min. Subsequently, a 2 h drug treatment was carried out in the presence of 1µM LysoTracker Deep Red (Invitrogen, Cat. # L12492). Lysosensor Green DND-189 was added to the complete medium at a concentration of 1 µM and the cells were incubated at 37 °C for 2 h. Nuclear staining was performed using Hoechst 33342 (ThermoFisher, Cat. #R3705; one drop per two ml of medium) in parallel with the drug treatment.

Electroporation of 2xFYVE-eGFP Plasmid into T cells

The pEGFP-2xFYVE plasmid, (a kind gift from Harald Stenmark; Addgene, Cat. # 140047) electroporation was performed using a 4D-Nucleofector (Lonza, Cat # AFF-1002B) with the P3 Nucleofector kit (Lonza, Cat. # V4SP-3096). Naïve murine CD8$^+$ T cells (2 x 10^6) were washed twice with PBS and resuspended in 20µl of P3 electroporation buffer containing 1 ng of the plasmid. The cell suspension was then added to an electroporation cuvette strip. Immediately after electroporation, 130 µl of prewarmed complete medium with 20 ng / ml IL-7 was added to the cuvette, and the cells were allowed to rest for 10 min at 37 °C. The cell suspension was mixed, centrifuged at 200 x g for 5 min, and resuspended in 1 ml of prewarmed complete medium with 20 ng / ml IL-7. The cells were prepared for imaging on the following day.

Flow Cytometric Analysis of F-Actin Polymerization, Live / Dead Staining, S6K Phosphorylation, and CCL19 Uptake

For F-actin staining, 7.5 x 10^4 naïve murine CD8$^+$ T cells were treated with either a vehicle, VPS34In-1, or Apilimod and then stimulated for 1 min with 0.5 µg / ml CCL19. The cells were fixed directly in the medium with 4% PFA for 15 minutes, washed in PBS, and permeabilized with 0.2 % Triton-X in PBS for 15 minutes. F-actin was stained with AF-488 phalloidin (1 drop in 4 ml FACS buffer; Invitrogen, Cat. # R37110) for 30 minutes, washed thrice, and then acquired in FACS buffer (PBS & 5% BSA).

To assess the effect of VPS34 or PIKFYVE inhibition on murine CD8$^+$ T cell blast viability, cells were treated with inhibitors for 6 hours and then stained with Zombie Aqua (BioLegend, Cat. # 423101) following the manufacturer's instructions.

S6K phosphorylation was measured by intracellular staining in murine CD8$^+$ T cells activated for 24 h with plate-bound anti-CD3 (coated at 5 µg / ml for 14 h at 4 °C in PBS; BioLegend, Cat.

100331) and 1 µg / ml soluble anti-CD28 (BioLegend, Cat. # 1002116). Cells were stained for live/dead cells, fixed, and permeabilized for 15 min, followed by overnight staining with a primary anti-pS6K antibody at 4 °C and one hour of secondary antibody staining at RT (**Table 3**). This staining procedure was carried out with the Transcription Factor Staining Buffer Set (Invitrogen, Cat. # 00-5523-00).

CCL19 uptake in naïve CD8$^+$ T cells was measured by adding 20 nM of DY-649P1-CCL19 to the cell culture medium for 0, 30, or 90 min. The cells were then subjected to live / dead staining and washed in FACS buffer. All samples were acquired with a CytoFlex (Beckman Coulter) and analyzed using Flowjo (BD).

Preparation and Acquisition of Electron Microscopy Samples

A total of 1 x 10^7 cells were fixed by adding a 2x concentrated EM fixative (comprising a final solution of 2.5 % glutaraldehyde (Sigma-Aldrich, Cat. # G5882) and 2.0 % paraformaldehyde (Science Services, Cat. # E15710) in 100 mM PIPES buffer (pH 7.2; Sigma-Aldrich, Cat. # P6757) to the cell culture medium (1:1) for 20 min at RT. After removing the fixative, it was replaced with a 1x fixative containing 0.01 % green malachite (Sigma-Aldrich, Cat. # 32745) for 2 h on ice. The cells were rinsed six times with PIPES buffer before being embedded in a 2 % low melt agarose (Roth, Cat. # 6351.1). Embedded cell pellets were washed five times for 3 min each in cacodylate buffer (0.15 M cacodylate with 4 mM CaCl2; Electron Microscopy Sciences, Cat. # 12300) before being post-fixed with osmium-ferricyanide (2 % OsO4, Electron Microscopy Sciences, Cat. # 19100; 1% K3Fe(III)(CN)6, Electron Microscopy Sciences, Cat. # 20150; in cacodylate buffer) for 30 minutes on ice. After five washes with ddH$_2$O for 3 min each, cell pellets were immersed in a thiocarbohydrazide (TCH, Sigma-Aldrich, Cat. # 223220) solution for 30 min. Subsequently, cell pellets were treated with 1% OsO4 in water for 30 min at RT, washed five times, and immersed in 1 % uranyl acetate (Electron Microscopy Sciences, Cat. # 22400) overnight at 4 °C. On the following day, cells were washed and treated with Walton's lead aspartate (0.66% lead nitrate in 0.4 % aspartic acid solution) for 1 h. After another wash, the cells underwent dehydration using an ethanol series (25 %, 50 %, 75 %, 90 %, and 2x 100 %) for 5 min each. The cell pellets were then infiltrated with Durcupan (Electron Microscopy Sciences, Cat. # 14040) using an ethanol-Durcupan gradient (20%, 50%, 70%, 90%, and 2x 100%) for 3 min each in the microwave. This was followed by a 30 min immersion in a 1:1 Ethanol:Durcupan resin and a subsequent overnight immersion in 100 % Durcupan solution.

The next day, cells were immersed in freshly prepared resin for 1 h. Resin blocks were polymerized at 60 °C for 3 d. The polymerized samples were mounted on SEM stubs and imaged on either an FEI Helios NanoLab 650 (courtesy of NanoImaging Lab Basel; acquired pixel size: 8 x 8 x 16 nm) or a ZEISS Crossbeam 550 serial block face (courtesy of the Electron Microscopy Core Facility of EMBL Heidelberg; acquired pixel size: 8 x 8 x 40 nm). Image stacks were aligned using the SIFT module available on FIJI for analysis.[72]

In vivo **T cell homing assay**

For adoptive T cell transfer, isolated murine CD8$^+$ T cells were initially rested overnight and then divided into two groups. One group was labeled with 250 nM CellTrace Violet (CTV), while the other group was labeled with 1000 nM CellTrace Far Red (CTFR) (Invitrogen, Cat. # C34557 / C34564) for 15 minutes in PBS at 37 °C. Subsequently, the stained cells were separately treated with either 1:1000 DMSO or 2 µM Apilimod for 2 h at 37 °C, followed by washing. The cells were then combined in a 1:1 ratio in PBS. CD8$^+$ T cells with wild-type VPS34 (isolated from CD8a-cre$^{+/-}$, VPS34-Exon21$^{wt/wt}$ animals) were labeled with CTV, while those with catalytic-dead VPS34 (CD8a-cre$^{+/-}$, VPS34-Exon21$^{flox/flox}$ animals) were labeled with CTFR, and both were mixed in a 1:1 ratio. Generation and characterization of the VPS34-Exon21 flox model was described previously.[38] CD8a-cre and VPS34-Exon21-flox mice were bred and housed in a specific-pathogen-free facility at the University of Cambridge.

The labels were switched for each respective repetition experiment. For injection, a total of 3 x 10^6 cells (1.5 x 10^6 per condition) were administered into the tail vein of recipient mice. After 1 h spleens and lymph nodes (inguinal, axillary, and cervical) were harvested, and single-cell suspensions were obtained by passing the organs through a 70 µm cell strainer. Samples collected from spleens and organs were subjected to red blood cell lysis, followed by a single wash in FCS buffer and fixation with 4% PFA. The ratio of transferred cells was quantified using a CytoFlex (Beckman Coulter) or Aurora flow cytometer (Cytek). Subsequently, the homing index was calculated by determining the ratio of CTV-labeled cells to CTFR-labeled cells in comparison to the input ratio. The relative abundance of Apilimod-treated cells or cd-VPS34 T cells was normalized to their internal controls per recipient mouse.

Sequence alignment, phylogenetic analysis and FYVE-domain retrieval

The amino acid sequences were accessed through the public domain (UniProt; **Table 5**).[73] The Mega (Version 11.0.13) software was used to perform alignments with the MUSCLE algorithm and the phylogenetic analysis with the maximum likelihood method.[74] The FYVE domains were extracted by searching the InterPro for the FYVE zinc finger domain (IPR000306) for the analyzed animals and filtering out duplicate protein names.[55]

Table 5

Organism	**Gene / *orthologue***	**Accession #**
Arabidopsis thaliana	VPS34	P42339
	FAB1A **/** *PIKfyve*	Q0WUR5
Danio rerio	PIKfyve	B2KTE3
	p110α	F1QAD7
	VPS34	F1Q9F3
D. discoideum	PI5K3 / *PIKfyve*	B0G126
	pikA / *p110α*	P54673
	pikE / *VPS34*	P54676
	Mucolipin / *TRPML1*	Q54Y0
Homo sapiens	PIKfyve	Q9Y2I7
	p110α	P42336
	VPS34	Q8NEB9
Mus musculus	Pikfyve / *PIKfyve*	Q9Z1T6
	p110α	P42337
	VPS34	Q6PF93
	TRPML1	Q99J21
Saccharomyces cerevisiae (Saccharomyces cere.)	VPS34	P22543
	Fab1 / *PIKfyve*	P34756
Xenopus tropicalis	PIKfyve	A0A6I8Q3Y5
	p110α	B0BLW6
	VPS34	F6ZM84

Protein structure analysis and *in silico* docking

Protein structures for TRPML1 bound to $PI(3,5)P_2$ (*Mus musculus; experimentally determined*; UniProt Entry: Q99J21, Structure identifier: 7sq7) and Mucolipin (*D. discoideum; Alphafold model*; UniProt Entry: Q54EY0, Structure identifier: AF-Q54EY0) were sourced through the public domain (UniProt, AlphaFold).[73,75,76] Structures were aligned in PyMol and electrostatic potential was computed with the Adaptive Poisson-Boltzmann Solver (APBS) plug-in.[77] The *in* *silico* docking was performed with high ambiguity-driven protein-protein docking (HADDOCK 2.4).[78,79] The predicted mucolipin and PI(3,5)P_2 structures were inputted and the PI(3,5)P_2 binding AAs were added as interacting residues. The output model was then loaded into the PyMol and aligned with the TRPML1 structure.

References

1. Brunet, T. *et al.* A flagellate-to-amoeboid switch in the closest living relatives of animals. *eLife* **10**, e61037 (2021).
2. Tyson, R. A., Zatulovskiy, E., Kay, R. R. & Bretschneider, T. How blebs and pseudopods cooperate during chemotaxis. *Proc. Natl. Acad. Sci.* **111**, 11703–11708 (2014).
3. Schick, J. & Raz, E. Blebs—Formation, Regulation, Positioning, and Role in Amoeboid Cell Migration. *Front. Cell Dev. Biol.* **10**, (2022).
4. Tsai, T. Y.-C. *et al.* Efficient Front-Rear Coupling in Neutrophil Chemotaxis by Dynamic Myosin II Localization. *Dev. Cell* **49**, 189-205.e6 (2019).
5. Liu, Y.-J. *et al.* Confinement and Low Adhesion Induce Fast Amoeboid Migration of Slow Mesenchymal Cells. *Cell* **160**, 659–672 (2015).
6. Hons, M. *et al.* Chemokines and integrins independently tune actin flow and substrate friction during intranodal migration of T cells. *Nat. Immunol.* **19**, 606–616 (2018).
7. Renkawitz, J. *et al.* Adaptive force transmission in amoeboid cell migration. *Nat. Cell Biol.* **11**, 1438–1443 (2009).
8. Jacobelli, J., Chmura, S. A., Buxton, D. B., Davis, M. M. & Krummel, M. F. A single class II myosin modulates T cell motility and stopping, but not synapse formation. *Nat. Immunol.* **5**, 531–538 (2004).
9. Goor, D. V., Hyland, C., Schaefer, A. W. & Forscher, P. The Role of Actin Turnover in Retrograde Actin Network Flow in Neuronal Growth Cones. *PLOS ONE* **7**, e30959 (2012).
10. Lin, C. H., Espreafico, E. M., Mooseker, M. S. & Forscher, P. Myosin Drives Retrograde F-Actin Flow in Neuronal Growth Cones. *Neuron* **16**, 769–782 (1996).
11. Yam, P. T. *et al.* Actin–myosin network reorganization breaks symmetry at the cell rear to spontaneously initiate polarized cell motility. *J. Cell Biol.* **178**, 1207–1221 (2007).
12. Solanes, P. *et al.* Space exploration by dendritic cells requires maintenance of myosin II activity by IP3 receptor 1. *EMBO J.* **34**, 798–810 (2015).
13. Isotani, E. *et al.* Real-time evaluation of myosin light chain kinase activation in smooth muscle tissues from a transgenic calmodulin-biosensor mouse. *Proc. Natl. Acad. Sci.* **101**, 6279–6284 (2004).
14. Campello, S. *et al.* Orchestration of lymphocyte chemotaxis by mitochondrial dynamics. *J. Exp. Med.* **203**, 2879–2886 (2006).
15. Morlino, G. *et al.* Miro-1 Links Mitochondria and Microtubule Dynein Motors To Control Lymphocyte Migration and Polarity. *Mol. Cell. Biol.* **34**, 1412–1426 (2014).

16. Vestre, K. *et al.* Rab7b regulates dendritic cell migration by linking lysosomes to the actomyosin cytoskeleton. *J. Cell Sci.* **134**, jcs259221 (2021).

17. Bretou, M. *et al.* Lysosome signaling controls the migration of dendritic cells. *Sci. Immunol.* **2**, eaak9573 (2017).

18. Faroudi, M. *et al.* Critical roles for Rac GTPases in T-cell migration to and within lymph nodes. *Blood* **116**, 5536–5547 (2010).

19. Sánchez-Madrid, F. & Serrador, J. M. Bringing up the rear: defining the roles of the uropod. *Nat. Rev. Mol. Cell Biol.* **10**, 353–359 (2009).

20. Betz, C. & Hall, M. N. Where is mTOR and what is it doing there? *J. Cell Biol.* **203**, 563–574 (2013).

21. Haas, R. *et al.* Lactate Regulates Metabolic and Pro-inflammatory Circuits in Control of T Cell Migration and Effector Functions. *PLOS Biol.* **13**, e1002202 (2015).

22. Munk, R. *et al.* Involvement of mTOR in CXCL12 Mediated T Cell Signaling and Migration. *PLOS ONE* **6**, e24667 (2011).

23. Murooka, T. T., Rahbar, R., Platanias, L. C. & Fish, E. N. CCL5-mediated T-cell chemotaxis involves the initiation of mRNA translation through mTOR/4E-BP1. *Blood* **111**, 4892–4901 (2008).

24. Rageot, D. *et al.* Discovery and Preclinical Characterization of 5-[4,6-Bis({3-oxa-8-azabicyclo[3.2.1]octan-8-yl})-1,3,5-triazin-2-yl]-4-(difluoromethyl)pyridin-2-amine (PQR620), a Highly Potent and Selective mTORC1/2 Inhibitor for Cancer and Neurological Disorders. *J. Med. Chem.* **61**, 10084–10105 (2018).

25. Chi, H. Regulation and function of mTOR signalling in T cell fate decisions. *Nat. Rev. Immunol.* **12**, 325–338 (2012).

26. Marat, A. L. & Haucke, V. Phosphatidylinositol 3-phosphates—at the interface between cell signalling and membrane traffic. *EMBO J.* **35**, 561–579 (2016).

27. Dayam, R. M. *et al.* The Lipid Kinase PIKfyve Coordinates the Neutrophil Immune Response through the Activation of the Rac GTPase. *J. Immunol. Baltim. Md 1950* **199**, 2096–2105 (2017).

28. Giridharan, S. S. P. *et al.* Lipid kinases VPS34 and PIKfyve coordinate a phosphoinositide cascade to regulate retriever-mediated recycling on endosomes. *eLife* **11**, e69709 (2022).

29. Gillooly, D. J. *et al.* Localization of phosphatidylinositol 3-phosphate in yeast and mammalian cells. *EMBO J.* **19**, 4577–4588 (2000).

30. Kendirli, A. *et al.* A genome-wide in vivo CRISPR screen identifies essential regulators of T cell migration to the CNS in a multiple sclerosis model. *Nat. Neurosci.* **26**, 1713–1725 (2023).

31. Bago, R. *et al.* Characterization of VPS34-IN1, a selective inhibitor of Vps34, reveals that the phosphatidylinositol 3-phosphate-binding SGK3 protein kinase is a downstream target of class III phosphoinositide 3-kinase. *Biochem. J.* **463**, 413–427 (2014).

32. Cai, X. *et al.* PIKfyve, a Class III PI Kinase, Is the Target of the Small Molecular IL-12/IL-23 Inhibitor Apilimod and a Player in Toll-like Receptor Signaling. *Chem. Biol.* **20**, 912–921 (2013).

33. Gayle, S. *et al.* Identification of apilimod as a first-in-class PIKfyve kinase inhibitor for treatment of B-cell non-Hodgkin lymphoma. *Blood* **129**, 1768–1778 (2017).
34. Nombela-Arrieta, C. *et al.* A central role for DOCK2 during interstitial lymphocyte motility and sphingosine-1-phosphate–mediated egress. *J. Exp. Med.* **204**, 497–510 (2007).
35. Ronan, B. *et al.* A highly potent and selective Vps34 inhibitor alters vesicle trafficking and autophagy. *Nat. Chem. Biol.* **10**, 1013–1019 (2014).
36. Morin, N. A. *et al.* Nonmuscle myosin heavy chain IIA mediates integrin LFA-1 de-adhesion during T lymphocyte migration. *J. Exp. Med.* **205**, 195–205 (2008).
37. Smith, A., Bracke, M., Leitinger, B., Porter, J. C. & Hogg, N. LFA-1-induced T cell migration on ICAM-1 involves regulation of MLCK-mediated attachment and ROCK-dependent detachment. *J. Cell Sci.* **116**, 3123–3133 (2003).
38. Courreges, C. J. F. *et al.* Lack of phosphatidylinositol 3-kinase VPS34 in regulatory T cells leads to a fatal lymphoproliferative disorder without affecting their development. 2024.01.08.574346 Preprint at https://doi.org/10.1101/2024.01.08.574346 (2024).
39. Tadayon, S. *et al.* Clever-1 contributes to lymphocyte entry into the spleen via the red pulp. *Sci. Immunol.* **4**, eaat0297 (2019).
40. Chauveau, A. *et al.* Visualization of T Cell Migration in the Spleen Reveals a Network of Perivascular Pathways that Guide Entry into T Zones. *Immunity* **52**, 794-807.e7 (2020).
41. Chang, Y.-C., Nalbant, P., Birkenfeld, J., Chang, Z.-F. & Bokoch, G. M. GEF-H1 Couples Nocodazole-induced Microtubule Disassembly to Cell Contractility via RhoA. *Mol. Biol. Cell* **19**, 2147–2153 (2008).
42. Kolodney, M. S. & Elson, E. L. Contraction due to microtubule disruption is associated with increased phosphorylation of myosin regulatory light chain. *Proc. Natl. Acad. Sci.* **92**, 10252–10256 (1995).
43. Liu, B. P., Chrzanowska-Wodnicka, M. & Burridge, K. Microtubule Depolymerization Induces Stress Fibers, Focal Adhesions, and DNA Synthesis via the GTP-Binding Protein Rho. *Cell Adhes. Commun.* **5**, 249–255 (1998).
44. Kopf, A. *et al.* Microtubules control cellular shape and coherence in amoeboid migrating cells. *J. Cell Biol.* **219**, e201907154 (2020).
45. Hui, K. L. & Upadhyaya, A. Dynamic microtubules regulate cellular contractility during T-cell activation. *Proc. Natl. Acad. Sci.* **114**, E4175–E4183 (2017).
46. Riedl, J. *et al.* Lifeact: a versatile marker to visualize F-actin. *Nat. Methods* **5**, 605–607 (2008).
47. Gan, N. *et al.* Structural mechanism of allosteric activation of TRPML1 by PI(3,5)P2 and rapamycin. *Proc. Natl. Acad. Sci.* **119**, e2120404119 (2022).
48. Dong, X. *et al.* PI(3,5)P2 controls membrane trafficking by direct activation of mucolipin Ca2+ release channels in the endolysosome. *Nat. Commun.* **1**, 38 (2010).
49. Feng, X. *et al.* Drosophila TRPML Forms PI(3,5)P2-activated Cation Channels in Both Endolysosomes and Plasma Membrane *. *J. Biol. Chem.* **289**, 4262–4272 (2014).
50. Chen, C.-C. *et al.* A small molecule restores function to TRPML1 mutant isoforms responsible for mucolipidosis type IV. *Nat. Commun.* **5**, 4681 (2014).

51. Philippon, H., Brochier-Armanet, C. & Perrière, G. Evolutionary history of phosphatidylinositol- 3-kinases: ancestral origin in eukaryotes and complex duplication patterns. *BMC Evol. Biol.* **15**, 226 (2015).
52. Buckley, C. M. *et al.* PIKfyve/Fab1 is required for efficient V-ATPase and hydrolase delivery to phagosomes, phagosomal killing, and restriction of Legionella infection. *PLOS Pathog.* **15**, e1007551 (2019).
53. Yoshida, K. & Soldati, T. Dissection of amoeboid movement into two mechanically distinct modes. *J. Cell Sci.* **119**, 3833–3844 (2006).
54. Lima, W. C., Leuba, F., Soldati, T. & Cosson, P. Mucolipin controls lysosome exocytosis in Dictyostelium. *J. Cell Sci.* **125**, 2315–2322 (2012).
55. Paysan-Lafosse, T. *et al.* InterPro in 2022. *Nucleic Acids Res.* **51**, D418–D427 (2023).
56. Korolchuk, V. I. *et al.* Lysosomal positioning coordinates cellular nutrient responses. *Nat. Cell Biol.* **13**, 453–460 (2011).
57. Scerra, G. *et al.* Lysosomal positioning diseases: beyond substrate storage. *Open Biol.* **12**, 220155 (2022).
58. Burgoyne, T., Patel, S. & Eden, E. R. Calcium signaling at ER membrane contact sites. *Biochim. Biophys. Acta BBA - Mol. Cell Res.* **1853**, 2012–2017 (2015).
59. Atakpa, P., Thillaiappan, N. B., Mataragka, S., Prole, D. L. & Taylor, C. W. IP3 Receptors Preferentially Associate with ER-Lysosome Contact Sites and Selectively Deliver Ca2+ to Lysosomes. *Cell Rep.* **25**, 3180-3193.e7 (2018).
60. Peng, W., Wong, Y. C. & Krainc, D. Mitochondria-lysosome contacts regulate mitochondrial Ca2+ dynamics via lysosomal TRPML1. *Proc. Natl. Acad. Sci.* **117**, 19266–19275 (2020).
61. Bartok, A. *et al.* IP3 receptor isoforms differently regulate ER-mitochondrial contacts and local calcium transfer. *Nat. Commun.* **10**, 3726 (2019).
62. Oppelt, A. *et al.* PIKfyve, MTMR3 and their product PtdIns5P regulate cancer cell migration and invasion through activation of Rac1. *Biochem. J.* **461**, 383–390 (2014).
63. Shisheva, A. PIKfyve: Partners, significance, debates and paradoxes. *Cell Biol. Int.* **32**, 591–604 (2008).
64. Burke, J. E., Triscott, J., Emerling, B. M. & Hammond, G. R. V. Beyond PI3Ks: targeting phosphoinositide kinases in disease. *Nat. Rev. Drug Discov.* **22**, 357–386 (2023).
65. Fritz-Laylin, L. K., Lord, S. J. & Mullins, R. D. WASP and SCAR are evolutionarily conserved in actin-filled pseudopod-based motility. *J. Cell Biol.* **216**, 1673–1688 (2017).
66. Fritz-Laylin, L. K. & Titus, M. A. The evolution and diversity of actin-dependent cell migration. *Mol. Biol. Cell* **34**, pe6 (2023).
67. Heit, B. & Kubes, P. Measuring Chemotaxis and Chemokinesis: The Under-Agarose Cell Migration Assay. *Sci. STKE* **2003**, pl5–pl5 (2003).
68. Artinger, M., Matti, C., Gerken, O. J., Veldkamp, C. T. & Legler, D. F. A Versatile Toolkit for Semi-Automated Production of Fluorescent Chemokines to Study CCR7 Expression and Functions. *Int. J. Mol. Sci.* **22**, 4158 (2021).

69. Berg, S. *et al.* ilastik: interactive machine learning for (bio)image analysis. *Nat. Methods* **16**, 1226–1232 (2019).

70. Ershov, D. *et al.* TrackMate 7: integrating state-of-the-art segmentation algorithms into tracking pipelines. *Nat. Methods* **19**, 829–832 (2022).

71. Mangeol, P., Prevo, B. & Peterman, E. J. G. KymographClear and KymographDirect: two tools for the automated quantitative analysis of molecular and cellular dynamics using kymographs. *Mol. Biol. Cell* **27**, 1948–1957 (2016).

72. Lowe, D. G. Distinctive Image Features from Scale-Invariant Keypoints. *Int. J. Comput. Vis.* **60**, 91–110 (2004).

73. The UniProt Consortium. UniProt: the Universal Protein Knowledgebase in 2023. *Nucleic Acids Res.* **51**, D523–D531 (2023).

74. Tamura, K., Stecher, G. & Kumar, S. MEGA11: Molecular Evolutionary Genetics Analysis Version 11. *Mol. Biol. Evol.* **38**, 3022–3027 (2021).

75. Jumper, J. *et al.* Highly accurate protein structure prediction with AlphaFold. *Nature* **596**, 583–589 (2021).

76. Varadi, M. *et al.* AlphaFold Protein Structure Database: massively expanding the structural coverage of protein-sequence space with high-accuracy models. *Nucleic Acids Res.* **50**, D439–D444 (2022).

77. Jurrus, E. *et al.* Improvements to the APBS biomolecular solvation software suite. *Protein Sci.* **27**, 112–128 (2018).

78. van Zundert, G. C. P. *et al.* The HADDOCK2.2 Web Server: User-Friendly Integrative Modeling of Biomolecular Complexes. *J. Mol. Biol.* **428**, 720–725 (2016).

79. Honorato, R. V. *et al.* Structural Biology in the Clouds: The WeNMR-EOSC Ecosystem. *Front. Mol. Biosci.* **8**, (2021).

6.1.4 Extended Data, Material, and Methods

6.1.4.1 PIKfyve Inhibition Impairs T cell Recruitment and Bacterial Control in a Murine Peritonitis Model

To investigate whether PIKfyve inhibition influences T cell recruitment in an inflammatory setting *in vivo*, we employed an ovalbumin-expressing *Listeria monocytogenes* (LmOva)-infection peritonitis model. Immunization of mice with LmOva generates memory T cells that are rapidly recruited to sites of re-infections.[292,293] We utilized this model to treat LmOva-immunized mice with vehicle (PBS) or the PIKfyve inhibitor, Apilimod, one hour before peritoneal rechallenge with LmOva. 16 hours post-infection, a peritoneal lavage was carried out to collect cell infiltrating the peritoneum, and the spleen was harvested (**Fig. 5A**). The Apilimod-treated mice exhibited reduced numbers of infiltrating CD8+ and CD4+ T cells in the peritoneum (**Fig. 5B-C**). Further, an increased bacterial burden was detected in the peritoneum and spleen of Apilimod-treated animals (**Fig. 5D**). It remains unclear whether the infiltration is a direct effect of PIKfyve inhibition on T cells or a secondary effect (e.g. reduced chemokine production by innate cells) due to the systemic administration of Apilimod.

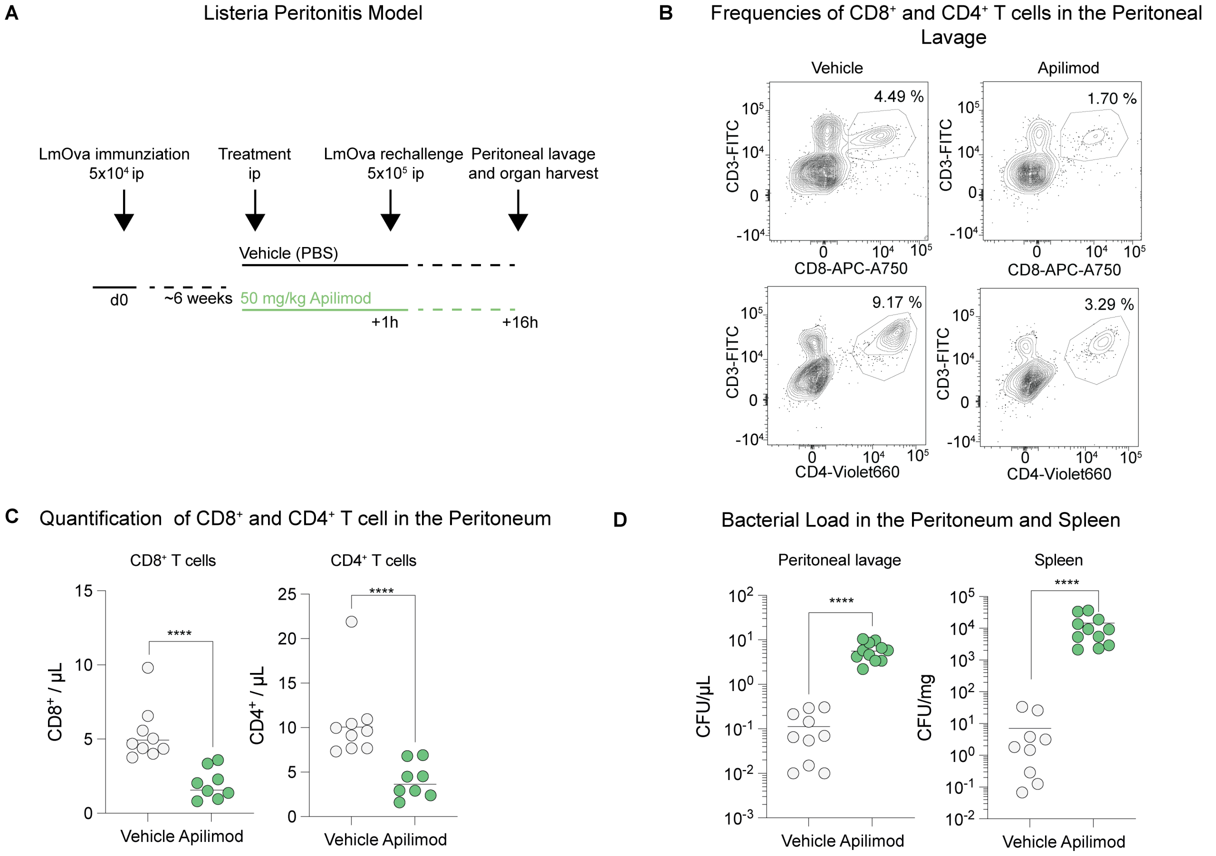

Figure 5: PIKfyve Inhibition Impairs T cell Recruitment and Bacterial Control in a Murine Peritonitis Model I A) Schematic of the LmOva peritonitis model: Six weeks post-immunization, mice were treated either with a vehicle or with Apilimod intraperitoneally (*ip*), followed by a rechallenge using LmOva *(ip)* **B)** Representative frequencies of $CD8^+$ (*upper panels*) and $CD4^+$ T cells (lower panels) in the live cell gate of the peritoneal fluid from a vehicle-treated (*left panels*) or Apilimod-treated (*right panels*) subject. **C)** Quantification of the $CD8^+$ (*left panel*) and $CD4^+$ T cells (*right panel*) present in the peritoneal fluid of subjects treated with the vehicle (n = 9) or Apilimod (n = 8). **D)** Quantification of CFU in the peritoneal fluid (*left pan*el) and spleen (*right panel*) 16 hours after the LmOva rechallenge in subjects treated with either the vehicle (n = 10) or Apilimod (n = 10). *For panels C and D, individual points represent data from single animals, which have been pooled from two independent experiments. A p-value of < 0.0001 (****), as determined by a Mann-Whitney test, indicates statistical significance.*

6.1.4.2 Material and Methods for the LmOva peritonitis model

LmOva (a gift from Ed Palmer) was grown in BHI-medium (Sigma Aldrich, Cat. # 70138) at 37 °C to an optical density of 0.5 - 1. 8 - 10-week-old C57BL/6NCrl mice were infected with 5×10^4 CFU LmOva in 100 μL PBS intraperitoneally (ip) for the immunization. After 6 weeks, 50 mg / kg body weight Apilimod (MedChem Express, Cat. # HY-14644A) or 100 μL PBS as vehicle control was administered ip, one hour before re-infection with 5×10^5 CFU LmOva. Sixteen hours after the secondary infection, the animals were euthanized using CO2 (**Fig. 5A**). A peritoneal lavage was conducted using 8 ml of PBS, followed by spleen extraction. The spleens were then weighed and homogenized using steel beads. Bacterial burden was determined by plating 50 μL of peritoneal lavage or homogenized spleen on petri dishes containing BHI agar (Sigma Aldrich, Cat. #70138) and colony forming units (CFU) counted after 16 h of incubation at 37 °C. To quantify T cell numbers in the peritoneal lavage, counting beads were added to 4 ml of the peritoneal lavage, followed by preparation for flow cytometry. A live-dead staining was performed as per the protocol outlined in the unpublished manuscript (*Section I, Prepared Manuscript, Material and Methods)*, followed by surface staining for 15 min at RT with antibodies against murine FITC anti-CD3e (Biolegend, Cat. # 553062), APC-Cy7 anti-CD8 (Biolegend, Cat. # 100713), and BV650 anti-CD4 (Biolegend, Cat. # 100555) antibodies. After the staining, the cells were fixed in a 4% paraformaldehyde solution and samples acquired using a CytoFlex (Beckman Coulter) flow cytometer.

6.2 Section II: Interrogation of Chemokine-Induced Metabolism in Naïve $CD8^+$ T cells

6.2.1 Summary

Amoeboid T cell migration relies on energy derived from both glycolysis and mitochondrial respiration, which in turn facilitates cytoskeleton dynamics.[67,109–113] Chemokine stimulation increases glycolysis and mitochondrial respiration, fostering migration in effector and regulatory T cells.[109–111] However, the intricacies of metabolic adaptations to chemokines are not fully explored. We, therefore, investigated the cellular metabolism of naïve murine $CD8^+$ T cells upon CCL19 treatment.

Following CCL19 exposure, a surrogate for glycolytic activity indicated enhanced glycolysis in naïve murine $CD8^+$ T cells. Moreover, CCL19 transiently increased cellular respiration and augmented maximal mitochondrial respiration. These results confirmed a metabolic reaction of naïve $CD8^+$ T cells to CCL19. Therefore, an unbiased metabolomic analysis was performed and revealed various differentially abundant metabolites, including metabolites from the TCA cycle upon chemokine treatment. These observations hint at a broad metabolic reshaping of naïve $CD8^+$ T cells following chemokine exposure, although they necessitate further targeted validation. Next, we hypothesized that migratory characteristics (e.g. speed) might correlate with the ability to engage metabolic pathways. A comparative transcriptome analysis revealed an increase in glycolytic and TCA cycle enzyme transcripts correlating with faster and more directed naïve $CD8^+$ T cell migration in a CCL19 gradient.

In summary, our preliminary findings in naïve $CD8^+$ T cells suggest a metabolic adaptation to CCL19 beyond glycolysis. The TCA cycle emerges as a promising candidate pathway for subsequent research. However, further studies are warranted – including validation as well as functional and metabolic analyses – to establish a functional connection between our observations and T cell migration.

6.2.2 Author Contribution

This study was supervised and coordinated by Christoph Hess and Matthias Mehling. Christoph Hess, Matthias Mehling, and Philippe Dehio conceived, designed, and interpreted the experimental results. The extracellular flux analysis was performed by Philippe Dehio, assisted by Jonas Lötscher (University of Basel). Sample extraction, mass spectrometry, analysis, and compound annotation were conducted by James West (University of Cambridge), and the statistical analysis was carried out by Philippe Dehio. Philip Dettinger (ETH Zürich) produced the microfluidic chips for the RNA-sequencing experiment. Corina Frick (University of Basel), Philip Dettinger, and Matthias Mehling developed and established the microfluidic platform. They assisted in adapting this platform to the migration and harvesting of murine naïve $CD8^+$ T cells. Philippe Dehio conducted the migration experiments and was responsible for cell harvesting and RNA isolation. The Genomics Facility (University of Basel, ETH Zürich) undertook the transcriptome sequencing, which included library preparation and amplification. Philippe Dehio performed the computational analysis of the transcriptome dataset with assistance of Julien Roux (University of Basel).

6.2.3 Introduction

Amoeboid T cell migration is indispensable for adaptive immunity and contributes to the pathogenesis of autoimmune diseases. Chemokines induce polarization and migration and are pivotal for directing T cells to appropriate effector sites.[262] Two major bioenergetic requirements of T cell migration are actin polymerization, met by glycolysis, and myosin IIA activity, facilitated by mitochondrial ATP synthesis.[67,111] Recent studies underscore the importance of chemokine-mediated metabolic shifts in optimizing T cell migration. For instance, the chemokine CXCL10 has been demonstrated to promote migration of effector $CD4^+$ T cells by augmenting glycolysis and elevating the expression of glycolytic enzymes.[110] Similarly, the chemokine CCL22 plays a critical role in regulating migration and actin polymerization in regulatory T cells.[111] Furthermore, exposure to CXCL12 augments glycolytic activity and mitochondrial function in effector $CD8^+$ T cells in the presence of ICAM-1.[109] However, the full extent to which chemokines modulate cellular metabolism remains unexplored. Compared to effector T cells, naïve T cells exhibit a quiescent metabolism, potentially aiding in the dissection of chemokine-induced metabolism.[267]

Given this background, our study aimed to pinpoint metabolic pathways influenced by exposure to CCL19, a chemokine recognized for its pro-migratory properties, in naïve $CD8^+$ T cells.

6.2.4 Results

6.2.4.1 CCL19 Alters Glycolysis and Cellular Respiration of Naïve $CD8^+$ T Cells

To test if naïve murine $CD8^+$ T cells alter glycolysis and cellular respiration upon CCL19 exposure, we monitored their metabolic activity using an extracellular flux analyzer. This allows the assessment of the extracellular acidification rate (ECAR) and the oxygen consumption rate (OCR), serving as a surrogate for glycolysis or cellular respiration, respectively. Using the same experimental setup, we performed a mitochondrial stress test using ETC inhibitors to assess the mitochondrial respiration.

Our data reveal that CCL19 exposure caused an immediate elevation in ECAR, indicative of increased glycolytic activity (**Fig. 6A**, *left panel*s). Concurrently, an initial surge in cellular respiration was detected post-CCL19 treatment, which subsequently reverted to baseline levels within approximately 30 minutes (**Fig. 6A**, *right panels*). A mitochondrial stress test unveiled that CCL19 enhanced maximal respiration without influencing ATP-linked or non-mitochondrial respiration (**Fig. 6B**).

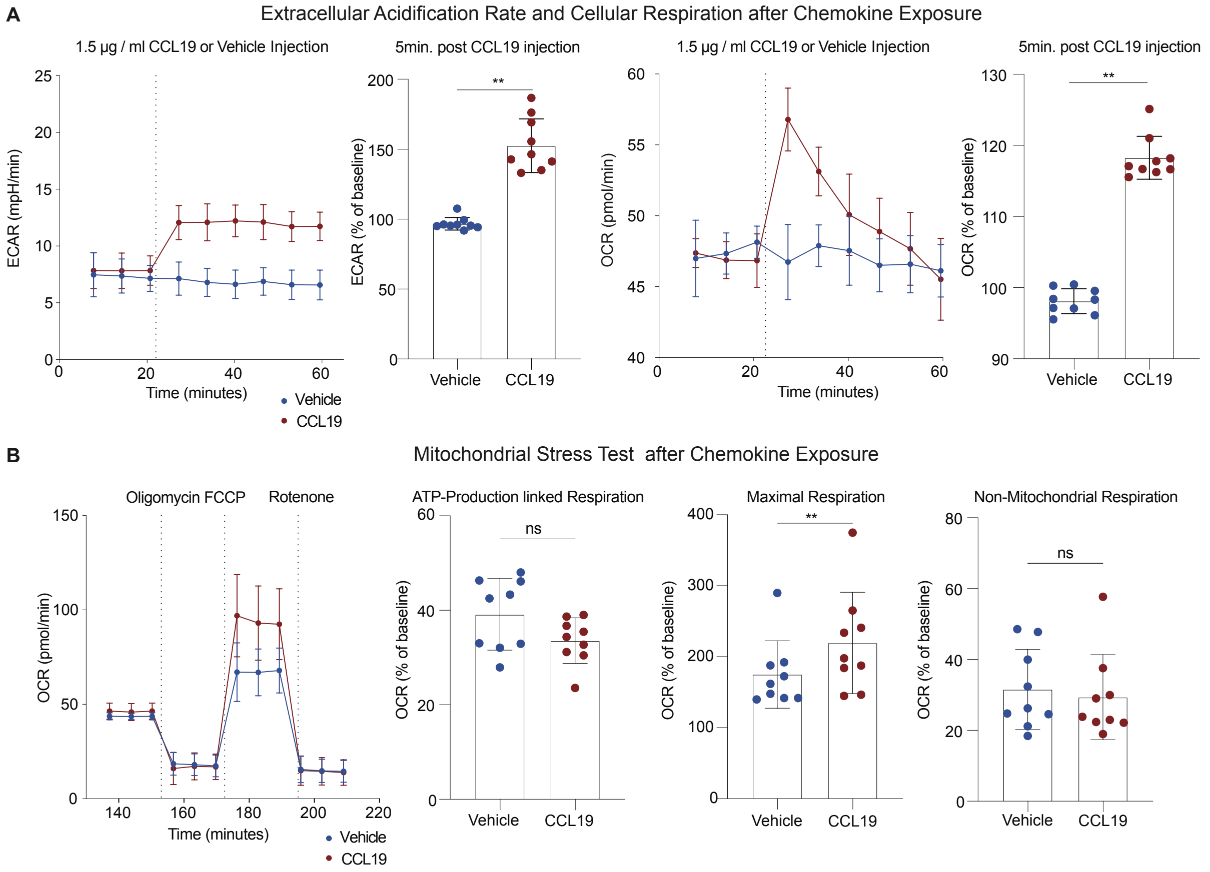

Figure 6: CCL19 Alters Glycolysis and Cellular Respiration of Naïve CD8+ T Cells I A) *Far left panel:* Representative ECAR profile of murine naïve CD8+ T cells. *Center left panel*: ECAR levels 5 minutes after CCL19 injection, based on nine biological replicates from three independent experiments. *Center right panel*: Representative oxygen consumption rate (OCR) profile for naïve CD8+ T cells. *Far right panel*: OCR levels 5 minutes after CCL19 injection. **B)** *Far left panel:* Representative mitochondrial stress test OCR profile 130 minutes after vehicle or CCL19 injection*; Center left:* ATP-Production linked Respiration (after Oligomycin injection), *Center right:* Maximal Respiration (after FCCP injection), and *Far right:* Non-Mitochondrial Respiration (after Rotenone injection). *For panels A, B: OCR and ECAR profiles wherein dots indicate the mean, error bars standard deviation of 4 technical replicates, and the dotted line marks the CCL19 / Vehicle injection. For comparison of OCR and ECAR levels, measurements were normalized to their last baseline measurement. Dots represent biological replicates (n = 9) from three independent experiments, and the bar graph indicates the mean and standard deviation. Statistical analysis: Wilcoxon matched-pairs signed rank test, p-value: ns > 0.05, ** < 0.01*

Collectively, this indicates that CCL19 treatment induces an augmentation in glycolysis in naïve murine CD8+ T cells — a metabolic signature resembling that seen in effector or regulatory CD4+ T cells upon stimulation with CXCL10 or CCL22, respectively.[110,111] In addition to this, we detected a temporary spike in cellular respiration paired with a boost in maximal mitochondrial respiration post-chemokine treatment.

6.2.4.2 CCL19 Broadly Alters Metabolism of Naïve CD8⁺ T Cells

The extracellular flux analysis revealed metabolic alterations in naïve CD8⁺ T cells upon CCL19 exposure. Consequently, we sought to directly examine the abundance of metabolites in cells treated with CCL19. To accomplish this, we conducted an unbiased metabolomics study on naïve murine CD8⁺ T cells treated for 4 hours with CCL19 or vehicle (**Fig. 7A**).

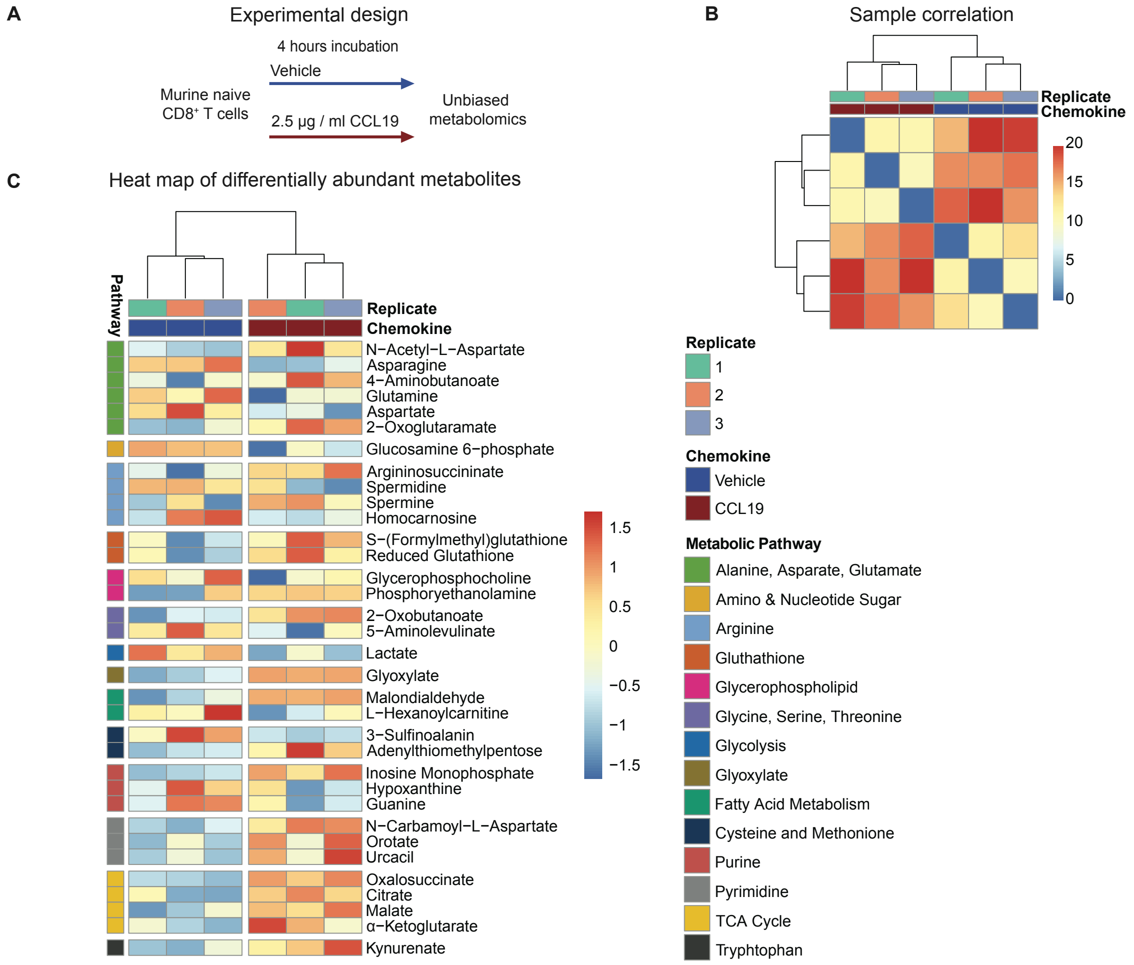

Figure 7: CCL19 Broadly Alters Metabolism of Naïve CD8⁺ T Cells I A) Experimental design of the unbiased metabolomics study. **B)** Sample correlation of the three biological replicates treated with either CCL19 or vehicle. **C)** Heat map of differentially abundant metabolites ordered by metabolic pathways with an adj. p-value < 0.05 with colors indicating the levels of abundance (red for higher abundance, blue for lower abundance).

The sample correlation analysis demonstrated a clear separation of the two groups, indicative of distinct metabolic profiles (**Fig. 7B**). Notably, we identified an accumulation of metabolites associated with the TCA cycle (citrate, α-ketoglutarate, oxalosuccinate, malate) and a decrease in lactate abundance in CCL19-treated naïve murine CD8⁺ T cells. Concurrently, chemokine treatment resulted in altered abundance of metabolites in various metabolic pathways, including amino acids (alanine, aspartate, glutamine, and asparagine), arginine-derived metabolites, as well as compounds linked to pyrimidine and purine pathways (**Fig. 7C**).

Thus, these results hint at a substantial metabolic reconfiguration in naïve CD8$^+$ T cells in response to CCL19 stimulation, including a decrease of lactate and increase of TCA cycle metabolites.

6.2.4.3 Glycolytic and TCA-cycle Transcript Levels Correlate with Faster and more Directed Naïve CD8$^+$ T Cell Migration

With the knowledge of altered metabolism upon CCL19 exposure, we hypothesized that the ability to engage metabolism (e.g. by different levels of metabolic enzyme transcript abundance) could correlate with migratory behavior of T cells. To test this hypothesis, we aimed to perform a comparative transcriptome analysis on naïve murine CD8$^+$ T cells that displayed varying migratory properties in a CCL19 gradient.

To this end, naïve murine CD8$^+$ T cells were placed in the lower third of a published microfluidic migration device coated with ICAM-1. (**Fig. 8A**, *far left panel,* **Fig. 9**).[294–296] Subsequently, a CCL19 gradient was established with FITC-dextran serving as a chemokine surrogate (**Fig. 8A**, *left panels*). Over four hours, cell migration was monitored as T cells distributed along the gradient, followed by cell harvesting (**Fig. 8A**, *center left panel*). The T cells that advanced to the upper two thirds of the migration chamber were designated as "*Responders*", whereas those remaining in the lower third were categorized as "*Non-Responders*" (**Fig. 8A**, *center left – far right panels*). Responder cells exhibited increased migration velocity, displacement speed, and directionality (**Fig. 8B**, *left and center right panels*). Moreover, a distinction was observed in the initial starting positions of the *Non-Responders* and *Responders*, with the latter predominantly commencing from a higher point within the chamber, as indicated by the Y-position (**Fig. 8B**, *far right panel*).

We employed a low-input RNA-sequencing protocol to retrieve transcriptome data from the harvested T cells. In the differential gene expression analysis, we encountered gene dropouts (= missing transcript detections in single or multiple data points), resulting in variable genome coverage. The analysis did not yield a clear distinction between groups and necessitated stringent data filtering to remove gene dropouts and accounting for genome coverage in the statistical model (**Fig. 8C**). We detected 209 downregulated and 202 upregulated genes in *responder* cells, which included metabolic genes like ATP-citrate lyase (*ACLY*), pyruvate kinase (*PKM*), serine hydroxymethyltransferase 2 (*SHMT2*), malic enzyme (*ME2*), and oxoglutarate dehydrogenase (*OGDH*; **Fig. 8D**).

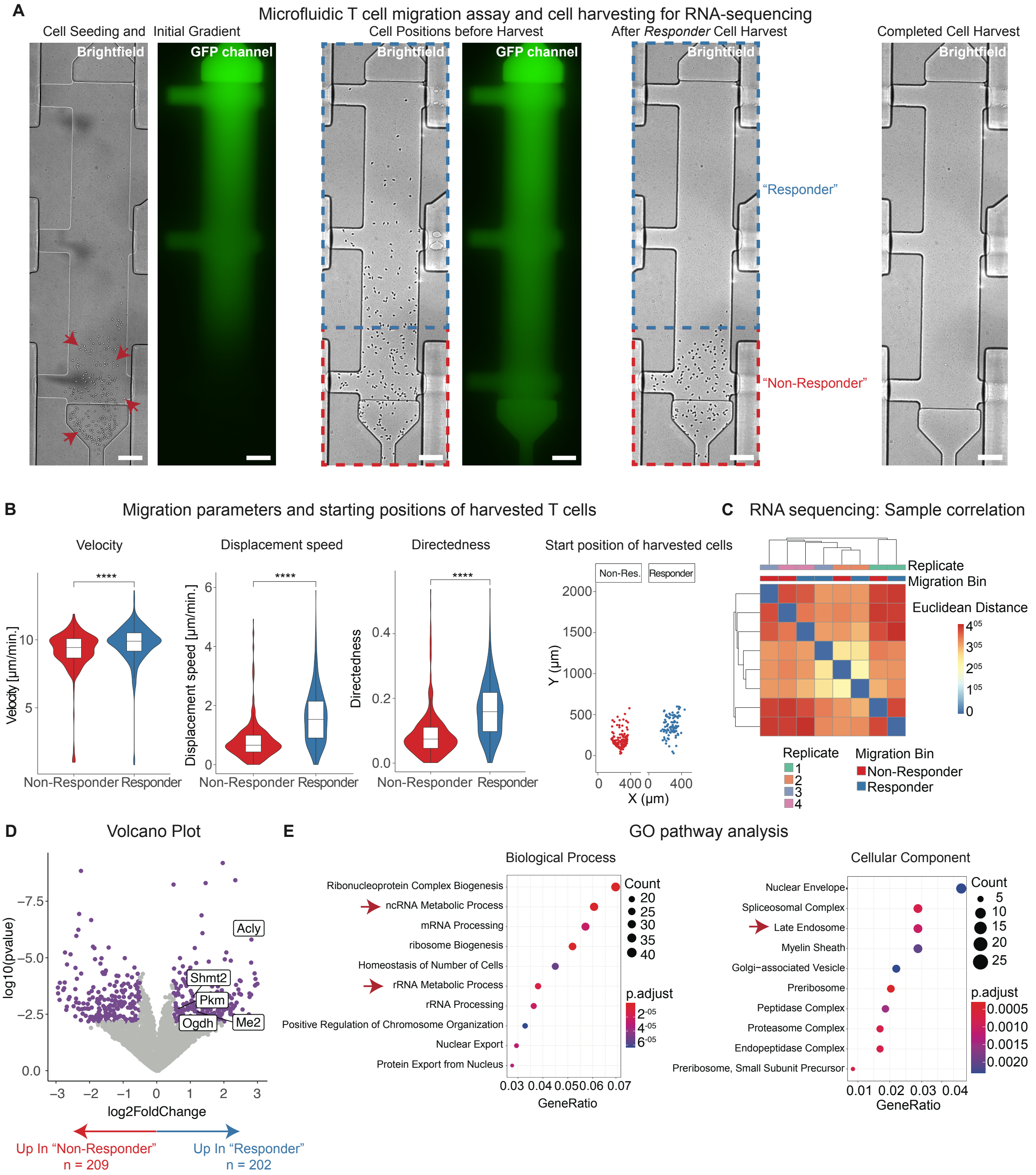

Figure 8: Glycolytic and TCA-cycle Transcript Levels Correlate with Faster and more Directed Naïve CD8$^+$ T Cell Migration I A) T cell migration and harvest experiment in a microfluidic device. *Far left:* Bright field image of seed T cells, with exemplary cell positions indicated by red arrows and the initial FITC-gradient shown in the GFP channel. *Center left:* Positions of cells before harvest after 4 hours of migration in the brightfield image and final FITC-dextran gradient (GFP channel). *Center right:* Bright field image following the harvest of Responder cells. *Far right:* Image of the migration chamber after complete cell harvest. *Scale bar: 100 µm*. **B)** Velocity (*far left*), displacement speed (calculated as Euclidean distance migrated divided by the observed time period, *center left*), directedness (*center right*) stratified by *Responder* (n = 288) and *Non-Responder* (n = 250) cells (data pooled from three migration chambers). *Far right*: Starting positions for *Non-Responder* and *Responder* cells. ***** p-Value < 0.0001; Wilcoxon-rank-sum test* **C)** Sample correlation of transcriptome data between *Non-Responder* and *Responder* cells, derived from four biological replicates across independent experiments. **D)** Volcano plot of differential gene expression of non- and responder T cells transcriptomes. Genes with an adj. p-value < 0.05 and a log2 fold change greater or smaller than 0.5 were considered as differentially expressed and colored in purple. **E)** Cellular component GO-term pathway analysis, comparing the transcriptomes of Non-Responder vs. Responder T cells. The red arrows indicate pathways of interest.

To further explore whether migratory behavior was associated not only with individual metabolic genes but also with metabolic pathways, we conducted a Gene Ontology (GO) pathway analysis. Though this analysis did not identify significantly differentially abundant pathways in intermediary metabolism within the "*Biological Process*" category, it highlighted differential expression in transcripts linked with non-coding and ribosomal RNA metabolism (**Fig. 8E,** *left panel*). In the "*Cellular Components*" category, late endosomal genes were found to be differentially abundant, an intriguing finding considering the role of endo-lysosomes as elucidated in Section 6.1, Part I of the results (**Fig. 8E,** *right panel*).

Thus, the comparative transcriptome analysis revealed an upregulation of several metabolic gene transcript, including a glycolytic gene and two TCA-cycle genes, correlating with faster and more directed migration of naïve CD8$^+$ T cells.

6.2.5 Discussion

In this study, we explored metabolic changes induced by the chemokine CCL19 in murine naïve CD8$^+$ T cells. We observed increased glycolysis and increased mitochondrial respiration following exposure to CCL19. An unbiased metabolomics analysis demonstrated significant alterations in metabolite abundance within CCL19-treated naïve CD8$^+$ T cells, including a decline in lactate levels alongside an elevation of TCA cycle metabolites. Additionally, an association between migratory characteristics and metabolic enzyme transcript levels in naïve CD8$^+$ T cells navigating a CCL19 gradient was detected.

The extracellular flux analysis indicated an increase of ECAR subsequent to CCL19 stimulation, indicative of increased glycolysis. The noted decline in cellular lactate abundance aligns with extracellular flux data, as lactate is a plausible driver of ECAR. Our finding concurs with prior research highlighting chemokine-induced glycolysis in various T cell subsets and DCs.[109–111,113] These studies also inferred a causal relationship of chemokine-induced glycolysis and cell migration. Whether CCL19-induced glycolysis regulates the migration of naïve CD8$^+$ T cells requires further functional studies. We also observed a temporary increase of cellular respiration and enhanced maximum respiratory capacity post-CCL19 treatment in immobilized naïve CD8$^+$ T cells. In contrast, effector CD8$^+$ T cells treated with CXCL12 display a sustained elevated respiration and maximum mitochondrial respiration, when plated on ICAM-1.[109] The underlying reasons for this discrepancy in cellular respiration might encompass variations in the T cell subset, cellular mobility, or the involvement of ICAM-1-LFA1 integrin signaling.

The comparative transcriptome analysis revealed an upregulation of several metabolic genes in *responder* cells, including the glycolytic gene *Pkm*. However, due to several confounders, it is unclear whether these differentially expressed transcripts play a causative role in the observed migratory phenotype. First, *responder* cells encounter higher levels of CCL19 in the upper parts of the migration chamber, possibly driving gene expression. This needs to be considered as *Pkm* expression is induced by the chemokine CXCL10 in effector CD4$^+$ T cells.[110] Next, cells starting closer to the chemokine source were more likely to become a *responder* cell, effectively arguing against a pure stratification on migratory behavior. DCs shape chemokine gradients by chemokine receptor mediated endocytosis. Their directed migration is driven by the cell collective depleting CCL19 from their close vicinity.[96] Speculatively, T cell migration in the microfluidic device might be influenced by a similar effect, thereby confounding the separation of T cells by their single-cell migratory behavior. Moreover, the issue of gene dropouts during transcriptome analysis needs to be addressed. This is a challenge encountered in single cell transcriptome sequencing.[297] A potential mitigation might entail increasing cell material or refinement of sequencing protocols. This could enhance the comprehensiveness of similar transcriptome analyses in the future. Nonetheless, the TCA cycle emerges as a candidate pathway for further interrogation of T cell migration from the convergence of increased TCA cycle genes in *responder* T cells, TCA cycle metabolites and maximal mitochondrial respiration upon CCL19 treatment.

In summary, we present evidence that CCL19 modulates glycolysis and cellular respiration in murine naïve CD8$^+$ T cells. An unbiased metabolomics analysis suggests an expansive metabolic engagement in response to chemokine stimulation. The TCA cycle stands out as promising candidate for further exploration. Connecting these findings functionally to amoeboid T cell migration demands targeted validation, coupled with metabolic tracing experiments, and genetic and metabolic interventions.

6.2.6 Material and Methods

6.2.6.1 Cell isolation and culture

Isolation and cell culture were performed as described in *Material and Methods* of the unpublished manuscript in *Section I* (*6.1.3*) of the results. In short, naïve CD8$^+$ T cells were isolated from spleens and lymph nodes of C57BL/6NrCl mice using negative magnetic cell separation and cultured overnight in complete medium (= RPMI 1640 supplemented with 10% heat-inactivated fetal calf serum, GlutaMax (1:100), 50 μM β-mercaptoethanol, 100 U/mL penicillin, 100 μg/mL streptomycin) supplemented with 10 ng/mL IL-7, before use.

6.2.6.2 Extracellular Flux Analysis

Analyses were conducted using the Seahorse XFe96 Analyzer (Agilent). XF 96-well plates (Agilent, Cat. # 103794-100) were coated with 22.4 μg / ml Cell-Tak (FisherScientific, Cat. # 10317081) in ddH2O + 0.1 mM sodium bicarbonate (pH 8) overnight. Concurrently, the sensor cartridge (Agilent, Cat. # 103792-100) was hydrated with 200 μl calibrant liquid (Agilent, Cat. # 100840-000) per well in an incubator at ambient CO_2-level at 37 °C. The following day, each well of the 96-well plate was rinsed with 200 μl sterile ddH2O and air-dried for 1 hour.

The following steps were all conducted in unbuffered RPMI1640 with glucose (pH 7.4; Sigma-Aldrich, Cat. # R65040). Murine naïve CD8$^+$ T cells were washed twice, counted, and resuspended to 2 x 10^6 cells / ml. Subsequently, 100 μl of cell suspension (= 2 x 10^5 cells) was dispensed per well in the dried 96-well plates. The plate was centrifuged to a speed of 45 g with an acceleration of 5 and deceleration of 4, turned 180°, and centrifuged to a speed of 95 g with an acceleration 4 and deceleration of 3. After centrifugation, 75 μl unbuffered RPMI1640 was added to each well, and the plate was placed in a CO_2-free incubator at 37 °C for 15 minutes.

For the assay, 25 μl of the following solutions diluted in unbuffered RPMI1640 were loaded into the respective injection ports of the sensor cartridge: Port A: 12 μg / ml CCL19 (Peprotech, Cat. # 250-27B) or vehicle, Port B: Oligomycin (8 mM; Sigma-Aldrich, Cat. # 75351), Port C: FCCP (20 μM; Sigma-Aldrich, Cat. # C2920), and Port D: Rotenone (10 μM; Sigma-Aldrich, Cat. # R8875). The cartridge was subsequently placed in the extracellular flux analyzer for calibration.

Post-calibration, the cell-containing plate was transferred to the analyzer. A 20-minute baseline measurement (4 cycles) was taken before the CCL19 injection. This was followed by a 2-hour measurement phase (20 cycles). Subsequent injections included oligomycin, FCCP, and rotenone, with each injection monitored over a 15-minute period (3 cycles). Data were processed and analyzed using the Prism software (GraphPad).

6.2.6.3 Microfluidic Device Fabrication, Operation, Cell Migration Assay, and Cell Harvest

The microfluidic device was fabricated and operated as previously described.[294–296] The devices were prepared by exposing the harvest outlet channels and then connecting the control layer to the solenoid valve control system, pressurizing it, and mounting it on the incubation system of the microscope stage (37 °C, 100% humidity, 5% CO2; **Fig. 9A**). After testing the control valves for functionality and integrity, the system was filled with PBS, and the migration chamber was coated overnight with 200 nM ICAM-1 (R&DSystem, Cat. # 720-IC-050) in PBS. The next day, the system was flushed for one hour with phenol-red-free complete medium.

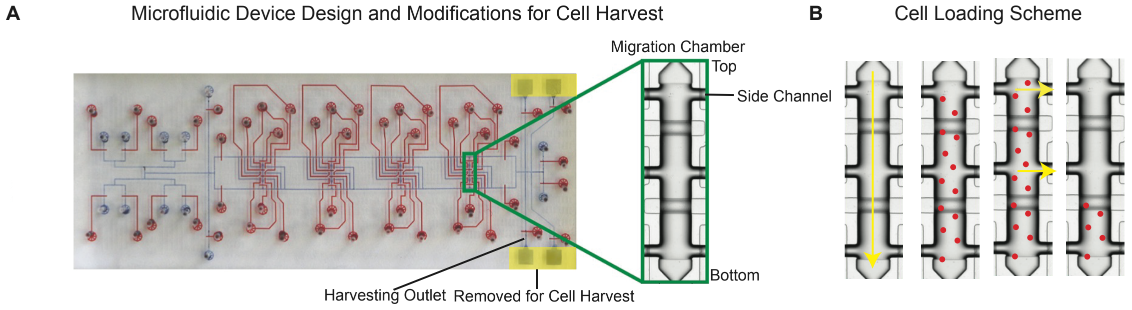

Figure 9: Microfluidic device and modifications for cell harvest I A) Photograph of the microfluidic device from the top with the flow layer (containing cells, medium and chemokine) channels in blue and the control layer (containing water to control the valves) in red. The device contains four migration chambers – one magnified (indicated by the green lines). The yellow areas were removed for the cell harvest. **B)** Cell loading scheme: Yellow arrows indicate direction flow and red dot represents cells. This figure was adapted by Frick et al. 2018 and amended.[295]

For cell loading, murine naïve CD8$^+$ T cells were counted, centrifuged for 5 min at 300 g, resuspended to a concentration of 1.2 x 10^7 cells / ml, and flushed into all four migration chambers from the top to the bottom. Top and middle parts of the chambers were subsequently flushed with medium to remove cells through the side channels, leaving only cells in the bottom third (**Fig. 9B**). After a 1-hour incubation, a CCL19 gradient was generated by flushing 2 μg / ml CCL19 through the top side channels and 1 μg / ml through the middle channel. The gradient was maintained by intermittently opening the chambers top or bottom valves to 3 μg / mL CCL19 or complete medium, respectively. The 3 μg / ml CCL19-containing medium was supplemented with 100 μg / ml 10 kDa FITC-dextran (Sigma-Aldrich, Cat. # FD10S) and diluted to 1 or 2 μg / ml, as needed. Immediately after gradient generation, brightfield images were captured every 15 seconds, and the gradient was imaged every 10 minutes for 4 hours using a Nikon Ti2E inverted microscope with a 10x objective (CFI Plan Apo Lambda, NA 0.45) and 1.5x optical zoom, equipped with a Photometrics camera. T cells were then flushed through the side channels from the chip into the harvesting outlets using PBS.

6.2.6.4 RNA Isolation, Library Preparation, Sequencing and Analysis

The resultant droplet containing the harvested cells was collected with a micropipette and RNA extracted according to the instructions of the PicoPure™ RNA Isolation Kit with a DNase digestion (ThermoFisher, Cat. # KIT0204). 4 μL of RNA solution was used to prepare cDNA libraries (with 18 preamplification cycles) with the SMART-Seq v4 Kit (Takara, Cat. # 634890). cDNA libraries were then sequenced with NovaSeq SP flow cell (Illumina). Reads were mapped against a reference genome (mm10) with STARsolo. Differential gene analysis was performed with DESeq2 on R (Version 4.0.0).[298]

6.2.6.5 Unbiased Metabolomics Analysis

5 x 10^6 naïve murine CD8$^+$ T cells were treated with either a vehicle or 2.5 μg/mL CCL19 for 4 hours in complete medium. The cells were washed twice with in ice-cold PBS and then snap frozen. Metabolites were subsequently extracted using the Floch's extraction method.[299] The preparation and methodology for LC-MS have been detailed previously.[300] Data acquisition was performed with the Xcalibur software (Version 4.1). An automated compound annotation was executed using Compound Discoverer (ThermoFisher). Subsequent statistical analyses were conducted in R, using a pipeline analogous to the differential gene expression analysis of the transcriptome study.

6.3 Section III: Acetate Modulates Memory $CD8^+$ T Cell Effector Function, Survival, and Migration During Bacterial Infections

6.3.1 Summary

In the published manuscript "*Memory $CD8^+$ T Cells Balance Pro- and Anti-inflammatory Activity by Reprogramming Cellular Acetate Handling at Sites of Infection*", presented in this results section, we investigated the dynamics of acetate levels at sites of bacterial infections and their subsequent influence on memory $CD8^+$ T cells, including their migration.

Our findings revealed that as bacterial infections progress in mice, acetate levels rise at the site of infection. Activated memory $CD8^+$ T cells ceased acetate assimilation by downregulating ACSS1 and ACSS2. Increased acetate concentrations augmented glutaminase activity, which subsequently promoted oxidative phosphorylation, thereby enhancing memory $CD8^+$ T cell survival. *In vivo* local acetate treatment increased memory $CD8^+$ T cell numbers. In conjunction, *in vitro* studies indicated impaired cell migration upon exposure to acetate, suggesting a trapping mechanism of memory $CD8^+$ T cells in acetate-rich environments. Moreover, acetate reduced free Ca^{2+} levels, thereby blunting activation-induced Ca^{2+} flux and compromising memory $CD8^+$ T cell activation. Consequently, the presence of acetate at infection sites mitigated immunopathology *in vivo*.

This study uncovers the pivotal role of acetate and the adaptations in its metabolism in memory $CD8^+$ T cells during bacterial infections. Initially, acetate assimilation fosters the function of memory $CD8^+$ T cells. As the infection advances, activated T cells at sites of infection reprogram their acetate metabolism to promote survival and high acetate levels inhibit their inflammatory capacity. This adaptation promotes memory $CD8^+$ T cell survival while controlling the magnitude of the inflammatory response.

6.3.2 Author Contribution

The research for the manuscript was spearheaded by the first author, Maria Balmer (University of Basel and University of Bern), and the principal investigator, Christoph Hess (University of Basel and University of Cambridge). As a member of the team working on this study, Philippe Dehio conducted the *in vitro* memory $CD8^+$ T cell migration assays.

6.3.3 Published Manuscript: *Memory $CD8^+$ T Cells Balance Pro- and Anti-inflammatory Activity by Reprogramming Cellular Acetate Handling at Sites of Infection*

The published manuscript is attached below and is accessible by the QR-code:

Cell Metabolism

Short Article

Memory CD8$^+$ T Cells Balance Pro- and Anti-inflammatory Activity by Reprogramming Cellular Acetate Handling at Sites of Infection

Graphical Abstract

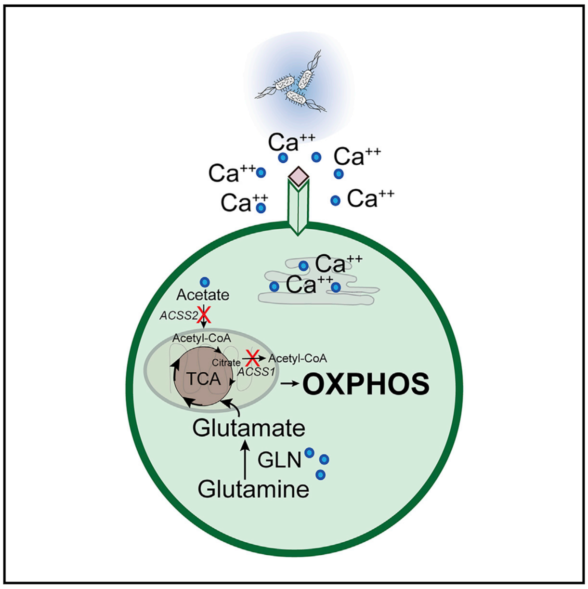

Authors

Maria L. Balmer, Eric H. Ma,
Andrew J. Thompson, ...,
Siegfried Hapfelmeier,
Russell G. Jones, Christoph Hess

Correspondence

maria.balmer@unibas.ch (M.L.B.),
chess@uhbs.ch (C.H.)

In Brief

Balmer et al. uncover that acetate abundance steadily increases at sites of inflammation. Acetate directly affects the activation and function of memory CD8$^+$ T cells by activating glutaminolysis and reducing calcium availability. *In vivo*, the integrated pro- and anti-inflammatory activities of acetate balance immune control with immunopathology.

Highlights

- Acetate concentrations are increased at sites of inflammation
- TCR signaling and acetate reduce ACSS1/2 expression in memory CD8$^+$ T cells
- Glutaminolysis is boosted and calcium flux inhibited by acetate
- Local acetate accumulation protects from immunopathology

Balmer et al., 2020, Cell Metabolism *32*, 457–467
September 1, 2020 © 2020 Elsevier Inc.
https://doi.org/10.1016/j.cmet.2020.07.004

CellPress

Cell Metabolism

CellPress

Short Article

Memory CD8$^+$ T Cells Balance Pro- and Anti-inflammatory Activity by Reprogramming Cellular Acetate Handling at Sites of Infection

Maria L. Balmer,[1,13,14,*] Eric H. Ma,[2,3,4] Andrew J. Thompson,[5] Raja Epple,[1] Gunhild Unterstab,[1] Jonas Lötscher,[1] Philippe Dehio,[1] Christian M. Schürch,[6] Jan D. Warncke,[1] Gaëlle Perrin,[1] Anne-Kathrin Woischnig,[7] Jasmin Grählert,[1] Jordan Löliger,[1] Nadine Assmann,[1] Glenn R. Bantug,[1] Olivier P. Schären,[8] Nina Khanna,[7] Adrian Egli,[9,10] Lukas Bubendorf,[11] Katharina Rentsch,[12] Siegfried Hapfelmeier,[8] Russell G. Jones,[2,3,4] and Christoph Hess[1,5,15,*]

[1]Department of Biomedicine, Immunobiology, University of Basel, 4031 Basel, Switzerland
[2]Center for Cancer and Cell Biology, Van Andel Institute, Grand Rapids, MI, USA
[3]Goodman Cancer Research Centre, McGill University, Montreal, QC, Canada
[4]Department of Physiology, McGill University, Montreal, QC, Canada
[5]Department of Medicine, CITIID, Jeffrey Cheah Biomedical Centre, University of Cambridge, Cambridge CB2 0AW, UK
[6]Baxter Laboratory for Stem Cell Biology, Department of Microbiology and Immunology, Stanford University School of Medicine, 269 Campus Drive, Stanford, CA 94305, USA
[7]Department of Biomedicine, Laboratory of Infection Biology, University of Basel and University Hospital Basel, 4031 Basel, Switzerland
[8]Institute for Infectious Diseases, University of Bern, 3010 Bern, Switzerland
[9]Clinical Microbiology, University Hospital Basel, 4031 Basel, Switzerland
[10]Applied Microbiology Research, Department of Biomedicine, University of Basel, 4031 Basel, Switzerland
[11]Institute for Pathology, University Hospital Basel, University of Basel, 4031 Basel, Switzerland
[12]Department of Laboratory Medicine, University Hospital Basel, University of Basel, 4031 Basel, Switzerland
[13]Present address: Department of Diabetes, Endocrinology, Nutritional Medicine and Metabolism, Bern University Hospital, University of Bern, 3010 Bern, Switzerland
[14]Present address: Diabetes Center Berne, 3010 Bern, Switzerland
[15]Lead Contact
*Correspondence: maria.balmer@unibas.ch (M.L.B.), chess@uhbs.ch (C.H.)
https://doi.org/10.1016/j.cmet.2020.07.004

SUMMARY

Serum acetate increases upon systemic infection. Acutely, assimilation of acetate expands the capacity of memory CD8$^+$ T cells to produce IFN-γ. Whether acetate modulates memory CD8$^+$ T cell metabolism and function during pathogen re-encounter remains unexplored. Here we show that at sites of infection, high acetate concentrations are being reached, yet memory CD8$^+$ T cells shut down the acetate assimilating enzymes ACSS1 and ACSS2. Acetate, being thus largely excluded from incorporation into cellular metabolic pathways, now had different effects, namely (1) directly activating glutaminase, thereby augmenting glutaminolysis, cellular respiration, and survival, and (2) suppressing TCR-triggered calcium flux, and consequently cell activation and effector cell function. *In vivo*, high acetate abundance at sites of infection improved pathogen clearance while reducing immunopathology. This indicates that, during different stages of the immune response, the same metabolite—acetate—induces distinct immunometabolic programs within the same cell type.

Context and Significance

The metabolic regulation of immunity offers opportunity for therapeutic interventions. In this approach, understanding how metabolites impact immune function at different stages of the inflammatory response is crucial. Previously, researchers at the University of Basel and their collaborators reported that with initial infection, transient acetate exposure boosts the capacity of memory T cells for glycolysis and inflammation. Here, they reveal that over time, acetate accumulates at sites of infection, where it again alters cellular metabolism and dampens T cell receptor signaling, thereby reducing the inflammatory response. Overall, they demonstrate that, depending on the stage of an immune response, one metabolite, acetate, can have distinct—and even opposing—effects on the same immune cell population.

INTRODUCTION

Memory CD8$^+$ T cells are a small population of long-lived immune cells with protective function and unique metabolic characteristics. Effector memory (EM) CD8$^+$ T cells circulate between the blood and the periphery and migrate into various peripheral tissues, where they are exposed to constantly changing microenvironments. At tissue sites, EM CD8$^+$ T cells rapidly respond upon re-encounter of cognate antigen by producing pro-inflammatory cytokines and other effector molecules (Harty and Badovinac, 2008). During differentiation from naive to effector to memory cells, CD8$^+$ T cells undergo important metabolic changes, which have been intimately linked to their functional properties.

Immune cells are able to respond to their environment and acquire a variety of context-dependent fates. However, we are only beginning to understand how immune cells sense these environmental cues, and how this impacts immune cell metabolism and function. Previously we observed that systemic acetate levels rapidly increase upon infection in mice, and that, acutely, acetate at ‘‘stress levels’’ enhances the glycolytic capacity and effector function of EM CD8$^+$ T cells upon subsequent re-stimulation in low acetate abundance (Balmer et al., 2016). Mechanistically, in the acute scenario acetate is assimilated via acetyl-CoA synthetase 2 (ACSS2) and is expanding the cellular acetyl-CoA pool in an ATP-citrate lyase (ACLY)-dependent manner, providing acetyl groups for acetylation reactions. Acetylation of GAPDH increases its enzymatic activity, leading to increased glycolytic activity upon activation and augmented EM CD8$^+$ T cell effector function. Consistent with this finding, another report recently found an improved response to influenza infection in mice fed a high-fiber diet. In this experimental system, diet-derived short-chain fatty acids (SCFAs), including acetate, enhanced cellular metabolism of CD8$^+$ T cells, thereby boosting anti-viral activity (Trompette et al., 2018).

To redirect immune cells to sites of infection, chemokine gradients are established and modulate lymphocyte trafficking (Kunkel and Butcher, 2002). Several metabolites also guide lymphocyte migration (Sigmundsdottir and Butcher, 2008), such as sphingosine-1-phosphate (Pappu et al., 2007), retinoic acid (Iwata et al., 2004; Svensson et al., 2008), or vitamin D3 (Reiss et al., 2001).

Metabolites, including acetate, may therefore be viewed as carrying information that can alter immune cell function. Whether, in extension of this concept, metabolites impact immune cell function according to the stage of an evolving immune response has not been explored. Here we extended our study of acetate acutely and transiently accumulating in the blood circulation to its role at sites of prolonged inflammation in murine and human memory CD8$^+$ T cells.

RESULTS

Acetate Levels Are Increased up to 100-Fold at Sites of Infection and Suppress ACSS1 and ACSS2 Expression in CD8$^+$ T Cells

Acetate rapidly accumulates in the circulation upon systemic infection in mice (Balmer et al., 2016). Several studies have shown dramatic changes in many metabolites in the setting of infection (Nguyen et al., 2015; Beisel, 1975; Dong et al., 2012). Here, we found that acetate accumulated in the peritoneal cavity of mice infected with *Listeria monocytogenes*, in a *Staphylococcus aureus* tissue-cage infection model, and in humans at sites of bacterial infection and inflammation (Figures 1A–1C; Table 1). We next assessed how increased local acetate levels per se impacted numbers of memory CD8$^+$ T cells in the peritoneal cavity. To this end, mice previously infected with *Listeria monocytogenes* expressing an OVA-peptide (LmOVA) were injected intraperitoneally (i.p.) with 10 mM acetate. Twenty-four hours after acetate injection, peritoneal CD8$^+$ T cell numbers in acetate-treated mice were significantly increased as compared to mice injected with PBS (Figure 1D). Most of these cells expressed phenotypic markers of memory CD8$^+$ T cells (Figure S1A). Re-challenging these mice i.p. in the presence versus absence of i.p. applied acetate also resulted in a significant acetate-dependent increase of CD8$^+$ T cells in the peritoneal fluid (Figure 1E). To assess the relation between *in vivo* accumulation of acetate at sites of inflammation and CD8$^+$ T cell counts, we analyzed leftover human fluid samples collected for clinical indications, as well as murine *Staphylococcus aureus* tissue-cage fluids. In both human and murine samples, CD8$^+$ T cell numbers and acetate abundance correlated positively up to approximately 100 mM. Beyond 100 mM acetate, CD8$^+$ T cell numbers started to decline (Figures 1F and 1G). More than 60% of the CD8$^+$ T cells recovered from tissue-cage fluid had a memory phenotype (Figure S1B). We then asked what the metabolic consequences of exposure to increased acetate abundance at sites of inflammation might be on CD8$^+$ T cells. Specifically, we tested how ACSS1 and ACSS2 were impacted in CD8$^+$ T cells 24 h after intraperitoneal injection of 100 mM acetate, as well as 24 h after intraperitoneal re-challenge of mice previously infected with LmOVA. In both models, transcript abundance of the acetate assimilating enzymes was reduced by approximately 50% (Figures 1H and 1I). Memory-like CD8$^+$ T cells can be generated *in vitro*, using an established protocol (Figure S1C) (van der Windt et al., 2012; Balmer et al., 2016). In such *in vitro* generated murine memory OT-I T cells, reduced abundance of ACSS1 and ACSS2 mRNA started to become apparent after 4 h of acetate exposure (Figures S1D and S1E). At the site of infection, cognate memory CD8$^+$ T cell activation occurs. We therefore also probed the effect of antigen-specific activation of murine memory OT-I T cells on transcript abundance of ACSS1 and ACSS2, *in vitro*. Both transcripts were strongly suppressed upon cognate re-stimulation (Figures 1J and 1K). Similar findings were made when activating human effector memory CD8$^+$ T cells in the presence of acetate (Figures S1F and S1G).

In all, these data identified high levels of acetate at sites of inflammation/infection, positively correlating with increased CD8$^+$ T cells counts up to 100 mM. We previously reported that acetate rapidly increased in the circulation of infected mice, and that, acutely, memory CD8$^+$ T cells assimilate acetate in an ACSS2-dependent manner, which leads to catalyzed glycolysis and increased IFN-γ production (Balmer et al., 2016). We now find that exposure of CD8$^+$ T cells to increased acetate concentrations, which we show to occur at sites of infection/inflammation, evoked downregulation of ACSS1 and ACSS2, a phenomenon further accentuated by TCR activation.

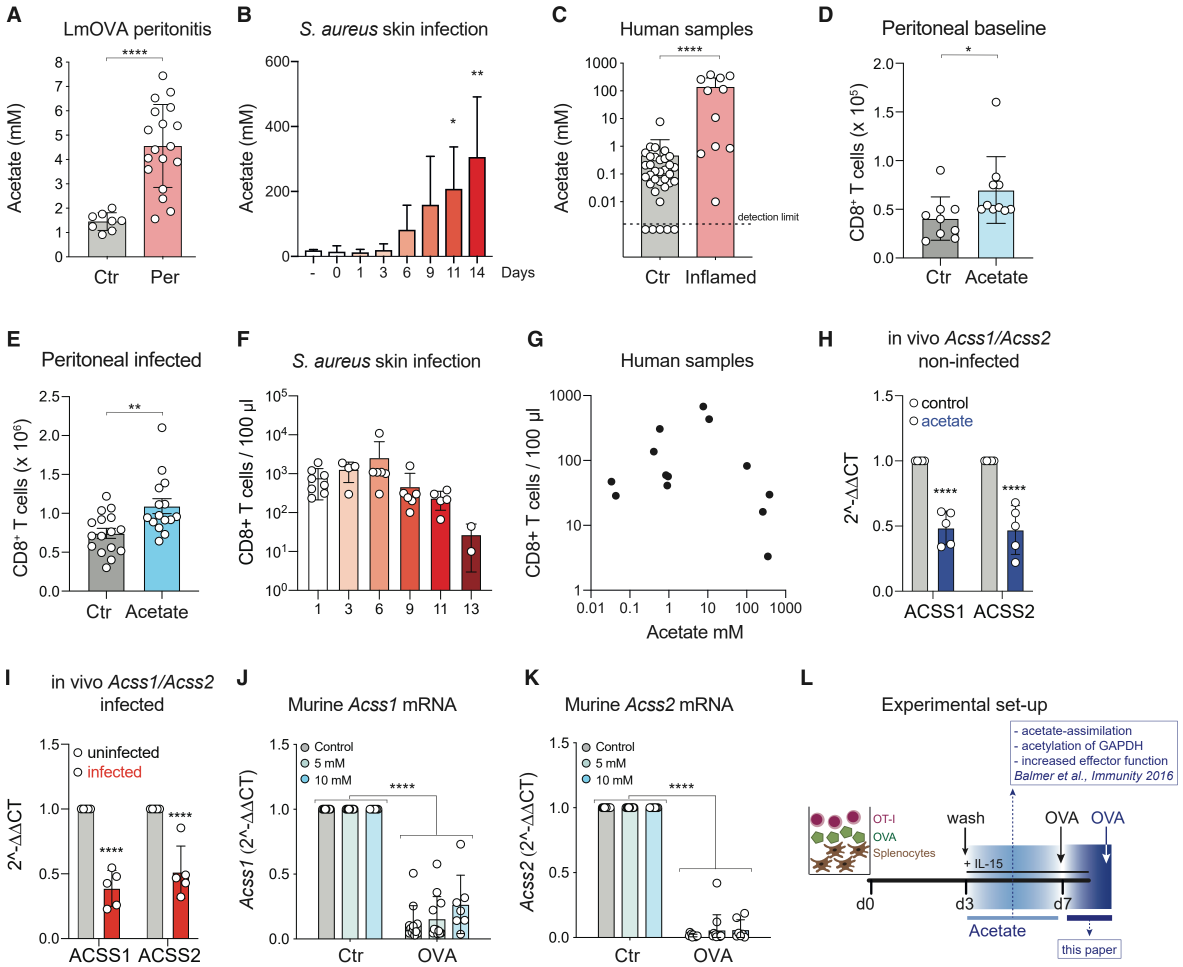

Figure 1. Acetate Levels Are up to 100-Fold Increased at Sites of Infection and Suppress ACSS1 and ACSS2 Expression in CD8+ T Cells

(A) Acetate levels in the peritoneal fluid, 24 h after intraperitoneal LmOVA infection in C57BL/6 mice.

(B) Acetate levels in tissue cages at the indicated time points following *S. aureus* infection.

(C) Acetate levels in human-infected body fluids (abscesses) as compared to non-inflamed control fluids.

(D) $CD8^+$ T cell numbers in the peritoneal fluid 24 h upon intraperitoneal administration of 10 mM acetate in LmOVA-immunized mice.

(E) $CD8^+$ T cell numbers in the peritoneal fluid 24 h upon intraperitoneal re-infection with LmOVA ± 10 mM acetate in LmOVA-immunized mice.

(F and G) Absolute numbers of $CD8^+$ T cells recovered from locally infected fluids shown in (B) and (C) as determined by flow cytometry.

(H and I) Expression of ACSS1 and ACSS2 in MACS-purified $CD8^+$ T cells from the peritoneal cavity of LmOVA-immunized mice upon injection of 100 mM acetate (H) or re-challenged with LmOVA (I).

(J and K) Expression of ACSS1 (J) and ACSS2 (K) in murine memory OT-I T cells upon OVA stimulation for 4 h in the presence or absence of the indicated acetate concentrations.

(L) Experimental set-up mimicking the time course of acetate exposure of memory $CD8^+$ T cells.

Each dot represents one mouse or sample; lines indicate means. Error bars are SD. Dashed lines indicate the detection limit. t test (A and C–E), one-way ANOVA (B and F), and two-way ANOVA (H–K) were used to compare the groups. $^*p < 0.05$, $^{**}p < 0.01$, $^{****}p < 0.0001$.

The experimental set-up capturing these scenarios, which, *in vivo*, plausibly form a continuum, is summarized in Figure 1L.

Acetate Promotes Glutaminolysis by Enhancing Glutaminase Enzymatic Activity

To further dissect the metabolic profile of memory $CD8^+$ T cells exposed to increased acetate levels at sites of infection, we analyzed murine memory OT-I T cells in a metabolic flux analyzer. Supplementation of acetate resulted in a significant increase in oxygen consumption rates (OCRs) compared to medium control, whereas glycolysis was unchanged (Figures 2A and S2A). Furthermore, re-stimulation of memory OT-I T cells with OVA-peptide in the presence of acetate also increased OCR when compared to medium control (Figure S2B). Addition

Table 1. Patient Characteristics

Gender (f/m)	6/5
Age (mean, years)	51
Source (n)	
Abscess/cyst	7
Wound	1
Ascites	1
Synovia	2
Pathogen Isolated (n)	
Staphylococcus aureus	1
Staphylococcus epidermidis	1
Mixed	4

of ^{13}C-acetate to memory OT-I T cells revealed that carbon derived from labeled acetate was found in only low amounts in citrate of memory cells stimulated with OVA (Figure 2B, left panel). Albeit also only low in abundance in non-activated cells, acetate-derived carbons were consistently reduced in other intermediates of the TCA cycle (Figure 2B, right three panels). Of note, expansion of acetate-fueled acetyl-CoA was also much reduced upon OVA activation of memory CD8$^+$ T cells (Figure 2C). These data indicated that (1) acetate assimilation was blunted in these re-stimulated memory cells, and (2) increased OCR did not primarily result from increased fueling of acetate into the TCA cycle (Figure 2D). We noted, however, that the presence of acetate was associated with a higher overall abundance of α-ketoglutarate, fumarate, and malate, hinting at the possibility of glutaminolysis-derived glutamate as a carbon source entering the TCA cycle (Figures 2B and 2D). To test this hypothesis, ^{13}C-glutamine tracing experiments were performed, which confirmed an increase of glutamine-derived carbons in glutamate (m+5) in the presence of acetate, both in non-activated and re-stimulated murine memory CD8$^+$ T cells (Figures 2E and S2C). This suggested that in this scenario acetate promoted increased glutaminolysis, TCA activity, and interlinked oxidative phosphorylation in memory CD8$^+$ T cells. Indeed, BPTES, an inhibitor of glutaminolysis, suppressed acetate-augmented OCR in murine and human memory CD8$^+$ T cells (Figures 2F and S2D). BPTES alone, as well as inhibition of ATP-citrate lyase, did not affect OCRs (Figures S2E and S2F). Notably, addition of acetate up to a concentration of 50–100 mM increased human and murine CD8$^+$ T cell viability (Figures 2G and S2G), a feature that was lost in the absence of glutamine in the cell culture medium (Figures 2H and S2H), or in presence of BPTES (Figure S2I). These data indicated that acetate-augmented glutaminolysis promoted increased cell respiration and viability. At sites of high acetate concentration *in vivo*, altered migratory behavior could further contribute to increased CD8$^+$ T cell numbers. We therefore also assessed spontaneous as well as CXCL12-directed migration of murine memory OT-I T cells in the presence or absence of acetate in transwell assays. In a dose-dependent manner, acetate inhibited spontaneous migration compared to medium control (Figure 2I), and also somewhat blunted chemokine-directed translocation (Figure 2J). These experiments indicated that, rather than being assimilated by members of the ACSS family and entering core metabolism, or providing acetyl groups for acetylation reactions (Comerford et al., 2014; Balmer et al., 2016), at the site of infection acetate modulated cellular metabolism, survival, and migration in a different way.

To elucidate how acetate mediated increased glutaminolysis in memory CD8$^+$ T cells, we measured expression of glutaminase (GLS), which converts glutamine to glutamate. Addition of acetate did not change overall abundance of GLS transcript or protein (Figures S2J–S2L). By contrast, glutaminase activity was significantly increased in memory CD8$^+$ T cells exposed to acetate (Figure 2K). To dissect whether the acetate-mediated increase in glutaminase activity was a direct or indirect effect, we analyzed the activity of recombinant human glutaminase in the presence versus absence of acetate. These experiments revealed a direct and dose-dependent effect of acetate on glutaminase activity (Figure S2M), which is in line with a previous publication proposing an increase in glutaminase activity by direct binding of acetate to the enzyme (O'Donovan and Lotspeich, 1966). To rationalize this pharmacological effect, we used *in silico* ligand docking of acetate into human glutaminase co-crystalized with bound glutamine. This identified four closely located docked-pose clusters, three of which lay close to the activation loop and one close to the substrate-binding pocket (Figure 2L, upper panel). Of these, clusters I and II contained the greatest number of energetically favorable poses (7/10) and predicted interactions with residues that are known to affect the actions of other allosteric activators (Ferreira et al., 2013; Li et al., 2016). For example, the allosteric activator phosphate is similarly located in the mouse apo structure, and its actions are strongly affected by mutation of residues G320 (G315 in 3VP0) and K325 (K317 in 3PV0) in humans (Figure 2L, middle panel) (Ferreira et al., 2013; Li et al., 2016). *E. coli* and *B. subtilis* both display poor amino acid conservation in this region of the enzyme and would be predicted not to be affected by acetate (Figure 2L, lower panel). When tested we found that, indeed, acetate did not enhance *E. coli* glutaminase activity but even decreased it (Figure S2N) (Brown et al., 2008; Stalnecker et al., 2017). To test, at the molecular level, the requirement of K317 for acetate to function as an allosteric activator (Figure 2L, middle and lower panel), wild-type recombinant human glutaminase (two versions: one commercially available, one mutation experiment control) and K317 → A317 mutated recombinant glutaminase were used. Again, activity of wild-type glutaminase was augmented by addition of acetate (20 mM), whereas K317 → A317 mutated glutaminase was unaffected—establishing essentiality of K317 for acetate's activity augmenting property (Figure 2M). In all, these data indicated that, upon recall, acetate promoted glutaminolysis by direct allosteric effects that increase glutaminase activity.

Acetate Suppresses TCR Re-stimulation by Reducing Calcium Flux

We next wondered how differential acetate handling of memory CD8$^+$ T cells re-engaging with cognate antigen related to their functionality. To begin to address this question, memory OT-I T cells were re-stimulated with OVA-peptide in the presence or absence of acetate, and calcium flux was measured by flow cytometry. Acetate significantly suppressed calcium flux upon OVA re-stimulation in a dose-dependent manner (Figure 3A), suggesting decreased TCR stimulation. Accordingly, glycolytic

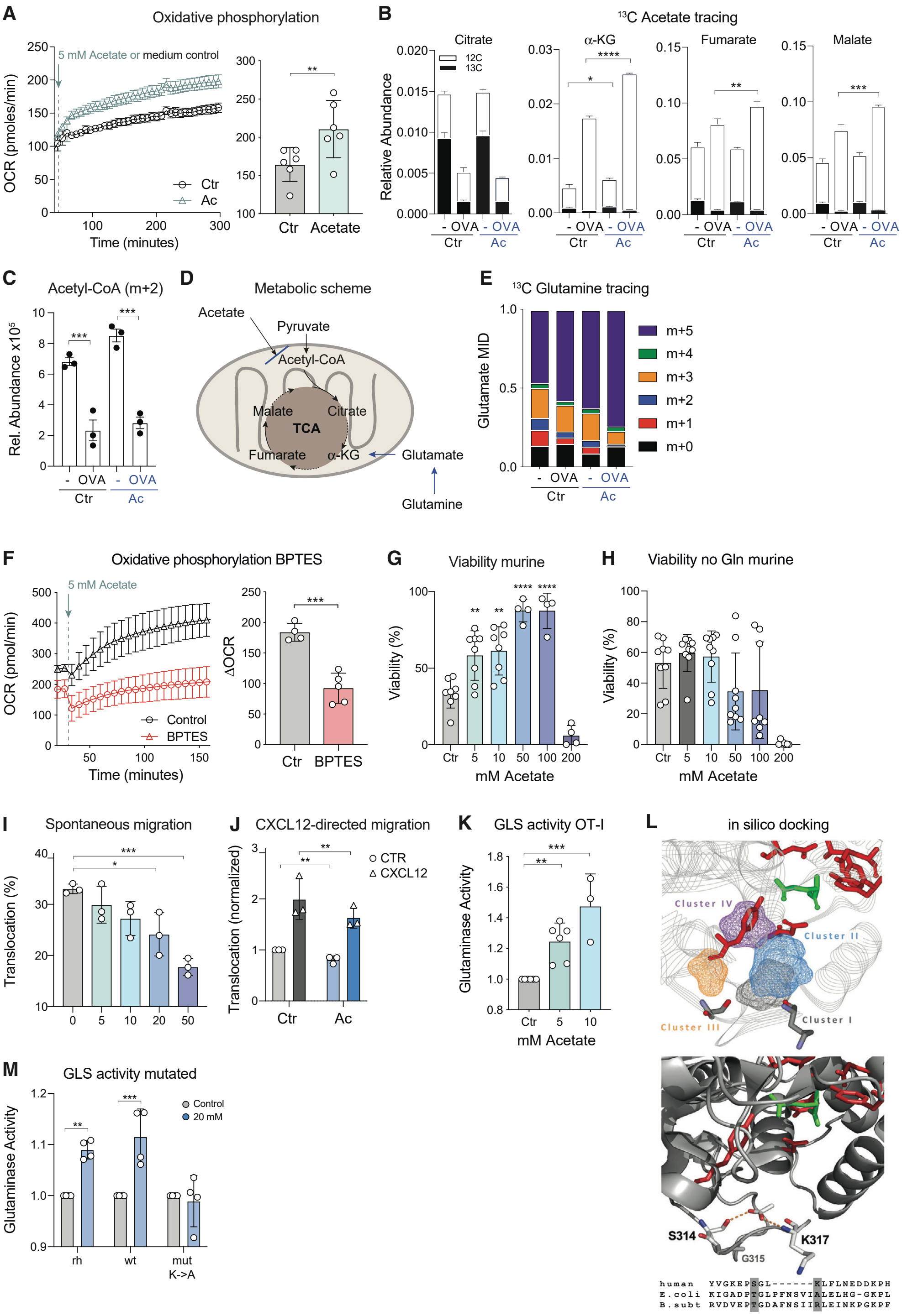

(legend on next page)

switching and IFN-γ production were suppressed in the presence of acetate in a dose-dependent manner in both murine and human memory CD8$^+$ T cells (Figures 3B–3F), whereas production of TNF was unchanged (Figure S3A). Notably, calcium add-back was able to correct acetate-mediated suppression of IFN-γ (Figure S3B). We reasoned that negatively charged acetate may interfere with biologically active (i.e., free) calcium, which would provide a mechanistic basis to the observed effect of acetate on calcium flux. We thus measured free calcium levels in the absence and in increasing concentrations of acetate, *in vitro*. To exclude protein modifications by acetate, we used PBS as a solute. In effect, free calcium levels dropped in the presence of acetate in a concentration-dependent manner (Figure 3G). Conversely, phosphate concentrations significantly increased (Figure 3H). To assess whether acetate also depleted calcium levels *in vivo*, we determined free calcium levels in murine and human fluids sampled from infectious and inflamed sites. Calcium levels were significantly depleted in both human-infected and sterile inflamed body fluids, and infected murine peritoneal fluids in the presence of acetate (Figures 3I and 3J). Inversely, phosphate levels were increased in murine *S. aureus* skin infection and in inflamed human body fluids (Figures 3K and 3L). To elucidate whether decreased calcium levels were responsible for reduced calcium flux upon TCR re-stimulation, we added excess calcium to acetate-exposed memory OT-I T cells upon OVA re-stimulation. Addition of 10 mM calcium was sufficient to normalize calcium flux back to control conditions (Figures 3M and S3C). Addition of 10 mM calcium was also sufficient to augment memory OT-I T cell migration, indicating that impaired cell activation and migration in the presence of acetate may be related to calcium depletion in the presence of acetate (Figure S3D). Of note, in the absence of glutamine, acetate also reduced IFN-γ production by memory OT-I T cells, indicating that the effect of acetate on glutaminase activity and its effect on calcium flux are distinct (data not shown). These data established that acetate suppressed memory CD8$^+$ T cell re-call responses as a consequence of reduced calcium availability when present during re-stimulation. To directly capture acetate's time- and concentration-dependent immune augmenting versus immuno-suppressive features, a time course experiment encompassing both features of this metabolite was performed (Figure 3N).

Acetate Suppresses Immunopathology at Sites of Infection and Modulates Tissue Remodeling

We went on and asked how, at the site of infection, acetate-mediated metabolic and functional re-programming of memory CD8$^+$ T cells modulated immune control. To address this question, we re-infected mice previously infected with LmOVA i.p. in the presence or absence of 10 mM acetate also administered i.p. at the same time as the pathogen. Similar to our previous findings, acetate promoted superior immune control as measured by bacterial loads in the liver and spleen (Figure 4A). However, immunopathology determined by local lactate dehydrogenase levels, as well as peritoneal IFN-γ, was suppressed in the presence of acetate (Figures 4B and 4C). Peritoneal concentrations of IL-10 tended to be elevated in the presence of acetate, indicating a possible immunomodulatory role of acetate (Figure S4A). Increased expression of PD-L1 on CD8$^+$ T cells recovered from peritoneal fluid would also align with this notion (Figure S1A). Histologically, peritoneal thickness—as another measure of immunopathology (Mizuno et al., 2009)—was also reduced in the presence of acetate (Figure 4D). To further characterize a potential immunomodulatory role of acetate at the site of infection, we performed a PCR array from peritoneal tissue of mice re-challenged with LmOVA in the presence or absence of acetate. This experiment revealed increased TGF-β transcript levels in the peritoneum from acetate-treated mice, whereas

Figure 2. Acetate Promotes Glutaminolysis by Enhancing Glutaminase Enzymatic Activity

(A) Memory OT-I T cells were analyzed by metabolic flux analysis upon injection of 5 mM acetate (blue) or medium control (black) at the beginning of the analysis (dashed line and arrow). Shown is a representative experiment of OCR values and pooled data from 5 independent experiments showing OCR values at 300 min post-injection.

(B and C) ^{13}C-acetate tracing experiment of murine memory OT-I T cells. Cells were incubated ± 5 mM ^{12}C-acetate (blue) and ± 10 μM OVA-peptide for 6 h and then all traced with ^{13}C-acetate for 6 h.

(B) Filled bars represent contribution of ^{13}C-acetate to the respective metabolite pool.

(C) Relative abundance of m+2 acetyl-CoA from ^{13}C-acetate.

(D) Schematic of mitochondrial metabolism and possible effects of acetate.

(E) Same experiment as in (B), but with ^{13}C-glutamine. The different colors indicate the number of radiolabeled carbons detected in glutamate.

(F) Memory OT-I T cells were pre-incubated for 2 h in the presence (red) or absence (black) of the glutaminolysis inhibitor BPTES or vehicle control. Cells were then analyzed by metabolic flux analysis upon injection of 5 mM acetate (dashed line and arrow). Shown is a representative experiment of OCR values and pooled data from 4 independent experiments assessing the net increase in OCR between 30 and 150 min.

(G and H) Viability of murine memory CD8$^+$ T cells cultured *in vitro* for 3 days in the presence (G) or absence (H) of glutamine and increasing acetate concentrations as determined by flow cytometry (% Annexin V and PI negative).

(I and J) Spontaneous (I) and chemokine-directed (J) migratory capacity of *in vitro* generated murine memory OT-I T cells analyzed in a transwell assay in increasing concentrations of acetate.

(K) Glutaminase activity in murine memory OT-I T cell extracts exposed for 4 h to the indicated acetate concentrations.

(L) Upper panel: a wireframe representation of the four docked pose clusters identified in our study is shown in one of the four subunits of the enzymatically active homo-tetramer of glutaminase. Middle: an example docked pose from cluster I, showing predicted hydrogen bond interactions (dashed orange lines) between acetate and the side chains of residues S319 (314) and K235 (317). The green molecule is bound glutamine. Bottom: an alignment showing the poor amino acid conservation in the predicted allosteric activation region of human (from the 3PV0 crystal structure used here) and prokaryotic glutaminase (P77454, *E. coli*; O31465, *B. subtilis*). The gray shade highlights S314 and K317.

(M) Glutaminase activity of human recombinant glutaminase (rh), wild-type human glutaminase (wt, mutation control), and human glutaminase with a K → A mutation at position 317, depicted in the lower panel of (L), assessed in the presence or absence of 20 mM acetate.

Each dot represents one mouse or human; lines indicate means. Error bars are SD. t test (A and F), one-way ANOVA (G–I and K), or two-way ANOVA (B, C, J, and M) was used to compare the groups. *$p < 0.05$, **$p < 0.01$, ***$p < 0.001$, ****$p < 0.0001$.

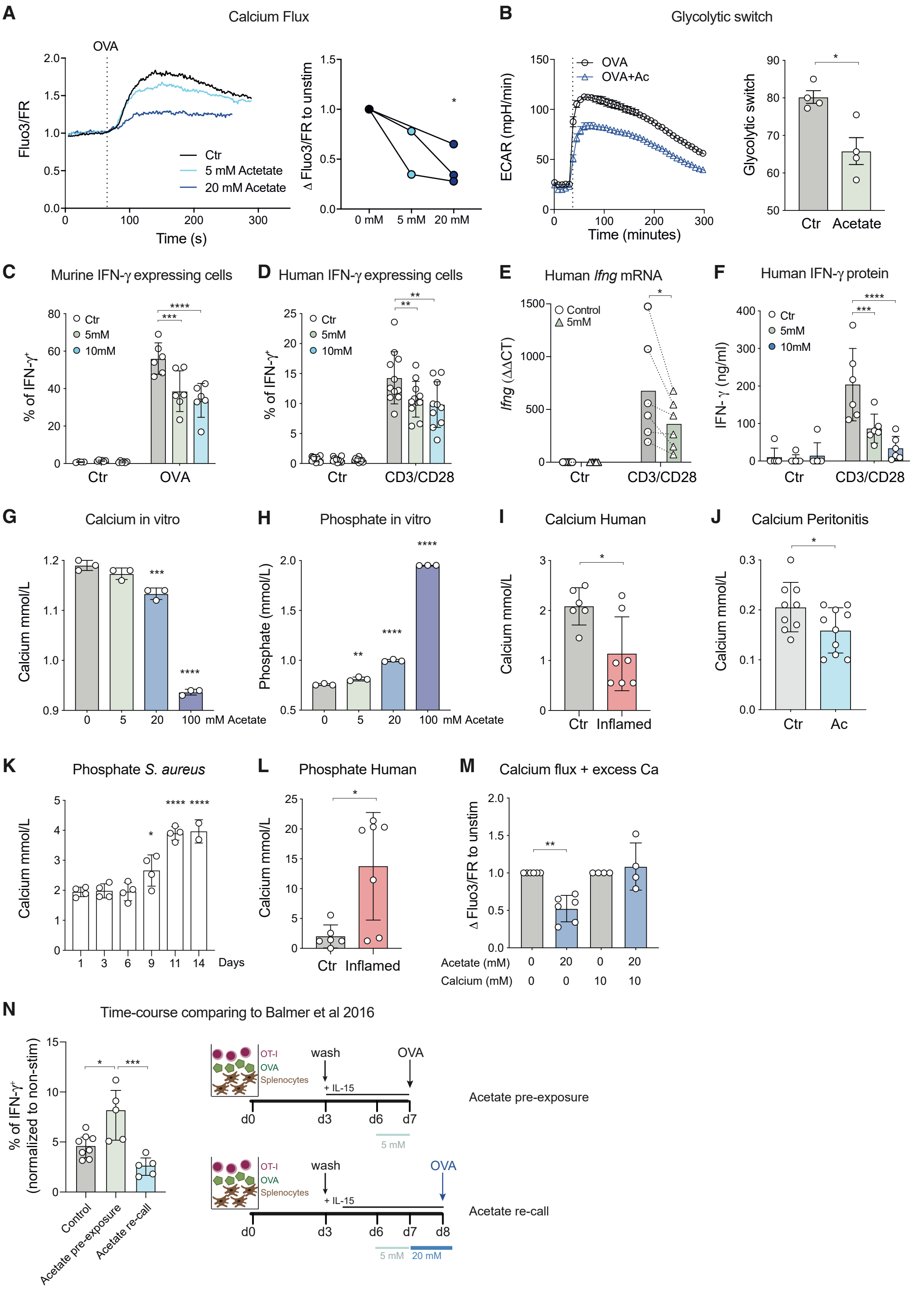

(legend on next page)

transcripts of the pro-inflammatory cytokines *Ifng* and *Tnf*, as well as transcripts of integrin- and collagen-family genes, were decreased in the presence of acetate (Figures 4E and S4B). Overall, these experiments suggested that, at the site of infection, acetate suppressed immunopathology.

Taken together, our data indicated that at sites of infection, acetate catalyzed glutaminolysis in memory CD8$^+$ T cells, augmenting mitochondrial respiration and cell survival. Further, by altering availability of free calcium, acetate suppressed TCR-triggered calcium flux, glycolytic switching, and IFN-γ production. In a time-resolved manner, acetate's glycolysis boosting capacity (Balmer et al., 2016) and the herein described effects were balancing pathogen clearance against immunopathology (Figure 4F).

DISCUSSION

The metabolic environment has been shown to critically impact the outcome of immune responses. Probably the best characterized example is the tumor microenvironment, which shapes immune cell metabolism and function. Here we show that acetate levels accumulate at sites of infection and reprogram memory CD8$^+$ T cell metabolism and function by boosting glutaminolysis and altering availability of calcium. Acetate levels can rise up to about 5 mM in the circulation upon systemic bacterial infection in mice (Balmer et al., 2016). At the site of infection, acetate levels are initially low but then can reach >100 mM. This implies that memory T cells are exposed to rising acetate concentrations at inflamed sites where they are likely to re-encounter antigen. While acute, transient exposure of ACSS competent memory CD8$^+$ T cells to acetate levels of 5 mM boosted glycolysis and cytokine secretion (Balmer et al., 2016), acetate also mediated a decrease of its assimilation machinery (i.e., ACSS1 and 2). On the one hand, non-metabolized acetate augmented glutaminase enzymatic activity, fueling the TCA cycle and mitochondrial respiration, thereby supporting cell viability. On the other hand, acetate present during antigen re-encounter reduced free calcium abundance, thus suppressing migration and TCR-triggered calcium flux, and subsequent effector function. This indicates that, before reaching the site of infection, memory CD8$^+$ T cells are boosted and thus prepared for rapid pathogen removal at acutely infected sites (Balmer et al., 2016). However, at the site of unresolved inflammation where acetate abundance is steadily increasing, their inflammatory capacity is gradually being suppressed, thereby balancing pathogen clearance and immunopathology. Depending on timing of exposure, the same metabolite—acetate—thus has opposing effects on memory CD8$^+$ T cells: in transit to the site of infection acetate is used to acetylate and catalyze GAPDH, enhancing glycolytic switch and interlinked inflammatory output of memory CD8$^+$ T cells early upon re-stimulation (i.e., when re-stimulated in low acetate abundance). At sites of prolonged inflammation, where acetate gradually accumulates, cells lose their capacity to assimilate acetate, and acetate catalyzes glutaminase activity and develops suppressive capacity by "buffering" calcium (Figure 4F). Mechanistically, acetate's effects on glutaminase activity and calcium flux are distinct. However, functionally they may well complement each other. Initially, prolonged survival allows for sufficient cell numbers available for efficient pathogen clearance, while later on this may support accumulation of inflammation resolving mediators.

Immunopathology plays a key role in many infectious and inflammatory diseases, contributing to morbidity and mortality. For example, during viral infections cytotoxic CD8$^+$ T cells, while effectively killing infected cells, can also cause non-specific, tissue-destructive inflammation (Rouse and Sehrawat, 2010). Likewise, immunopathology mediates autoimmune and chronic inflammatory diseases, such as inflammatory bowel disease. In the intestine, acetate concentrations reach up to 200 mM/kg wet weight (Huda-Faujan et al., 2010; Høverstad and Midtvedt, 1986), and were significantly reduced in patients with inflammatory bowel disease, indicating that these high acetate concentrations contribute to host-microbial mutualism and may protect from immunopathology (Huda-Faujan et al., 2010).

Acetate is an SCFA abundantly produced by the gut microbiota via fermentation of dietary fibers (Tremaroli and Bäckhed, 2012). However, germ-free animals also readily increase serum acetate levels upon metabolic stress, indicating efficient release of acetate from endogenous sources (Balmer et al., 2016). Further, we previously demonstrated that rising systemic acetate levels upon systemic bacterial infection are also not primarily bacteria-driven, since systemic infection with bacteria genetically incapable for acetate production induced stress levels of acetate in the host (Balmer et al., 2016). The source, or sources,

Figure 3. Acetate Suppresses TCR Re-stimulation by Reducing Calcium Availability

(A) Calcium flux as assessed by flow cytometry of murine memory OT-I T cells cultured in the presence (blue) or absence of acetate (black) for 30 min. One representative experiment (left) and pooled data from 2–3 independent experiments (right) are shown.

(B) Glycolytic switch upon OVA injection with (blue) or without (black) acetate in murine memory OT-I T cells as assessed by metabolic flux analysis. One representative experiment (left) and pooled data from 4 independent experiments (right) are shown. The glycolytic switch was calculated by subtracting the basal ECAR from maximal ECAR. The dashed line indicates the time of OVA (± acetate) injection.

(C and D) IFN-γ production as assessed by intracellular cytokine staining in murine (C) or human (D) memory CD8$^+$ T cells 4 h after re-stimulation with 10 μM OVA-peptide or anti-CD3/CD28 antibodies in the presence (blue) or absence (black) of indicated acetate concentrations.

(E and F) IFN-γ mRNA (E) and protein (F) in human memory CD8$^+$ T cells 4 h after re-stimulation with anti-CD3/CD28 antibodies in the presence (blue) or absence (black) of indicated acetate concentrations.

(G and H) Calcium (G) and phosphate levels (H) assessed *in vitro* in the presence (blue) or absence (black) of the indicated acetate concentrations.

(I–L) Calcium (I and J) and phosphate levels (K and L) in human and murine fluids as described in Figures 1A–1C.

(M) Calcium flux as described in (A) was assessed in the presence (blue) or absence (black) of acetate and additional calcium.

(N) IFN-γ production as assessed by intracellular cytokine staining in murine memory OT-I T cells exposed to acetate either prior to or during OVA re-stimulation for 4 h.

Each dot represents one mouse or human; lines indicate means. Error bars are SD. t test (B, I, J, and L), one-way ANOVA (G, H, K, M, and N), or two-way ANOVA (C–F) was used to compare the groups. *$p < 0.05$, **$p < 0.01$, ***$p < 0.001$, ****$p < 0.0001$.

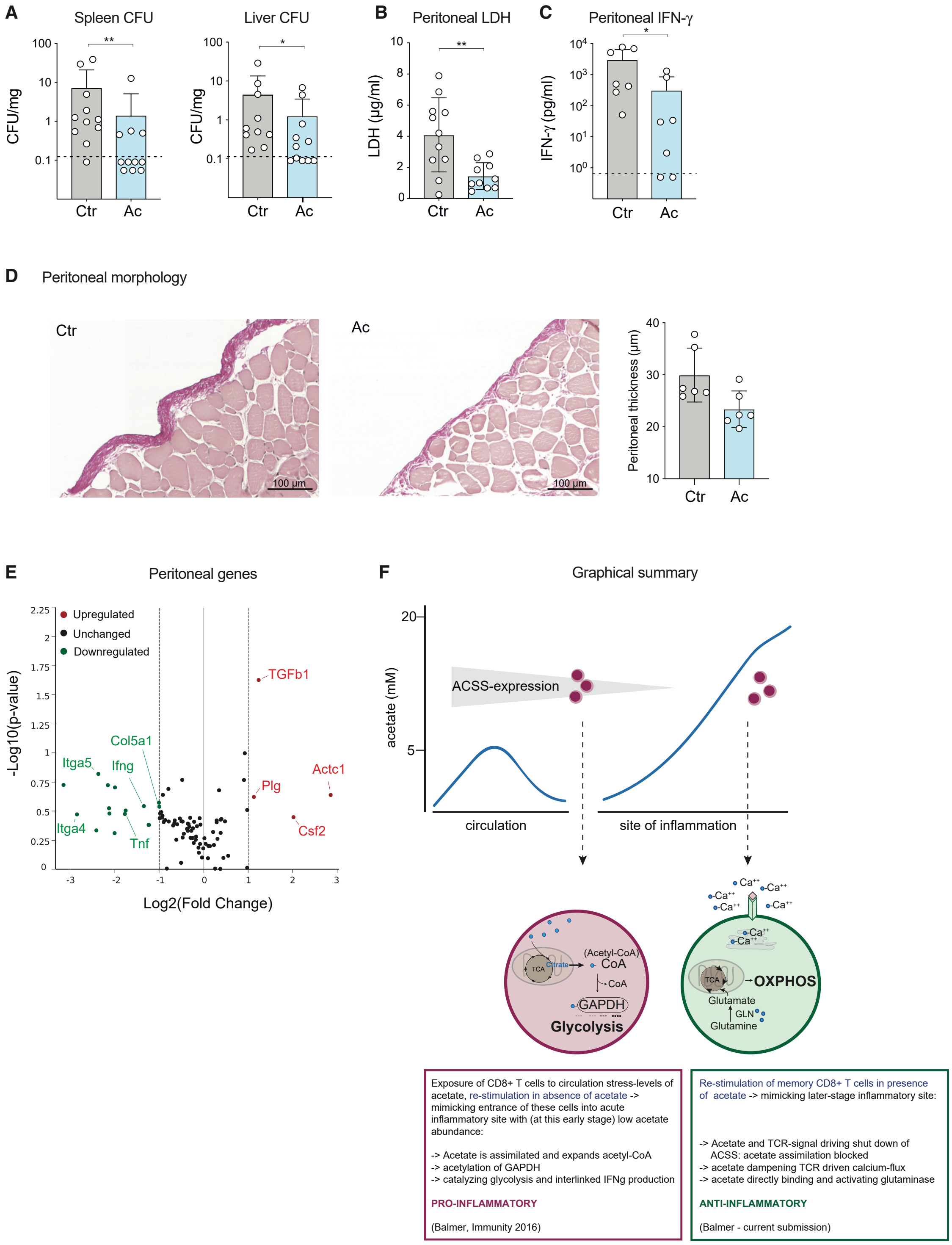

Exposure of CD8+ T cells to circulation stress-levels of acetate, re-stimulation in absence of acetate -> mimicking entrance of these cells into acute inflammatory site with (at this early stage) low acetate abundance:

-> Acetate is assimilated and expands acetyl-CoA
-> acetylation of GAPDH
-> catalyzing glycolysis and interlinked IFNg production

PRO-INFLAMMATORY

(Balmer, Immunity 2016)

Re-stimulation of memory CD8+ T cells in presence of acetate -> mimicking later-stage inflammatory site:

-> Acetate and TCR-signal driving shut down of ACSS: acetate assimilation blocked
-> acetate dampening TCR driven calcium-flux
-> acetate directly binding and activating glutaminase

ANTI-INFLAMMATORY

(Balmer - current submission)

(legend on next page)

of increased local acetate levels observed in this study thus remain unclear. Since at sterile inflammatory sites acetate abundance was also increased, a bacterial origin seems unlikely. Given the large amount of cell death within any inflammatory area, one possibility could be the accumulation of extracellular acetate that is released from intracellular sources upon cell death.

In conclusion, our data demonstrate that acetate can function as a rheostat of the immune response, balancing pro- and anti-inflammatory properties during the course of an immune response. Opposing effects on immune cell function driven by a single metabolite through distinct cellular metabolic effects emphasize the need to consider metabolic reprogramming in a time- and context-resolved manner.

Limitations of Study

The molecular mechanisms by which acetate and TCR signaling drive downregulation of ACSS1 and ACSS2 remain to be defined. Also, we could not measure memory CD8$^+$ T cell metabolism in real time *in vivo* during the course of an infection but focused on *ex vivo* analyses. Finally, while we also found increased accumulation of acetate at sites of inflammation in humans, how memory CD8$^+$ T cell metabolism is regulated at these sites needs to be explored.

STAR★METHODS

Detailed methods are provided in the online version of this paper and include the following:

- KEY RESOURCES TABLE
- RESOURCE AVAILABILITY
    - ○ Lead Contact
    - ○ Materials Availability
    - ○ Data and Code Availability
- EXPERIMENTAL MODEL AND SUBJECT DETAILS
    - ○ Animal Husbandry
    - ○ Human Abscess Fluids
    - ○ Isolation of Human Effector Memory (EM) CD8$^+$ T Cells
    - ○ Cell Culture
- METHOD DETAILS
    - ○ *In Vitro* Memory Differentiation
    - ○ Acetate Measurement in Murine and Human Samples
    - ○ Measurement of Cell Viability
    - ○ Transwell migration assay
    - ○ Murine Peritonitis Model
    - ○ S. aureus Tissue Cage Model
    - ○ Histology
    - ○ Seahorse Experiments
    - ○ Metabolic Tracing
    - ○ Quantitative PCR
    - ○ Glutaminase Activity Assay
    - ○ Glutaminase-Acetate *In Silico* Docking
    - ○ Glutaminase Mutagenesis
    - ○ Calcium Flux
    - ○ Calcium and Phosphate Quantification
    - ○ Intracellular Cytokine Staining
    - ○ Cytometric Bead Array
    - ○ Immunoblot Analysis
- QUANTIFICATION AND STATISTICAL ANALYSIS

SUPPLEMENTAL INFORMATION

Supplemental Information can be found online at https://doi.org/10.1016/j.cmet.2020.07.004.

ACKNOWLEDGMENTS

M.L.B. was supported by SNSF grant PMPDP3_171261/1 and Novartis Foundation grant 17C141. C.H. was supported by SNSF grants 31003A_172848 and 310030_192677.

AUTHOR CONTRIBUTIONS

M.L.B. designed, performed, and analyzed most experiments and wrote the manuscript; E.H.M. and R.G.J. performed metabolic tracing experiments; A.J.T. performed *in silico* docking experiments; R.E. performed experiments and analyzed data; G.U. performed immunoblot analyses; J. Lötscher performed calcium-flux experiments; P.D. performed migration experiments; C.M.S. examined and scored the histopathological samples; J.D.W. performed immunoblot, RT-PCR, migration, and calcium-flux experiments; G.P. and G.R.B. established glutaminase-activity assays; A.-K.W., J.G., and N.K. performed MSSA tissue cage experiments; A.E. and L.B. provided clinical samples for acetate measurements; K.R. measured calcium and phosphate concentrations; J. Löliger and N.A. helped with metabolic tracing experiments; O.P.S. and S.H. performed PCR arrays; and C.H. designed, supervised, and coordinated the study and wrote the manuscript. All authors revised the manuscript and approved its final version.

DECLARATION OF INTERESTS

The authors declare no conflicts of interest.

Received: August 17, 2019
Revised: April 21, 2020
Accepted: July 12, 2020
Published: July 31, 2020

Figure 4. Acetate Suppresses Immunopathology at Sites of Infection and Modulates Tissue Remodeling

(A) LmOVA-immunized mice were i.p. re-infected with 10^5 CFU LmOVA in the presence (blue) or absence (black) of 10 mM acetate, and bacterial burdens in spleen and liver were assessed by bacterial plating 24 h post-infection.

(B) LDH levels in the peritoneal fluid of mice described in (A) were analyzed using a commercially available assay kit.

(C) IFN-γ levels in the peritoneal fluid of mice described in (A) were determined by cytometric bead array.

(D) Peritoneal morphology on formalin-fixed, paraffin-embedded samples stained with elastica van Gieson. Shown are representative samples of one control (Ctr) and one acetate-treated (Ac) animal. Peritoneal thickness was quantified (right panel).

(E) Volcano plot of PCR array analysis of the peritoneal samples shown in (D). Red-highlighted genes were upregulated; green-highlighted genes downregulated in the presence of acetate.

(F) Schematic depiction of the proposed model of acetate, playing opposing roles during an immune response in a time- and context-dependent manner.

Each dot in (A)–(D) represents one mouse. Shown are pooled data from 2 independent experiments with 3–7 animals per group. Lines indicate means; error bars are SD. Dashed lines in (A) and (C) indicate the detection limit. t test was used to compare the groups. $^*p < 0.05$, $^{**}p < 0.01$.

REFERENCES

Balmer, M.L., Ma, E.H., Bantug, G.R., Grählert, J., Pfister, S., Glatter, T., Jauch, A., Dimeloe, S., Slack, E., Dehio, P., et al. (2016). Memory CD8(+) T cells require increased concentrations of acetate induced by stress for optimal function. Immunity *44*, 1312–1324.

Beisel, W.R. (1975). Metabolic response to infection. Annu. Rev. Med. *26*, 9–20.

Blagih, J., Coulombe, F., Vincent, E.E., Dupuy, F., Galicia-Vázquez, G., Yurchenko, E., Raissi, T.C., van der Windt, G.J.W., Viollet, B., Pearce, E.L., et al. (2015). The energy sensor AMPK regulates T cell metabolic adaptation and effector responses in vivo. Immunity *42*, 41–54.

Brown, G., Singer, A., Proudfoot, M., Skarina, T., Kim, Y., Chang, C., Dementieva, I., Kuznetsova, E., Gonzalez, C.F., Joachimiak, A., et al. (2008). Functional and structural characterization of four glutaminases from Escherichia coli and Bacillus subtilis. Biochemistry *47*, 5724–5735.

Comerford, S.A., Huang, Z., Du, X., Wang, Y., Cai, L., Witkiewicz, A.K., Walters, H., Tantawy, M.N., Fu, A., Manning, H.C., et al. (2014). Acetate dependence of tumors. Cell *159*, 1591–1602.

Dong, F., Wang, B., Zhang, L., Tang, H., Li, J., and Wang, Y. (2012). Metabolic response to Klebsiella pneumoniae infection in an experimental rat model. PLoS ONE *7*, e51060.

Faubert, B., Vincent, E.E., Griss, T., Samborska, B., Izreig, S., Svensson, R.U., Mamer, O.A., Avizonis, D., Shackelford, D.B., Shaw, R.J., and Jones, R.G. (2014). Loss of the tumor suppressor LKB1 promotes metabolic reprogramming of cancer cells via HIF-1α. Proc. Natl. Acad. Sci. USA *111*, 2554–2559.

Ferreira, A.P.S., Cassago, A., Gonçalves, K. de A., Dias, M.M., Adamoski, D., Ascenção, C.F.R., Honorato, R.V., de Oliveira, J.F., Ferreira, I.M., Fornezari, C., et al. (2013). Active glutaminase C self-assembles into a supratetrameric oligomer that can be disrupted by an allosteric inhibitor. J. Biol. Chem. *288*, 28009–28020.

Harty, J.T., and Badovinac, V.P. (2008). Shaping and reshaping CD8+ T-cell memory. Nat. Rev. Immunol. *8*, 107–119.

Høverstad, T., and Midtvedt, T. (1986). Short-chain fatty acids in germfree mice and rats. J. Nutr. *116*, 1772–1776.

Huda-Faujan, N., Abdulamir, A.S., Fatimah, A.B., Anas, O.M., Shuhaimi, M., Yazid, A.M., and Loong, Y.Y. (2010). The impact of the level of the intestinal short chain fatty acids in inflammatory bowel disease patients versus healthy subjects. Open Biochem. J. *4*, 53–58.

Iwata, M., Hirakiyama, A., Eshima, Y., Kagechika, H., Kato, C., and Song, S.-Y. (2004). Retinoic acid imprints gut-homing specificity on T cells. Immunity *21*, 527–538.

John, A.-K., Schmaler, M., Khanna, N., and Landmann, R. (2011). Reversible daptomycin tolerance of adherent staphylococci in an implant infection model. Antimicrob. Agents Chemother. *55*, 3510–3516.

Kunkel, E.J., and Butcher, E.C. (2002). Chemokines and the tissue-specific migration of lymphocytes. Immunity *16*, 1–4.

Li, Y., Erickson, J.W., Stalnecker, C.A., Katt, W.P., Huang, Q., Cerione, R.A., and Ramachandran, S. (2016). Mechanistic basis of glutaminase activation: a key enzyme that promotes glutamine metabolism in cancer cells. J. Biol. Chem. *291*, 20900–20910.

McGuirk, S., Gravel, S.-P., Deblois, G., Papadopoli, D.J., Faubert, B., Wegner, A., Hiller, K., Avizonis, D., Akavia, U.D., Jones, R.G., et al. (2013). PGC-1α supports glutamine metabolism in breast cancer. Cancer Metab. *1*, 22.

Mizuno, M., Ito, Y., Hepburn, N., Mizuno, T., Noda, Y., Yuzawa, Y., Harris, C.L., Morgan, B.P., and Matsuo, S. (2009). Zymosan, but not lipopolysaccharide, triggers severe and progressive peritoneal injury accompanied by complement activation in a rat peritonitis model. J. Immunol. *183*, 1403–1412.

Nguyen, C.T.Q., Shetty, V., and Maresso, A.W. (2015). Global metabolomic analysis of a mammalian host infected with Bacillus anthracis. Infect. Immun. *83*, 4811–4825.

Nowakowska, J., Landmann, R., and Khanna, N. (2014). Foreign body infection models to study host-pathogen response and antimicrobial tolerance of bacterial biofilm. Antibiotics (Basel) *3*, 378–397.

O'Donovan, D.J., and Lotspeich, W.D. (1966). Activation of kidney mitochondrial glutaminase by inorganic phosphate and organic acids. Nature *212*, 930–932.

Pappu, R., Schwab, S.R., Cornelissen, I., Pereira, J.P., Regard, J.B., Xu, Y., Camerer, E., Zheng, Y.-W., Huang, Y., Cyster, J.G., and Coughlin, S.R. (2007). Promotion of lymphocyte egress into blood and lymph by distinct sources of sphingosine-1-phosphate. Science *316*, 295–298.

Reiss, Y., Proudfoot, A.E., Power, C.A., Campbell, J.J., and Butcher, E.C. (2001). CC chemokine receptor (CCR)4 and the CCR10 ligand cutaneous T cell-attracting chemokine (CTACK) in lymphocyte trafficking to inflamed skin. J. Exp. Med. *194*, 1541–1547.

Rouse, B.T., and Sehrawat, S. (2010). Immunity and immunopathology to viruses: what decides the outcome? Nat. Rev. Immunol. *10*, 514–526.

Sigmundsdottir, H., and Butcher, E.C. (2008). Environmental cues, dendritic cells and the programming of tissue-selective lymphocyte trafficking. Nat. Immunol. *9*, 981–987.

Stalnecker, C.A., Erickson, J.W., and Cerione, R.A. (2017). Conformational changes in the activation loop of mitochondrial glutaminase C: A direct fluorescence readout that distinguishes the binding of allosteric inhibitors from activators. J. Biol. Chem. *292*, 6095–6107.

Svensson, M., Johansson-Lindbom, B., Zapata, F., Jaensson, E., Austenaa, L.M., Blomhoff, R., and Agace, W.W. (2008). Retinoic acid receptor signaling levels and antigen dose regulate gut homing receptor expression on CD8+ T cells. Mucosal Immunol. *1*, 38–48.

Tremaroli, V., and Bäckhed, F. (2012). Functional interactions between the gut microbiota and host metabolism. Nature *489*, 242–249.

Trompette, A., Gollwitzer, E.S., Pattaroni, C., Lopez-Mejia, I.C., Riva, E., Pernot, J., Ubags, N., Fajas, L., Nicod, L.P., and Marsland, B.J. (2018). Dietary fiber confers protection against flu by shaping Ly6c$^-$ patrolling monocyte hematopoiesis and CD8$^+$ T cell metabolism. Immunity *48*, 992–1005.e8.

van der Windt, G.J.W., Everts, B., Chang, C.-H., Curtis, J.D., Freitas, T.C., Amiel, E., Pearce, E.J., and Pearce, E.L. (2012). Mitochondrial respiratory capacity is a critical regulator of CD8+ T cell memory development. Immunity *36*, 68–78.

van der Windt, G.J.W., O'Sullivan, D., Everts, B., Huang, S.C.-C., Buck, M.D., Curtis, J.D., Chang, C.-H., Smith, A.M., Ai, T., Faubert, B., et al. (2013). CD8 memory T cells have a bioenergetic advantage that underlies their rapid recall ability. Proc. Natl. Acad. Sci. USA *110*, 14336–14341.

STAR★METHODS

KEY RESOURCES TABLE

REAGENT or RESOURCE	SOURCE	IDENTIFIER
Antibodies		
BUV395 rat anti-mouse CD44	BD	Cat# 740215
APC rat anti-mouse CD8	Biolegend	Cat# 100712
BV421 hamster anti-mouse KLRG1	Biolegend	Cat# 138413
PE rat anti-mouse CD62L	Biolegend	Cat# 104408
APC-Cy7 rat anti-mouse CD43	Biolegend	Cat# 121220
BV421 rat anti-mouse PDL1	Biolegend	Cat# 124315
PE-Cy5 rat anti-mouse CD127	eBioscience	Cat# 15-1271-82
PE rat anti-mouse CD25	Biolegend	Cat# 101904
BV510 hamster anti-mouse CD27	Biolegend	Cat# 124229
FITC rat anti-mouse CD3	BD	Cat# 555274
PE rat anti-mouse CD8	Biolegend	Cat# 100708
APC mouse anti-human CD62L	ImmunoTools	Cat# 21819626
Pacific Blue anti-CD45RA	Beckman Coulter	Cat# A86050
Bacterial and Virus Strains		
Listeria monocytogenes expressing chicken Ovalbumin (AA134–387)	Prof. Ed Palmer, University Basel, CH	N/A
Biological Samples		
Human body fluids	University Hospital Basel	N/A
Chemicals, Peptides, and Recombinant Proteins		
Liberase TL Research Grade	Roche	Cat#05 401 020 001
APC Annexin V	Immunotools	Cat#31490016
BPTES	Sigma Aldrich	Cat#SML0601
SB204990	Tocris	Cat#4962
Recombinant murine CXCL12	Peprotech	Cat#250-20A
Recombinant human glutaminase	R&D Systems	Cat#10115-GL-020
Glutaminase from *E. coli*	Megazyme	Cat#E-GLUTEC
Critical Commercial Assays		
Acetate fluorimetric assay kit	BioAssay Systems	Cat#EOAC-100
LDH Assay Kit	Abcam	Cat#ab102526
Glutaminase Microplate Assay Kit	Cohesion Biosciences	Cat#CAK1065
Experimental Models: Organisms/Strains		
Mouse: B6.129S6-Rag2tm1Fwa Tg(TcraTcrb)1100Mjb	Taconic	Model #2334
Mouse: C57BL/6	Charles River and Janvier	N/A
Oligonucleotides		
ms ACSS1 (forward 5′-GTTTGGGACA CTCCTTACCATAC-3′ and reverse 5′-AGGCAGTTGACAGACACATTC-3′)	Invitrogen	This paper
ms ACSS2 (forward 5′-GTGAAAGGAT CTTGGATTCCAGT-3′ and reverse 5′-CAGATGTTTGACCACAATGCAG-3′)	Invitrogen	This paper
Gls: Mm01257297_m1	Thermo Fisher	Cat#4331182
Ifng: Mm01168134_m1	Thermo Fisher	Cat#4331182

(*Continued on next page*)

Continued

REAGENT or RESOURCE	SOURCE	IDENTIFIER
ms 18S primers (forward 5′-GGGAGC CTGAGAAACGGC-3′ and reverse 5′-GGGTCGGGAGTGGGTAATTT-3′)	Microsynth	This paper
hs ACSS1 (forward 5′-CACAGGACAG ACAACAAGGTC-3′ and reverse 5′-CCTGGGTATGGAACGATGCC-3′)	Invitrogen	This paper
hs ACSS2 (forward 5′-AAAGGAGCAA CTACCAACATCTG-3′ and reverse 5′-GCTGAACTGACACACTTGGAC-3′)	Invitrogen	This paper
Human 18S	Applied Biosystems	Cat#4310893E
Recombinant DNA		
pGEX-4T-1-GLS2_WT (C-terminal GST)	Genscript	N/A
pGEX-4T-1-GLS2_K253A (C-terminal GST)	Genscript	N/A
Software and Algorithms		
FlowJo	BD	https://www.flowjo.com
GOLD Suite v5.7.0	The Cambridge Crystallographic Data Centre, Cambridge, UK	https://www.ch.cam.ac.uk/computing/software/gold-suite
PyMol v1.3	Schrödinger	https://pymol.org/2/
ImageJ	N/A	https://imagej.net/Welcome
GraphPad Prism	N/A	https://www.graphpad.com/scientific-software/prism/

RESOURCE AVAILABILITY

Lead Contact

Further information and requests for resources and reagents should be directed to and will be fulfilled by the Lead Contact, Christoph Hess (ch818@cam.ac.uk; chess@uhbs.ch).

Materials Availability

This study did not generate new unique reagents.

Data and Code Availability

The published article includes all datasets generated or analyzed during this study.

EXPERIMENTAL MODEL AND SUBJECT DETAILS

Animal Husbandry

Male and female C57BL/6 or MHC class I-restricted OVA-specific T cell receptor (OT-I) transgenic mice were 6-8 weeks of age and housed in IVC cages on racks in a room with controlled temperature (22-24°C) and humidity (40%–60%). Mice were maintained on a 12 h light-dark cycle. All mice were fed a standard diet (Kliba AG, #3436 EX). Health checks were conducted on all mice at least once daily. For experimental control groups, littermates were used. All animal experiments were approved by the Animal Care Committee of the Veterinary Office Basel, Switzerland.

Human Abscess Fluids

Human abscess fluids were obtained from the division of Clinical Microbiology of the University Hospital Basel after informed consent of the patients and ethical approval of the ethics committee of both Basels. As controls, non-inflamed samples (e.g., sterile ascites, cyst-fluids, pleural transudate) were used. Samples were stored at 4°C prior to measurement. Patient characteristics are summarized in Table 1.

Isolation of Human Effector Memory (EM) CD8$^+$ T Cells

Peripheral blood mononuclear cells were isolated by standard density-gradient centrifugation protocols (Lymphoprep; Fresenis Kabi) from healthy male and female blood donors, > 18 years of age. Results were not stratified by age or sex, since we did not have this information at the time of analysis. MACS beads and LS columns (both Milteny Biotec) were used to sort CD8$^+$ positive T cells. The positively selected CD8$^+$ T cells were incubated with APC anti-CD62L mAb (ImmunoTools) and Pacific Blue anti-CD45RA

(Beckman Coulter) and sorted by flow cytometry (BD FACSAria III or BD Influx Cell Sorter). Experiments using blood donor derived cells were approved by the blood transfusion service of the Swiss Red Cross.

Cell Culture

Primary cells of male and female mice were cultured in RPMI medium (RPMI 1640 containing 10% FCS, 100 U/mL penicillin, 100 µg streptomycin, 0.29 mg/mL L-glutamine, 50 µM 2-Mercaptoethanol) at 37°C and 5% CO2.

METHOD DETAILS

In Vitro Memory Differentiation

Memory OT-I T cells were generated as described previously (Balmer et al., 2016; van der Windt et al., 2013). Briefly, the lymph nodes from MHC class I-restricted OVA-specific T cell receptor (OT-I) transgenic mice and the spleen of C57BL/6 mice were aseptically removed and incubated in liberase TL (Roche) for 30 min. After mashing through a 70 µm cell strainer (BD Biosciences), red blood cells were lysed with RBC Lysis Buffer Solution (eBioscience). The isolated cell suspensions were washed in RPMI medium (RPMI 1640 containing 10% FCS, 100 U/mL penicillin, 100 µg streptomycin, 0.29 mg/mL L-glutamine, 50 µM 2-Mercaptoethanol (Life Technologies)) and re-suspended to 10^6 cells/mL. The splenocytes and OT-I cells were pooled in a ratio of 1:1 and activated with OVA peptide (Eurogentec) at 10^{-9} M at 37°C for 3 days. The cells were then washed and re-suspended to 2×10^6 cells/mL and cultured in the presence of IL-15 (10 ng/mL) at 37°C for another 3 days to generate OVA-specific memory CD8$^+$ T cells. Phenotyping was performed using BUV395-anti CD44 (BD), APC-anti CD8, BV421-anti KLRG1, PE-anti-CD62L, APC-Cy7-anti CD43, BV421-anti PDL1, PE-anti-CD25, BV510-anti CD27 (all Biolegend) and PE-Cy5-anti CD127 (eBioscience).

Acetate Measurement in Murine and Human Samples

Acetate concentrations in peritoneal fluids and human samples were determined using the acetate fluorimetric assay kit (Bioassay Systems), following the manufacturer's instructions.

Measurement of Cell Viability

To measure the viability, 10^5 mouse or human memory CD8$^+$ T cells were plated in a 96-well plate in RPMI medium. The cells were incubated at 37°C for up to 7 days. The cells were washed in Annexin V Binding Buffer (BD PharMingen) and stained with APC Annexin V (ImmunoTools) and PI (Sigma Aldrich). Samples were acquired on an Accuri® C6 Flow Cytometer and analyzed with FlowJo-Software (FlowJo 10.2). Viable cells were defined as Annexin V and PI double negative. Where indicated, cells were incubated in presence of BPTES (Sigma Aldrich) at 50 µM or in glutamine-free RPMI containing dialyzed FCS (Life Technologies).

Transwell migration assay

For the *in vitro* migration assay 2-5 × 10^5 cells were resuspended in 80% full medium and 20% PBS, supplemented with varying concentration of sodium acetate, calcium chloride and sodium chloride. 100 µL of cell suspension was seeded in 5 µm pore cell culture inserts (Sigma, CLS3421) with 500 µL of the corresponding medium in the well. After 3 h incubation at 37°C, the volumes in the insert and the well were measured with a pipette. The cell density was measured by acquiring 30 µL of the insert and well with a CytoFlex flow cytometer (Beckman Coulter) by counting the number of events in the live gate using FlowJo. The translocation index was calculated by dividing the cell number of the cell culture insert with the total cell number. Every condition was assessed by technical triplicates and every experiment was repeated at least three times. Where indicated, CXCL12 (Peptrotech) at 50 ng/mL was used.

Murine Peritonitis Model

C57BL/6 mice were intra-peritoneally (i.p.) infected with 5000 CFU *Listeria monocytogenes* expressing the OVA-peptide (LmOVA). 28 days later, mice were re-infected with 10^5 CFU LmOVA i.p. in presence or absence of 5 mM acetate. Mice were sacrificed 24 h later and peritoneal fluid, spleen, liver and serum harvested. Spleens and livers were homogenized in 0.5% Terigitol/PBS using a Tissue-lyser (QIAGEN) and sterile stainless-steel ball bearings. Organ suspensions were then plated on BHI agar-plates and colonies counted upon 24 h incubation at 37°C. Peritoneal fluids were centrifuged and the cells analyzed by flow-cytometry upon staining with FITC-anti-CD3, BUV395-anti CD44 (both BD), BV421-anti PDL1, APC-Cy7-anti CD43, BV510-anti CD27 and PE-anti CD8 antibodies, Zombie-Red viability staining (all Biolegend) or by RT-PCR upon MACS-purification and storage in Trizol Reagent (Thermo Fisher Scientific). Peritoneal fluids and sera were frozen at −80°C prior to further analysis. LDH concentrations in peritoneal fluids were measured using a commercially available assay kit (Abcam). All experiments were performed in accordance with local rules for the care and use of laboratory animals.

S. aureus Tissue Cage Model

The mouse model of foreign-body infection (John et al., 2011; Nowakowska et al., 2014) was used in the present study. Briefly, a sterile tissue cage (Angst + Pfister AG, Zurich, Switzerland) was implanted subcutaneously in the back of female C57BL/6 mice, 13 weeks old (janvierlab, France). After complete wound healing (2 weeks), cages were tested for sterility by culturing the aspirated tissue cage fluid (TCF). Teflon cages were infected with 785 CFU of MSSA ATCC 29213. The infection was confirmed at day 1 directly before treatment start by plating. Mice were i.p. treated twice a day with 5% glucose for 11 days. Tissue cage fluid (TCF) was aspirated at different time points (day 3, 6, 9, 11 and 14) and apropriate dilutions were plated to determine the amount of planktonic MSSA. Tissue cage fluids were then analyzed for acetate, calcium and phosphate levels and CD8$^+$ T cells isolated by MACS-purification and frozen in Trizol Reagent (Thermo Fisher Scientific). For phenotyping, cells were stained with APC-anti CD8 (Biolegend), BUV395-anti CD44 (BD), PE-anti CD62L (Biolegend) antibodies and Zombie-Red Viability staining (Biolegend).

Histology

Small pieces (0.5 × 0.5 cm) of peritoneum were fixed in 4% formaldehyde for 24 h. Samples were then paraffin-embedded, cut, and stained with H&E and elastica van Gieson on an automated-stainer according to standard procedures. Peritoneal thickness was measured from the mesothelial surface to the border of the loose connective tissue between compact zone and muscular layer by a board-certified pathologist in a blinded manner as described in (Mizuno et al., 2009).

Seahorse Experiments

Oxygen consumption rates (OCR, in pMoles/min) and extracellular acidification rates (ECAR, in mpH/min) were measured in plated cells (2.5×10^5 per well) kept in serum-free unbuffered RPMI-1640 medium (Sigma-Aldrich), under basal conditions, and in response to OVA-peptide (10 μM) or acetate (5 mM) injection using the instrument's multi-injection ports. Where indicated, cells were pretreated with the ACLY-inhibitor SB204990 (Tocris) at 30 μM or BPTES (Sigma Aldrich) at 50 μM 2 h prior to and during metabolic flux analysis or vehicle control. All data were generated using the XF-96 Extracellular Flux Analyzer (Seahorse Bioscience).

Metabolic Tracing

GC-MS metabolite analysis was conducted as previously described (Blagih et al., 2015) (Balmer et al., 2016). Briefly, 5×10^6 IL-15 expanded OT-I memory cells were cultured in standard or glutamine-free RPMI (with 10% dialyzed FCS) containing 10 mM 1,2-[13C]-acetate or 10 mM 13C-glutamine (Cambridge Isotope Laboratories) for 6 h. Metabolites were extracted from cells using ice-cold 80% methanol, followed by sonication and removal of cellular debris by centrifugation at 4°C. Metabolite extracts were dried, derivatized as tert-butyldimethylsilyl (TBDMS) esters, and analyzed via GC-MS as previously described (Faubert et al., 2014). Uniformly deuterated myristic acid (750 ng/sample) was added as an internal standard following cellular metabolite extraction, and metabolite abundance was expressed relative to the internal standard and normalized to cell number. Mass isotopomer distribution was determined using a custom algorithm developed at McGill University, CA (McGuirk et al., 2013).

Quantitative PCR

Quantitative PCR for mouse ACSS1 and ACSS2 mRNA was done in triplicates with SYBR Green Supermix (Promega). The following primers were used: ms ACSS1 (forward 5′-GTTTGGGACACTCCTTACCATAC-3′ and reverse 5′-AGGCAGTTGACAGACACATTC-3′), ms ACSS2 (forward 5′-GTGAAAGGATCTTGGATTCCAGT-3′ and reverse 5′-CAGATGTTTGACCACAATGCAG-3′) (both Invitrogen). The following primers were used to analyze glutaminase mRNA: Mm01257297_m1 (Thermo Fisher Scientific). *IFNg* mRNA was measured using primers Mm01168134_m1 (Thermo Fisher Scientific). As a housekeeping gene mouse 18S mRNA was measured using ms 18S primers (forward 5′-GGGAGCCTGAGAAACGGC-3′ and reverse 5′-GGGTCGGGAGTGGGTAATTT-3′) (Microsynth). Quantitative PCR for human ACSS1 and ACSS2 mRNA was done in triplicates with SYBR Green Supermix (Promega). The following primers were used: hs ACSS1 (forward 5′-CACAGGACAGACAACAAGGTC-3′ and reverse 5′-CCTGGGTATGGAACGATGCC-3′), hs ACSS2 (forward 5′-AAAGGAGCAACTACCAACATCTG-3′ and reverse 5′-GCTGAACTGACACACTTGGAC-3′) (both Invitrogen). As a housekeeping gene 18S was used (4310893E, Applied Biosystems). Peritoneal immunopathology was assessed using the mouse Wound Healing RT^2 Profiler PCR Array following the manufacturer's instructions (QIAGEN). RNA-quality was checked prior to the assay using the Bioanalyzer RNA-kit (Agilent).

Glutaminase Activity Assay

To analyze the activity of glutaminase in memory CD8$^+$ T cells, the Glutaminase Microplate Assay Kit (Cohesion Biosciences) was used. After incubation, cells (4 Mio) were sonicated in the assay buffer (40 μl) provided with the kit and then processed according to the manufacturer's instructions. Recombinant human glutaminase at 1 μg/mL (R&D Systems) and glutaminase from *E. coli* at 6 U/mL (Megazyme) were tested in the Glutaminase Microplate Assay (Cohesion Biosciences).

Glutaminase-Acetate *In Silico* Docking

We used a template of the human glutaminase co-crystallized with bound glutamine (PDB ID 3VP0). The three-dimensional structure of acetate was constructed *ab initio* in Chem3D Pro v14.0 (CambridgeSoft, Cambridge, UK) and energy-minimized using the integrated MM2 force field. The binding site of acetate was defined as being within 20 Å of the centroid around the α-carbon of Y446, a centrally located residue that interacts with glutamine in the substrate binding site. Acetate was docked as a flexible ligand into the ligand-occupied structure using GOLD Suite v5.7.0 (The Cambridge Crystallographic Data Centre, Cambridge, UK) with the GoldScore function and default settings. Ten docked poses were generated and visualized with PyMol v1.3.

Glutaminase Mutagenesis

Human GLS2 was cloned into the multiple cloning site of a pGEX-4T-1 bacterial expression vector containing a C-terminal glutathione-S-transferase (GST) tag. The K253A variant was generated by site-directed mutagenesis which corresponds to the GLS1 sequence K->A shown in Figure 2L. The *E. coli* strain BL21(DE3) was then transformed with wild type or K253A mutant pGEX-4T-1-GLS2 vectors. Recombinant GLS2-GST was purified from bacterial cell lysate using GST hiTRAP and Superdex 200 columns and eluted in 5mM Tris, 150mM HCl buffer (pH 7.5). Wildtype and mutant glutaminase was used at a concentration of 1 μg/mL for measuring glutaminase activity as described above.

Calcium Flux

In vitro differentiated memory OT-I T cells were loaded with 1 μM Fluo4 (Invitrogen) and 1 μM Fura Red (Invitrogen) with indicated acetate or calcium concentrations for 30 min at 37°C. After washing, T cells were activated with 10 μM OVA-peptide under continuous acquisition using an Accuri C6 (BD) or Cytoflex (Beckmann coulter) flow cytometer. Analysis was performed with FlowJo software using kinetics tool (ratio of geometric mean fluorescence intensity of Fluo4/FuraRed) and Prism software.

Calcium and Phosphate Quantification

Calcium and phosphate concentrations were measured in collaboration with the diagnostics department of the University Hospital Basel using a fotometric Assay (Cobas, Roche). For *in vitro* calcium-measurements, PBS was supplemented with increasing concentrations of acetate and calcium-concentrations measured immediately.

Intracellular Cytokine Staining

200,000 cells per condition were re-activated with CD3/CD28 beads (1:10) or OVA-peptide (10 μM) in presence or absence of the indicated concentrations of acetate or calcium for 4 h. Brefeldin A (Biolegend) was added after 1 h of incubation. Fixation and permeabilization with BD Cytofix/Cytoperm and BD Perm/Wash was done according to the instruction of the manufactorer (BD Biosciences). Cells were then stained with FITC-anti-human IFN-γ (BD Biosciences) or FITC-anti-mouse IFN-γ (Biolegend), aquired on an Accuri C6 Flow Cytometer and analyzed using FlowJo-Software (FlowJo 10.2).

Cytrometric Bead Array

Cytokine concentrations in cell culture supernatants and peritoneal fluids were determined using the LegendPlex cytrometric bead Array Th1-Pannel (Biolegend), according to the manufacturer's instructions.

Immunoblot Analysis

Memory T cells were lysed in RIPA buffer (Thermo Scientific) containing protease- and phosphatase-inhibitors (Roche, #05 892 970 001 and #04 906 837 001), and protein concentrations determined with a BCA protein assay kit (Thermo Scientific). Whole-cell lysates were separated by 4%–20% SDS-PAGE and transferred to nitrocellulose or PVDF membranes. Membranes were probed with anti-glutaminase mAb (Protein Tech, #19958-1-AP) and anti-actin mAb (Sigma #A1978). Blots were then stained with the appropriate secondary antibody (IRDye 800CW– conjugated goat polyclonal antibody to rabbit IgG (926-32211) from LI-COR). The Odyssey imaging system (LICOR) was used for detection, and the ImageJ software (1.48v) for quantification.

QUANTIFICATION AND STATISTICAL ANALYSIS

Differences were analyzed for statistical significance using Prism 7 for Macintosh (GraphPad Software Inc.). The details of the tests carried out are indicated in each figure legend. Where data were approximately normally distributed, values were compared using either a Student's t test, one-way or two-way ANOVA. Where data were non-normally distributed Wilcoxon-tests were applied. In all cases, p values < 0.05 were considered significant.

6.4 Section IV: Development of a Volatile Metabolomics Platform for Dendritic Cells to Investigate Cellular Metabolism in Real-Time

6.4.1 Summary

In the manuscript, titled "*Real-Time Volatile Metabolomics Analysis of Dendritic Cells*", we detail the development of a mass spectrometry method that enables real-time analysis of dendritic cell (DC) metabolism by examining the volatile phase of *in vitro* cell cultures. This platform couples DC cultures with secondary electrospray ionization-high resolution mass spectrometry to identify volatile organic compounds (VOCs).

Three exploratory studies were conducted to investigate the capabilities of this approach. Study I revealed the ability to capture VOCs emitted from DCs responding to the bacterial supernatant stimulation. Next in study II, we probed the capacity of this platform to detect and trace the incorporation of isotopically labeled metabolites into cellular metabolism. When exposed to ^{13}C-glucose, DCs emitted glucose-derived ^{13}C-labelled VOCs, demonstrating the platform's potential to accommodate metabolic tracing. Lastly, study III delineated the capability to discern differential metabolic states of vehicle and LPS-treated DCs by ^{13}C-glucose tracing and metabolic pathway analysis.

In conclusion, our work presents a non-invasive mass spectrometry method adept at the real-time analysis of DC metabolism by probing the volatile phase. A limitation of this method is the requirement for VOC identity validation by targeted mass spectrometry. However, this platform holds potential to complement current techniques by offering dynamic and unbiased insights into cellular metabolism.

6.4.2 Author Contribution

This study was designed and conceived in a collaborative effort, led by Pablo Sinues (University of Basel) and Maria Balmer (University of Basel and University of Bern), along with Christoph Hess (University of Basel and University of Cambridge), Kim Arnold (University of Bern), Jonas Lötscher (University of Basel), and Philippe Dehio (University of Basel). Jonas Lötscher and Philippe Dehio conducted the cell culture experiments relevant to this study. Philippe Dehio contributed to the data analysis and interpretation and was involved in drafting, editing, and reviewing the manuscript, in collaboration with Pablo Sinues, Maria Balmer, and Christoph Hess.

6.4.3 Published Manuscript: *Real-Time Volatile Metabolomics Analysis of Dendritic Cells*

The published manuscript is attached below and is accessible by the QR-code:

analytical chemistry

pubs.acs.org/ac

Technical Note

Real-Time Volatile Metabolomics Analysis of Dendritic Cells

Kim Arnold,[△] Philippe Dehio,[△] Jonas Lötscher, Kapil Dev Singh, Diego García-Gómez, Christoph Hess, Pablo Sinues,[*,●] and Maria L. Balmer[*,●]

Cite This: *Anal. Chem.* 2023, 95, 9415−9421

Read Online

ACCESS | Metrics & More | Article Recommendations | * Supporting Information

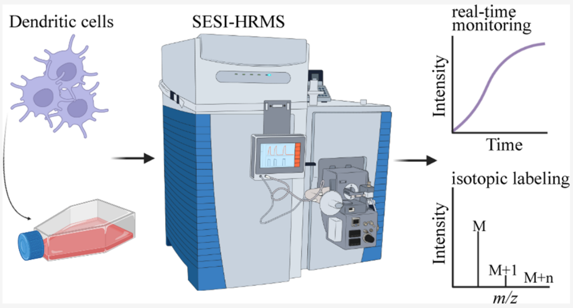

ABSTRACT: Dendritic cells (DCs) actively sample and present antigen to cells of the adaptive immune system and are thus vital for successful immune control and memory formation. Immune cell metabolism and function are tightly interlinked, and a better understanding of this interaction offers potential to develop immunomodulatory strategies. However, current approaches for assessing the immune cell metabolome are often limited by end-point measurements, may involve laborious sample preparation, and may lack unbiased, temporal resolution of the metabolome. In this study, we present a novel setup coupled to a secondary electrospray ionization-high resolution mass spectrometric (SESI-HRMS) platform allowing headspace analysis of immature and activated DCs in real-time with minimal sample preparation and intervention, with high technical reproducibility and potential for automation. Distinct metabolic signatures of DCs treated with different supernatants (SNs) of bacterial cultures were detected during real-time analyses over 6 h compared to their respective controls (SN only). Furthermore, the technique allowed for the detection of ^{13}C-incorporation into volatile metabolites, opening the possibility for real-time tracing of metabolic pathways in DCs. Moreover, differences in the metabolic profile of naïve and activated DCs were discovered, and pathway-enrichment analysis revealed three significantly altered pathways, including the TCA cycle, α-linolenic acid metabolism, and valine, leucine, and isoleucine degradation.

■ INTRODUCTION

With the recent rise of metabolomics technologies, research on immunometabolism has boomed during the past years, especially due to findings that metabolic reprogramming is essential for cell maintenance, function, and differentiation.[1,2] Characterizing and understanding cells at the metabolic level are relevant to better understand and potentially modify immune functionality in various diseases from infections to autoimmune diseases. A particular focus hereby may be given to dendritic cells (DCs), as they are the key mediators between the innate and adaptive immune system and their metabolic rewiring during development and activation is still incompletely understood.[3]

Currently, various techniques are deployed to assess cells' immunometabolism depending on the hypothesis and cell system used.[1] Usually, to get a first impression on metabolic alterations, quick and cost efficient measurements on nitric oxide (NO) consumption/arginase production or glucose consumption/lactate production can be combined with functional assays such as enzyme-linked immunosorbent assays (ELISA).[4] For more in-depth metabolic characterization, real-time extracellular flux analysis (EFA) enables a parallel readout on glycolysis and oxidative phosphorylation (OXPHOS).[5] However, the important limitations of all the aforementioned methods are that they mainly provide information on only a few parameters related to specific core pathways at a single time point (except EFA) or that they may affect the metabolic state of the cells when pretreatment of cells is required.[4] To get a more detailed metabolic picture, previously described techniques can be combined with gold standard liquid chromatography−mass spectrometry (LC-MS) and gas chromatography−mass spectrometric (GC-MS) methods. Through targeted and untargeted LC-MS and GC-MS experiments, detailed information on metabolites of interest can be captured; however, those methods require time-consuming sample preparation and do not provide information on dynamic processes without using isotopically labeled substrates.[6,7]

Secondary electrospray ionization−high resolution mass spectrometry (SESI-HRMS) is an emerging technique and may be an attractive alternative metabolomics approach, as it can provide quick, sensitive, noninvasive, and real-time results with minimal sample preparation. SESI is a soft ionization

Received: February 3, 2023
Accepted: May 17, 2023
Published: June 13, 2023

https://doi.org/10.1021/acs.analchem.3c00516

method, operates at ambient pressure, and is able to detect volatile organic compounds (VOCs) with limits of detection in the low parts per trillion (ppt) range.[8] When combined with HRMS it, in addition, allows the resolving of fine isotopic structures, which is suitable for isotopic tracing.[9] Several mass spectrometric methods have been described in the literature to assess VOCs emitted from living organisms in enclosed controlled environments. These include bacteria,[10] yeast,[11,12] plants,[13] mammalian cells,[14−16] and small-animal models.[17] Thus, the objective of the current study was to evaluate the potential of SESI-HRMS to assess DC metabolism as a model immune cell. Such a system could potentially open new possibilities for delivering valuable dynamic information on the crosstalk between immunity and cell metabolism.

EXPERIMENTAL SECTION

The applicability of the new technical setup was subdivided into three studies. In study I we characterized VOCs emitted by DCs in real-time upon stimulation with two bacterial supernatants from two different time points (SN1 and SN2) of an *E. coli* culture. In study II, ^{13}C-incorporation from labeled glucose (Glc $^{13}C_6$) in VOCs emitted by DCs was monitored in real-time over 4 h. In study III, we assessed ^{13}C-incorporation from Glc $^{13}C_6$ in VOCs emitted by DCs after 24 h incubation with and without long time bacterial lipopolysaccharide (LPS) stimulation. In study I, bacterial SN was used as a surrogate stimulus for DC activation, since it contains a variety of bacterial structural components (PAMPs) as well as bacterial metabolites. SNs from two different time points were used in order to mimic different bacterial concentrations and growth rates. To narrow down the stimulation to toll-like receptor-agonists only, LPS was used in study III, as it is the best studied stimulus in the literature with a well-characterized metabolic response in DCs. In the following, the key experimental information, including sample preparation and the main analytical instrumentation, is described. Detailed information on SESI-HRMS data analysis, LC-MS/MS analysis performed in the case of compound identification, and flow cytometric viability analysis is provided in the Supporting Information.

Cell Culture and Differentiation of Bone-Marrow-Derived Dendritic Cells (BMDCs). Murine bone marrow for BMDC differentiation was isolated from the tibias and femurs of 5−10-week-old C57BL/6NCrl mice by flushing with complete medium (RPMI1640 containing 10% heat-inactivated fetal calf serum; FCS). Animals were kept in a specific pathogen-free facility. A total of 2×10^6 bone marrow cells per Petri dish were incubated in the presence of 10 ng/mL GM-CSF for 8 days with a medium exchange on days 3 and 6. After 8 days, the floating cells were harvested and frozen in 10% DMSO and 90% FCS. On the days of the experiments, the cells were thawed, counted, and 5×10^6 cells (unless indicated differently) were plated in a cell culture flask (Jet Biofil) and rested for 2 h at 37 °C preceding the measurement. For the measurements, four flasks with different conditions were simultaneously compared. For isotopic ^{13}C glucose tracing, the medium was supplemented with dialyzed heat-inactivated FCS.

Sample Preparation Study I. For experiments with bacterial SN, *E. coli* JM83 was incubated in LB-medium at 37 °C, shaken, and grown to an optical density (OD) of 0.4 (SN1) or 1.4 (SN2), centrifuged and sterile-filtered through a 0.22 μm filter. Two flasks contained DCs in 5 mL of medium, and the other two flasks contained 5 mL of medium only. A baseline headspace measurement was conducted for 1 h while switching between the four flasks every 5 min using the valve system. After the baseline measurement, sterile-filtered bacterial SN was diluted 1:4 in 5 mL of medium, which was then used to replace the medium used for baseline measurement in all four culture flasks. After the addition of the respective SN, real-time SESI-HRMS measurements were conducted in positive ionization mode for 6 h while switching between the four flasks every 5 min. This experiment was repeated on three different days with three different biological replicates/cell batches ($n = 3$).

Sample Preparation Study II. To investigate the incorporation of ^{13}C over time, three biological replicates/cell batches were used ($n = 3$); one batch each for two flasks, respectively. A total of 5×10^6 cells were used for the batches DC1 and DC2, whereas 10^7 cells were used for batch DC3. A baseline measurement of 40 min was conducted with cells resting in glucose-free medium. Afterward, Glc $^{12}C_6$ or Glc $^{13}C_6$ was dissolved in glucose-free medium to reach a concentration of 66 mM. One mL of the 66 mM solution was then added to each flask containing 5 mL of glucose-free medium to reach a final concentration of 11 mM, which is equal to the glucose concentration found in complete medium. For each of the three cell batches, one flask contained Glc $^{12}C_6$ and the other contained Glc $^{13}C_6$. After the addition of the glucose, real-time SESI-HRMS measurements were conducted in the positive ionization mode for 4 h, while switching between the flasks every 5 min.

Sample Preparation Study III. To evaluate ^{13}C-incorporation with and without long-time LPS stimulation, a total of 20 flasks with four different cell batches were prepared. Four flasks ($n = 4$) were always assigned to one of five groups, named G1 (Glc $^{12}C_6$ in medium + LPS), G2 (Glc $^{12}C_6$ in medium + DC), G3 (Glc $^{12}C_6$ in medium + DC + LPS), G4 (Glc $^{13}C_6$ in medium + DC), and G5 (Glc $^{13}C_6$ in medium + DC + LPS), respectively. The glucose concentrations were the same as described in study II. All flasks were incubated for 24−27 h at 37 °C, 5% CO_2. After incubation, the four flasks of each group were sequentially measured by SESI-HRMS for 5 min each. The experiment was conducted in positive and negative ionization mode.

Real-Time Cell Culture Headspace Measurement with SESI-HRMS. A scheme of the general experimental setup is shown in Figure 1. Briefly, the setup consisted of four cell-culture flasks sealed airtight with inert rubber stoppers (HUBERLAB, Aesch) containing two holes for introducing polytetrafluoroethylene (PTFE) tubes. Stainless steel 3-way ball valves (Swagelok) enabled alternating switching between the four flasks simultaneously, connected via PTFE tubes to the SESI-HRMS. The flasks were placed on a multipoint heating plate (Carl Roth, Arlesheim) and were kept at a temperature of 37 °C during the experiments. A gas mixture (5% CO_2, 16% O_2, and 79% N_2) was used to pervade the system at a flow rate of 0.3 L/min and carried the VOCs emitted by the respective flasks' contents toward the SESI-HRMS. To prevent the contents in the flasks from drying out, a bottle filled with LC-MS-grade water was built into the system to ensure a humid environment. Usually, a time-span of 5 min was needed to measure a single flask. To ensure reproducibility of measurements on different days, a quality control standard gas mixture was infused 1 h before the start of

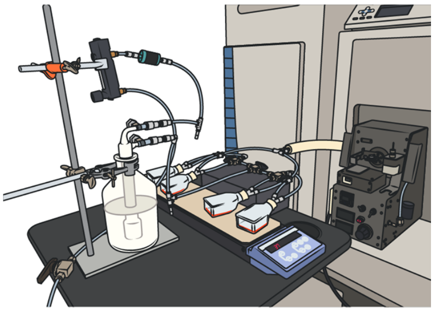

Figure 1. Experimental setup for DC headspace measurement by SESI-HRMS. Cell culture flasks were simultaneously attached to the SESI-HRMS via PTFE tubes and kept at 37 °C using a multipoint heating plate. Integrated 3-way ball valves allowed switching between the samples. The system was pervaded with a humidified gas mixture at a flow rate of 0.3 L/min to carry VOCs emitted by DCs toward the SESI-HRMS for real-time analysis.

each experiment. The protocol followed for quality control measurements is detailed by Gisler et al.[18]

SESI-HRMS Analytical Platform. The analytical platform consisted of an ion source (Super SESI, FIT, Spain) coupled to a high-resolution mass spectrometer (Q-Exactive Plus, Thermo Fisher Scientific, Germany). Mass spectra were acquired via Thermo Exactive Plus Tune software (version 2.9) in full scan mode (scan range 50−400 *m*/*z*, polarity positive or negative, microscan number 10, ACG target 106, and maximum injection time 500 ms) at a resolution of 280000 at *m*/*z* 200. For the formation of the electrospray, 20 *μ*m ID TaperTip silica capillary emitter (New Objective, U.S.A.) was used in study I, and a 20 *μ*m ID nanoelectrospray capillary (Fossil Ion Tech, Spain) was used in studies II and III along with 0.1% formic acid in water. Pressure of the SESI solvent environment was set to 1.3 bar (study I) and 0.8 bar (studies II and III). The electrospray voltage was set to 3.5 kV in positive and 2.8 kV in negative ionization mode. The temperatures of the ionization chamber and sampling line were set to 90 and 130 °C, respectively. Capillary temperature was 275 °C, sheath gas was set to 60, and S-lens RF level was set to 55.0. The mass flow controller exhaust set point was 0.7 L/min, and a nitrogen stream through the source was set to 0.4 L/min to ensure a constant flow of the headspace gas to the ionizer (0.3 L/min). In addition, the system was calibrated weekly internally and externally using common background contaminant lock masses and room air.[19,20]

RESULTS AND DISCUSSION

Study I: Stimulation of Cells by Bacterial SN. In study I we investigated whether the method can detect VOCs emitted by DCs and furthermore if the technique discriminates differences in the cellular response to different bacterial SNs. In total, 71 VOCs were significantly different ($p \leq 0.05$) between SN1 vs SN1 + DC (Table S1) and 59 significantly different ($p \leq 0.05$) between SN2 vs SN2 + DC (Table S2), showing a log 2FC ≥ 1 compared to their respective baselines

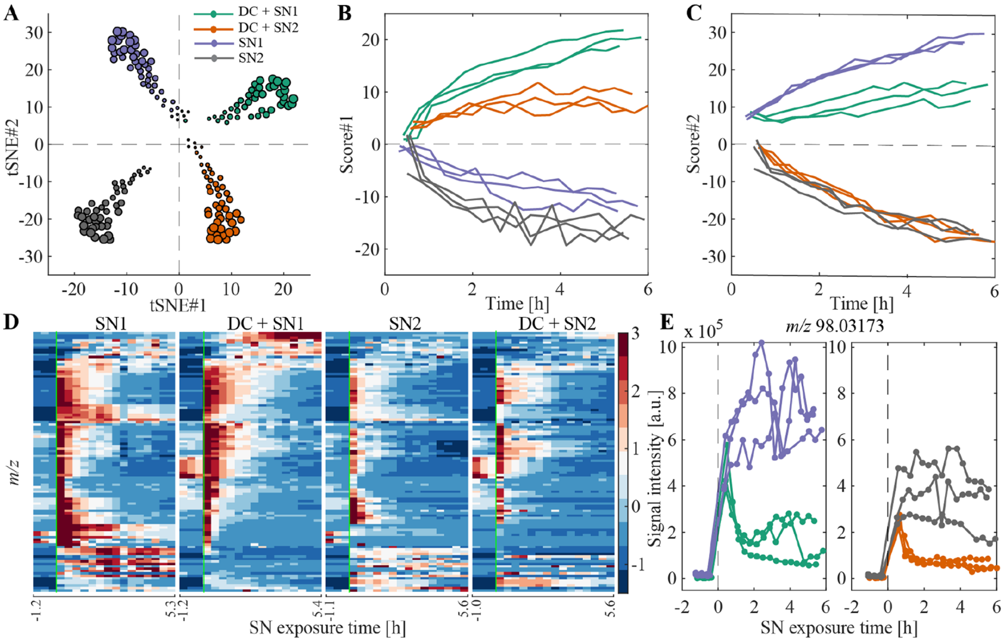

Figure 2. Distinguishing experimental conditions with high technical and biological reproducibility. (A) tSNE plot after SN addition of total 108 features which were significantly different ($p \leq 0.05$) between DC + SN1 and SN1 or significantly different ($p \leq 0.05$) between DC + SN2 and SN2 and showed a log 2FC ≥ 1 vs their respective baselines. The size of the symbols represents increasing time upon SN addition. (B) tSNE score 1 over time, separating samples containing DCs vs SN. (C) tSNE score 2 over time, separating samples containing SN1 vs SN2. (D) Heatmaps of 108 significant features shown for one biological replicate of each of the four groups. The color bar represents *z*-scored signal intensities. The green line indicates the time-point of addition of the SN. (E) Time trace of the positive ion at *m*/*z* 98.03173. This feature was significantly different between DC+ SN1 and SN1 as well as significantly different between DC + SN2 vs SN2. It represents an example of a feature with decreased abundance in samples containing DCs.

(before SN addition). Taken together, 108 unique VOCs were then used to perform t-distributed stochastic neighbor embedding (tSNE) and hierarchical cluster analysis, as illustrated in Figure 2. The variables included in the tSNE show a clear segregation between the four groups and their respective baselines (Figures 2A and S1A). Score 1 over time mainly discriminates between samples containing DCs and samples containing SN only (Figure 2B), whereas score 2 separates SN1 from SN2 (Figure 2C). The heatmaps of the cluster analysis (Figures 2D, S1B, and S1C) interestingly revealed two time trace patterns. On one hand, some features decreased over time in samples containing DCs, as exemplified for m/z 98.03173 in Figure 2E, compared to samples containing SN only, indicating uptake and/or active metabolism by DCs. On the other hand, a few features increased over time in samples containing DCs, as exemplified for m/z 182.00907 in Figure S1D compared to SN1 samples, compatible with active production and/or release by DCs. Such behavior may be explained by consumption of certain substrates required for maintenance of cell functions and active cell metabolism when DCs are in an activated vs steady state (e.g., increased glycolysis).[21,22] Interestingly, besides m/z 182.00907, we also found two further features with increased abundance in DC + SN1 compared to SN1 over time (Figure S1D). These two features, at m/z 183.01252 and m/z 184.00495, were confirmed to be the isotopes of m/z 182.00907 via isotopic pattern matching (Figure S2). Via LC-MS/MS analysis (Figure S3), the compound was identified as 2-(methylthio) benzothiazole (SCH3-BTH). Benzothiazoles (BTH) represent a class of chemicals widely used in industry, but they are also present, for example, in tap water or indoor dust.[23] Despite their ubiquitous nature, BTH have also been detected in the exhaled breath of humans, and it has been shown that they are not just artifacts from room air, but also from an endogenous origin.[24] Interestingly, BTH-based compounds also feature promising antimicrobial activities.[25] Although the relevance of the higher abundance of SCH3-BTH in the samples with SN1 + DC remains unclear, it suggests an active production of this compound by DCs which may be related to an active antibacterial strategy adopted by the cells.

Intra-coefficient of variation (CV) was assessed during baseline measurements (DCs in medium, $n = 6$ samples with 3 repeated measures each) for compound SCH3-BTH and showed very low intra-experimental variation of ~7%, which is comparable to a standard Seahorse XF Pro Analysis showing an intraplate CV $\leq$ 15%.[26] Therefore, the method shows high technical and good biological reproducibility (e.g., heatmaps Figures 2D, S1B, and S1C). As the experiments were performed with three different biological replicates and on three different days, we could rule out the possibility that our observations resulted from a batch effect. Importantly, cell integrity during real-time measurement is preserved, as shown in Figure S4. Cells after headspace analysis of 6 h showed the same viability (~95%) when compared to DCs kept in an incubator over the same time period. Another important point to highlight in terms of efficiency is the possibility of measuring multiple conditions (e.g., samples and controls) in one run, which reduces day-to-day variability and overall lead time of experiments.

Study II: Monitoring ^{13}C-Incorporation from Labeled Glucose into VOCs in Real-Time. After we have shown that the method is able to distinguish between different experimental conditions with high reproducibility, we sought to determine whether the technique is able to detect ^{13}C-incorporation into volatile metabolites in real-time over 4 h. Figure 3 illustrates the ^{13}C/^{12}C ratio time trace of the feature at m/z 75.04404 obtained for three biological replicates (DC1−3) exposed to Glc $^{13}C_6$ or standard glucose (Glc $^{12}C_6$), respectively. The feature shows incorporation of two ^{13}C with the highest ^{13}C/^{12}C ratio detected directly after glucose addition, followed by a decreasing ratio close to zero after ~2 h. As expected, ^{13}C/^{12}C ratios of samples containing DCs with Glc $^{12}C_6$ remained constant at natural abundance level. m/z 75.04404 was putatively assigned to the compound lactaldehyde which plays a role in pyruvate and carbohydrate metabolism, two core metabolic pathways. However, it must be mentioned that only one feature showed consistent ^{13}C-incorporation (according the criteria defined in the data analysis of study II), which may be explained by the fact that DCs initially rely on intrinsic glycogen stocks to sustain metabolic functions and that a certain time-span is required for intracellular metabolites to reach isotopic steady state, especially for nonreplicating cells with lower metabolic activity.[27,28] Study II shows a high reproducibility among conducted measurements using different biological replicates and demonstrates the feasibility to trace ^{13}C-incorporation into volatile metabolites emitted by DCs in real-time. Importantly, this technique can be expanded to beyond ^{13}C tracers and potentially accommodate simultaneous tracing of multiple substrates with different labels (e.g., deuterium and ^{13}C).

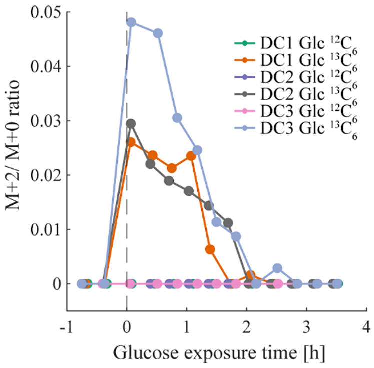

Figure 3. Real-time metabolic ^{13}C-incorporation in VOCs emitted by DCs. Real-time ^{13}C-incorporation for three DC cell batches exposed to Glc $^{13}C_6$ was observed for the feature at m/z 75.04404 (lactaldehyde) with MF $[C_3H_7O_2]^+$, whereas incorporation for DCs exposed to Glc $^{12}C_6$ remained at natural abundance. This was consistent for all biological replicates with 5 × 10^6 cells for DC1 and DC2 and 10^7 cells for DC3.

Study III: ^{13}C-Incorporation with and without Long-Time LPS Stimulation. Since the given method allows real-time monitoring of ^{13}C-incorporation into VOCs, we next assessed whether the technique detects different metabolic states of DCs. It has been shown previously that LPS simulation rewires DC metabolism within 24 h.[22] Therefore, DCs were exposed to Glc $^{13}C_6$ with and without LPS for 24 h. In addition, we also included control groups with DCs exposed to Glc $^{12}C_6$ to account for the natural abundance of ^{13}C (Figure 4, conditions G1, G2, and G3). We found 22 features (Table S3)/63 isotopologue pairs (Figures 4 and S5) showing significant incorporation ($p \leq 0.05$) of one up to several ^{13}C in

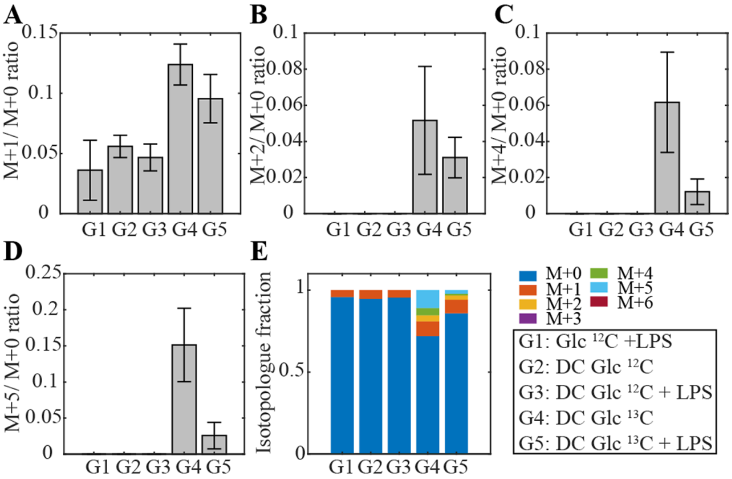

Figure 4. ^{13}C-incorporation illustrated for the example feature at *m/z* 181.07176 with MF $[C_6H_{13}O_6]^-$ detected in negative ionization mode after 24 h stimulation with LPS, shown for all five groups. (A) Incorporation of one, (B) two, (C) four, and (D) five ^{13}C was observed in DCs exposed to Glc $^{13}C_6$, whereas the incorporation was higher in naïve DCs (G4) than in activated DCs (G5). As expected ^{13}C-incorporation in G1, G2, and G3 remained at the natural abundance level. (E) Isotopologue distribution is shown for all groups. Error bars indicate standard deviation ($n = 4$).

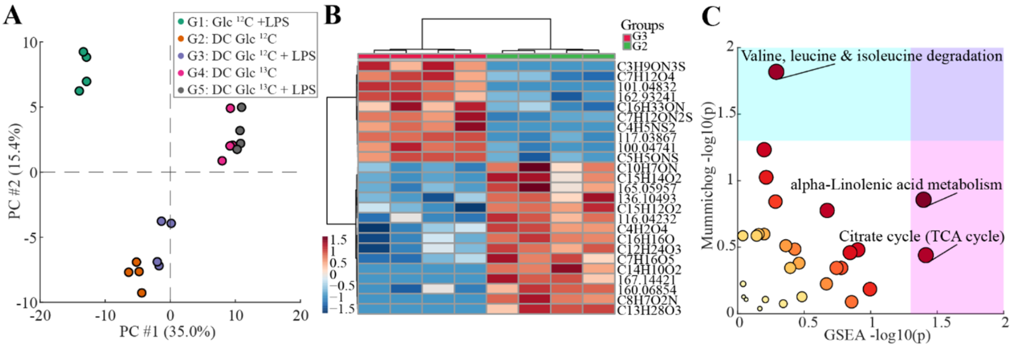

Figure 5. Differences between naïve and activated DCs by LPS stimulation. (A) PCA of significant features (raw $p \leq 0.05$) that are different between the five groups after ANOVA. (B) Heatmap showing the top 25 different features between G2 and G3. (C) Scatter plot for altered pathways between naïve (G2) and activated DCs (G3). Color and size of the circles correspond to the statistical significance of combined *p*-values from both algorithms.

G4 or G5 vs G1, G2, and G3. Figure 4 depicts an example of metabolic ^{13}C-incorporation for the negative ion at *m/z* 181.07176. Incorporation of one, two, four, and five ^{13}C was observed (Figure 4A–D). Moreover, the isotopologue distribution (Figure 4E) reflects the metabolic reprogramming of DCs upon LPS-stimulation (G5) compared to immature counterparts (G4). This is especially evident in the M + 4 and M + 5 isotopologue fraction of the two groups for the negative ion at *m/z* 181.07176 (Figure 4C,D). As expected, ratios for G1, G2, and G3 remained at a natural abundance level. *m/z* 181.07176 was putatively assigned to a sugar (e.g., sorbitol, galacticol) involved in fructose/mannose or galactose metabolism.

To get a global overview of the five groups, principal component analysis (PCA) was conducted. Figure S6 shows a PCA considering all features. A clear separation of G1 (without DCs) from the other groups and a slight clustering of the replicates according to group is visible. Analysis of variance (ANOVA) was then conducted and revealed 865 features significantly different (raw $p \leq 0.05$) between the five groups. Figure 5A depicts a PCA including the significant features and a clear distinction between all five groups is visible. Again, the separation of G1 from the other groups is evident. A separation of G2 and G3 from G4 and G5 is also visible, mainly driven by ^{13}C isotopes. As differences in the isotopologue distribution between naïve (G4) and activated (G5) DCs were visible, we then used G2 and G3 (naïve and activated DCs exposed to Glc $^{12}C_6$) for PCA visualization (Figure S7), which revealed a clear separation between the two groups. Furthermore, we ran a paired *t* test in order to identify features significantly different between the two groups. We found 9 features which were significantly different (fdr adj. $p \leq 0.05$) between G2 and G3. We then visualized the top 25 most relevant features in a heatmap (Figure 5B and Table S4). Afterward, we conducted a pathway enrichment analysis to see which pathways may be altered between the two groups. A total of 29 pathways were altered between naïve and activated DCs (Table S5). The top three pathways significantly altered ($p \leq 0.05$) in either mummichog or GSEA algorithm included: (i) α-linolenic acid metabolism, (ii) valine, leucine, and isoleucine degradation, and (iii) TCA cycle (Figure 5C). Rewiring of the TCA cycle, such as accumulation of TCA intermediate metabolites in activated DCs, has been previously reported.[22] A further altered pathway was the degradation of essential branched chain amino acids (BCAAs) valine, leucine, and isoleucine. Previous studies indicate that AA play an important role in regulating DC-function.[29] For example, enhanced uptake of valine, leucine, and isoleucine has been shown in monocyte-derived DCs upon LPS stimulation which fits well with our findings from the enrichment analysis.[30] Furthermore, depletion of BCAAs from the culture media led to an impaired maturation upon LPS stimulation.[31] α-Linolenic acid metabolism was another metabolic pathway altered between the two groups. α-Linolenic acid belongs to the group of omega (ω)-3 long-chain polyunsaturated fatty acids (LCPUFAs). Intracellular signaling pathways related to ω-3 LCPUFAs are largely unknown, however, a recent study has shown that ω-3 LCPUFAs, mediated via DCs *in vitro* and *in vivo*, suppressed T-cell proliferation, which suggests that inflammation mediated by T-cells is attenuated.[32] Taken together, study III exemplifies how this novel method in combination with labeled substrates can be used to gain enhanced insights into VOCs emitted from DCs and underlying metabolic pathways.

Certain limitations with regard to the technical setup need to be considered. This includes the nonautomatized switch of the valves between cell culture flasks (automation would make the data acquisition and measurement procedure more efficient). Moreover, evaporation of the cell culture medium might be observed during substantially long experimental runs, therefore, a sufficient amount of medium, along with constant humidification, must be ensured during the experimental runs. Furthermore, studies I and II were only performed in positive ionization mode, reducing the panel of features that could have been detected. Finally, the identity of the features presented needs to be confirmed, and the interpretation of their potential role in metabolic pathways needs to be further investigated. As the focus of this study was on the technical aspect, this was not within the scope of the current study.

■ CONCLUSION

The proposed mass spectrometric platform allows the monitoring of metabolic trajectories emitted by DCs in real-time. The setup poses an attractive complementary approach to standard metabolomics methods due to its short analysis time, sensitive detection, minimal sample preparation, and high efficiency in measuring multiple probes simultaneously. In combination with labeled substrates, the technique has the potential to provide new insights into metabolic pathways that play a key role in immunological responses triggered by different types of cells.

■ ASSOCIATED CONTENT

Supporting Information

The Supporting Information is available free of charge at https://pubs.acs.org/doi/10.1021/acs.analchem.3c00516.

Additional details on experiments, materials, methods, data analysis, including supplemental figures and tables (PDF)

■ AUTHOR INFORMATION

Corresponding Authors

Maria L. Balmer − *Department of Biomedicine, Immunobiology, University of Basel and University Hospital of Basel, 4031 Basel, Switzerland; Department of Biomedical Research (DBMR), University of Bern, 3008 Bern, Switzerland; University Clinic for Diabetes, Endocrinology, Clinical Nutrition and Metabolism, Inselspital, 3010 Bern, Switzerland; Diabetes Center Bern (DCB), 3010 Bern, Switzerland;* orcid.org/0000-0003-0356-6352; Email: maria.balmer@unibe.ch

Pablo Sinues − *University Children's Hospital Basel (UKBB), 4056 Basel, Switzerland; Department of Biomedical Engineering, University of Basel, 4123 Allschwil, Switzerland;* orcid.org/0000-0001-5602-2880; Email: pablo.sinues@unibas.ch

Authors

Kim Arnold − *University Children's Hospital Basel (UKBB), 4056 Basel, Switzerland; Department of Biomedical Engineering, University of Basel, 4123 Allschwil, Switzerland*

Philippe Dehio − *Department of Biomedicine, Immunobiology, University of Basel and University Hospital of Basel, 4031 Basel, Switzerland*

Jonas Lötscher − *Department of Biomedicine, Immunobiology, University of Basel and University Hospital of Basel, 4031 Basel, Switzerland*

Kapil Dev Singh − *University Children's Hospital Basel (UKBB), 4056 Basel, Switzerland; Department of Biomedical Engineering, University of Basel, 4123 Allschwil, Switzerland;* orcid.org/0000-0002-5682-0708

Diego García-Gómez − *Department of Analytical Chemistry, Nutrition and Food Science, University of Salamanca, 37008 Salamanca, Spain;* orcid.org/0000-0001-5753-2962

Christoph Hess − *Department of Biomedicine, Immunobiology, University of Basel and University Hospital of Basel, 4031 Basel, Switzerland; Department of Medicine, CITIID, Jeffrey Cheah Biomedical Centre, University of Cambridge, Cambridge CB2 0AW, United Kingdom*

Complete contact information is available at: https://pubs.acs.org/10.1021/acs.analchem.3c00516

Author Contributions

△These authors contributed equally.

Author Contributions

●These senior authors contributed equally.

Author Contributions

Conception and design: K.A., P.D., J.L., C.H., P.S., and M.L.B. Cell isolation and preparation: P.D. and J.L. SESI-HRMS experiments: K.A. LC-MS/MS experiments: D.G.G. Data analysis and interpretation: K.A., P.D., K.D.S., P.S., and M.L.B. Manuscript draft: K.A., P.D., P.S., and M.L.B. Writing, review and editing: K.A., P.D., J.L., K.D.S., D.G.G., C.H., P.S., and M.L.B. All authors read and approved the final manuscript.

Notes

The authors declare the following competing financial interest(s): P.S. is cofounder of Deep Breath Intelligence A.G. (Switzerland), which develops breath-based diagnostic tools. K.D.S. is a consultant for Deep Breath Intelligence A.G. (Switzerland).

■ ACKNOWLEDGMENTS

The authors thank Fiona Beck for critical reading of the manuscript. Parts of the graphical abstract were created with BioRender.com. This work was supported by a grant from the Fondation Botnar (Switzerland) and the Swiss National

Science Foundation No. PCEGP3_181300 to P.S. and PCEFP3_194618/1 to M.L.B.

■ REFERENCES

(1) Voss, K.; Hong, H. S.; Bader, J. E.; Sugiura, A.; Lyssiotis, C. A.; Rathmell, J. C. *Nat. Rev. Immunol* **2021**, *21* (10), 637−652.

(2) Boothby, M.; Rickert, R. C. *Immunity* **2017**, *46* (5), 743−755.

(3) Banchereau, J.; Briere, F.; Caux, C.; Davoust, J.; Lebecque, S.; Liu, Y. J.; Pulendran, B.; Palucka, K. *Annu. Rev. Immunol.* **2000**, *18*, 767−811.

(4) Verberk, S. G. S.; de Goede, K. E.; Gorki, F. S.; van Dierendonck, X.; Arguello, R. J.; Van den Bossche, J. *Cell Rep. Methods* **2022**, *2* (4), 100192.

(5) Pelgrom, L. R.; van der Ham, A. J.; Everts, B. *Toll-Like Receptors, 2 Edition* **2016**, *1390*, 273−285.

(6) Zeki, O. C.; Eylem, C. C.; Recber, T.; Kir, S.; Nemutlu, E. *J. Pharm. Biomed Anal* **2020**, *190*, 113509.

(7) Fang, M.; Ivanisevic, J.; Benton, H. P.; Johnson, C. H.; Patti, G. J.; Hoang, L. T.; Uritboonthai, W.; Kurczy, M. E.; Siuzdak, G. *Anal. Chem.* **2015**, *87* (21), 10935−41.

(8) Martinez-Lozano, P.; Rus, J.; Fernandez de la Mora, G.; Hernandez, M.; Fernandez de la Mora, J. *J. Am. Soc. Mass Spectrom.* **2009**, *20* (2), 287−94.

(9) Arnold, K.; Chen, X.; Zhang, H.; Singh, K. D.; Yin, Z.; Yao, Y.; Luan, T.; Sinues, P.; Li, X. *Journal of Bio-X Research* **2022**, *5* (2), 81−89.

(10) Gomez-Mejia, A.; Arnold, K.; Bar, J.; Singh, K. D.; Scheier, T. C.; Brugger, S. D.; Zinkernagel, A. S.; Sinues, P. *iScience* **2022**, *25* (10), 105080.

(11) Tejero Rioseras, A.; Garcia Gomez, D.; Ebert, B. E.; Blank, L. M.; Ibanez, A. J.; Sinues, P. M. *Sci. Rep* **2017**, *7* (1), 14236.

(12) Chang, C.-H.; Urban, P. L. *Analytical chemistry* **2018**, *90* (23), 13848−13854.

(13) Barrios-Collado, C.; Garcia-Gomez, D.; Zenobi, R.; Vidal-de-Miguel, G.; Ibanez, A. J.; Martinez-Lozano Sinues, P. *Anal. Chem.* **2016**, *88* (4), 2406−12.

(14) He, J.; Sinues, P. M.-L.; Hollmén, M.; Li, X.; Detmar, M.; Zenobi, R. *Sci. Rep.* **2014**, *4* (1), 1−6.

(15) Traxler, S.; Bischoff, A.-C.; Trefz, P.; Schubert, J. K.; Miekisch, W. *Journal of Breath Research* **2018**, *12* (4), No. 041001.

(16) Choueiry, F.; Zhu, J. *Anal. Chim. Acta* **2022**, *1189*, 339230.

(17) Zhu, J.; Bean, H. D.; Wargo, M. J.; Leclair, L. W.; Hill, J. E. *J. Breath Res.* **2013**, *7* (1), No. 016003.

(18) Gisler, A.; Singh, K. D.; Zeng, J.; Osswald, M.; Awchi, M.; Decrue, F.; Schmidt, F.; Sievi, N. A.; Chen, X.; Usemann, J. *iScience* **2022**, *25*, 105557.

(19) Keller, B. O.; Sui, J.; Young, A. B.; Whittal, R. M. *Anal. Chim. Acta* **2008**, *627* (1), 71−81.

(20) Schlosser, A.; Volkmer-Engert, R. *J. Mass Spectrom* **2003**, *38* (5), 523−5.

(21) Moller, S. H.; Wang, L.; Ho, P. C. *Cell Mol. Immunol.* **2022**, *19* (3), 370−383.

(22) Wculek, S. K.; Khouili, S. C.; Priego, E.; Heras-Murillo, I.; Sancho, D. *Front Immunol.* **2019**, *10*, 775.

(23) Liao, C.; Kim, U. J.; Kannan, K. *Environ. Sci. Technol.* **2018**, *52* (9), 5007−5026.

(24) Garcia-Gomez, D.; Bregy, L.; Nussbaumer-Ochsner, Y.; Gaisl, T.; Kohler, M.; Zenobi, R. *Environ. Sci. Technol.* **2015**, *49* (20), 12519−24.

(25) Gjorgjieva, M.; Tomasic, T.; Kikelj, D.; Masic, L. P. *Curr. Med. Chem.* **2019**, *25* (38), 5218−5236.

(26) Agilent. Seahorse XF Pro Analyzer, https://www.agilent.com/en/product/cell-analysis/real-time-cell-metabolic-analysis/xf-analyzers/seahorse-xf-pro-analyzer-1980223 (accessed 19 January, 2023).

(27) Antoniewicz, M. R. *Experimental & molecular medicine* **2018**, *50* (4), 1−13.

(28) Thwe, P. M.; Pelgrom, L. R.; Cooper, R.; Beauchamp, S.; Reisz, J. A.; D'Alessandro, A.; Everts, B.; Amiel, E. *Cell Metab* **2017**, *26* (3), 558−567.

(29) Brombacher, E. C.; Everts, B. *Front. Endocrinol. (Lausanne)* **2020**, *11*, 555.

(30) Kakazu, E.; Kondo, Y.; Kogure, T.; Ninomiya, M.; Kimura, O.; Ueno, Y.; Shimosegawa, T. *Sci. Rep.* **2013**, *3*, 3459.

(31) Kakazu, E.; Kanno, N.; Ueno, Y.; Shimosegawa, T. *J. Immunol* **2007**, *179* (10), 7137−46.

(32) Uchi, S. H.; Yanai, R.; Kobayashi, M.; Hatano, M.; Kobayashi, Y.; Yamashiro, C.; Nagai, T.; Tokuda, K.; Connor, K. M.; Sonoda, K. H.; Kimura, K. *PLoS One* **2019**, *14* (7), No. e0219405.

https://doi.org/10.1021/acs.analchem.3c00516
Anal. Chem. 2023, 95, 9415−9421

7. Conclusion and Future Perspectives

7.1 Relating Uropod Ultrastructure to Functional Amoeboid Migration

Cell migration holds a central role in the homeostasis of organisms and is implicated in the pathogenesis of various human diseases. Amoeboid cell migration is a conserved mode of cellular locomotion that requires cellular polarization and dynamic cytoskeleton activity for efficient movement. The relation between cell organellar positioning and associated pathways with amoeboid migration remains largely unexplored.

7.1.1 Organellar Positioning Spatially Targets Signaling to the Uropod

In *6.1 Section I* of the *Results* chapter, electron microscopy imaging studies demonstrate a substantial shift of cell organelles, including endo-lysosomes, towards the uropod of polarized, naive CD8$^+$ T cells. This contrasted with non-polarized T cells where endo-lysosomes were dispersed around the nucleus. The re-location of endo-lysosomes to the uropod effectively compartmentalized the activity of the VPS34–PIKfyve axis to this region, as evidenced by imaging PI(3)P in migrating T cells. The inhibition of VPS34 and PIKfyve reduced T cell velocity and myosin IIA activity, a critical promoter of retrograde actin flow and the force-generating mechanism of amoeboid cell migration.[31,37] We propose a mechanism where PI(3,5)P$_2$, the product of PIKfyve, promotes Ca^{2+} efflux from endo-lysosomes through TRPML1, subsequently activating myosin IIA in a Ca^{2+}-dependent manner and enhancing cell speed.

The re-location of endo-lysosomes mirrors mitochondrial dynamics during T cell polarization and migration. Mitochondria also re-locate to the uropod, a process facilitated by microtubules.[68] The precise mechanics behind the redistribution of endo-lysosomes during cell polarization, and how this effectively localizes the activity of the VPS34–PIKfyve pathway to the uropod, requires further study. Mechanistically, mitochondrial ATP synthesis is required for myosin IIA activity.[67] The underlying mitochondrial metabolism mediating this energy production remains elusive and will be revisited in *Conclusion and Future Perspectives 7.2.3*. However, endo-lysosomal signaling and mitochondrial ATP synthesis collaborate at the uropod to effectively activate myosin IIA.

From a more general perspective, organellar positioning at the uropod serves an active purpose in amoeboid cell migration by recruiting organelle-associated, distal signaling pathways to the uropod. With this example in mind, other organelle-specific signaling relays might contribute to amoeboid migration and could be revisited in future studies.

7.1.2 Receptor Recycling at the Uropod

Endocytosis at the uropod facilitates cell detachment, a process that necessitates the removal of integrins from the cell surface and relies on the function of myosin IIA.[92–94,301,302] Concurrently, endocytosis initiates the recycling of ligated chemokine receptors. The chemokine CCL19 undergoes receptor-mediated endocytosis via CCR7 and is subsequently directed to endo-lysosomes for degradation. CCR7 is repurposed and transported back to the plasma membrane.[95,96] Prior studies have indicated a role for VPS34 and PIKfyve in facilitating integrin recycling during mesenchymal cell migration.[194] However, the uptake of CCL19 was not found to be influenced by the inhibition of VPS34 or PIKfyve, suggesting that the endocytosis and recycling pathways of CCR7 might remain unaffected. To further delineate a potential role of VPS34 and PIKfyve in the recycling of chemokine receptors and integrins, additional studies are warranted.

From a broader perspective, some aspects of membrane protein recycling in amoeboid migrating cells remain elusive. While the localization of endocytosis is well documented, the exact spatial locations of exocytosis have not been clearly mapped. The fountain-flow hypothesis, delineated in the introduction (*4.1.7*), postulates that recycling endosomes are delivered to the leading edge, facilitating the replenishment of membranes, integrins, and chemokine receptors. Yet, our imaging studies have not identified endosomes or other specific vesicular structures in the leading edge of polarized T cells. This raises questions regarding this prevalent hypothesis, at least in naïve CD8$^+$ T cells. Further exploration pinpointing the exact localization of exocytosis would significantly enhance our comprehension of protein recycling routes that play a crucial role in amoeboid cell migration.

7.1.3 Integration of Endo-Lysosomes into the Uropod Ca^{2+} Homeostasis

We identified the synthesis of $PI(3,5)P_2$, thereby promoting Ca^{2+} efflux from endo-lysosomes through TRPML1 and myosin IIA activation as an effector mechanism of the VPS34–PIKfyve pathway. Our current findings demonstrate that TRPML1 agonism partly counteracts the reduced migration and rescues myosin IIA activity seen with VPS34 inhibition. In line, TRPML1 agonism also promotes myosin IIA activity in DCs.[103,104] A direction for future investigations entails a detailed dissection of TRPML1-dependent Ca^{2+} signaling and myosin IIA activity in the uropod of T cells. Further, Ca^{2+} efflux through TRPML1 could be spatiotemporally resolved with a genetically encoded calcium sensor fused to the cytoplasmic side of TRPML1.[222]

In general, the exact mechanisms governing the spatial and temporal dynamics of calcium fluctuations in migrating amoeboid cells, and their relationship with myosin IIA activation remain unexplored. Membrane contact sites (MCS) between the endoplasmic reticulum, endo-lysosomes, and mitochondria, with their respective calcium channels IP_3R, TRPML1, and VDAC1, have been implicated in calcium buffering.[80,104,218,223,227] A speculative proposition is that MCS might spatially control calcium concentrations and, consequently enabling localized activation of calcium-dependent signaling within the uropod. Hence, in parallel to the cooperation of endo-lysosomes and mitochondria in myosin IIA activity, there might be an intricate complex organelle network controlling Ca^{2+} levels and signaling at the uropod.

7.1.4 Possible Roles of TRPML1-Dependent Migration in the Pathogenesis of Mucolipidosis Type IV

Considering the demonstrated regulatory role of TRPML1 in cell migration, it is worth exploring possible implications for pathogenesis of human diseases. Specific mutations in TRPML1 have been pinpointed as causal drivers for Mucolipidosis type IV (MLIV). This rare autosomal recessive disorder is characterized by cognitive impairment, psychomotor delay, and ocular manifestation like retinopathy.[239] Brain development relies on precise migration of neurons during development and amoeboid-like cell migration is required for retinal development.[6,7,303] Exploring this hypothesis with MLIV mouse models, might provide insights into a potential contribution of altered cell migration contributing to neurological and ocular manifestations observed in MLIV patients.[304] Given the established role of TRPML1 in cell migration, a natural history study of MLIV patients focused on immune status in conjunction with *in vitro* migration assays, might unveil potential connections to immune dysregulation and altered immune responses in this patient population.

7.2 Metabolic Adaptations Underpinning Amoeboid Migration

Amoeboid cell migration is dependent on cellular metabolism. Two major energy demands of amoeboid cell propulsion are related to the actin polymerization and myosin IIA activation. Actin polymerization necessitates ATP, which is facilitated through glycolysis, while mitochondrial ATP production seemingly aids myosin IIA activation at the uropod. Even though chemokines have been observed to influence glycolysis and mitochondrial function in T cells and dendritic cells, the extent of metabolic reprogramming induced by chemokines has not yet been comprehensively explored.[109–111,113] In *6.2 Section II* of the results the focus was to examine potential effects of the chemokine CCL19 on the metabolism of murine naïve $CD8^+$ T cells. Our observations hint at a substantial engagement of cellular metabolism following chemokine exposure but warrant further validation and research to establish a connection to T cell migration. However, the TCA cycle and mitochondrial metabolism emerged as a promising venture point for further investigation.

7.2.1 Revisiting the Role of Mitochondria in Amoeboid Migrating Cells

The role of mitochondrial respiration in facilitating T cell migration interrogated previously, primarily through experiments utilizing ATP synthase inhibitors, mitochondrial decouplers, and optogenetic tools.[67,109] The TCA cycle, pivotal for fueling the ATP synthase, has not yet been conclusively linked to T cell migration. In this context, the role of mitochondrial carbon sources possibly sustaining chemokine-induced T cell migration remains unexplored. A future study could employ metabolic tracing of various ^{13}C-labelled mitochondrial carbon sources (e.g., glucose, glutamine, citrate, etc.) to pinpoint pathways fueling mitochondria in chemokine activated cells.[279]

Research has also begun to illustrate the nuanced impacts of mitochondrial respiration in specific disease states and T cell subsets. $CD4^+$ T cells derived from individuals with rheumatoid arthritis demonstrate a reduction in mitochondrial respiration. This, in turn, results in an augmented concentration of acetyl-CoA, which facilitates T cell uropod formation by stabilizing microtubules through acetylation.[305] Furthermore, different dependencies on mitochondrial ATP synthesis are seen in naïve and memory $CD4^+$ T cells with regards to both spontaneous or CXCL12-dependent migration. While naïve $CD4^+$ T cell migration is impaired by ATP synthase inhibition, the migration capabilities of memory $CD4^+$ T cells remain unaffected.[108] This suggests that mitochondrial ATP production is not an unequivocal requirement for amoeboid migration. Moreover, the role of acetyl-CoA in promoting uropod formation hints at a broader involvement of cellular metabolism in T cell migration, extending beyond energy production.

The role of mitochondrial metabolism in amoeboid cell migration remains elusive and possibly extends beyond mere energy production. Detailed investigations into mitochondrial carbon sources, mitochondrial function and cell migration in different cell types encompasses an avenue for forthcoming studies.

7.2.2 Cellular Polarization and Compartmentalized Energy Production

Looking at the broader perspective, an existing paradigm proposes a compartmentalized energy production during amoeboid cell migration, with glycolysis occurring at the sites of actin polymerization and mitochondrial metabolism facilitating myosin IIA activity at the uropod.[116] In an analogous manner to the cell organelles and their signaling in polarized T cells (interrogated in *6.1 Section I* of the *Results*), metabolic pathways for ATP synthesis would be spatially distributed within polarized cells. Glycolytic enzymes have indeed been associated with actin, yet, the exact relationship between the glycolytic machinery and the regulation of actin dynamics, remains unexplored.[111,114] A way forward could entail imaging studies that map the distribution of glycolytic enzymes in polarized T cells or monitoring actin dynamics in tandem with biosensors for glycolysis.[284] Glycolysis is a carbon source for mitochondrial metabolism.[279] If, there is a not solely a spatial but also a metabolic separation between glycolysis-driven actin polymerization and mitochondrial-driven myosin IIA activity could be revealed by tracing studies suggested in the preceding paragraph *7.2.1*.

Arguably, the paradigm of compartmentalized energy production in amoeboid cell migration presents an intriguing hypothesis entailing local energy for actomyosin dynamics by spatially separated metabolic pathways. However, this paradigm requires detailed validation across various cellular systems, especially considering various dependencies on mitochondrial function across T cell subsets and their migration.

7.2.3 The Metabolite Acetate Modulates Memory CD8$^+$ T Cell Migration

Cellular metabolism fundamentally underpins T cell functions, beyond migration. During the initial stages of bacterial infections, systemic acetate levels have been found to optimize the functions of memory CD8$^+$ T cells, thereby aiding in bacterial clearance.[280] The published manuscript in *6.3 Section III*, further delineates how acetate metabolism is rewired in memory CD8$^+$ T cells during the later stages of bacterial infections to curb their heightened inflammatory and promote cell survival.

We also noted that acetate exposure inhibited the migration of memory CD8$^+$ T cells *in vitro*. Together with observations of increased cell numbers upon local acetate administration, this suggests a trapping mechanism of memory CD8$^+$ T cells at sites of inflammation. However, the detailed molecular mechanism mediating this effect has not been delineated. A plausible explanation for the reduced T cell migration could be the acetate-induced decline in free Ca^{2+} concentrations. Central to this hypothesis is the role of Ca^{2+}-calmodulin-MLCK-dependent myosin IIA activation, similar to the proposed mechanism in the preprint of *6.1 Section I* of the results. To test this hypothesis, future studies could assess and alter myosin IIA activity by monitoring RLC phosphorylation levels in the presence and absence of acetate.

In conclusion, acetate emerges as a significant modulator of memory CD8$^+$ T cell functions during bacterial infections. This includes dampening the migration of memory CD8$^+$ T cells and future studies could investigate the underlying mechanism of this observation.

7.2.4 Probing the Volatile Phase by Mass Spectroscopy as a Complementary Tool for Metabolic Interrogations

The results in *6.3 Section III* of the results exemplify how the acetate impacts cellular metabolism and function of memory CD8$^+$ T cells.[280,306] Moreover, in *6.2 Section II*, chemokine-stimulation was demonstrated to alter the metabolism of naïve CD8$^+$ T cells within minutes by extracellular flux analysis. However, interrogation of cellular metabolism, especially in an unbiased and real-time manner remains challenging.[307] In the published manuscript in *6.4 Section IV*, we introduce a novel technique proficient at detecting cellular metabolism of DCs in within the cell culture headspace.[308] This platform distinguishes different metabolic states in DCs. Further, it enables the tracing of isotopic metabolites, thereby offering robust real-time monitoring of non-disturbed cell cultures without the necessity for sample preparation.

Despite these advances, there is a need for further development to fully leverage this platform as a potential discovery platform. A significant hurdle remains the assignment of the molecular entities corresponding to the detected masses, which is a prerequisite for in-depth biological interpretation. While the current configuration may yield molecular formulas, the molecular identities of detected VOCs frequently remain elusive without supplementary analyses. In our study, we confirmed the molecular identity of a specific mass using a LC-MS/MS analysis. Hence, a prospective experimental workflow might encompass an initial phase of exploration using the real-time volatile metabolomics approach, followed by the validation of potential candidate masses via established LC-MS/MS techniques. This workflow feasibly extends to metabolic studies in of other cell types. For instance, it might be able to complement insight into the dynamics of chemokine-induced metabolism of T cell explored in *6.2. Section II*.

In conclusion, this novel platform holds the potential to complement standard approaches in cellular metabolism studies by analyzing the volatile phase of cell cultures in unbiased manner and in real-time. In concert with standard metabolic interrogations, this approach might contribute to a more comprehensive understanding of cellular metabolism and its dynamics.

8. References

1. Rossine, F. W., Vercelli, G. T., Tarnita, C. E. & Gregor, T. Structured foraging of soil predators unveils functional responses to bacterial defenses. *Proc. Natl. Acad. Sci.* **119**, e2210995119 (2022).
2. Dormann, D., Vasiev, B. & Weijer, C. J. Becoming Multicellular by Aggregation; The Morphogenesis of the Social Amoebae Dicyostelium discoideum. *J. Biol. Phys.* **28**, 765–780 (2002).
3. Brunet, T. *et al.* A flagellate-to-amoeboid switch in the closest living relatives of animals. *eLife* **10**, e61037 (2021).
4. Tran, P. B. & Miller, R. J. Chemokine receptors: signposts to brain development and disease. *Nat. Rev. Neurosci.* **4**, 444–455 (2003).
5. Mayya, C., Kharbhanda, S., Haque, A. & Bhatia, D. Mechanisms of Collective Cell Migration in Wound Healing: Physiology and Disease. in *Wound Healing Research: Current Trends and Future Directions* (eds. Kumar, P. & Kothari, V.) 55–74 (Springer, 2021). doi:10.1007/978-981-16-2677-7_2.
6. Nadarajah, B. & Parnavelas, J. G. Modes of neuronal migration in the developing cerebral cortex. *Nat. Rev. Neurosci.* **3**, 423–432 (2002).
7. Ayala, R., Shu, T. & Tsai, L.-H. Trekking across the Brain: The Journey of Neuronal Migration. *Cell* **128**, 29–43 (2007).
8. Rognoni, E. *et al.* Fibroblast state switching orchestrates dermal maturation and wound healing. *Mol. Syst. Biol.* **14**, e8174 (2018).
9. Stein, J. V. T Cell Motility as Modulator of Interactions with Dendritic Cells. *Front. Immunol.* **6**, (2015).
10. Harris, T. H. *et al.* Generalized Lévy walks and the role of chemokines in migration of effector CD8+ T cells. *Nature* **486**, 545–548 (2012).
11. Zhang, Q. *et al.* DOCK8 regulates lymphocyte shape integrity for skin antiviral immunity. *J. Exp. Med.* **211**, 2549–2566 (2014).
12. Biggs, C. M., Keles, S. & Chatila, T. A. DOCK8 deficiency: Insights into pathophysiology, clinical features and management. *Clin. Immunol.* **181**, 75–82 (2017).
13. van Langelaar, J., Rijvers, L., Smolders, J. & van Luijn, M. M. B and T Cells Driving Multiple Sclerosis: Identity, Mechanisms and Potential Triggers. *Front. Immunol.* **11**, (2020).
14. Elfeky, M., Kamimura, D., Arima, Y., Murakami, M. & Steinman, L. Targeting molecules involved in immune cell trafficking to the central nervous system for therapy in multiple sclerosis. *Clin. Exp. Neuroimmunol.* **8**, 183–191 (2017).
15. Raudenská, M. *et al.* Engine shutdown: migrastatic strategies and prevention of metastases. *Trends Cancer* **9**, 293–308 (2023).
16. Gardel, M. L., Schneider, I. C., Aratyn-Schaus, Y. & Waterman, C. M. Mechanical Integration of Actin and Adhesion Dynamics in Cell Migration. *Annu. Rev. Cell Dev. Biol.* **26**, 315–333 (2010).
17. Lämmermann, T. & Sixt, M. Mechanical modes of 'amoeboid' cell migration. *Curr. Opin. Cell Biol.* **21**, 636–644 (2009).
18. Hind, L. E., Vincent, W. J. B. & Huttenlocher, A. Leading from the Back: The Role of the Uropod in Neutrophil Polarization and Migration. *Dev. Cell* **38**, 161–169 (2016).
19. Welch, M. D. Cell Migration, Freshly Squeezed. *Cell* **160**, 581–582 (2015).
20. Yoshida, K. & Soldati, T. Dissection of amoeboid movement into two mechanically distinct modes. *J. Cell Sci.* **119**, 3833–3844 (2006).
21. Tyson, R. A., Zatulovskiy, E., Kay, R. R. & Bretschneider, T. How blebs and pseudopods cooperate during chemotaxis. *Proc. Natl. Acad. Sci.* **111**, 11703–11708 (2014).
22. Lämmermann, T. *et al.* Rapid leukocyte migration by integrin-independent flowing and squeezing. *Nature* **453**, 51–55 (2008).
23. Liu, Y.-J. *et al.* Confinement and Low Adhesion Induce Fast Amoeboid Migration of Slow Mesenchymal Cells. *Cell* **160**, 659–672 (2015).
24. Ruprecht, V. *et al.* Cortical Contractility Triggers a Stochastic Switch to Fast Amoeboid Cell Motility. *Cell* **160**, 673–685 (2015).
25. Sahai, E. & Marshall, C. J. Differing modes of tumour cell invasion have distinct requirements for Rho/ROCK signalling and extracellular proteolysis. *Nat. Cell Biol.* **5**, 711–719 (2003).
26. Barry, N. P. & Bretscher, M. S. Dictyostelium amoebae and neutrophils can swim. *Proc. Natl. Acad. Sci.* **107**, 11376–11380 (2010).
27. Aoun, L. *et al.* Amoeboid Swimming Is Propelled by Molecular Paddling in Lymphocytes. *Biophys. J.* **119**, 1157–1177 (2020).

28. Stroka, K. M. *et al.* Water Permeation Drives Tumor Cell Migration in Confined Microenvironments. *Cell* **157**, 611–623 (2014).
29. Hui, T. H. *et al.* An electro-osmotic microfluidic system to characterize cancer cell migration under confinement. *J. R. Soc. Interface* **16**, 20190062 (2019).
30. Gilpin, W., Bull, M. S. & Prakash, M. The multiscale physics of cilia and flagella. *Nat. Rev. Phys.* **2**, 74–88 (2020).
31. Renkawitz, J. *et al.* Adaptive force transmission in amoeboid cell migration. *Nat. Cell Biol.* **11**, 1438–1443 (2009).
32. Goor, D. V., Hyland, C., Schaefer, A. W. & Forscher, P. The Role of Actin Turnover in Retrograde Actin Network Flow in Neuronal Growth Cones. *PLOS ONE* **7**, e30959 (2012).
33. Tsai, T. Y.-C. *et al.* Efficient Front-Rear Coupling in Neutrophil Chemotaxis by Dynamic Myosin II Localization. *Dev. Cell* **49**, 189-205.e6 (2019).
34. Lin, C. H., Espreafico, E. M., Mooseker, M. S. & Forscher, P. Myosin Drives Retrograde F-Actin Flow in Neuronal Growth Cones. *Neuron* **16**, 769–782 (1996).
35. Barnhart, E. L., Lee, K.-C., Keren, K., Mogilner, A. & Theriot, J. A. An Adhesion-Dependent Switch between Mechanisms That Determine Motile Cell Shape. *PLOS Biol.* **9**, e1001059 (2011).
36. Belotti, Y., McGloin, D. & Weijer, C. J. Analysis of barotactic and chemotactic guidance cues on directional decision-making of Dictyostelium discoideum cells in confined environments. *Proc. Natl. Acad. Sci.* **117**, 25553–25559 (2020).
37. Hons, M. *et al.* Chemokines and integrins independently tune actin flow and substrate friction during intranodal migration of T cells. *Nat. Immunol.* **19**, 606–616 (2018).
38. Reversat, A. *et al.* Cellular locomotion using environmental topography. *Nature* **582**, 582–585 (2020).
39. Pinot, M. *et al.* Confinement induces actin flow in a meiotic cytoplasm. *Proc. Natl. Acad. Sci.* **109**, 11705–11710 (2012).
40. Yam, P. T. *et al.* Actin–myosin network reorganization breaks symmetry at the cell rear to spontaneously initiate polarized cell motility. *J. Cell Biol.* **178**, 1207–1221 (2007).
41. Jacobelli, J., Chmura, S. A., Buxton, D. B., Davis, M. M. & Krummel, M. F. A single class II myosin modulates T cell motility and stopping, but not synapse formation. *Nat. Immunol.* **5**, 531–538 (2004).
42. Hughes, C. E. & Nibbs, R. J. B. A guide to chemokines and their receptors. *Febs J.* **285**, 2944–2971 (2018).
43. Kimura, K. *et al.* Regulation of Myosin Phosphatase by Rho and Rho-Associated Kinase (Rho-Kinase). *Science* **273**, 245–248 (1996).
44. Lamarche, N. *et al.* Rac and Cdc42 Induce Actin Polymerization and G1 Cell Cycle Progression Independently of p65PAK and the JNK/SAPK MAP Kinase Cascade. *Cell* **87**, 519–529 (1996).
45. Vargas, P. *et al.* Innate control of actin nucleation determines two distinct migration behaviours in dendritic cells. *Nat. Cell Biol.* **18**, 43–53 (2016).
46. Wong, K., Pertz, O., Hahn, K. & Bourne, H. Neutrophil polarization: Spatiotemporal dynamics of RhoA activity support a self-organizing mechanism. *Proc. Natl. Acad. Sci.* **103**, 3639–3644 (2006).
47. Gérard, A., Mertens, A. E. E., van der Kammen, R. A. & Collard, J. G. The Par polarity complex regulates Rap1- and chemokine-induced T cell polarization. *J. Cell Biol.* **176**, 863–875 (2007).
48. Niederman, R. & Pollard, T. D. Human platelet myosin. II. In vitro assembly and structure of myosin filaments. *J. Cell Biol.* **67**, 72–92 (1975).
49. Svitkina, T. M., Verkhovsky, A. B. & Borisy, G. G. Improved Procedures for Electron Microscopic Visualization of the Cytoskeleton of Cultured Cells. *J. Struct. Biol.* **115**, 290–303 (1995).
50. Brito, C. & Sousa, S. Non-Muscle Myosin 2A (NM2A): Structure, Regulation and Function. *Cells* **9**, 1590 (2020).
51. Scholey, J. M., Taylor, K. A. & Kendrick-Jones, J. Regulation of non-muscle myosin assembly by calmodulin-dependent light chain kinase. *Nature* **287**, 233–235 (1980).
52. Matsumura, F. Regulation of myosin II during cytokinesis in higher eukaryotes. *Trends Cell Biol.* **15**, 371–377 (2005).
53. Sellers, J. R., Pato, M. D. & Adelstein, R. S. Reversible phosphorylation of smooth muscle myosin, heavy meromyosin, and platelet myosin. *J. Biol. Chem.* **256**, 13137–13142 (1981).
54. Ikebe, M., Hartshorne, D. J. & Elzinga, M. Identification, phosphorylation, and dephosphorylation of a second site for myosin light chain kinase on the 20,000-dalton light chain of smooth muscle myosin. *J. Biol. Chem.* **261**, 36–39 (1986).

55. Griffith, L. M., Downs, S. M. & Spudich, J. A. Myosin light chain kinase and myosin light chain phosphatase from Dictyostelium: effects of reversible phosphorylation on myosin structure and function. *J. Cell Biol.* **104**, 1309–1323 (1987).
56. Taylor, D. A. & Stull, J. T. Calcium dependence of myosin light chain phosphorylation in smooth muscle cells. *J. Biol. Chem.* **263**, 14456–14462 (1988).
57. Lukas, T. J., Burgess, W. H., Prendergast, F. G., Lau, W. & Watterson, D. M. Calmodulin binding domains: characterization of a phosphorylation and calmodulin binding site from myosin light chain kinase. *Biochemistry* **25**, 1458–1464 (1986).
58. Bhadriraju, K. *et al.* Activation of ROCK by RhoA is regulated by cell adhesion, shape, and cytoskeletal tension. *Exp. Cell Res.* **313**, 3616–3623 (2007).
59. Ishizaki, T. *et al.* Pharmacological Properties of Y-27632, a Specific Inhibitor of Rho-Associated Kinases.
60. Chang, Y.-C., Nalbant, P., Birkenfeld, J., Chang, Z.-F. & Bokoch, G. M. GEF-H1 Couples Nocodazole-induced Microtubule Disassembly to Cell Contractility via RhoA. *Mol. Biol. Cell* **19**, 2147–2153 (2008).
61. Kolodney, M. S. & Elson, E. L. Contraction due to microtubule disruption is associated with increased phosphorylation of myosin regulatory light chain. *Proc. Natl. Acad. Sci.* **92**, 10252–10256 (1995).
62. Liu, B. P., Chrzanowska-Wodnicka, M. & Burridge, K. Microtubule Depolymerization Induces Stress Fibers, Focal Adhesions, and DNA Synthesis via the GTP-Binding Protein Rho. *Cell Adhes. Commun.* **5**, 249–255 (1998).
63. Kopf, A. *et al.* Microtubules control cellular shape and coherence in amoeboid migrating cells. *J. Cell Biol.* **219**, e201907154 (2020).
64. Kovács, M., Tóth, J., Hetényi, C., Málnási-Csizmadia, A. & Sellers, J. R. Mechanism of Blebbistatin Inhibition of Myosin II*. *J. Biol. Chem.* **279**, 35557–35563 (2004).
65. Martinelli, S. *et al.* Ezrin/Radixin/Moesin Proteins and Flotillins Cooperate to Promote Uropod Formation in T Cells. *Front. Immunol.* **4**, (2013).
66. Faroudi, M. *et al.* Critical roles for Rac GTPases in T-cell migration to and within lymph nodes. *Blood* **116**, 5536–5547 (2010).
67. Campello, S. *et al.* Orchestration of lymphocyte chemotaxis by mitochondrial dynamics. *J. Exp. Med.* **203**, 2879–2886 (2006).
68. Morlino, G. *et al.* Miro-1 Links Mitochondria and Microtubule Dynein Motors To Control Lymphocyte Migration and Polarity. *Mol. Cell. Biol.* **34**, 1412–1426 (2014).
69. Yoo, S. K. *et al.* The role of microtubules in neutrophil polarity and migration in live zebrafish. *J. Cell Sci.* **125**, 5702–5710 (2012).
70. Xu, J., Wang, F., Van Keymeulen, A., Rentel, M. & Bourne, H. R. Neutrophil microtubules suppress polarity and enhance directional migration. *Proc. Natl. Acad. Sci.* **102**, 6884–6889 (2005).
71. Gudima, G. O., Vorobjev, I. A. & Chentsov, Y. S. Centriolar location during blood cell spreading and motion in vitro: An ultrastructural analysis. *J. Cell Sci.* **89**, 225–241 (1988).
72. Ishikawa-Ankerhold, H., Kroll, J., Heuvel, D. van den, Renkawitz, J. & Müller-Taubenberger, A. Centrosome Positioning in Migrating Dictyostelium Cells. *Cells* **11**, 1776 (2022).
73. Laufer, J. M. *et al.* Chemokine Receptor CCR7 Triggers an Endomembrane Signaling Complex for Spatial Rac Activation. *Cell Rep.* **29**, 995-1009.e6 (2019).
74. Mastrogiovanni, M., Juzans, M., Alcover, A. & Di Bartolo, V. Coordinating Cytoskeleton and Molecular Traffic in T Cell Migration, Activation, and Effector Functions. *Front. Cell Dev. Biol.* **8**, (2020).
75. Luxton, G. G. & Gundersen, G. G. Orientation and function of the nuclear–centrosomal axis during cell migration. *Curr. Opin. Cell Biol.* **23**, 579–588 (2011).
76. Kupfer, A., Louvard, D. & Singer, S. J. Polarization of the Golgi Apparatus and the Microtubule-Organizing Center in Cultured Fibroblasts at the Edge of an Experimental Wound. *Proc. Natl. Acad. Sci. U. S. A.* **79**, 2603–2607 (1982).
77. Oppelt, A. *et al.* PIKfyve, MTMR3 and their product PtdIns5P regulate cancer cell migration and invasion through activation of Rac1. *Biochem. J.* **461**, 383–390 (2014).
78. Buss, F. *et al.* The Localization of Myosin VI at the Golgi Complex and Leading Edge of Fibroblasts and Its Phosphorylation and Recruitment into Membrane Ruffles of A431 Cells after Growth Factor Stimulation. *J. Cell Biol.* **143**, 1535–1545 (1998).
79. Ravichandran, Y., Goud, B. & Manneville, J.-B. The Golgi apparatus and cell polarity: Roles of the cytoskeleton, the Golgi matrix, and Golgi membranes. *Curr. Opin. Cell Biol.* **62**, 104–113 (2020).

80. Solanes, P. *et al.* Space exploration by dendritic cells requires maintenance of myosin II activity by IP3 receptor 1. *EMBO J.* **34**, 798–810 (2015).
81. Renkawitz, J. *et al.* Nuclear positioning facilitates amoeboid migration along the path of least resistance. *Nature* **568**, 546–550 (2019).
82. Thottacherry, J. J., Sathe, M., Prabhakara, C. & Mayor, S. Spoiled for Choice: Diverse Endocytic Pathways Function at the Cell Surface. *Annu. Rev. Cell Dev. Biol.* **35**, 55–84 (2019).
83. Maxfield, F. R. & Yamashiro, D. J. Endosome Acidification and the Pathways of Receptor-Mediated Endocytosis. in *Immunobiology of Proteins and Peptides IV: T-Cell Recognition and Antigen Presentation* (ed. Atassi, M. Z.) 189–198 (Springer US, 1987). doi:10.1007/978-1-4684-5442-0_16.
84. Rink, J., Ghigo, E., Kalaidzidis, Y. & Zerial, M. Rab Conversion as a Mechanism of Progression from Early to Late Endosomes. *Cell* **122**, 735–749 (2005).
85. Huotari, J. & Helenius, A. Endosome maturation. *EMBO J.* **30**, 3481–3500 (2011).
86. Runquist, E. A. & Havel, R. J. Acid hydrolases in early and late endosome fractions from rat liver. *J. Biol. Chem.* **266**, 22557–22563 (1991).
87. Bonifacino, J. S. & Hurley, J. H. Retromer. *Curr. Opin. Cell Biol.* **20**, 427–436 (2008).
88. Pfeffer, S. R. Multiple routes of protein transport from endosomes to the trans Golgi network. *FEBS Lett.* **583**, 3811–3816 (2009).
89. Damer, C. K. & O’Halloran, T. J. Spatially Regulated Recruitment of Clathrin to the Plasma Membrane during Capping and Cell Translocation. *Mol. Biol. Cell* **11**, 2151–2159 (2000).
90. Stanley, P., Tooze, S. & Hogg, N. A role for Rap2 in recycling the extended conformation of LFA-1 during T cell migration. *Biol. Open* **1**, 1161–1168 (2012).
91. Chandrasekar, I. *et al.* Nonmuscle Myosin II Is a Critical Regulator of Clathrin-Mediated Endocytosis. *Traffic* **15**, 418–432 (2014).
92. Lawson, M. A. & Maxfield, F. R. Ca2+- and calcineurin-dependent recycling of an integrin to the front of migrating neutrophils. *Nature* **377**, 75–79 (1995).
93. Pierini, L. M., Lawson, M. A., Eddy, R. J., Hendey, B. & Maxfield, F. R. Oriented endocytic recycling of α5β1 in motile neutrophils. *Blood* **95**, 2471–2480 (2000).
94. Subramanian, B. C., Moissoglu, K. & Parent, C. A. The LTB4–BLT1 axis regulates the polarized trafficking of chemoattractant GPCRs during neutrophil chemotaxis. *J. Cell Sci.* **131**, jcs217422 (2018).
95. Otero, C., Groettrup, M. & Legler, D. F. Opposite Fate of Endocytosed CCR7 and Its Ligands: Recycling versus Degradation1. *J. Immunol.* **177**, 2314–2323 (2006).
96. Alanko, J. *et al.* CCR7 acts as both a sensor and a sink for CCL19 to coordinate collective leukocyte migration. *Sci. Immunol.* **8**, eadc9584 (2023).
97. Levayer, R., Pelissier-Monier, A. & Lecuit, T. Spatial regulation of Dia and Myosin-II by RhoGEF2 controls initiation of E-cadherin endocytosis during epithelial morphogenesis. *Nat. Cell Biol.* **13**, 529–540 (2011).
98. Wayt, J., Cartagena-Rivera, A., Dutta, D., Donaldson, J. G. & Waterman, C. M. Myosin II isoforms promote internalization of spatially distinct clathrin-independent endocytosis cargoes through modulation of cortical tension downstream of ROCK2. *Mol. Biol. Cell* **32**, 226–236 (2021).
99. O’Neill, P. R. *et al.* Membrane Flow Drives an Adhesion-Independent Amoeboid Cell Migration Mode. *Dev. Cell* **46**, 9-22.e4 (2018).
100. Tanaka, M. *et al.* Turnover and flow of the cell membrane for cell migration. *Sci. Rep.* **7**, 12970 (2017).
101. Lachuer, H., Le, L., Lévêque-Fort, S., Goud, B. & Schauer, K. Spatial organization of lysosomal exocytosis relies on membrane tension gradients. *Proc. Natl. Acad. Sci.* **120**, e2207425120 (2023).
102. Campisi, D. *et al.* The core autophagy protein ATG9A controls dynamics of cell protrusions and directed migration. *J. Cell Biol.* **221**, e202106014 (2022).
103. Bretou, M. *et al.* Lysosome signaling controls the migration of dendritic cells. *Sci. Immunol.* **2**, eaak9573 (2017).
104. Vestre, K. *et al.* Rab7b regulates dendritic cell migration by linking lysosomes to the actomyosin cytoskeleton. *J. Cell Sci.* **134**, jcs259221 (2021).
105. Nakatani, T. *et al.* The lysosomal Ragulator complex plays an essential role in leukocyte trafficking by activating myosin II. *Nat. Commun.* **12**, 1–15 (2021).
106. Ferreira, L. M. R. *et al.* Intermediary metabolism: An intricate network at the crossroads of cell fate and function. *Biochim. Biophys. Acta BBA - Mol. Basis Dis.* **1866**, 165887 (2020).

107. Simula, L. *et al.* Drp1 Controls Effective T Cell Immune-Surveillance by Regulating T Cell Migration, Proliferation, and cMyc-Dependent Metabolic Reprogramming. *Cell Rep.* **25**, 3059-3073.e10 (2018).
108. Dimeloe, S. *et al.* The Immune-Metabolic Basis of Effector Memory CD4+ T Cell Function under Hypoxic Conditions. *J. Immunol.* **196**, 106–114 (2016).
109. Amitrano, A. M. *et al.* Optical Control of CD8+ T Cell Metabolism and Effector Functions. *Front. Immunol.* **12**, (2021).
110. Haas, R. *et al.* Lactate Regulates Metabolic and Pro-inflammatory Circuits in Control of T Cell Migration and Effector Functions. *PLOS Biol.* **13**, e1002202 (2015).
111. Kishore, M. *et al.* Regulatory T Cell Migration Is Dependent on Glucokinase-Mediated Glycolysis. *Immunity* **47**, 875-889.e10 (2017).
112. Guak, H. *et al.* Glycolytic metabolism is essential for CCR7 oligomerization and dendritic cell migration. *Nat. Commun.* **9**, 2463 (2018).
113. Liu, J. *et al.* CCR7 Chemokine Receptor-Inducible lnc-Dpf3 Restrains Dendritic Cell Migration by Inhibiting HIF-1α-Mediated Glycolysis. *Immunity* **50**, 600-615.e15 (2019).
114. Masters, C. Interactions between glycolytic enzymes and components of the cytomatrix. *J. Cell Biol.* **99**, 222s–225s (1984).
115. Hauser, M. A. *et al.* Inflammation-Induced CCR7 Oligomers Form Scaffolds to Integrate Distinct Signaling Pathways for Efficient Cell Migration. *Immunity* **44**, 59–72 (2016).
116. Guak, H. & Krawczyk, Connie. M. Implications of cellular metabolism for immune cell migration. *Immunology* **161**, 200–208 (2020).
117. Payrastre, B. *et al.* Phosphoinositides : key players in cell signalling, in time and space. *Cell. Signal.* **13**, 377–387 (2001).
118. De Craene, J.-O., Bertazzi, D. L., Bär, S. & Friant, S. Phosphoinositides, Major Actors in Membrane Trafficking and Lipid Signaling Pathways. *Int. J. Mol. Sci.* **18**, 634 (2017).
119. Bochud, A. & Conzelmann, A. The active site of yeast phosphatidylinositol synthase Pis1 is facing the cytosol. *Biochim. Biophys. Acta BBA - Mol. Cell Biol. Lipids* **1851**, 629–640 (2015).
120. Tu-Sekine, B. & Kim, S. F. The Inositol Phosphate System—A Coordinator of Metabolic Adaptability. *Int. J. Mol. Sci.* **23**, 6747 (2022).
121. Balla, T. Phosphoinositides: Tiny Lipids With Giant Impact on Cell Regulation. *Physiol. Rev.* **93**, 1019–1137 (2013).
122. Zewe, J. P. *et al.* Probing the subcellular distribution of phosphatidylinositol reveals a surprising lack at the plasma membrane. *J. Cell Biol.* **219**, (2020).
123. Ohashi, Y., Tremel, S. & Williams, R. L. VPS34 complexes from a structural perspective. *J. Lipid Res.* **60**, 229–241 (2019).
124. Nascimbeni, A. C. *et al.* ER–plasma membrane contact sites contribute to autophagosome biogenesis by regulation of local PI3P synthesis. *EMBO J.* **36**, 2018–2033 (2017).
125. Axe, E. L. *et al.* Autophagosome formation from membrane compartments enriched in phosphatidylinositol 3-phosphate and dynamically connected to the endoplasmic reticulum. *J. Cell Biol.* **182**, 685–701 (2008).
126. Lees, J. A., Li, P., Kumar, N., Weisman, L. S. & Reinisch, K. M. Insights into Lysosomal PI(3,5)P2 Homeostasis from a Structural-Biochemical Analysis of the PIKfyve Lipid Kinase Complex. *Mol. Cell* **80**, 736-743.e4 (2020).
127. Zolov, S. N. *et al.* In vivo, Pikfyve generates PI(3,5)P2, which serves as both a signaling lipid and the major precursor for PI5P. *Proc. Natl. Acad. Sci.* **109**, 17472–17477 (2012).
128. Tronchère, H. *et al.* Production of Phosphatidylinositol 5-Phosphate by the Phosphoinositide 3-Phosphatase Myotubularin in Mammalian Cells *. *J. Biol. Chem.* **279**, 7304–7312 (2004).
129. Kim, S.-A., Taylor, G. S., Torgersen, K. M. & Dixon, J. E. Myotubularin and MTMR2, Phosphatidylinositol 3-Phosphatases Mutated in Myotubular Myopathy and Type 4B Charcot-Marie-Tooth Disease *. *J. Biol. Chem.* **277**, 4526–4531 (2002).
130. Berger, P., Bonneick, S., Willi, S., Wymann, M. & Suter, U. Loss of phosphatase activity in myotubularin-related protein 2 is associated with Charcot–Marie–Tooth disease type 4B1. *Hum. Mol. Genet.* **11**, 1569–1579 (2002).
131. Schaletzky, J. *et al.* Phosphatidylinositol-5-Phosphate Activation and Conserved Substrate Specificity of the Myotubularin Phosphatidylinositol 3-Phosphatases. *Curr. Biol.* **13**, 504–509 (2003).
132. He, Y. *et al.* Targeting PI3K/Akt signal transduction for cancer therapy. *Signal Transduct. Target. Ther.* **6**, 1–17 (2021).

133. Vanhaesebroeck, B., Guillermet-Guibert, J., Graupera, M. & Bilanges, B. The emerging mechanisms of isoform-specific PI3K signalling. *Nat. Rev. Mol. Cell Biol.* **11**, 329–341 (2010).
134. Hirsch, E. *et al.* Central Role for G Protein-Coupled Phosphoinositide 3-Kinase γ in Inflammation. *Science* **287**, 1049–1053 (2000).
135. Wang, F. *et al.* Lipid products of PI(3)Ks maintain persistent cell polarity and directed motility in neutrophils. *Nat. Cell Biol.* **4**, 513–518 (2002).
136. Nombela-Arrieta, C. *et al.* Differential Requirements for DOCK2 and Phosphoinositide-3-Kinase γ during T and B Lymphocyte Homing. *Immunity* **21**, 429–441 (2004).
137. Chung, C. Y., Funamoto, S. & Firtel, R. A. Signaling pathways controlling cell polarity and chemotaxis. *Trends Biochem. Sci.* **26**, 557–566 (2001).
138. Li, Z. *et al.* Roles of PLC-β2 and -β3 and PI3Kγ in Chemoattractant-Mediated Signal Transduction. *Science* **287**, 1046–1049 (2000).
139. Funamoto, S., Meili, R., Lee, S., Parry, L. & Firtel, R. A. Spatial and Temporal Regulation of 3-Phosphoinositides by PI 3-Kinase and PTEN Mediates Chemotaxis. *Cell* **109**, 611–623 (2002).
140. Li, X. *et al.* Mutually inhibitory Ras-PI(3,4)P2 feedback loops mediate cell migration. *Proc. Natl. Acad. Sci.* **115**, E9125–E9134 (2018).
141. Kuhn, J., Lin, Y. & Devreotes, P. N. Using Live-Cell Imaging and Synthetic Biology to Probe Directed Migration in Dictyostelium. *Front. Cell Dev. Biol.* **9**, (2021).
142. Banerjee, T. *et al.* Spatiotemporal dynamics of membrane surface charge regulates cell polarity and migration. *Nat. Cell Biol.* **24**, 1499–1515 (2022).
143. Posor, Y. *et al.* Spatiotemporal control of endocytosis by phosphatidylinositol-3,4-bisphosphate. *Nature* **499**, 233–237 (2013).
144. Boukhalfa, A. *et al.* PI3KC2α-dependent and VPS34-independent generation of PI3P controls primary cilium-mediated autophagy in response to shear stress. *Nat. Commun.* **11**, 294 (2020).
145. Braccini, L. *et al.* PI3K-C2γ is a Rab5 effector selectively controlling endosomal Akt2 activation downstream of insulin signalling. *Nat. Commun.* **6**, 7400 (2015).
146. Herman, P. K. & Emr, S. D. Characterization of VPS34, a Gene Required for Vacuolar Protein Sorting and Vacuole Segregation in Saccharomyces cerevisiae†. *Mol. Cell. Biol.* **10**, 6742–6754 (1990).
147. Philippon, H., Brochier-Armanet, C. & Perrière, G. Evolutionary history of phosphatidylinositol- 3-kinases: ancestral origin in eukaryotes and complex duplication patterns. *BMC Evol. Biol.* **15**, 226 (2015).
148. Volinia, S. *et al.* A human phosphatidylinositol 3-kinase complex related to the yeast Vps34p-Vps15p protein sorting system. *EMBO J.* **14**, 3339–3348 (1995).
149. Kutateladze, T. G. Mechanistic similarities in docking of the FYVE and PX domains to phosphatidylinositol 3-phosphate containing membranes. *Prog. Lipid Res.* **46**, 315–327 (2007).
150. Itakura, E., Kishi, C., Inoue, K. & Mizushima, N. Beclin 1 Forms Two Distinct Phosphatidylinositol 3-Kinase Complexes with Mammalian Atg14 and UVRAG. *Mol. Biol. Cell* **19**, 5360–5372 (2008).
151. Panaretou, C., Domin, J., Cockcroft, S. & Waterfield, M. D. Characterization of p150, an Adaptor Protein for the Human Phosphatidylinositol (PtdIns) 3-Kinase: SUBSTRATE PRESENTATION BY PHOSPHATIDYLINOSITOL TRANSFER PROTEIN TO THE p150·;PtdIns 3-KINASE COMPLEX *. *J. Biol. Chem.* **272**, 2477–2485 (1997).
152. Huang, W. *et al.* Crystal structure and biochemical analyses reveal Beclin 1 as a novel membrane binding protein. *Cell Res.* **22**, 473–489 (2012).
153. Rostislavleva, K. *et al.* Structure and flexibility of the endosomal Vps34 complex reveals the basis of its function on membranes. *Science* **350**, aac7365 (2015).
154. Ohashi, Y. Activation Mechanisms of the VPS34 Complexes. *Cells* **10**, 3124 (2021).
155. Park, J.-M. *et al.* The ULK1 complex mediates MTORC1 signaling to the autophagy initiation machinery via binding and phosphorylating ATG14. *Autophagy* **12**, 547–564 (2016).
156. Russell, R. C. *et al.* ULK1 induces autophagy by phosphorylating Beclin-1 and activating VPS34 lipid kinase. *Nat. Cell Biol.* **15**, 741–750 (2013).
157. Koyama-Honda, I., Itakura, E., Fujiwara, T. K. & Mizushima, N. Temporal analysis of recruitment of mammalian ATG proteins to the autophagosome formation site. *Autophagy* **9**, 1491–1499 (2013).
158. Karanasios, E. *et al.* Dynamic association of the ULK1 complex with omegasomes during autophagy induction. *J. Cell Sci.* **126**, 5224–5238 (2013).
159. Dooley, H. C. *et al.* WIPI2 Links LC3 Conjugation with PI3P, Autophagosome Formation, and Pathogen Clearance by Recruiting Atg12–5-16L1. *Mol. Cell* **55**, 238–252 (2014).

160. Knævelsrud, H. *et al.* UVRAG mutations associated with microsatellite unstable colon cancer do not affect autophagy. *Autophagy* **6**, 863–870 (2010).
161. Takáts, S. *et al.* Interaction of the HOPS complex with Syntaxin 17 mediates autophagosome clearance in Drosophila. *Mol. Biol. Cell* **25**, 1338–1354 (2014).
162. Christoforidis, S. *et al.* Phosphatidylinositol-3-OH kinases are Rab5 effectors. *Nat. Cell Biol.* **1**, 249–252 (1999).
163. Murray, J. T. & Backer, J. M. Analysis of hVps34/hVps15 Interactions with Rab5 In Vivo and In Vitro. in *Methods in Enzymology* vol. 403 789–799 (Academic Press, 2005).
164. Simonsen, A. *et al.* EEA1 links PI(3)K function to Rab5 regulation of endosome fusion. *Nature* **394**, 494–498 (1998).
165. Christoforidis, S., McBride, H. M., Burgoyne, R. D. & Zerial, M. The Rab5 effector EEA1 is a core component of endosome docking. *Nature* **397**, 621–625 (1999).
166. Nielsen, E. *et al.* Rabenosyn-5, a Novel Rab5 Effector, Is Complexed with Hvps45 and Recruited to Endosomes through a Fyve Finger Domain. *J. Cell Biol.* **151**, 601–612 (2000).
167. Sun, W., Yan, Q., Vida, T. A. & Bean, A. J. Hrs regulates early endosome fusion by inhibiting formation of an endosomal SNARE complex. *J. Cell Biol.* **162**, 125–137 (2003).
168. Poteryaev, D., Datta, S., Ackema, K., Zerial, M. & Spang, A. Identification of the Switch in Early-to-Late Endosome Transition. *Cell* **141**, 497–508 (2010).
169. Nordmann, M. *et al.* The Mon1-Ccz1 Complex Is the GEF of the Late Endosomal Rab7 Homolog Ypt7. *Curr. Biol.* **20**, 1654–1659 (2010).
170. Cabrera, M. *et al.* The Mon1–Ccz1 GEF activates the Rab7 GTPase Ypt7 via a longin-fold–Rab interface and association with PI3P-positive membranes. *J. Cell Sci.* **127**, 1043–1051 (2014).
171. Law, F. *et al.* The VPS34 PI3K negatively regulates RAB-5 during endosome maturation. *J. Cell Sci.* **130**, 2007–2017 (2017).
172. Munson, M. J. *et al.* mTOR activates the VPS34–UVRAG complex to regulate autolysosomal tubulation and cell survival. *EMBO J.* **34**, 2272–2290 (2015).
173. Boutry, M. *et al.* Arf1-PI4KIIIβ positive vesicles regulate PI(3)P signaling to facilitate lysosomal tubule fission. *J. Cell Biol.* **222**, e202205128 (2023).
174. Gillooly, D. J. *et al.* Localization of phosphatidylinositol 3-phosphate in yeast and mammalian cells. *EMBO J.* **19**, 4577–4588 (2000).
175. Ellson, C. D. *et al.* PtdIns(3)P regulates the neutrophil oxidase complex by binding to the PX domain of p40phox. *Nat. Cell Biol.* **3**, 679–682 (2001).
176. Zhou, X., Takatoh, J. & Wang, F. The Mammalian Class 3 PI3K (PIK3C3) Is Required for Early Embryogenesis and Cell Proliferation. *PLOS ONE* **6**, e16358 (2011).
177. Petiot, A., Ogier-Denis, E., Blommaart, E. F. C., Meijer, A. J. & Codogno, P. Distinct Classes of Phosphatidylinositol 3′-Kinases Are Involved in Signaling Pathways That Control Macroautophagy in HT-29 Cells*. *J. Biol. Chem.* **275**, 992–998 (2000).
178. Wu, Y.-T. *et al.* Dual Role of 3-Methyladenine in Modulation of Autophagy via Different Temporal Patterns of Inhibition on Class I and III Phosphoinositide 3-Kinase *. *J. Biol. Chem.* **285**, 10850–10861 (2010).
179. Jaber, N. *et al.* Class III PI3K Vps34 plays an essential role in autophagy and in heart and liver function. *Proc. Natl. Acad. Sci.* **109**, 2003–2008 (2012).
180. Willinger, T. & Flavell, R. A. Canonical autophagy dependent on the class III phosphoinositide-3 kinase Vps34 is required for naive T-cell homeostasis. *Proc. Natl. Acad. Sci.* **109**, 8670–8675 (2012).
181. Bago, R. *et al.* Characterization of VPS34-IN1, a selective inhibitor of Vps34, reveals that the phosphatidylinositol 3-phosphate-binding SGK3 protein kinase is a downstream target of class III phosphoinositide 3-kinase. *Biochem. J.* **463**, 413–427 (2014).
182. Dowdle, W. E. *et al.* Selective VPS34 inhibitor blocks autophagy and uncovers a role for NCOA4 in ferritin degradation and iron homeostasis in vivo. *Nat. Cell Biol.* **16**, 1069–1079 (2014).
183. Honda, A. *et al.* Potent, Selective, and Orally Bioavailable Inhibitors of VPS34 Provide Chemical Tools to Modulate Autophagy in Vivo. *ACS Med. Chem. Lett.* **7**, 72–76 (2016).
184. Ronan, B. *et al.* A highly potent and selective Vps34 inhibitor alters vesicle trafficking and autophagy. *Nat. Chem. Biol.* **10**, 1013–1019 (2014).
185. Pasquier, B. *et al.* Discovery of (2S)-8-[(3R)-3-Methylmorpholin-4-yl]-1-(3-methyl-2-oxobutyl)-2-(trifluoromethyl)-3,4-dihydro-2H-pyrimido[1,2-a]pyrimidin-6-one: A Novel Potent and Selective Inhibitor of Vps34 for the Treatment of Solid Tumors. *J. Med. Chem.* **58**, 376–400 (2015).

186. Zhou, X. *et al.* Deletion of PIK3C3/Vps34 in sensory neurons causes rapid neurodegeneration by disrupting the endosomal but not the autophagic pathway. *Proc. Natl. Acad. Sci.* **107**, 9424–9429 (2010).
187. Cabezas, A., Pattni, K. & Stenmark, H. Cloning and subcellular localization of a human phosphatidylinositol 3-phosphate 5-kinase, PIKfyve/Fab1. *Gene* **371**, 34–41 (2006).
188. Rutherford, A. C. *et al.* The mammalian phosphatidylinositol 3-phosphate 5-kinase (PIKfyve) regulates endosome-to-TGN retrograde transport. *J. Cell Sci.* **119**, 3944–3957 (2006).
189. Sbrissa, D., Ikonomov, O. C. & Shisheva, A. Phosphatidylinositol 3-Phosphate-interacting Domains in PIKfyve: BINDING SPECIFICITY AND ROLE IN PIKfyve ENDOMEMBRANE LOCALIZATION *. *J. Biol. Chem.* **277**, 6073–6079 (2002).
190. Hasegawa, J., Strunk, B. S. & Weisman, L. S. PI5P and PI(3,5)P_2: Minor, but Essential Phosphoinositides. *Cell Struct. Funct.* **42**, 49–60 (2017).
191. Vines, J. H. *et al.* A PI(3,5)P2 reporter reveals PIKfyve activity and dynamics on macropinosomes and phagosomes. *J. Cell Biol.* **222**, e202209077 (2023).
192. Gan, N. *et al.* Structural mechanism of allosteric activation of TRPML1 by PI(3,5)P2 and rapamycin. *Proc. Natl. Acad. Sci.* **119**, e2120404119 (2022).
193. Ikonomov, O. C. *et al.* Active PIKfyve Associates with and Promotes the Membrane Attachment of the Late Endosome-to-trans-Golgi Network Transport Factor Rab9 Effector p40*. *J. Biol. Chem.* **278**, 50863–50871 (2003).
194. Giridharan, S. S. P. *et al.* Lipid kinases VPS34 and PIKfyve coordinate a phosphoinositide cascade to regulate retriever-mediated recycling on endosomes. *eLife* **11**, e69709 (2022).
195. Oppelt, A. *et al.* Production of phosphatidylinositol 5-phosphate via PIKfyve and MTMR3 regulates cell migration. *EMBO Rep.* **14**, 57–64 (2013).
196. Dayam, R. M. *et al.* The Lipid Kinase PIKfyve Coordinates the Neutrophil Immune Response through the Activation of the Rac GTPase. *J. Immunol. Baltim. Md 1950* **199**, 2096–2105 (2017).
197. Gayle, S. *et al.* Identification of apilimod as a first-in-class PIKfyve kinase inhibitor for treatment of B-cell non-Hodgkin lymphoma. *Blood* **129**, 1768–1778 (2017).
198. Mei, S. *et al.* Disruption of PIKFYVE causes congenital cataract in human and zebrafish. *eLife* **11**, e71256 (2022).
199. Min, S. H. *et al.* Loss of PIKfyve in platelets causes a lysosomal disease leading to inflammation and thrombosis in mice. *Nat. Commun.* **5**, 4691 (2014).
200. Choy, C. H. *et al.* Lysosome enlargement during inhibition of the lipid kinase PIKfyve proceeds through lysosome coalescence. *J. Cell Sci.* **131**, jcs213587 (2018).
201. Ikonomov, O. C. *et al.* The Phosphoinositide Kinase PIKfyve Is Vital in Early Embryonic Development: PREIMPLANTATION LETHALITY OF PIKfyve–/– EMBRYOS BUT NORMALITY OF PIKfyve+/– MICE*. *J. Biol. Chem.* **286**, 13404–13413 (2011).
202. Jefferies, H. B. J. *et al.* A selective PIKfyve inhibitor blocks PtdIns(3,5)P2 production and disrupts endomembrane transport and retroviral budding. *EMBO Rep.* **9**, 164–170 (2008).
203. Wada, Y. *et al.* Selective abrogation of Th1 response by STA-5326, a potent IL-12/IL-23 inhibitor. *Blood* **109**, 1156–1164 (2006).
204. Burakoff, R. *et al.* A phase 1/2A Trial of STA 5326, an oral interleukin-12/23 inhibitor, in patients with active moderate to severe Crohn's disease. *Inflamm. Bowel Dis.* **12**, 558–565 (2006).
205. Magid Diefenbach, C. S. *et al.* Results of a completed phase I study of LAM-002 (apilimod dimesylate), a first-in-class phosphatidylinositol-3-phosphate 5 kinase (PIKfyve) inhibitor, administered as monotherapy or with rituximab or atezolizumab to patients with previously treated follicular lymphoma or other B-cell cancers. *J. Clin. Oncol.* **38**, 8017–8017 (2020).
206. Hung, S.-T. *et al.* PIKFYVE inhibition mitigates disease in models of diverse forms of ALS. *Cell* **186**, 786-802.e28 (2023).
207. Lakkaraju, A. K. K. *et al.* Loss of PIKfyve drives the spongiform degeneration in prion diseases. *EMBO Mol. Med.* **13**, e14714 (2021).
208. Rivero-Ríos, P. & Weisman, L. S. Roles of PIKfyve in multiple cellular pathways. *Curr. Opin. Cell Biol.* **76**, 102086 (2022).
209. Kang, Y.-L. *et al.* Inhibition of PIKfyve kinase prevents infection by Zaire ebolavirus and SARS-CoV-2. *Proc. Natl. Acad. Sci.* **117**, 20803–20813 (2020).
210. Luo, Z. *et al.* Inhibition of PIKFYVE kinase interferes ESCRT pathway to suppress RNA virus replication. *J. Med. Virol.* **95**, e28527 (2023).
211. Berridge, M. J., Lipp, P. & Bootman, M. D. The versatility and universality of calcium signalling. *Nat. Rev. Mol. Cell Biol.* **1**, 11–21 (2000).

212. Williams, R. J. P. The evolution of calcium biochemistry. *Biochim. Biophys. Acta BBA - Mol. Cell Res.* **1763**, 1139–1146 (2006).
213. Lloyd-Evans, E. & Waller-Evans, H. Lysosomal Ca2+ Homeostasis and Signaling in Health and Disease. *Cold Spring Harb. Perspect. Biol.* **12**, a035311 (2020).
214. Kilpatrick, B. S., Eden, E. R., Schapira, A. H., Futter, C. E. & Patel, S. Direct mobilisation of lysosomal Ca2+ triggers complex Ca2+ signals. *J. Cell Sci.* **126**, 60–66 (2013).
215. Shen, D., Wang, X. & Xu, H. Pairing phosphoinositides with calcium ions in endolysosomal dynamics. *BioEssays* **33**, 448–457 (2011).
216. Christensen, K. A., Myers, J. T. & Swanson, J. A. pH-dependent regulation of lysosomal calcium in macrophages. *J. Cell Sci.* **115**, 599–607 (2002).
217. Pittman, J. K. Vacuolar Ca2+ uptake. *Cell Calcium* **50**, 139–146 (2011).
218. Garrity, A. G. *et al.* The endoplasmic reticulum, not the pH gradient, drives calcium refilling of lysosomes. *eLife* **5**, e15887 (2016).
219. Atakpa, P., Thillaiappan, N. B., Mataragka, S., Prole, D. L. & Taylor, C. W. IP3 Receptors Preferentially Associate with ER-Lysosome Contact Sites and Selectively Deliver Ca2+ to Lysosomes. *Cell Rep.* **25**, 3180-3193.e7 (2018).
220. Calcraft, P. J. *et al.* NAADP mobilizes calcium from acidic organelles through two-pore channels. *Nature* **459**, 596–600 (2009).
221. Dong, X. *et al.* PI(3,5)P2 controls membrane trafficking by direct activation of mucolipin Ca2+ release channels in the endolysosome. *Nat. Commun.* **1**, 38 (2010).
222. Kilpatrick, B. S., Yates, E., Grimm, C., Schapira, A. H. & Patel, S. Endo-lysosomal TRP mucolipin-1 channels trigger global ER Ca2+ release and Ca2+ influx. *J. Cell Sci.* **129**, 3859–3867 (2016).
223. Peng, W., Wong, Y. C. & Krainc, D. Mitochondria-lysosome contacts regulate mitochondrial Ca2+ dynamics via lysosomal TRPML1. *Proc. Natl. Acad. Sci.* **117**, 19266–19275 (2020).
224. Feng, X. *et al.* Drosophila TRPML Forms PI(3,5)P2-activated Cation Channels in Both Endolysosomes and Plasma Membrane *. *J. Biol. Chem.* **289**, 4262–4272 (2014).
225. Shen, D. *et al.* Lipid storage disorders block lysosomal trafficking by inhibiting a TRP channel and lysosomal calcium release. *Nat. Commun.* **3**, 731 (2012).
226. Chen, C.-C. *et al.* A small molecule restores function to TRPML1 mutant isoforms responsible for mucolipidosis type IV. *Nat. Commun.* **5**, 4681 (2014).
227. Medina, D. L. *et al.* Lysosomal calcium signalling regulates autophagy through calcineurin and TFEB. *Nat. Cell Biol.* **17**, 288–299 (2015).
228. Scotto Rosato, A. *et al.* TRPML1 links lysosomal calcium to autophagosome biogenesis through the activation of the CaMKKβ/VPS34 pathway. *Nat. Commun.* **10**, 5630 (2019).
229. Lima, W. C., Leuba, F., Soldati, T. & Cosson, P. Mucolipin controls lysosome exocytosis in Dictyostelium. *J. Cell Sci.* **125**, 2315–2322 (2012).
230. Samie, M. *et al.* A TRP Channel in the Lysosome Regulates Large Particle Phagocytosis via Focal Exocytosis. *Dev. Cell* **26**, 511–524 (2013).
231. Cao, Q., Yang, Y., Zhong, X. Z. & Dong, X.-P. The lysosomal Ca2+ release channel TRPML1 regulates lysosome size by activating calmodulin. *J. Biol. Chem.* **292**, 8424–8435 (2017).
232. Sun, J. *et al.* LAMTOR1 inhibition of TRPML1-dependent lysosomal calcium release regulates dendritic lysosome trafficking and hippocampal neuronal function. *EMBO J.* **41**, e108119 (2022).
233. Dayam, R. M., Saric, A., Shilliday, R. E. & Botelho, R. J. The Phosphoinositide-Gated Lysosomal Ca2+ Channel, TRPML1, Is Required for Phagosome Maturation. *Traffic* **16**, 1010–1026 (2015).
234. Pryor, P. R., Mullock, B. M., Bright, N. A., Gray, S. R. & Luzio, J. P. The Role of Intraorganellar Ca2+In Late Endosome–Lysosome Heterotypic Fusion and in the Reformation of Lysosomes from Hybrid Organelles. *J. Cell Biol.* **149**, 1053–1062 (2000).
235. Santoni, G. *et al.* Pathophysiological Role of Transient Receptor Potential Mucolipin Channel 1 in Calcium-Mediated Stress-Induced Neurodegenerative Diseases. *Front. Physiol.* **11**, (2020).
236. Bargal, R. *et al.* Identification of the gene causing mucolipidosis type IV. *Nat. Genet.* **26**, 118–122 (2000).
237. Sun, M. *et al.* Mucolipidosis type IV is caused by mutations in a gene encoding a novel transient receptor potential channel. *Hum. Mol. Genet.* **9**, 2471–2478 (2000).
238. Slaugenhaupt, S. A. *et al.* Mapping of the Mucolipidosis Type IV Gene to Chromosome 19p and Definition of Founder Haplotypes. *Am. J. Hum. Genet.* **65**, 773–778 (1999).
239. Wakabayashi, K., Gustafson, A. M., Sidransky, E. & Goldin, E. Mucolipidosis type IV: An update. *Mol. Genet. Metab.* **104**, 206–213 (2011).

240. Kogot-Levin, A., Zeigler, M., Ornoy, A. & Bach, G. Mucolipidosis Type IV: The Effect of Increased Lysosomal pH on the Abnormal Lysosomal Storage. *Pediatr. Res.* **65**, 686–690 (2009).
241. Ruf, B., Greten, T. F. & Korangy, F. Innate lymphoid cells and innate-like T cells in cancer — at the crossroads of innate and adaptive immunity. *Nat. Rev. Cancer* **23**, 351–371 (2023).
242. Hunter, M. C., Teijeira, A. & Halin, C. T Cell Trafficking through Lymphatic Vessels. *Front. Immunol.* **7**, (2016).
243. Bell, E. T cells and DCs get it together. *Nat. Rev. Immunol.* **4**, 86–86 (2004).
244. Krummel, M. F., Bartumeus, F. & Gérard, A. T cell migration, search strategies and mechanisms. *Nat. Rev. Immunol.* **16**, 193–201 (2016).
245. Künzli, M. & Masopust, D. CD4+ T cell memory. *Nat. Immunol.* **24**, 903–914 (2023).
246. Jiang, S. & Dong, C. A complex issue on CD4+ T-cell subsets. *Immunol. Rev.* **252**, 5–11 (2013).
247. Pennock, N. D. *et al.* T cell responses: naïve to memory and everything in between. *Adv. Physiol. Educ.* **37**, 273–283 (2013).
248. Farber, D. L., Yudanin, N. A. & Restifo, N. P. Human memory T cells: generation, compartmentalization and homeostasis. *Nat. Rev. Immunol.* **14**, 24–35 (2014).
249. Carter, S. B. Haptotaxis and the Mechanism of Cell Motility. *Nature* **213**, 256–260 (1967).
250. LEY, K. Arrest Chemokines. *Microcirculation* **10**, 289–295 (2003).
251. Nibbs, R. J. B. & Graham, G. J. Immune regulation by atypical chemokine receptors. *Nat. Rev. Immunol.* **13**, 815–829 (2013).
252. Sankaran, B., Osterhout, J., Wu, D. & Smrcka, A. V. Identification of a Structural Element in Phospholipase C β2 That Interacts with G Protein βγ Subunits *. *J. Biol. Chem.* **273**, 7148–7154 (1998).
253. Barr, A. J., Ali, H., Haribabu, B., Snyderman, R. & Smrcka, A. V. Identification of a Region at the N-Terminus of Phospholipase C-β3 That Interacts with G Protein βγ Subunits. *Biochemistry* **39**, 1800–1806 (2000).
254. Legler, D. F. & Thelen, M. New insights in chemokine signaling. Preprint at https://doi.org/10.12688/f1000research.13130.1 (2018).
255. Volkov, Y., Long, A., McGrath, S., Eidhin, D. N. & Kelleher, D. Crucial importance of PKC-β(I) in LFA-1–mediated locomotion of activated T cells. *Nat. Immunol.* **2**, 508–514 (2001).
256. Fukui, Y. *et al.* Haematopoietic cell-specific CDM family protein DOCK2 is essential for lymphocyte migration. *Nature* **412**, 826–831 (2001).
257. Nombela-Arrieta, C. *et al.* A central role for DOCK2 during interstitial lymphocyte motility and sphingosine-1-phosphate–mediated egress. *J. Exp. Med.* **204**, 497–510 (2007).
258. Ueda, Y. *et al.* Rap1 organizes lymphocyte front-back polarity via RhoA signaling and talin1. *iScience* **26**, 107292 (2023).
259. Shimonaka, M. *et al.* Rap1 translates chemokine signals to integrin activation, cell polarization, and motility across vascular endothelium under flow. *J. Cell Biol.* **161**, 417–427 (2003).
260. Lewis, M., Tarlton, J. F. & Cose, S. Memory versus naive T-cell migration. *Immunol. Cell Biol.* **86**, 226–231 (2008).
261. Bajénoff, M. *et al.* Stromal Cell Networks Regulate Lymphocyte Entry, Migration, and Territoriality in Lymph Nodes. *Immunity* **25**, 989–1001 (2006).
262. Griffith, J. W., Sokol, C. L. & Luster, A. D. Chemokines and Chemokine Receptors: Positioning Cells for Host Defense and Immunity. *Annu. Rev. Immunol.* **32**, 659–702 (2014).
263. Breitfeld, D. *et al.* Follicular B Helper T Cells Express Cxc Chemokine Receptor 5, Localize to B Cell Follicles, and Support Immunoglobulin Production. *J. Exp. Med.* **192**, 1545–1552 (2000).
264. Schaerli, P. *et al.* Cxc Chemokine Receptor 5 Expression Defines Follicular Homing T Cells with B Cell Helper Function. *J. Exp. Med.* **192**, 1553–1562 (2000).
265. Tangye, S. G., Ma, C. S., Brink, R. & Deenick, E. K. The good, the bad and the ugly — TFH cells in human health and disease. *Nat. Rev. Immunol.* **13**, 412–426 (2013).
266. Groom, J. R. & Luster, A. D. CXCR3 in T cell function. *Exp. Cell Res.* **317**, 620–631 (2011).
267. Chapman, N. M., Boothby, M. R. & Chi, H. Metabolic coordination of T cell quiescence and activation. *Nat. Rev. Immunol.* **20**, 55–70 (2020).
268. MacIver, N. J., Michalek, R. D. & Rathmell, J. C. Metabolic Regulation of T Lymphocytes. *Annu. Rev. Immunol.* **31**, 259–283 (2013).
269. Bantug, G. R., Galluzzi, L., Kroemer, G. & Hess, C. The spectrum of T cell metabolism in health and disease. *Nat. Rev. Immunol.* **18**, 19–34 (2018).
270. Michalek, R. D. *et al.* Cutting Edge: Distinct Glycolytic and Lipid Oxidative Metabolic Programs Are Essential for Effector and Regulatory CD4+ T Cell Subsets. *J. Immunol.* **186**, 3299–3303 (2011).

271. Menk, A. V. *et al.* Early TCR Signaling Induces Rapid Aerobic Glycolysis Enabling Distinct Acute T Cell Effector Functions. *Cell Rep.* **22**, 1509–1521 (2018).
272. Gubser, P. M. *et al.* Rapid effector function of memory CD8+ T cells requires an immediate-early glycolytic switch. *Nat. Immunol.* **14**, 1064–1072 (2013).
273. Reinfeld, B. I. *et al.* Cell-programmed nutrient partitioning in the tumour microenvironment. *Nature* **593**, 282–288 (2021).
274. Ho, P.-C. *et al.* Phosphoenolpyruvate Is a Metabolic Checkpoint of Anti-tumor T Cell Responses. *Cell* **162**, 1217–1228 (2015).
275. Chang, C.-H. *et al.* Metabolic Competition in the Tumor Microenvironment Is a Driver of Cancer Progression. *Cell* **162**, 1229–1241 (2015).
276. Knowles, S. E., Jarrett, I. G., Filsell, O. H. & Ballard, F. J. Production and utilization of acetate in mammals. *Biochem. J.* **142**, 401–411 (1974).
277. Buckley, B. M. & Williamson, D. H. Origins of blood acetate in the rat. *Biochem. J.* **166**, 539–545 (1977).
278. Pietrocola, F., Galluzzi, L., Bravo-San Pedro, J. M., Madeo, F. & Kroemer, G. Acetyl Coenzyme A: A Central Metabolite and Second Messenger. *Cell Metab.* **21**, 805–821 (2015).
279. Kaymak, I. *et al.* Carbon source availability drives nutrient utilization in CD8+ T cells. *Cell Metab.* **34**, 1298-1311.e6 (2022).
280. Balmer, M. L. *et al.* Memory CD8+ T Cells Require Increased Concentrations of Acetate Induced by Stress for Optimal Function. *Immunity* **44**, 1312–1324 (2016).
281. Qiu, J. *et al.* Acetate Promotes T Cell Effector Function during Glucose Restriction. *Cell Rep.* **27**, 2063-2074.e5 (2019).
282. van der Windt, G. J. W., Chang, C.-H. & Pearce, E. L. Measuring Bioenergetics in T Cells Using a Seahorse Extracellular Flux Analyzer. *Curr. Protoc. Immunol.* **113**, 3.16B.1-3.16B.14 (2016).
283. Pelgrom, L. R., van der Ham, A. J. & Everts, B. Analysis of TLR-Induced Metabolic Changes in Dendritic Cells Using the Seahorse XFe96 Extracellular Flux Analyzer. in *Toll-Like Receptors: Practice and Methods* (ed. McCoy, C. E.) 273–285 (Springer, 2016). doi:10.1007/978-1-4939-3335-8_17.
284. Koberstein, J. N. *et al.* Monitoring glycolytic dynamics in single cells using a fluorescent biosensor for fructose 1,6-bisphosphate. *Proc. Natl. Acad. Sci.* **119**, e2204407119 (2022).
285. Hu, Q. *et al.* Genetically encoded biosensors for evaluating NAD+/NADH ratio in cytosolic and mitochondrial compartments. *Cell Rep. Methods* **1**, 100116 (2021).
286. Zeki, Ö. C., Eylem, C. C., Reçber, T., Kır, S. & Nemutlu, E. Integration of GC–MS and LC–MS for untargeted metabolomics profiling. *J. Pharm. Biomed. Anal.* **190**, 113509 (2020).
287. Jang, C., Chen, L. & Rabinowitz, J. D. Metabolomics and Isotope Tracing. *Cell* **173**, 822–837 (2018).
288. Lemfack, M. C., Nickel, J., Dunkel, M., Preissner, R. & Piechulla, B. mVOC: a database of microbial volatiles. *Nucleic Acids Res.* **42**, D744–D748 (2014).
289. Tejero Rioseras, A. *et al.* Comprehensive Real-Time Analysis of the Yeast Volatilome. *Sci. Rep.* **7**, 14236 (2017).
290. He, J. *et al.* Fingerprinting Breast Cancer vs. Normal Mammary Cells by Mass Spectrometric Analysis of Volatiles. *Sci. Rep.* **4**, 5196 (2014).
291. Gómez-Mejia, A. *et al.* Rapid detection of Staphylococcus aureus and Streptococcus pneumoniae by real-time analysis of volatile metabolites. *iScience* **25**, 105080 (2022).
292. Berg, R. E., Crossley, E., Murray, S. & Forman, J. Memory CD8+ T Cells Provide Innate Immune Protection against Listeria monocytogenes in the Absence of Cognate Antigen. *J. Exp. Med.* **198**, 1583–1593 (2003).
293. Boutet, M. *et al.* Memory CD8+ T cells mediate early pathogen-specific protection via localized delivery of chemokines and IFNγ to clusters of monocytes. *Sci. Adv.* **7**, eabf9975 (2021).
294. Mehling, M., Frank, T., Albayrak, C. & Tay, S. Real-time tracking, retrieval and gene expression analysis of migrating human T cells. *Lab. Chip* **15**, 1276–1283 (2015).
295. Frick, C. *et al.* Nano-scale microfluidics to study 3D chemotaxis at the single cell level. *PLOS ONE* **13**, e0198330 (2018).
296. Schwarz, J. *et al.* A microfluidic device for measuring cell migration towards substrate-bound and soluble chemokine gradients. *Sci. Rep.* **6**, 36440 (2016).
297. Haque, A., Engel, J., Teichmann, S. A. & Lönnberg, T. A practical guide to single-cell RNA-sequencing for biomedical research and clinical applications. *Genome Med.* **9**, 75 (2017).

298. Love, M. I., Huber, W. & Anders, S. Moderated estimation of fold change and dispersion for RNA-seq data with DESeq2. *Genome Biol.* **15**, 550 (2014).
299. Eggers, L. F. & Schwudke, D. Liquid Extraction: Folch. in *Encyclopedia of Lipidomics* (ed. Wenk, M. R.) 1–6 (Springer Netherlands, 2016). doi:10.1007/978-94-007-7864-1_89-1.
300. Cader, M. Z. *et al.* FAMIN Is a Multifunctional Purine Enzyme Enabling the Purine Nucleotide Cycle. *Cell* **180**, 278-295.e23 (2020).
301. Samaniego, R., Sánchez-Martín, L., Estecha, A. & Sánchez-Mateos, P. Rho/ROCK and myosin II control the polarized distribution of endocytic clathrin structures at the uropod of moving T lymphocytes. *J. Cell Sci.* **120**, 3534–3543 (2007).
302. Smith, A., Bracke, M., Leitinger, B., Porter, J. C. & Hogg, N. LFA-1-induced T cell migration on ICAM-1 involves regulation of MLCK-mediated attachment and ROCK-dependent detachment. *J. Cell Sci.* **116**, 3123–3133 (2003).
303. Amini, R. *et al.* Amoeboid-like migration ensures correct horizontal cell layer formation in the developing vertebrate retina. *eLife* **11**, e76408 (2022).
304. Grishchuk, Y. *et al.* Behavioral deficits, early gliosis, dysmyelination and synaptic dysfunction in a mouse model of mucolipidosis IV. *Acta Neuropathol. Commun.* **2**, 133 (2014).
305. Wu, B. *et al.* Succinyl-CoA Ligase Deficiency in Pro-inflammatory and Tissue-Invasive T Cells. *Cell Metab.* **32**, 967-980.e5 (2020).
306. Balmer, M. L. *et al.* Memory CD8+ T Cells Balance Pro- and Anti-inflammatory Activity by Reprogramming Cellular Acetate Handling at Sites of Infection. *Cell Metab.* **32**, 457-467.e5 (2020).
307. Khanijou, J. K. *et al.* Metabolomics and modelling approaches for systems metabolic engineering. *Metab. Eng. Commun.* **15**, e00209 (2022).
308. Arnold, K. *et al.* Real-Time Volatile Metabolomics Analysis of Dendritic Cells. *Anal. Chem.* **95**, 9415–9421 (2023).